Journal of Research

of the

National Bureau of Standards

UNIVERSITY OF MICHIGAN
NOV 5 - 1958
PHYSICS LIBRARY

SEPTEMBER 1958

VOLUME 61 NUMBER 3

UNIVERSITY OF MICHIGAN
GENERAL LIBRARY
DOCUMENTS DIVISION
1276 ANN ARBOR MICH

U. S. DEPARTMENT OF COMMERCE
Sinclair Weeks, Secretary
NATIONAL BUREAU OF STANDARDS
A. V. Astin, Director

SEPTEMBER • 1958
VOLUME • 61
NUMBER • 3

JOURNAL OF RESEARCH
of the
NATIONAL BUREAU OF STANDARDS

The National Bureau of Standards

Functions and Activities

The functions of the National Bureau of Standards are set forth in the Act of Congress, March 3, 1901, as amended by Congress in Public Law 619, 1950. These include the development and maintenance of the national standards of measurement and the provision of means and methods for making measurements consistent with these standards; the determination of physical constants and properties of materials; the development of methods and instruments for testing materials, devices, and structures; advisory services to Government Agencies on scientific and technical problems; invention and development of devices to serve special needs of the Government; and the development of standard practices, codes, and specifications. The work includes basic and applied research, development, engineering, instrumentation, testing, evaluation, calibration services, and various consultation and information services. Research projects are also performed for other government agencies when the work relates to and supplements the basic program of the Bureau or when the Bureau's unique competence is required. The scope of activities is suggested by the listing of divisions and sections on the inside of the back cover.

Publications

The results of the Bureau's work take the form of either actual equipment and devices or published papers. These papers appear either in the Bureau's own series of publications or in the journals of professional and scientific societies. The Bureau itself publishes three monthly periodicals, available from the Government Printing Office: The Journal of Research, which presents complete papers reporting technical investigations; the Technical News Bulletin, which presents summary and preliminary reports on work in progress; and Basic Radio Propagation Predictions, which provides data for determining the best frequencies to use for radio communications throughout the world. There are also five series of nonperiodical publications: The Applied Mathematics Series, Circulars, Handbooks, Building Materials and Structures Reports, and Miscellaneous Publications.

Information on the Bureau's publications can be found in NBS Circular 460, Publications of the National Bureau of Standards ($1.25) and its Supplement ($1.50), available from the Superintendent of Documents, Government Printing Office, Washington 25, D. C.

Order all publications from the Superintendent of Documents
U. S. Government Printing Office, Washington 25, D. C.

Use of funds for printing this publication approved by the Director of the Bureau of the Budget (June 24, 1958)

Journal of Research of the National Bureau of Standards Vol. 61, No. 3, September 1958 Research Paper 2894

Vibration-Rotation Bands of Ammonia:[1] 1. The Combination Bands $\nu_2+(\nu_1, \nu_3)$

William S. Benedict,[2] Earle K. Plyler, and Eugene D. Tidwell

A general discussion is given of methods used in the analysis of NH_3 vibration-rotation spectra, including the derivation of molecular constants and the determination of line strengths and line widths. Results are given for the region 2.15 to 2.48 μ (4,060 to 4,700 cm^{-1}), in which more than 800 lines have been measured. These have been analyzed into the inversion-doubled perpendicular combination band $\nu_2+\nu_3$ (ν_0=4416.908 and 4434.610 cm^{-1}; band strength=19.7 cm^{-2} atm^{-1}) and the inversion-doubled parallel combination band $\nu_1+\nu_2$ (ν_0=4293.716 and 4320.030 cm^{-1}; band strength=2.9 cm^{-2} atm^{-1}). Complete energy levels for these bands have been found up to $J=12$ and 10, respectively, permitting determinations of molecular constants, which include numerous higher-order effects involving the interaction of rotation, vibration, and inversion. The line widths range from a maximum of 0.57 cm^{-1} atm^{-1}, when $K=J$ to a minimum of <0.2 cm^{-1} atm^{-1}, when $K \ll J$.

1. Introduction

The vibration-rotation spectrum of ammonia, NH_3, has been extensively studied in the past [1],[3] and the main features of the molecular structure are understood.

It is a pyramidal molecule (symmetry C_{3v}) with the N atom approximately 0.38×10^{-8} cm above the plane of the three hydrogens, and the N-H distance approximately 1.02×10^{-8} cm. The rotational structure is that of a symmetric top. Because the pyramid is relatively flat, and the potential barrier to inversion of the nitrogen relatively low, each state is not only characterized by the six vibrational quantum numbers $v_1v_2v_3^{l_3}v_4^{l_4}$ and the rotational quantum numbers J, $K(-J \leq K \leq J)$, but also by the symmetry (s,a) with respect to the inversion plane. The inversion splitting in the ground vibrational state is ~0.79 cm^{-1}.

Although the basic structural features just mentioned are established, there are a number of respects in which additional study with the high resolution afforded by modern infrared spectrometers appears desirable. Only one parallel band, the ν_2 fundamental near 10 μ has been [2] observed with resolution sufficient to separate the K-substructure of the lines, and only a partial analysis has been given [3] of the perpendicular fundamental ν_3 near 2.9 μ. For the other fundamentals, the parallel ν_1 near 3 μ, and the perpendicular ν_4 near 6 μ, only approximate values of the molecular constants are known, and there are no satisfactory analyses of any of the numerous combination and overtone bands, which have been observed extending into the visible region [4,5]. Hence neither a full set of anharmonic vibrational constants, which are needed to establish the equilibrium vibrational frequencies, nor the rotation-vibration interaction constants, which are needed to establish the equilibrium moments of inertia, are at hand. The magnitude of the inversion doubling is accurately known as a function of J and K for the ground vibrational state, as a result of measurements in the microwave region [6], but except for partial results in ν_2 [2], for which the splitting is greatly increased, and for ν_3 [3] (which appear, however, to have been incorrectly interpreted), similar data are not known for the excited vibrational states. The observation of a sufficient number of vibration-rotation bands to establish the variation of the inversion splitting with vibration-rotation would thus be desirable.

In symmetric top molecules the perpendicular bands occupy a special role, and a number of such bands must be studied in order to obtain the constants C, D^K, and ζ corresponding to rotation about the symmetry axis. This is because perpendicular bands, i. e., those in which the dipole moment changes perpendicular to the symmetry axis, occur when one of the vibrational states is doubly degenerate; and in such states there is a component of angular momentum $C_v\zeta_v$ due to vibration that interacts with the rotational angular momentum to remove the K-degeneracy. Hence the observed spacings of the lines yield $C_v(1-\zeta_v)$ rather than C_v. If ζ_v can be observed for both fundamentals, the theoretical relation $\zeta_3+\zeta_4=(B/2C)-1$ permits the calculation of C. This relation, however, is strictly true only for infinitesimal vibrations, and in order to obtain accurate molecular constants it is necessary to establish empirically the variation of the ζ with the other vibrational quantum numbers. For this purpose, as many perpendicular bands as possible must be analyzed.

In the overtone and combination bands, both perpendicular and parallel, numerous cases of near-resonance interaction are possible between the various levels of the same total symmetry. This introduces additional complications. The cases of resonance must be recognized and evaluated in order to derive the molecular potential function from the observed molecular constants. Inasmuch as it appears that it will be difficult to achieve a satisfactory derivation of the harmonic and anharmonic potential function

[1] This research was supported in part by the United States Air Force under Contract AF 18(600)-1557 monitored by the Air Force Office of Scientific Research of the Air Research and Development Command, and in part by the Atomic Energy Commission.
[2] Laboratory of Astrophysics and Physical Meteorology, The Johns Hopkins University, Baltimore, Md.
[3] Figures in brackets indicate the literature references at the end of this paper.

of the ammonia molecule from the bands of NH_3 alone, it is desirable to study the additional bands obtained with the deuterium substituted compounds ND_3, which preserves the molecular symmetry, and ND_2H and NHD_2, which are asymmetric tops. Only by such a program can one hope to obtain definitive values of the equilibrium molecular structure and potential constants.

Another respect in which the infrared spectrum of the ammonias deserves further study concerns the strength, width, shape, and possible pressure-shift of the lines. The observed spectrum, for a given condition of pressure and path length, depends upon these factors, and from a quantitative study of the variation of absorption with length and pressure it is possible to deduce the strengths, widths, and shapes of individual lines [7]. NH_3 is a particularly interesting molecule for such studies, because experiments in the microwave region have shown that the collision diameter varies markedly with the rotational quantum number. The results are in good agreement with those calculated by Anderson [8], on the basis of his general theory of collision broadening as caused by dipole-dipole forces. The same theory should apply in the infrared bands, and predicts that the widths should be nearly independent of the vibrational quantum numbers, so long as the upper state is a member of a narrow inversion doublet, as is the case for the microwave lines. When, however, the upper state has a wider inversion doubling, as in ν_2 and its combinations and overtones, the possibilities of resonant dipole interactions are reduced and the widths should be less. Because of the strong resonance interactions the half-widths are among the greatest that have been observed in molecular spectra, ranging up to 0.75 cm^{-1} at 1-atm pressure. Hence they may be measured directly in the infrared region whenever overlapping from other lines does not interfere.

The microwave collision diameters were obtained at low pressures; other interesting results were found in that region [9] at pressures from 10 cm to 1 atm. The individual lines of the inversion Q-branch are no longer resolved, but absorption in their overlapping long-wavelength wing can be measured throughout the frequency range 0.6 to 0 cm^{-1}, thus providing a test of the line shape. It is found that the absorption is considerably increased over that given by the Lorentz-Van Vleck-Weisskopf theory [10]. This has been interpreted [11] in terms of a shift of the resonance frequency of the lines toward zero frequency, as a result of the intermolecular forces. It would thus appear of great interest to study the line shape in the infrared, particularly because no gross evidence of a corresponding pressure shift of the inversion splitting toward zero is apparent [12].

An extensive series of measurements of the ammonia rotation-vibration spectrum in the region 1,700 to 7,100 cm^{-1} has been undertaken, with the purpose of clarifying as many as possible of the points mentioned above. Preliminary reports have been given of some aspects of the results [13].

In the present paper are described in detail the general methods used in analyzing the spectra, particularly those of the perpendicular-type bands which predominate in the combination and overtone regions. These will be illustrated by the analysis of the bands in the region of 2.3 μ, where fall the combination bands $(\nu_1,\nu_3+\nu_2)$,[4] a region in which the identification of lines has been nearly complete. Some results of intensity and line-width studies in this region will also be given. Subsequent papers will deal with further problems of line width and shape, and with analysis of other bands of NH_3 and its isotopic modifications.

2. Experimental Details and Method of Analysis

The spectrometer was the 15,000-lines-per-inch grating spectrometer of the National Bureau of Standards. Its construction and operation have been described elsewhere. Wavelength calibrations were by interferometric fringes, between secondary standards of the krypton arc. Under the most favorable conditions absorption lines separated by 0.08 cm^{-1} could be resolved, and the frequency measurements are believed reliable to ± 0.03 cm^{-1} for unblended lines.

Inasmuch as it was desired to study strength, width, and shapes of the lines,[5] cells of various lengths were used; for optimum resolution a path length of 1,000 cm was required, with pressures varying from a few millimeters to 30 cm. Two shorter cells, of lengths 5.0 and 15.5 cm, with the gas at pressures from 2 cm to 1 atm, were employed to give spectra for which the lines were more nearly in the linear region of the curve of growth.

A large number of tracings of the spectrum were obtained between 2.15 and 2.5 μ (4,000 to 4,700 cm^{-1}). NH_3 lines occur throughout this region. The strongest absorption is from 4,200 to 4,500 cm^{-1}, and decreases in intensity to both directions. At the long-wavelength limit NH_3 absorption is still fairly strong at 10 m and 30-cm pressure, but is obscured by the 2.7-μ water-vapor band; near 4,700 cm^{-1} the NH_3 absorption reaches a minimum, other absorption (to be described in a subsequent paper) due to the 2.0-μ group of bands giving increasing intensity at shorter wavelengths.

The general expressions for the line positions and line strengths in NH_3 are now presented. For a review of the basic theory on which we rely, see Nielsen [14]. In his article the pyramidal XY_3 molecule, of which NH_3 is an example, is described in some detail. The present notation with a few obvious variations, will follow that recommended by Mulliken [15]. The energy levels may be written

$$T(v,p,J,K)=G(v)+F(v,J,K)\ \pm\frac{1}{2}E_{ins}(v,J,K), \quad (1)$$

where G is the contribution to the energy from vibration, and depends on the six vibrational quantum numbers, $V_i(i=1,2,3,4)$ and $l_i(i=3,4)$; F is the con-

[4] These bands have been observed previously [4], but with insufficient resolution to obtain accurate constants.

[5] For the methods used, see reference [7].

tribution from rotation, depending on the rotational quantum numbers J and $|K|$(and when $\Sigma l_i \neq 0$ on the sign of K), and on rotational constants, which are functions of the vibrational state; and E_{inv} is the splitting of the levels due to inversion, a function of all the quantum numbers. In eq (1) v stands for the six vibrational quantum numbers, and p for the parity of the inversion level, taking the values + and − corresponding to the sign before E_{inv}. Inasmuch as E_{inv} is written as a separate term, the vibrational energy formula refers to the average energy of the pair of inversion-doubled states, and may be written

$$G=\sum_{i=1}^{4}\nu_i v_i+\sum_{i=1}^{4}\sum_{j=1}^{4}x_{ij}(v_i-1)(v_j-1)+\sum_{i=3}^{4}\sum_{j=3}^{4}g_{ij}(v_i-l_i)(v_j-l_j)+\text{terms cubic in } v_i \pm E_{res}. \quad (2)$$

The ν_i are the observed positions of the fundamental bands ($v_i=1, v_j=0$), which for NH_3 have the approximate values (cm^{-1}) $\nu_1(A_1)=3336.9$, $\nu_2(A_1)=950.0$, $\nu_3(E)=3443.4$, $\nu_4(E)=1626.3$. The x's and g's are the anharmonic constants that it is desired to derive from measurements of combination and overtone bands ($v_i>1$ or $v_j>0$). E_{res} is an additional term that it may be necessary to introduce when two vibrational levels of like symmetry lie close together; for NH_3 the most important case of vibrational (Fermi) resonance occurs for all states with $v_1 \neq 0$, since $2\times\nu_4 \cong \nu_1$.

The rotational portion of the energy expression is

$$F(v,J,K)=B_v J(J+1)+(C_v-B_v)K^2-D_v^J J^2(J+1)^2-D_v^{JK}J(J+1)K^2-D_v^K K^4+\ \ldots \pm 2C_s\zeta_v K \mp \zeta_v^J J(J+1)K \mp \zeta_v^K K^3+\ \ldots, \quad (3)$$

where the rotational constants on the first line apply to all v, and the additional terms on the second line are needed for states where $l \neq 0$, and represent the contribution of the angular momentum of the degenerate vibrational mode, through Coriolis forces. The terms with coefficients ζ^J and ζ^K, representing the effect of centrifugal stretching on the Coriolis interaction, will be small; if higher-order interaction terms are unimportant

$$\zeta^J \cong (2D^{JK}+4D^J)\zeta \quad (3a)$$

and

$$\zeta^K \cong (2D^{JK}+4D^K)\zeta. \quad (3b)$$

In any given degenerate vibrational state, the symmetry properties of the K-split levels are different, so that the sets of levels with upper and lower signs are associated with different transitions, $K'-K''=+1$ for one sign and -1 for the other. In addition to the standard terms in F given in eq (3), additional terms resulting from Coriolis-type interactions may occasionally be encountered when the energy differences between states of like over-all (vibrational and rotational) symmetry are small.

The energy terms resulting from inversion may conveniently be expressed in the form

$$E_{inv}(v,J,K)=E_v^t(v)\exp[b_v^t J(J+1)+(c_v^t-b_v^t)K^2+d_v^{tJ}J^2(J+1)^2+d_v^{tJK}J(J+1)K^2+d_v^{tK}K^4+\ \ldots \pm \tfrac{1}{2}f_n^t(A_1A_2), \quad (4)$$

where $E^0{}_{inv}$ is the splitting in the rotationless level, and the constants b^r, etc., represent the interaction of rotation and inversion. The term $f_n^t(A_1A_2)$ applies to the levels where states with over-all symmetry A_1 and A_2 form a nearly degenerate pair. There will then be an additional splitting term, depending on the value n of the K for which the degeneracy occurs. For $K=3$, in states of vibrational symmetry A (ground level, etc.), Nielsen and Dennison [16] have shown that

$$f_3^t(A_1A_2)=\beta_{3,v}(J-2)(J-1)J(J+1)(J+2)(J+3). \quad (4a)$$

For $K=2$, in one K-component of states of vibrational symmetry E,

$$f_2^t(A_1A_2)=\beta_{2,v}(J-1)J(J+1)(J+2) \quad (4b)$$

and for $K=1$, in the other K-component of states of vibrational symmetry E,

$$f_1^t(A_1A_2)=\beta_{1,v}J(J+1). \quad (4c)$$

Costain [17] has shown that the form (4) gives a much more rapidly convergent fit to the inversion of the ground state, for which data have been measured with very great accuracy [6], than does the representation in a simple power series in $J(J+1)$ and K^2. This is found to hold also for the vibrationally excited levels.

The values of the inversion constants for the ground state are $E_0^t=0.7934$ cm^{-1}; $b_0^t=-6.36996\times10^{-3}$, $c_0^t-b_0^t=8.88986\times10^{-3}$, $d_0^{tJ}=8.6922\times10^{-7}$, $d_0^{tJK}=-1.7845\times10^{-6}$, $d_0^{tK}=5.3075\times10^{-7}$, $\beta_{3,0}-1.17\times10^{-8}$ cm^{-1}. The resulting calculated values of E_{inv} $(0,J,K)$ are presented in table 1.

Spectral-line positions are given by subtracting lower-state energies from upper-state energies, both as given by eq (1) to (4). The selection rules governing the possible transitions are the well-known rules for the symmetric rotator, $\Delta J=\pm1,0$; $\Delta K=\pm1,0$, with additional restrictions upon the parity of the inversion state in eq (1) and the sign of the K-split state in eq (3), as imposed by the over-all symmetry. The bands analyzed are of the types whose rules are summarized in table 2. The notation s and a refers to the states whose wave functions are symmetric or antisymmetric with respect to the inversion plane; and the + or − signs under Δp refer to the actual algebraic sign in eq (1) corresponding to this symmetry. In perpendicular bands, only one of the two K-substates combines with the ground state, one sign being associated with transitions in the ${}^RP$-, ${}^RQ$-, and ${}^RR$-branches ($K'-K''=+1$) and the other with the ${}^PP$, ${}^PQ$, and ${}^PR$-branches ($K'-K''=-1$).

TABLE 1. *Calculated inversion splittings, $0^a - 0^s$ (cm^{-1})*

J	$K=0\rightarrow$	1	2	3	4	5	6	7	8	9	10	11	12	13	14	15
0	0.793															
1	.783	0.790														
2	.764	.771	0.791													
3	.735	.742	.762	0.796												
4	.699	.705	.724	.757	0.805											
5	.656	.662	.680	.710	.756	0.818										
6	.608	.614	.630	.659	.700	.758	0.836									
7	.557	.562	.577	.601	.641	.694	.765	0.858								
8	.504	.508	.522	.553	.580	.627	.691	.775	0.885							
9	.450	.454	.466	.474	.518	.560	.617	.692	.789	0.917						
10	.398	.401	.412	.458	.457	.495	.544	.610	.696	.807	0.954					
11	.348	.351	.360	.327	.398	.432	.473	.532	.606	.703	.830	0.998				
12	.300	.303	.311	.404	.344	.372	.409	.459	.521	.605	.714	.857	1.048			
13	.256	.258	.265	.147	.294	.317	.349	.390	.444	.514	.606	.728	0.889	1.106		
14	.216	.218	.224	.432	.249	.268	.294	.329	.374	.433	.510	.611	.744	0.926	1.172	
15	.181	.182	.187	.080	.207	.224	.245	.274	.311	.360	.424	.507	.618	.767	0.969	1.247

TABLE 2. *Selection rules for* NH_3

Type	ΔJ	ΔP	ΔK	$\mp$ sign in eq (3)	Example
$\parallel$, $a-s$	0	$+\leftarrow-$	0		$\nu_1+\nu_2$, upper, $\nu_0=4{,}320$ cm^{-1}.
$\parallel$, $s-a$	0	$-\leftarrow+$	0		$\nu_1+\nu_2$, lower, $\nu_0=4{,}294$ cm^{-1}.
$\perp$, $a-s$	$1\leftarrow0$	$-\leftarrow-$	±1	$\mp$	$\nu_3+\nu_2$, lower, $\nu_0=4{,}417$ cm^{-1}.
$\perp$, $s-a$	$1\leftarrow0$	$+\leftarrow+$	±1	$\mp$	$\nu_3+\nu_2$, upper, $\nu_0=4{,}435$ cm^{-1}.
$\perp$	$2\leftarrow0$		±1	$\pm$	$2\nu_2^2$ $\nu_0=6{,}850$ cm^{-1}.

The line strengths are given to first approximation by the familiar Hönl-London formulas [18], which apply rigorously to symmetric-top molecules in which there are no interactions between vibrations or between vibration and rotations. Such interactions are of nearly universal occurrence in molecules, but their magnitude is unpredictable, varies from band to band, and is frequently not large, so that the rigid line strengths are of essential value as guides to the relative intensities to be expected in all bands of a given molecule. The line strength may be written formally

$$S_{vv'}(v',\ v'',\ J',\ J'',\ K',\ K'')=S_v H^0(J,\ K)g(J,\ K)F(v,\ J,\ K)\exp\left[-E''(J'',\ K'')/kT\right]/Q_r. \quad (5)$$

$S_{vv'}$ is the strength of each vibration-rotation line, where S_v is the total strength of all lines in the vibrational transition; $H^0(J,\ K)$ are the Hönl-London factors; $g(J,\ K)$ is the statistical weight; $F(v,\ J,\ K)$ is the correction factor for vibration-rotation interactions; $E''(J'',\ K'')$ is the ground-state energy, and Q_r is the rotational state-sum, $Q_r=\sum_{JK} ge^{-E''/kT}$.

For the ground levels (s, a) of NH_3, with three equivalent nuclei of spin 1/2,

$$g=\begin{cases} 4(2J+1) & \text{for } K=0,\ J \text{ even } (a) \text{ and } J \text{ odd } (s) \\ 0 & \text{for } K=0,\ J \text{ odd } (a) \text{ and } J \text{ even } (s) \\ 2(2J+1) & \text{for } K=1,\ 2,\ 4,\ 5,\ \ldots \\ 4(2J+1) & \text{for } K=3,\ 6,\ 9,\ \ldots \end{cases}$$

The Hönl-London factors are

Branch	$K'-K''$	$J'-J''$	$H^0(J'',K'')$	
^qP	0	-1	$(J^2-K^2)/J(2J+1)$	(5a)
^qQ	0	0	$K^2/J(J+1)$	(5b)
^qR	0	$+1$	$[(J+1)^2-K^2]/(J+1)(2J+1)$	(5c)
^pP	-1	-1	$(J-1+K)(J+K)/4J(2J+1)$	(5d)
^pQ	-1	0	$(J+1-K)(J+K)/4J(J+1)$	(5e)
^pR	-1	$+1$	$(J+2-K)(J+1-K)/4(J+1)(2J+1)$	(5f)
^rP	$+1$	-1	$(J-1-K)(J-K)/4J(2J+1)$	(5j)
^rQ	$+1$	0	$(J+1+K)(J-K)/4J(J+1)$	(5k)
^rR	$+1$	$+1$	$(J+2+K)(J+1+K)/4(J+1)(2J+1)$.	(5l)

In (5j), (5k), and (5l), when $K=0$, an additional factor 2 is required.

Using formulas (5), values of E'' calculated from the rotational constants to be derived and presented at a later point, and assuming $F=1$, values of $S_{vv'}/S_v$ have been calculated for $T=298°$ K. These are presented in table 3, as normalized to the value $S_v=10{,}000$.

The entries with $K''=0$ carry suffixes s or a to indicate which one of the inversion levels is present and that the line is absent in the other band. The other entries apply to both a-s and s-a bands, except that in the calculation the energy difference between

the 0^s and 0^a states was ignored, so that the values given are averages; actually for a-s bands the strengths will be about 0.2 percent higher, and for s-a, 0.2 percent lower than tabulated.

When lines in an observed band are arranged as in table 3, by (J',K'), the derivation of molecular constants is facilitated. Rotational analyses are presented in tables of similar format. It will be noted that the strengths entered in table 3 range from a maximum of 236 down to 0.02, on the scale for which the total strength of lines in an inversion pair of bands is 10,000. It has not seemed necessary to extend the tables further, since only in exceptionally strong bands with excellent resolution will the weakest lines be observable. In most bands, however, lines down to $S_r=0.2$ should be observed if they can be resolved from stronger neighbors. In many of the parallel bands the lines with J' constant may not be fully resolved into their K-components, especially for low K.

The analysis of parallel bands presents no great difficulty. The Q-branches (which contain altogether 39.2 percent of the total band strength) can in general be recognized readily. They are never completely resolved; even when $(B'-B'')$ and $(C''-C''')$ are both large, there is considerable overlapping, and the weakest lines, those where $K<J$, are difficult to distinguish. The strongest Q-branch lines, as table 3 shows, are those with $K=J$, and these can usually be picked out, forming a regular series with $\nu\cong\nu_0+(B'-B'')J+(C''-C''')J^2$. (These remarks apply to each of the inversion-doubling bands; the two bands may overlap, but in many cases are widely separated.) The P- and R-branches may then be located, the K-substructure of each J-line, with the number of components increasing with J, forming when resolved, a characteristic pattern of lines with $\nu\cong\nu_{m,0}+aK^2$, and with the intensity of every third line enhanced. Arrangement of the lines of the three branches into tabular form should reveal constant combination differences

$$\Delta_1F''(J',K')={}^QR(J+1,K)-{}^QQ(J+1,K)={}^QQ(J,K)-{}^QP(J,K)=2(B_0-D_0^{JK}K^2)J-4D_0^JJ^3 \qquad (6)$$

or, when the Q-branch line is too weak to observe

$$\Delta_2F''(J',K')={}^QR(J,K)-{}^QP(J,K)=(4J+2)[B_0-D_0^{JK}K^2-2D_0^J(J^2+J+1)]. \qquad (6a)$$

In the analysis of perpendicular bands when observed under high-resolution conditions, it has been desirable to proceed rather differently from the manner usually reported in the literature, which applies when resolution is insufficient to separate the groups of lines constituting the ${}^PQ$- and ${}^RQ$-branches. With such incomplete resolution, only the mean position of all lines with common K, but varying J, is measured,

TABLE 3. *Rotational line strengths in* NH_3

The tabulated quantity is $10^4\,S_\nu/S_0$, calculated by eq (5) for $T=298°$ K.

	Parallel bands			Perpendicular bands					
J'_K	${}^QP$	${}^QQ$	${}^QR$	${}^PP$	${}^PQ$	${}^PR$	${}^RP$	${}^RQ$	${}^RR$
0	62.0[a]	.....	.....	15.7	.....	.....	.....	.....	.....
1_0	102.0[a]	.....	68.0[a]	19.5	23.6	.....	.....	.....	.....
1_1	39.0	47.2	.....	42.5	.....	.....	25.5[a]	93.0[a]	68.0[a]
2_0	115.2[a]	.....	123.5[a]	19.5	32.5	7.87	.....	.....	.....
2_1	52.0	21.7	47.2	34.3	22.9	.....	38.4[a]	125.7[a]	93.0[a]
2_2	34.3	91.6	.....	112.5	.....	.....	3.25	21.7	47.2
3_0	104.2[a]	.....	152.9[a]	17.0	34.1	12.99	.....	.....	.....
3_1	49.9	11.35	69.3	26.3	30.0	4.57	39.1[a]	134.3[a]	102.0[a]
3_2	42.1	48.0	45.7	80.4	39.4	.....	4.98	28.4	43.3
3_3	53.7	236.2	.....	60.8	.....	.....	1.75	18.0	68.6
4_0	81.1[a]	.....	153.5[a]	12.35	29.9	14.61	.....	.....	.....
4_1	39.5	5.98	73.1	18.26	28.4	7.71	32.4[a]	117.3[a]	96.0[a]
4_2	36.5	25.2	61.7	53.2	48.3	5.62	4.94	26.9	36.5
4_3	60.8	124.1	78.7	38.7	15.63	.....	2.61	22.1	54.0
4_4	19.35	125.0	.....	56.8	.....	.....	1.90	27.6	157.5
5_0	54.7[a]	.....	130.4[a]	8.09	21.3	13.28	.....	.....	.....
5_1	27.1	3.02	63.8	11.44	22.3	8.42	22.8[a]	89.2[a]	78.2[a]
5_2	26.1	12.74	58.9	32.1	41.8	9.20	3.87	21.1	28.0
5_3	48.1	62.6	98.1	22.7	17.74	1.737	2.45	19.1	39.3
5_4	20.2	63.1	31.3	32.6	11.57	.....	2.67	31.3	110.4
5_5	13.0	115.7	.....	95.1	.....	.....	0.504	9.86	78.2
6_0	32.9[a]	.....	97.3[a]	4.84	15.09	10.30	.....	.....	.....
6_1	16.59	1.44	48.0	6.46	15.17	7.24	14.08[a]	59.1[a]	56.7[a]
6_2	16.18	6.06	46.4	17.64	29.8	9.50	2.59	14.37	19.2
6_3	31.4	29.8	85.4	12.19	14.05	2.69	1.795	13.65	26.1
6_4	14.61	30.0	35.8	17.15	12.10	1.052	2.35	24.8	71.2
6_5	12.47	55.0	23.1	49.6	16.06	.....	0.664	10.31	49.3
6_6	16.42	192.6	.....	36.2	.....	.....	.260	6.60	69.4
7_0	17.47[a]	.....	63.8[a]	2.51	9.06	6.96	.....	.....	.....
7_1	8.79	0.648	31.8	3.30	9.09	5.25	7.66[a]	35.2[a]	36.4[a]
7_2	8.82	2.69	31.5	8.81	18.37	7.64	1.461	8.74	11.97
7_3	17.61	13.22	61.1	5.97	9.14	2.60	0.760	8.42	15.75
7_4	8.69	13.28	28.5	8.27	8.77	1.522	1.602	16.16	42.0
7_5	8.28	24.4	24.4	23.4	13.00	0.618	0.543	7.48	28.5
7_6	14.41	85.2	32.1	17.0	5.23	.....	.318	5.35	39.6
7_7	4.86	73.2	.....	25.4	.....	.....	.257	8.28	112.4

TABLE 3. *Rotational line strengths in* NH_3—Continued

	Parallel bands			Perpendicular bands					
J'_K	^QP	^QQ	^QR	^PP	^PQ	^PR	^RP	^RQ	^RR
8_0	8.41[a]	--------	37.5[a]	1.185	4.73	4.23	--------	--------	--------
8_1	4.21	0.263	19.04	1.526	4.85	3.30	3.73[a]	18.58[a]	21.12[a]
8_2	4.27	1.110	18.94	4.00	9.98	5.14	0.738	4.80	6.80
8_3	8.72	5.44	37.7	2.67	5.13	1.938	.582	4.67	8.64
8_4	4.44	5.48	18.60	3.64	5.20	1.364	.908	9.08	22.64
8_5	4.50	10.01	17.75	10.19	10.21	1.657	.342	4.44	15.12
8_6	8.72	35.0	30.8	7.32	4.59	0.348	.240	4.20	20.69
8_7	3.90	30.0	10.46	10.95	3.19	--------	.291	3.65	58.0
8_8	2.74	51.1	--------	34.5	--------	--------	.061	4.89	41.8
9_0	3.62[a]	--------	19.69[a]	0.507	2.25	2.23	--------	--------	--------
9_1	1.826	0.100	9.91	.641	2.31	1.83	1.634[a]	8.87[a]	10.93[a]
9_2	1.863	.421	10.05	1.651	4.82	2.99	0.333	2.20	3.40
9_3	3.85	2.07	20.50	1.085	2.53	1.206	.272	2.21	4.31
9_4	2.00	2.15	10.46	1.464	2.66	0.942	.444	4.49	11.10
9_5	2.09	3.80	10.56	4.05	5.53	1.373	.179	2.27	7.31
9_6	4.32	13.28	20.61	2.88	2.78	0.432	.139	2.28	9.89
9_7	2.16	11.34	9.23	4.42	2.60	.188	.202	4.42	27.45
9_8	2.08	19.58	6.39	12.73	3.68	--------	.064	1.97	19.59
9_9	2.83	66.3	--------	9.91	--------	--------	.029	1.376	28.75
10_0	1.419[a]	--------	9.35[a]	0.196	0.967	1.066	--------	--------	--------
10_1	0.715	--------	4.69	.244	1.001	0.902	0.634[a]	3.80[a]	5.13[a]
10_2	.732	0.148	4.79	.621	2.100	1.531	.134	0.948	1.57
10_3	1.526	.725	9.91	.403	1.116	0.646	.113	.964	1.95
10_4	0.807	.729	5.17	.538	1.198	.540	.191	1.980	4.96
10_5	.862	1.281	5.40	1.466	2.578	.873	.081	1.025	3.10
10_6	1.832	4.62	11.17	1.038	1.375	.329	.067	1.065	4.32
10_7	0.978	3.96	5.60	1.505	1.490	.217	.108	2.191	11.88
10_8	1.005	7.07	5.21	4.51	2.700	.194	.0405	1.092	8.40
10_9	1.897	23.02	7.36	3.48	0.996	--------	.0264	1.049	12.39
10_{10}	0.695	19.93	--------	5.53	--------	--------	.0238	1.421	38.77
11_0	0.500[a]	--------	3.98[a]	0.069	0.379	0.460	--------	--------	--------
11_1	.253	--------	2.01	.084	.390	.396	0.229[a]	1.48[a]	2.17[a]
11_2	.261	0.048	2.06	.213	.824	.693	.049	0.371	0.654
11_3	.546	.235	4.31	.136	.441	.304	.042	.377	.804
11_4	.291	.235	2.28	.180	.481	.265	.072	.785	2.02
11_5	.316	.429	2.44	.488	1.053	.460	<.02	.411	1.30
11_6	.689	1.488	5.22	.342	0.584	.192		.439	1.72
11_7	.380	1.274	2.77	.492	.642	.158		.929	4.69
11_8	.415	2.16	3.00	1.462	1.365	.203		.495	3.29
11_9	.875	7.36	5.41	1.120	0.668	.046		.505	5.00
11_{10}	.426	6.36	1.99	1.77	.504	--------		.954	14.21
11_{11}	.322	11.10	--------	5.83	--------	--------		.349	10.95
12_0	0.155[a]	--------	1.544[a]	<0.02	0.132	0.180	--------	--------	--------
12_1	.081	--------	0.780	--------	.137	.158	0.074[a]	0.529[a]	0.837[a]
12_2	.084	--------	.804	.068	.281	.281	<.02	.131	.248
12_3	.178	0.070	1.686	.042	.149	.127		.134	.301
12_4	.095	.070	0.903	.056	.173	.116		.292	.749
12_5	.104	.128	.978	.148	.386	.207		.158	.478
12_6	.230	.441	2.136	.104	.210	.093		.161	.642
12_7	.130	.377	1.182	.147	.249	.079		.349	1.68
12_8	.147	.638	1.291	.433	.561	.131		.192	1.18
12_9	.368	2.17	2.738	.330	.308	.046		.208	1.69
12_{10}	.179	1.866	1.339	.519	.309	.022		.441	5.03
12_{11}	.171	3.26	1.008	1.69	.488	--------		.215	3.84
12_{12}	.282	11.68	--------	1.43	--------	--------		.161	6.05
13_0	0.044[a]	--------	0.542[a]	--------	0.042	0.064	--------	--------	--------
13_1	.023	--------	.278	--------	.044	.057	0.022[a]	0.167[a]	0.292[a]
13_2	.024	--------	.286	--------	.094	.103	--------	.042	.086
13_3	.051	--------	.597	--------	.051	.047	--------	.043	.102
13_4	.029	--------	.322	--------	.056	.044	--------	.092	.255
13_5	.031	--------	.359	0.047	.127	.082	--------	.049	.161
13_6	.070	0.120	.780	.032	.073	.039	--------	.053	.210
13_7	.040	.103	.443	.047	.085	.034	--------	.117	.560
13_8	.047	.174	.500	.119	.199	.064	--------	.066	.388
13_9	.108	.587	1.254	.090	.115	.0267	--------	.075	.552
13_{10}	.063	.505	0.616	.137	.131	.0195	--------	.166	1.625
13_{11}	.071	.878	.586	.46	.273	.0195	--------	.091	1.236
13_{12}	.147	3.39	.978	.38	.110	--------	--------	.091	1.94
13_{13}	.058	2.87	--------	.65	--------	--------	--------	.141	6.34
14_0		--------	0.173[a]				--------	--------	--------
14_1			.089					0.049[a]	0.087[a]
14_2			.093			0.0339			.024
14_3			.195						.032
14_4			.104					.026	.076
14_5			.115			.0290			.049
14_6			.258						.064
14_7			.147					.035	.169
14_8			.173			.0262			.117
14_9		0.146	.403						.165
14_{10}		.128	.234					.054	.481
14_{11}		.190	.263	0.107					.350
14_{12}	0.048	.783	.550	.086					.568
14_{13}		.723	.217	.15				.075	1.84
14_{14}		1.39	--------	.59				.029	1.54
15_{10}									0.121
15_{11}									.094
15_{12}		0.18							.143
15_{13}		.16							.456
15_{14}		.31		0.12					.40
15_{15}		1.27		.13					.74
16_{13}		0.028							0.083
16_{14}		.062							.069
16_{15}		.27							.116
16_{16}		.27							.63

and form a parabolic series around the band center. In NH_3, however, $(B'-B'')$ is in most bands so high that for each K, the ${}^RQ$ and ${}^PQ$ lines (each of which is in a series with $\nu=\nu_{Q0}+(B'-B'')J(J+1)+\ldots$) extend over several K-intervals, and the region of the band center is confusingly complex. A much simpler pattern is found in the band wings, containing the ${}^PP$- and ${}^RR$-branches, which are the stongest individual lines, and which may be arranged into J series with $K=J$, $K=J-1$, $K=J-n$, . . ., whose intensity falls off with increasing n.

From eq (3), and the selection rules neglecting the centrifugal-stretching terms, it may be shown that the frequencies of the ${}^RR(J''K'')$ and ${}^PP(J'',K'')$ lines are given by

$$\nu=\nu_0+(B''-C'')+2n(B''-C''+C\zeta)+n^2(B''-B'-C''+C')\pm J[2(C''-C'\zeta)\pm(B'-B'')-2n(B''-B'-C''+C')]+J^2(C'-C''). \quad (7)$$

Therefore, the mean spacing in the series of strongest lines with $n=0$ is $\sim 2(C_0-C_v\zeta)$. Since approximate values of $C_0\sim(6.2\ \mathrm{cm}^{-1})$ and ζ_v are known from previous work, the ${}^PP$ and ${}^RR$ series can usually be located, with tentative numberings. The identifications may then be corroborated by finding lines of the other branches with the same ground-state combination differences as found in the parallel bands and with intensities roughly paralleling the theoretical line strengths. For the combination differences in perpendicular bands, eq (6) applies, except that in the branches involved are ${}^RR-{}^RQ$, ${}^PR-{}^PQ$, etc.

3. Results

3.1. Molecular Constants

The NH_3 spectrum between 4,060 and 4,720 cm^{-1} contains over 800 resolved features, many of which are blends of lines whose separation is less 0.10 cm^{-1}, the highest resolution obtained. Practically all the lines at frequencies above 4,250 cm^{-1}, and a large proportion of the strong lines from 4,060 to 4,250 cm^{-1}, have been analyzed into the inversion-doubled perpendicular bands $\nu_2+\nu_3$ and the weaker inversion-doubled parallel bands $\nu_1+\nu_2$. The analysis has yielded complete energy levels of $\nu_1+\nu_2$ up to $J=10$; and of $\nu_2+\nu_3$ up to $J=12$, in addition to some of the levels of higher J in both bands. The levels have been fitted to rotational-energy expressions of the forms of eq (3) and (4). The specific methods of deriving the constants and their values will be presented shortly. The line positions as calculated from the equations and constants are presented in tables 4 and 5, for the parallel and perpendicular bands, respectively. Following the calculated frequency (in cm^{-1}) is tabulated the difference (in $10^{-2}\ \mathrm{cm}^{-1}$) between the observed frequency and that calculated. Suffixes are added to the difference when the observed feature is a blend, the suffix *a* designating a line principally due to the calculated line; *b*, a line of which about one-half the intensity is contributed by the calculated line; and *c*, a feature principally due to a line other than the one in question. It will be noted that the differences, except for the latter types of blends, and for the levels of highest J for which the calculation is relatively uncertain, are less than 0.1 cm^{-1}, and average about 0.02 cm^{-1}.

Representative spectra from 4,230 to 4,530 cm^{-1} are presented in figures 1 and 2. These were obtained at pressures of less than 1 cm in the 10-m cell. Some of the more prominent lines are indicated above the spectra. Below the spectra are plotted lines whose position is that of ν_{calc}, and whose height is proportional to

$$W=[(\nu/\nu_0)k(S^0_{vr}/S^0_v)\gamma^0]^{1/2}, \quad (8)$$

in which S^0_{vr}/S^0_v is the rigid rotational line strength (table 3), and k is an empirical factor to represent the relative strength of the perpendicular and parallel transitions, here taken as 100:15. The ν/ν_0 factor gives the small frequency dependence of line strength, ν_0 being taken as the mean band origins, 4,307 cm for $\nu_1+\nu_2$ and 4,426 cm for $\nu_2+\nu_3$. γ^0 is the collision half-width, whose evaluation and dependence upon (J,K) is discussed later. For nonoverlapping lines, eq (8) is a good representation of the equivalent width (integrated fractional absorption) [7], and hence the heights of the vertical lines

TABLE 4. *Calculated and observed frequencies in* $\nu_1+\nu_2$, NH_3

The first entry is $\nu_{\mathrm{calc}}(\mathrm{cm}^{-1})$; the second entry is $\nu_{\mathrm{obs}}-\nu_{\mathrm{calc}}$ $(10^{-2}\ \mathrm{cm}^{-1})$.

J'_K	p''	^QP	^QQ	^QR
0_0	s	4300.17 03	----------	----------
1_0	a	4253.85 $\overline{08}^b$	----------	4313.47 $\overline{01}$
1_1	s	79.99 00	4319.75 03	----------
1_1	a	53.74 03^b	4293.49 08	----------
2_0	s	4259.32 00^b	----------	4358.66 01^a
2_1	s	59.39 $\overline{07}^b$	4318.98 $\overline{02}^a$	58.75 $\overline{09}^c$
2_1	a	33.68 $\overline{02}$	4293.24 07	32.99 01
2_2	s	59.60 $\overline{01}$	4319.23 01	----------
2_2	a	33.36 $\overline{01}$	4292.95 $\overline{03}^a$	----------
3_0	a	4213.62 $\overline{02}^b$	----------	4352.51 $\overline{01}^a$
3_1	s	38.45 $\overline{03}$	4317.83 02	77.43 $\overline{05}^b$
3_1	a	13.52 10^b	4292.87 11^c	52.43 07^b
3_2	s	38.66 $\overline{07}^a$	4318.07 $\overline{03}$	77.70 $\overline{03}$
3_2	a	13.20 00	4292.58 02^a	52.17 14^c
3_3	s	39.00 $\overline{04}^a$	4318.48 04^b	----------
3_3	a	12.66 $\overline{02}$	4292.09 04^a	----------
4_0	s	4217.20 $\overline{02}^b$	----------	4395.63 00^b
4_1	s	17.26 $\overline{08}^b$	4316.33 02^c	95.71 $\overline{08}^b$
4_1	a	4193.31 00	4292.34 ^{c}	71.69 07
4_2	s	4217.44 $\overline{07}$	4316.56 01	95.97 00^b
4_2	a	4192.99 $\overline{02}$	4292.07 06^c	71.45 $\overline{07}$
4_3	s	4217.75 $\overline{03}^a$	4316.94 01^b	96.42 01
4_3	a	4192.46 04	4291.60 10^b	71.04 01
4_4	s	4218.21 01	4317.51 01	----------
4_4	a	4191.68 04	4290.92 05^b	----------
5_0	a	4173.16 $\overline{03}^b$	----------	4390.78 $\overline{05}^b$

See footnotes at end of table.

TABLE 4. *Calculated and observed frequencies in* $\nu_1+\nu_2$, NH_3—Continued

The first entry is ν_{calc}(cm^{-1}); the second entry is $\nu_{obs}-\nu_{calc}$ (10^{-2} cm^{-1}).

J'_K	p''	^qP	^qQ	^qR
5_1	s	95.80 $\overline{01}$	4314.48 [c]	4413.55 07[b]
5_1	a	73.04 09[b]	4291.67 [c]	4390.70 03
5_2	s	95.96 $\overline{07}$[a]	4314.68 $\overline{03}$	4413.80 $\overline{04}$
5_2	a	72.74 08	4291.42 00	4390.49 04[c]
5_3	s	96.23 $\overline{01}$	4315.05 $\overline{02}$[b]	4414.24 02[b]
5_3	a	72.21 00	4290.98 01[b]	4390.12 00[b]
5_4	s	96.64 $\overline{03}$	4315.59 01	4414.88 00
5_4	a	71.44 02	4290.33 01	4389.57 01
5_5	s	97.22 $\overline{02}$	4316.32 03[a]	.....
5_5	a	70.41 04	4289.45 00	.....
6_6	s	4174.10 08[b]	.....	4430.89 12[b]
6_1	s	74.14 04[b]	4312.30 [c]	30.97 04[b]
6_1	a	52.75 07[b]	4290.85 [c]	09.48 02[b]
6_2	s	74.28 $\overline{10}$[b]	4312.49 [c]	31.22 02[b]
6_2	a	52.44 02[b]	4290.61 09[c]	09.28 00
6_3	s	74.52 00	4312.84 04	31.66 02
6_3	a	51.91 03	4290.18 04[b]	08.94 00[a]
6_4	s	74.87 02	4313.34 08[b]	32.28 02
6_4	a	51.17 09	4289.57 00[a]	08.46 02[c]
6_5	s	75.37 00	4314.02 01	33.12 08[c]
6_5	a	50.16 08	4288.75 01[b]	07.78 05[a]
6_6	s	76.04 05	4314.92 11[a]	.....
6_6	a	48.86 12	4287.67 06[a]	.....
7_0	a	4132.51 01[b]	.....	4428.03 01[b]
7_1	s	52.30 12[b]	4309.81 [c]	47.96 22[b]
7_1	a	32.41 14[b]	4289.87	27.97 05[c]
7_2	s	52.42 00[b]	4310.00 02	48.21 03
7_2	a	32.11 04[b]	4289.63 06[c]	27.80 13[c]
7_3	s	52.64 04[b]	4310.31 06[c]	48.63 15
7_3	a	31.60 03[b]	4289.24 06	27.50 04
7_4	s	52.91 12	4310.77 08[c]	49.24 06
7_4	a	30.87 05[b]	4288.67 07[c]	27.07 04
7_5	s	53.33 06	4311.40 19[b]	50.05 03[c]
7_5	a	29.86 10	4287.89 02	26.48 05
7_6	s	53.90 04	4312.23 09[a]	51.19 10[b]
7_6	a	28.62 10	4286.88 04[a]	25.69 15[c]
7_7	s	54.67 03	4313.31 05[b]	.....
7_7	a	27.04 24	4285.60 10	.....
8_0	s	4130.33 07[b]	.....	4464.47 17[b]
8_1	s	30.36 10[b]	4307.05 02[c]	64.55 04[b]
8_1	a	12.06 08	4288.70 [c]	46.15 01[b]
8_2	s	30.44 07[b]	4307.21 16[c]	64.79 08[b]
8_2	a	11.77 23[c]	4288.48 [c]	46.00 14[b]
8_3	s	30.58 07[b]	4307.50 13[c]	65.19 12
8_3	a	11.28 17	4288.12 00	45.76 04
8_4	s	30.83 09[b]	4307.92 16	65.78 24[c]
8_4	a	10.56 09	4287.58 03[c]	45.38 08
8_5	s	31.16 09	4308.49 25	66.56 22
8_5	a	09.61 09[b]	4286.87 05[a]	44.87 07[c]
8_6	s	31.63 00[b]	4309.25 13	67.55 15
8_6	a	08.39 19[b]	4285.93 23[a]	44.19 01[b]
8_7	s	32.27 12[b]	4310.23 14[c]	68.87 10
8_7	a	06.86 05	4284.74 08[b]	43.29 07
8_8	s	33.13 02	4311.49 10[b]	.....
8_8	a	04.97 17	4283.24 02[b]	.....
9_0	a	4091.78 17[b]	.....	4464.02 01[b]
9_1	s	4108.32 12[b]	4304.03 [c]	80.72 02[b]
9_1	a	4091.69 26[b]	4287.34 [c]	63.98 05[b]
9_2	s	4108.38 18[b]	4304.18 [c]	80.95 22[b]
9_2	a	4091.40 18	4287.14 [c]	63.86 17[b]
9_3	s	4108.51 19[b]	4304.43 40[c]	81.35 11[c]
9_3	a	4090.90 08	4286.81 11[c]	63.64 14[b]
9_4	s	4108.66 04[b]	4304.81 02[c]	81.90 21
9_4	a	4090.24 15	4362.28 15[c]	63.34 16[b]

TABLE 4. *Calculated and observed frequencies in* $\nu_1+\nu_2$, NH_3—Continued

The first entry is ν_{calc}(cm^{-1}); the second entry is $\nu_{obs}-\nu_{calc}$ (10^{-2} cm^{-1}).

J'_K	p''	^qP	^qQ	^qR
9_5	s	4108.90 20[b]	4305.32 02[c]	82.65 02
9_5	a	4089.32 04[c]	4285.66 04[c]	62.92 $\overline{04}$[c]
9_6	s	4109.27 25[b]	4306.01 $\overline{14}$	83.62 $\overline{46}$[c]
9_6	a	4088.14 09[c]	4284.80 14[b]	62.35 $\overline{13}$
9_7	s	4109.77 25	4306.89 14[a]	4484.83 05
9_7	a	4086.68 05	4283.71 09[b]	61.59 07[c]
9_8	s	4110.46 19[b]	4308.02 19	86.39 13
9_8	a	4084.87 18	4282.33 07[b]	60.60 15[b]
9_9	s	4111.41 03[b]	4309.48 16	.....
9_9	a	4082.66 01	4280.61 05[b]	.....
10_0	s	4086.25 05[c]	.....	4496.41 23[b]
10_1	s	86.26 04[c]	4300.78	96.48 16[b]
10_1	a	71.31 11[b]	4285.78	81.46 00[c]
10_2	s	86.29 01[c]	4300.91	96.70 06[b]
10_2	a	71.04 16[b]	4285.61	81.34 12[c]
10_3	s	86.27 03[c]	4301.09 [c]	97.04 $\overline{04}$[c]
10_3	a	70.65 05[c]	4285.35 [c]	81.25 08
10_4	s	86.46 16[c]	4301.17 16[c]	97.62 [c]
10_4	a	69.91	4284.86 [c]	80.94 24[b]
10_5	s	86.63 10[b]	4301.93 07[c]	98.34 34[b]
10_5	a	69.02 $\overline{24}$	4284.26 [c]	80.60 10[b]
10_6	s	86.88 15[b]	4302.53 10	99.27 $\overline{10}$
10_6	a	67.90 15	4283.48 22[c]	80.14 04
10_7	s	87.24 06	4303.32 08	4500.43 $\overline{15}$
10_7	a	66.49 27[c]	4282.48 $\overline{22}$[b]	4479.52 $\overline{13}$
10_8	s	87.76 05[c]	4304.32 $\overline{44}$[c]	4501.88 $\overline{29}$[c]
10_8	a	64.86 21[c]	4281.24 10[b]	4478.70 $\overline{22}$[c]
10_9	s	88.50 01	4305.61 05	4503.67 05
10_9	a	62.68 12	4279.68 03[b]	4477.63 09
10_{10}	s	89.53 25[c]	4307.26 11[a]	.....
10_{10}	a	60.11 39[c]	4277.72 02	.....
11_0	a	4051.02 24	.....	4498.51 17[b]
11_1	s	64.27	4297.63	4512.45 [c]
11_1	a	50.15	83.57	4498.26 08[b]
11_2	s	64.41 24[c]	98.78 16	4514.44 49
11_2	a	47.75 17	82.04	4497.62 [c]
11_3	s	64.71 05[c]	99.54 [c]	4515.62 [c]
11_3	a	46.50 25	81.24 10[b]	4497.24 [c]
11_4	s	65.08 [c]	4300.43 24	4516.99 [c]
11_4	a	44.68 [c]	4279.94 [c]	4496.41 23[c]
11_5	s	65.61 20	4301.56 07	4518.67 [c]
11_5	a	42.81 01[c]	4278.65 30	4495.66 19
11_{10}	s	66.38 [c]	4303.00 00[b]	4520.73
11_{10}	a	40.30	4276.80 08[c]	4494.41 18
11_{11}	s	67.50 [c]	4304.87 04[b]	.....
11_{11}	a	37.34	4274.57 22[b]	.....
12_0	s	.....	4297.52 18	4533.47 56
12_0	a	.....	77.36 24	13.20 [c]
12_{10}	s	.....	98.67 05[b]	35.30 23
12_{10}	a	.....	75.67 03[c]	12.17 [c]
12_{11}	s	.....	4300.19 22	37.56 [c]
12_{11}	a	.....	4273.67 24	10.90
12_{12}	s	.....	4302.28 28	.....
12_{12}	a	.....	4271.28 14	.....
13_{12}	s	.....	4297.23 $\left\{\begin{matrix}220\\206\end{matrix}\right.$	4554.20 $\left\{\begin{matrix}220\\210\end{matrix}\right.$
13_{12}	a	.....	70.33 07[c]	27.14
13_{13}	s	.....	99.71 42	.....
13_{13}	a	.....	67.99 16[b]	.....

[a] Blend, principally due to calculated line.
[b] Blend, approximately one-half due to calculated line.
[c] Blend, principally due to other line.

TABLE 5. *Calculated and observed frequencies in* $\nu_2+\nu_3$, NH_3

The first entry is ν_{calc} (cm^{-1}); the second entry is $\nu_{obs}-\nu_{calc}$ (10^{-2} cm^{-1}).

J'_K	p''	^PP	^PQ	^PR	^RP	^RQ	^RR
0	s	4400.79 07[b]	.....	.....	.....	.....	.....
0	a	18.50 00	.....	.....	.....	.....	.....
1_0	s	4380.66 06	4420.42 06	.....	.....	.....	.....
1_0	a	98.10 05	37.84 09	.....	.....	.....	.....
1_1	s	4388.53 03	.....	.....	.....	4412.54 03	.....
1_1	a	4406.20 04	.....	.....	4390.42 03	.....	4450.04 02[b]
2_0	s	4360.18 00	4419.77 01	4459.54 02	.....	.....	.....
2_0	a	77.35 03[b]	36.92 02	76.67 01	.....	.....	.....
2_1	s	68.08 02	27.70 03	.....	4352.31 00[b]	.....	4451.66 04
2_1	a	85.39 07[b]	44.98 00	.....	.....	4429.24 03	.....
2_2	s	76.04 01	.....	.....	44.60 01	04.19 03	43.96 05
2_2	a	93.81 02	.....	.....	62.24 06	21.81 03	61.56 04
3_0	s	4339.48 01	4418.86 02	4478.45 03	.....	.....	.....
3_0	a	56.13.05	35.47 02	95.04 02[c]	.....	.....	.....
3_1	s	47.36 03	26.78 02	86.40 03	.....	4411.10 00	.....
3_1	a	64.14 03	43.52 02	4503.11 00	4348.38 03	.....	4487.27 03
3_2	s	55.31 01	34.78 03	.....	23.93 06[c]	03.32 00	62.91 01
3_2	a	72.52 03	51.96 04	.....	41.04 01	20.38 02	79.95 01
3_3	s	63.37 00	.....	.....	16.20 15[c]	4395.61 02	55.23 01
3_3	a	81.25 06	.....	.....	33.96 04	4413.34 04	72.93 00
4_0	s	4318.56 04[c]	4417.64 03	4497.02 02	.....	.....	.....
4_0	a	34.54 03	33.56 00[a]	4512.91 00[c]	.....	.....	.....
4_1	s	26.42 00	25.54 00	04.96 02	4310.67 04[c]	.....	4489.10 04
4_1	a	42.51 07	41.59 06[b]	20.97 04	.....	4425.99 01	.....
4_2	s	34.33 06	33.52 04	13.00 11[c]	03.07 07	02.15 03	81.53 07
4_2	a	50.87 03	50.01 01[b]	29.47 02	19.48 00	18.51 04	97.85 00
4_3	s	42.36.04	41.66 01	.....	4295.38 00	4394.50 00	73.91 02
4_3	a	59.55 06	58.80 07	.....	4312.38 06	4411.46 02	90.84 02
4_4	s	50.47 05	.....	.....	4287.66 04[c]	4386.86 01	66.33 02
4_4	a	68.63 02	.....	.....	4305.57 04	4404.72 04[b]	84.15 03
5_0	s	4297.43 07[b]	4416.11 04[b]	4515.18 01[b]	.....	.....	.....
5_0	a	4312.58 05	31.21 03	30.24 03	.....	.....	.....
5_1	s	05.26 04	23.99 04	23.11 03	.....	4408.48 00	.....
5_1	a	20.53 03	39.20.01	38.28 04	4304.79 03	.....	4522.42 01
5_2	s	13.18.10	32.00 01	31.19 02	4282.00 00	00.68 04	4499.75 04
5_2	a	28.79.05	47.55 03	46.70 06[b]	97.56 06	16.19.04[b]	4515.22 03
5_3	s	21.15 03	40.09 02	39.38 01	74.34 01	4393.07 08[a]	4492.18 00
5_3	a	37.45 03[c]	56.34 07	55.58 03	90.49 09[c]	4409.15 07	4508.23 07[b]
5_4	s	29.23 03	48.33 02	.....	66.66 04	4385.48 02[b]	4484.67 00
5_4	a	46.46 02	65.50 04	.....	83.65.15[c]	4402.41 03	4501.56 03
5_5	s	37.36 12[a]	.....	.....	58.93 06	4377.87 06	4477.16 02
5_5	a	55.84 07	.....	.....	77.09 21[c]	95.97 00[a]	95.21 11
6_0	s	4276.10 04	4414.26 00	4532.93 14[c]	.....	.....	.....
6_0	a	90.32 00[c]	28.42 01	47.05 01	.....	.....	.....
6_1	s	83.90 10[c]	22.12 02	40.84 02	4268.18 06	.....	4524.97 03[b]
6_1	a	98.22 06	36.39 03	55.06 01	.....	4420.99 00	.....
6_2	s	91.70 00[b]	30.02 08	48.84 01	60.74 19	4398.90 14	17.57 23
6_2	a	4306.53 08[a]	44.79 01	63.55 04	75.34 02	4413.44 04	32.07 01
6_3	s	4299.73 01	38.20 03	57.14 04	53.12 02	4391.34 06	10.06 01
6_3	a	4315.03 00[c]	53.44 20	72.32 03	68.26 02	4406.42 01	25.10 10[b]
6_4	s	07.79 02	46.44 06	65.54 01	45.48 01	4383.80 04[a]	02.62 03
6_4	a	23.97 02[a]	62.54 01	81.58 03	61.42 01	99.69 03[a]	18.45 04
6_5	s	15.94 01	54.82 02	.....	37.79 12[c]	76.26 02	4495.20 04
6_5	a	33.28 01	72.09 01	.....	54.83.07[b]	93.24 03	4512.12 00
6_6	s	24.14 06	.....	.....	30.00 15[c]	68.65 00[c]	4487.75 01
6_6	a	43.02 02	.....	.....	45.49 00[b]	87.07 04	4506.11 01
7_0	s	4254.58 04	4412.08 00	4550.24 02	.....	.....	.....
7_0	a	67.77 06	25.22 00	63.32 08[b]	.....	.....	.....
7_1	s	62.34 01	19.92 02	58.13 05[b]	.....	4404.62 06	.....
7_1	a	75.63 01	33.15 05[b]	71.32 00	4259.95 01	.....	4555.47 05

See footnotes at end of table.

TABLE 5. *Calculated and observed frequencies in* $\nu_2+\nu_3$, NH_3—Continued

The first entry is ν_{calc} (cm^{-1}); the second entry is $\nu_{obs}-\nu_{calc}$ (10^{-2} cm^{-1}).

J'_K	ν''	^PP	^PQ	^PR	^RP	^RQ	^RR
7_2	s	70.28 $\overline{02}$	27.97 05	66.29 $\overline{07}$	39.21 22	4396.81 20	34.96 $\overline{11}^b$
7_2	a	83.71 09^b	41.35 04	79.61 03	52.85 $\overline{06}^c$	4410.31 01	48.41 00
7_3	s	78.11 01^b	35.97 $\overline{01}$	74.43 $\overline{04}$	31.72 00	4389.30 01	27.52 07^b
7_3	a	92.31 $\overline{18}^c$	50.11 $\overline{09}^c$	88.51 $\overline{14}$	45.78 $\overline{01}^a$	4403.30 02^c	41.46 00
7_4	s	4286.15 02	4444.22 $\overline{04}$	4582.87 $\overline{06}^b$	4224.14 03	4381.84 06	4520.16 04
7_4	a	4301.15 01	59.15 $\overline{01}$	97.74 $\overline{04}$	38.44 $\overline{02}^c$	96.57 06	34.83 01
7_5	s	4294.28 $\overline{02}$	52.61 $\overline{03}$	91.49 $\overline{05}$	16.51 05^c	74.37 09	12.83 08
7_5	a	4310.35 02^b	68.61 $\overline{01}$	4607.42 04^b	32.32 03	90.12 00^b	28.53 02
7_6	s	02.47 $\overline{07}$	61.10 00	.....	08.78 12	66.85 04	05.50 06
7_6	a	19.99 $\overline{01}$	78.54 06^c	.....	25.94 15	83.94 $\overline{10}^c$	22.53 04
7_7	s	10.69 02^b	.....	.....	00.88 09	59.21 04	4498.09 04
7_7	a	30.06 $\overline{02}$	.....	.....	19.79 04	78.05 $\overline{08}$	4516.85 09
8_0	s	4232.90 00	4409.59 $\overline{09}^b$	4567.09 $\overline{02}$	.....	.....	.....
8_0	a	45.00 $\overline{02}$	21.64 04	79.04 00	.....	.....	.....
8_1	s	40.61 03	17.38 $\overline{06}$	74.96 $\overline{06}$	4224.97 $\overline{11}$	.....	4559.12 $\overline{10}$
8_1	a	52.81 $\overline{02}^b$	29.53 $\overline{01}$	87.05 02	.....	4414.37 $\overline{11}^a$	.....
8_2	s	48.20 $\overline{08}$	25.12 $\overline{10}$	82.81 00^b	17.72 00^c	4394.41 09^c	51.91 00
8_2	a	61.13 04^a	37.96 $\overline{03}$	95.60 $\overline{03}$	30.15 10^a	4406.79 03	64.24 $\overline{08}$
8_3	s	56.31 $\overline{05}$	33.40 00^c	91.26 $\overline{04}$	10.19 04	4386.96 $\overline{11}^c$	44.54 05^b
8_3	a	69.35 $\overline{17}^b$	46.37 01^c	4604.17 $\overline{12}$	23.09 03	99.80 $\overline{08}^c$	57.32 $\overline{02}$
8_4	s	64.31 04	41.64 00^c	4599.71 $\overline{01}$	02.64 05	79.55 07	37.24 $\overline{01}$
8_4	a	78.12 $\overline{02}^b$	55.37 $\overline{15}^c$	4613.38 $\overline{08}$	16.26 $\overline{12}^b$	93.10 07^c	50.73 $\overline{01}$
8_5	s	72.42 $\overline{07}$	50.04 $\overline{02}^c$	08.36 $\overline{05}$	4195.11 $\overline{01}$	72.20 02	30.05 $\overline{04}$
8_5	a	87.19 01	64.73 02^a	22.99 $\overline{02}$	4209.62 03	86.64 06	44.44 05^b
8_6	s	80.60 $\overline{04}^b$	58.57 $\overline{06}$	17.20 $\overline{16}^c$	4187.45 03	64.77 07	22.84 03
8_6	a	96.69 $\overline{01}$	74.57 00	33.12 $\overline{02}$	4203.20 $\overline{06}$	80.46 04	38.46 02
8_7	s	88.83 $\overline{09}^b$	67.19 $\overline{02}$	.....	4179.64 03	57.25 07	15.58 $\overline{03}$
8_7	a	4306.62 $\overline{01}^b$	84.89 $\overline{10}$	.....	96.99 $\overline{04}$	74.54 04	32.79 00
8_8	s	4297.05 $\overline{01}$	.....	.....	71.60 $\overline{18}^c$	49.56 06	08.20 $\overline{04}^b$
8_8	a	4317.02 $\overline{07}^b$	.....	.....	91.01 04	68.89 03	27.45 $\overline{01}$
9_0	s	4211.06 $\overline{04}$	4406.76 $\overline{03}$	4583.45 $\overline{05}$	.....	.....	.....
9_0	a	22.05 $\overline{11}$	17.71 $\overline{08}^c$	94.35 $\overline{01}^b$	.....	.....	.....
9_1	s	18.72 $\overline{01}$	14.52 $\overline{07}$	91.29 $\overline{07}^b$	.....	4399.47 05	.....
9_1	a	29.81 04	25.55 $\overline{01}^c$	4602 26 03	4214.24 $\overline{17}$	.....	4586.48 $\overline{13}$
9_2	s	26.78 $\overline{09}$	22.70 $\overline{04}$	4599.61 $\overline{06}$	4195.98 $\overline{09}^c$	91.69 06^b	68.38 00
9_2	a	37.55 12	33.45 $\overline{05}^b$	4610.29 10	4207.28 $\overline{21}$	4402.93 $\overline{10}$	79.57 09
9_3	s	4234.34 $\overline{04}$	4430.49 02	4607.58 $\overline{12}^b$	4188.51 03	4384.31 $\overline{03}$	4561.08 $\overline{04}$
9_3	a	46.19 $\overline{12}$	42.27 $\overline{05}$	19.29 $\overline{08}$	4200.24 $\overline{07}$	95.97 00^c	72.70 $\overline{06}$
9_4	s	42.32 $\overline{13}$	38.73 $\overline{05}$	16.06 $\overline{05}$	4181.06 $\overline{03}$	77.00 $\overline{02}$	53.90 $\overline{03}^b$
9_4	a	54.83 $\overline{07}$	51.17 04^b	28.43 $\overline{06}$	93.39 08^c	89.28 03^b	66.12 $\overline{01}$
9_5	s	50.40 $\overline{06}$	47.13 $\overline{07}$	24.75 $\overline{08}$	73.57 $\overline{29}$	69.71 $\overline{07}$	46.80 $\overline{04}$
9_5	a	63.82 $\overline{02}$	60.48 $\overline{03}$	38.02 $\overline{04}$	86.76 $\overline{01}$	82.84 $\overline{05}$	59.86 $\overline{02}$
9_6	s	58.57 $\overline{10}$	55.68 $\overline{07}$	33.64 $\overline{09}$	65.99 01	62.40 03	39.73 00
9_6	a	73.18 $\overline{09}$	70.22 $\overline{05}$	48.10 $\overline{09}^b$	80.30 $\overline{06}$	76.65 $\overline{01}$	53.91 04^b
9_7	s	66.78 $\overline{08}$	64.34 $\overline{04}^b$	42.70 00	58.28 01	55.02 08	32.63 03
9_7	a	82.94 $\overline{02}$	80.41 $\overline{04}$	58.67 01^b	74.06 $\overline{12}^c$	70.72 $\overline{02}$	48.26 $\overline{03}$
9_8	s	75.03 $\overline{06}^a$	73.09 $\overline{04}^b$	.....	50.34 $\overline{05}$	47.45 01^c	25.42 $\overline{03}$
9_8	a	93.18 $\overline{08}$	91.13 $\overline{06}$	.....	67.98 $\overline{03}^c$	65.02 $\overline{00}$	42.90 $\overline{00}$
9_9	s	83.26 $\overline{00}$	.....	.....	42.11	39.67 07	18.03 05
9_9	a	4303.95 $\overline{07}$	.....	.....	62.16	59.62 $\overline{01}^c$	37.89 $\overline{03}$
10_0	s	4189.10 $\overline{13}$	4403.62 $\overline{30}^c$	4599.33 $\overline{09}$	.....	.....	.....
10_0	a	98.95 19	13.43 05^c	4609.08 02	.....	.....	.....
10_1	s	96.71 $\overline{10}^c$	11.34 10^c	07.13 $\overline{05}$	4181.22 $\overline{01}$	.....	4591.38 $\overline{16}^b$
10_1	a	4206.64 02	21.21 09^c	16.95 09^b	.....	4406.32 11^c	.....
10_2	s	03.95 $\overline{10}$	18.78 06^c	14.70 02^b	74.14 04^c	4388.66 14	84.37 $\overline{05}$
10_2	a	15.08 00	29.77 14	25.67 04	83.26 $\overline{17}$	98.73 03^c	94.38 04^b
10_3	s	12.24 $\overline{06}$	27.26 05	23.40 $\overline{02}$	66.74 $\overline{12}$	81.36 $\overline{05}^c$	77.15 $\overline{11}$
10_3	a	22.86 04^b	37.81 12^c	33.89 $\overline{05}$	77.29 $\overline{17}$	91.86 $\overline{11}^b$	87.60 $\overline{11}$
10_4	s	20.19 $\overline{02}$	35.49 00^c	31.90 $\overline{06}$	59.35 $\overline{14}$	74.14 $\overline{08}$	70.08 $\overline{12}$
10_4	a	31.40 $\overline{02}^b$	46.63 01^b	42.97 $\overline{02}$	70.41 07^c	85.13 33^c	81.02 05

See footnotes at end of table.

TABLE 5. *Calculated and observed frequencies in* $\nu_2+\nu_3$, NH_3—Continued

The first entry is ν_{calc} (cm^{-1}); the second entry is $\nu_{obs}-\nu_{calc}$ (10^{-2} cm^{-1}).

J'_K	p''	^PP	^PQ	^PR	^RP	^RQ	^RR
10_5	s	28.25 $\overline{14}$	43.90 03[c]	40.64 $\overline{08}$	51.95 $\overline{07}$[c]	66.97 $\overline{07}$[c]	63.11 $\overline{11}$
10_5	a	40.25 03	55.83 01	52.49 03	63.75 $\overline{31}$	78.70 06	74.78 $\overline{02}$
10_6	s	36.39 $\overline{09}$	52.47 11[c]	49.58 05	44.45 11[c]	59.75 $\overline{11}$[c]	56.16 $\overline{10}$
10_6	a	49.48 $\overline{07}$	65.48 $\overline{18}$	62.51 $\overline{01}$	57.28 19[c]	72.51 01[c]	68.95 $\overline{12}$
10_7	s	44.62 $\overline{12}$	61.18 $\overline{08}$[b]	58.73 $\overline{05}$[b]	36.94	52.49 01[c]	49.23 $\overline{05}$
10_7	a	59.10 00	75.57 00	73.03 01	50.97	66.55 02	63.21 03[b]
10_8	s	52.85 $\overline{06}$[b]	69.98 01	68.05 $\overline{01}$	29.02	45.10 01	42.21 02
10_8	a	69.13 05[b]	86.14 07	84.09 07	44.83	60.82 03	57.86 03
10_9	s	4261.11 06[b]	4478.84 20	----------	4120.92	4337.48 00[c]	4535.04 03[b]
10_9	a	79.65 00	97.25 $\overline{25}$[c]	----------	38.88	55.35 00[c]	52.82 02
10_{10}	s	69.32 16	----------	----------	----------	29.50 05	27.56 03[b]
10_{10}	a	90.77 $\overline{25}$[a]	----------	----------	----------	50.10 02	48.05 07
11_0	s	4167.03 $\overline{19}$	4400.16 $\overline{01}$	4614.68 04[b]	----------	----------	----------
11_0	a	75.76 05	08.84 10[c]	23.32 06[c]	----------	----------	----------
11_1	s	74.58 [c]	07.82 $\overline{09}$[c]	22.44 08[b]	----------	4393.02 13[c]	----------
11_1	a	83.39 13	16.57 23	31.14 14	4168.00 $\overline{27}$	----------	4615.49 $\overline{23}$
11_2	s	82.92 $\overline{25}$	16.27 $\overline{12}$[c]	31.09 $\overline{07}$	52.19 [c]	85.32 14[c]	4599.84. $\overline{14}$[b]
11_2	a	90.59 $\overline{27}$	24.02 $\overline{07}$[c]	38.70 00[b]	61.16 16	94.24 26[c]	4608.72 $\overline{05}$
11_3	s	90.02 $\overline{09}$	23.68 27[c]	38.69 01[b]	44.86 $\overline{30}$	78.10 $\overline{29}$[c]	4592.72 $\overline{19}$
11_3	a	99.43 15	33.03 17[c]	47.98 03[b]	54.17 [c]	87.35 06	4601.92 $\overline{06}$
11_4	s	97.95 $\overline{26}$	31.93 06[c]	47.23 $\overline{02}$	37.55 $\overline{28}$	70.96 $\overline{22}$	4585.74 $\overline{19}$
11_4	a	4207.89 $\overline{31}$	41.80 [c]	57.03 $\overline{10}$	47.35 $\overline{34}$	80.70 [c]	95.43 $\overline{08}$
11_5	s	05.94. $\overline{03}$	40.31 $\overline{20}$[c]	55.96 00	30.22 [c]	63.88 $\overline{15}$	78.89 $\overline{33}$
11_5	a	16.71 47[c]	50.90 31[c]	66.48. 31	40.69. $\overline{18}$	74.29 [c]	89.24 $\overline{09}$
11_6	s	14.07 00[b]	48.89 $\overline{11}$[c]	64.97 $\overline{01}$	----------	56.08 $\overline{37}$[b]	72.10 $\overline{33}$
11_6	a	26.14 05	60.43 02[c]	76.42 11	----------	68.11 05[c]	83.34 $\overline{09}$[b]
11_7	s	22.29 $\overline{03}$	57.64. $\overline{01}$	74.20 $\overline{02}$	----------	49.68 $\overline{35}$	65.33 $\overline{39}$
11_7	a	35.65.08	70.39 19	86.87 18	----------	62.14 $\overline{26}$	77.73 $\overline{02}$[b]
11_8	s	30.57 07	66.51 25[b]	83.62 14	----------	42.44 $\overline{47}$	58.52 $\overline{34}$[b]
11_8	a	44.98 32	80.82 35[b]	97.83 39	----------	56.38. 05[b]	72.38 $\overline{03}$
11_9	s	38.83 60[b]	75.45 58	93.18 49[b]	----------	35.06 $\overline{15}$	51.60 $\overline{15}$
11_9	a	55.26 34	91.77 41[c]	4709.37 35	----------	50.86 04[c]	67.33 $\overline{01}$
11_{10}	s	47.05 $\overline{20}$	84.42 [c]	----------	----------	27.31 13	44.42 07[b]
11_{10}	a	66.07 03	4503.30 $\overline{19}$	----------	----------	45.57. $\overline{10}$[b]	62.57 04
11_{11}	s	55.21 $\overline{21}$	----------	----------	----------	19.19 05[c]	36.93 03
11_{11}	a	77.46 $\overline{58}$	----------	----------	----------	40.57 $\overline{16}$	58.17 01[a]
12_0	s	----------	4396.37 [c]	4629.50 01	----------	----------	----------
12_0	a	----------	4403.97 [c]	37.06 04[a]	----------	----------	----------
12_1	s	----------	03.98 [c]	37.22 10	4137.05 $\overline{37}$	----------	4621 62 $\overline{61}$
12_1	a	----------	11.65 $\overline{01}$	44.83 29	----------	4397.01 37	----------
12_2	s	4158.99 22[c]	10.91 [c]	44.25 29	----------	81.67 [c]	14.80 $\overline{08}$[c]
12_2	a	68.85 $\overline{11}$[c]	20.50 18	53.93 26	----------	89.48 [c]	22.57 20
12_3	s	----------	4419.76 [c]	4653.43 17	----------	4374.52 [c]	4607.77 $\overline{31}$[c]
12_3	a	----------	27.95 [c]	61.55 54[a]	----------	82.63 [c]	15.82 00
12_4	s	----------	27.97 [c]	61.95 14[a]	----------	67.49 $\overline{08}$	00.90 $\overline{55}$[b]
12_4	a	----------	36.62 [c]	70.52 38[b]	----------	76.02 17	09.37 $\overline{13}$
12_5	s	4183.54 09	36.38 [c]	70.74 16	----------	60.52 [c]	4594.18 $\overline{30}$[c]
12_5	a	92.88 [c]	45.65 [c]	79.94 38	----------	69.64 00[c]	4603.24 $\overline{10}$
12_6	s	91.68 21	45.02 [c]	79.84 16	----------	53.60	4587.58 $\overline{36}$[b]
12_6	a	4201.76 09	55.02 [c]	89.76 34	----------	63.40 [c]	97.31 $\overline{05}$
12_7	s	4199.83 14	53.74 [c]	89.09 33	----------	46.58 $\overline{111}$[b]	80.94 $\overline{108}$
12_7	a	4211.07 67	64.91 [c]	4700.17 57	----------	57.48 07	91.78 $\overline{12}$
12_8	s	08.11 37	62.66 [c]	4698.61 31	----------	39.50 $\overline{94}$	74.33 $\overline{120}$
12_8	a	20.74 120[b]	75.20 113	4711.05 110	----------	51.71 $\overline{16}$	86.45 $\overline{10}$[c]
12_9	s	16.41 [c]	71.69 [c]	08.31 61	----------	32.28 $\overline{38}$	67.62 $\overline{55}$[b]
12_9	a	30.87 85[b]	85.98 87	----------	----------	46.14 $\overline{05}$	81.41 $\overline{03}$[b]
12_{10}	s	24.68 84	80.78 [c]	----------	----------	24.78 $\overline{108}$	60.73 $\overline{89}$[b]
12_{10}	a	41.36	97.31 [c]	----------	----------	40.77 03	76.62 01
12_{11}	s	32.85 50[c]	89.82 43	----------	----------	16.93 [c]	53.65 $\overline{03}$
12_{11}	a	52.43 36[c]	4509.25 17	----------	----------	35.66 10	72.16 02
12_{12}	s	40.94 67	----------	----------	----------	08.58	45.95 36
12_{12}	a	63.97	----------	----------	----------	30.85 01	68.07 $\overline{05}$

See footnotes at end of table.

TABLE 5. *Calculated and observed frequencies in* $\nu_2+\nu_3$, NH_3—Continued

J'_K	p''	^PR	^RR	J'_K	p	^RR
13_0	s	4643.80 22	4642.53 29	14_1	a	4650.26 116
13_0	a	50.30 35	.....	14_1	a	35.88 07[b]
				14_2	a	29.87 26
13_1	s	51.48 38	29.24 07[b]	14_2	a	24.12 25
13_1	a	58.03	35.92 03[b]	14_3	a	18.63 29
				14_3	a	13.36 06[c]
13_2	s	60.60 35	22.31 21[c]	14_4	a	08.33 16
13_2	a	65.04 44	29.26 09[b]			
				14_{10}	s	4591.80 [c]
13_3	s	67.44	15.50 32[c]	14_{10}	a	4603.53 17
13_3	a	74.53 67	22.85 08[b]			
				14_{11}	s	4585.26 22
13_4	s	76.16 38[c]	08.84 17[c]	14_{11}	a	99.01 06
13_4	a	83.58 18[c]	16.76 14			
				14_{12}	s	78.44{154 142
13_5	s	84.95 56	02.41 22	14_{12}	a	94.78 08
13_5	a	92.89 78[b]	10.94 25			
				14_{13}	s	71.11{186 202
13_6	s	94.04 61	4596.04 17	14_{13}	a	90.84 03
13_6	a	4702.69 110	4605.39 22			
				14_{14}	s	63.16 08[c]
13_7	s	03.41 98	4589.61 24	14_{14}	a	87.34 12
13_7	a	12.97	4600.10 19[b]			
13_8	s	13.01	4583.24 01[c]	15_{15}	a	4603.67 18
13_8	a	.....	95.07 19	15_{14}	a	4599.90 01
13_9	s	.....	76.53 145	15_{15}	s	71.34{109 179
13_9	a	.....	90.28 07	15_{15}	a	96.70 18
13_{10}	s	.....	69.68{236[b] 57	16_{16}	s	4579.25{235 61
13_{10}	a	.....	85.77 00	16_{16}	a	4605.90 29
13_{11}	s	.....	62.45{329 45			
13_{11}	a	.....	81.59 23			
13_{12}	s	.....	54.70{270 170			
13_{12}	a	.....	77.80 09[b]			
13_{13}	s	.....	.....			
13_{13}	a	.....	.....			

[a] Blend, principally due to calculated line.
[b] Blend, approximately one-half due to calculated line.
[c] Blend, principally due to other line.

should be approximately proportional to the area of the observed absorptions. In figures 1 and 2 this is seen to be the case, with very few exceptions, and it will be further noted that practically all of the observed absorption has been accounted for.

The central panel of figure 1 covers the region of the ^QQ-branches, in which the inversion-doublet separations range from 18 cm^{-1}, for levels with $J \gg K$, to >30 cm^{-1} for $J>12$ in the series with $J=K$, which includes the most intense lines. Throughout this region, and in the other panels of figure 1, there fall the lines of the ^PP- and ^RP-branches. Since the perpendicular bands are more intense by a factor of about seven, the individual lines in them are the strongest single lines in the region, although not as prominent a feature as the parallel Q-branches. In the top panel, the perpendicular lines are becoming weaker; the ^QP-branch "lines" are obvious, and show resolution of the K-structure, the low-K components lying at lower frequencies in the a-s and at higher frequencies in the s-a members of the inversion doublet.

In figure 2 the region covered is that near the origin of the perpendicular bands. ^QR-lines are present but are relatively weak. The J-divergence of the ^RQ-and ^PQ-branches with the same ΔK is considerable, high-J components lying at lower frequencies in both inversion-doublets. The inversion doubling ranges from 21.4 cm^{-1} at ^RQ (11,11) to 8.7 cm^{-1} for ^PQ (11,0).[6] In the bottom panel of figure 2 the ^RR series dominate the absorption.

A further extension to higher frequencies is shown in figure 3. As one proceeds to higher frequencies the intensities drop rapidly in the ^RR-branches, and somewhat less rapidly in the ^PR-branches, so that the latter are the strongest beyond 4,600 cm^{-1}. Even though one is dealing here with very weak lines from levels of high J, it will be noted that a quite complete identification has been achieved. Above 4,680 cm^{-1}, lines of higher-frequency bands begin to appear.

The constants of the NH_3 molecule needed to fit eq (3) and (4) to the line-position data were derived in the following manner. For the ground state, combination differences Δ_1F and Δ_2F were obtained from all pairs of lines listed in tables 4 and 5 that did not involve heavy blends. The combination differences were larger by a few hundredths of a wave number in the s inversion substates than in

[6] For a few observed levels with $K'=2$ the doubling is even lower, because of the (A_1A_2) interaction. Both components of ^PR (12,3) appear, split by only 4.44 cm^{-1}.

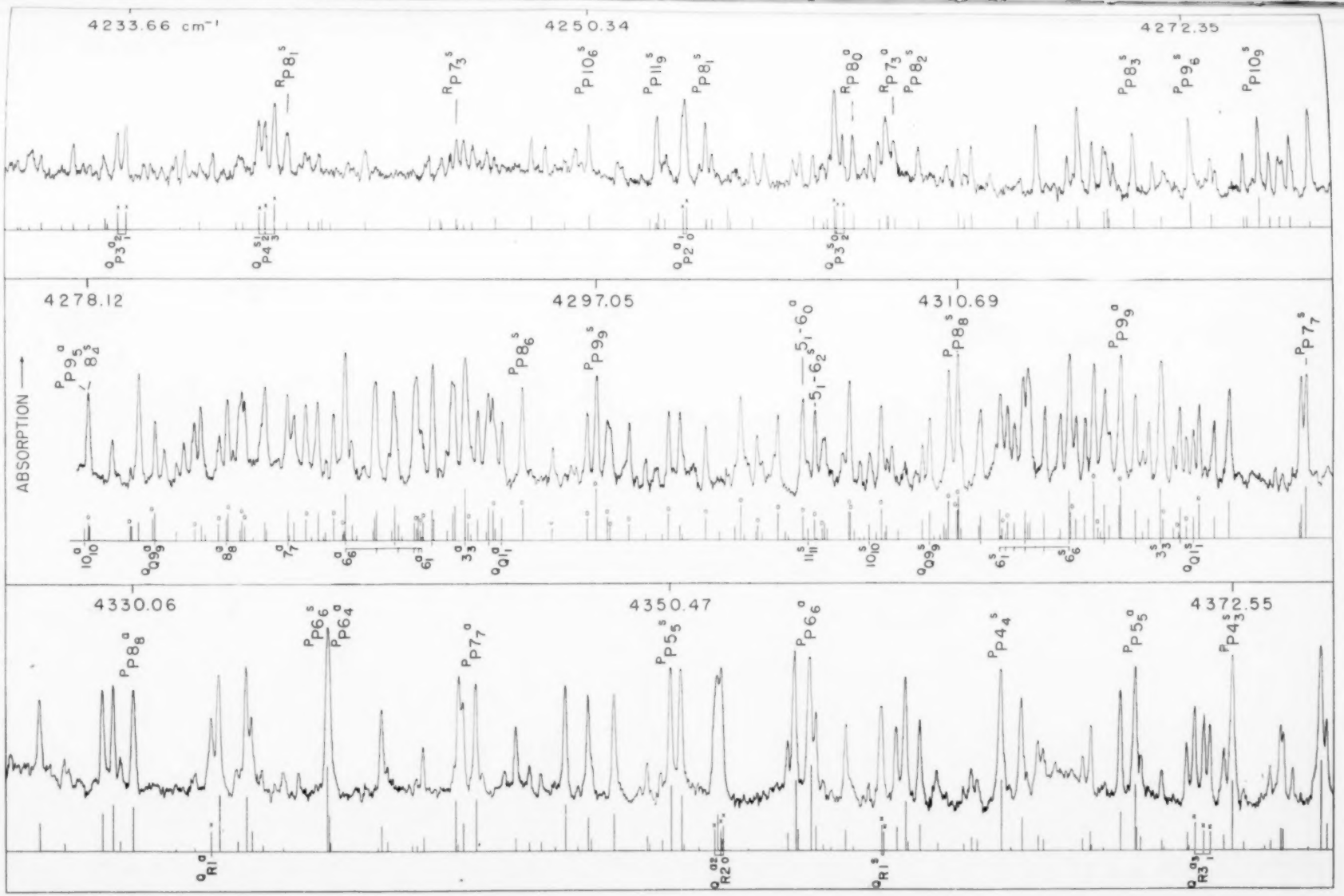

FIGURE 1. NH_3 *spectra, 4,230 to 4,380 cm*$^{-1}$.

Cell length, 10 m; pressure, <1 cm (Hg). Calculated positions and relative intensities are indicated. Lines of the parallel bands $\nu_1+\nu_2$ are distinguished by x in panels 1 and 3; lines of the perpendicular bands $\nu_2+\nu_3$ by 0 in the central panel. Some prominent features are labeled by branch and $(J\,\frac{E}{g})''$.

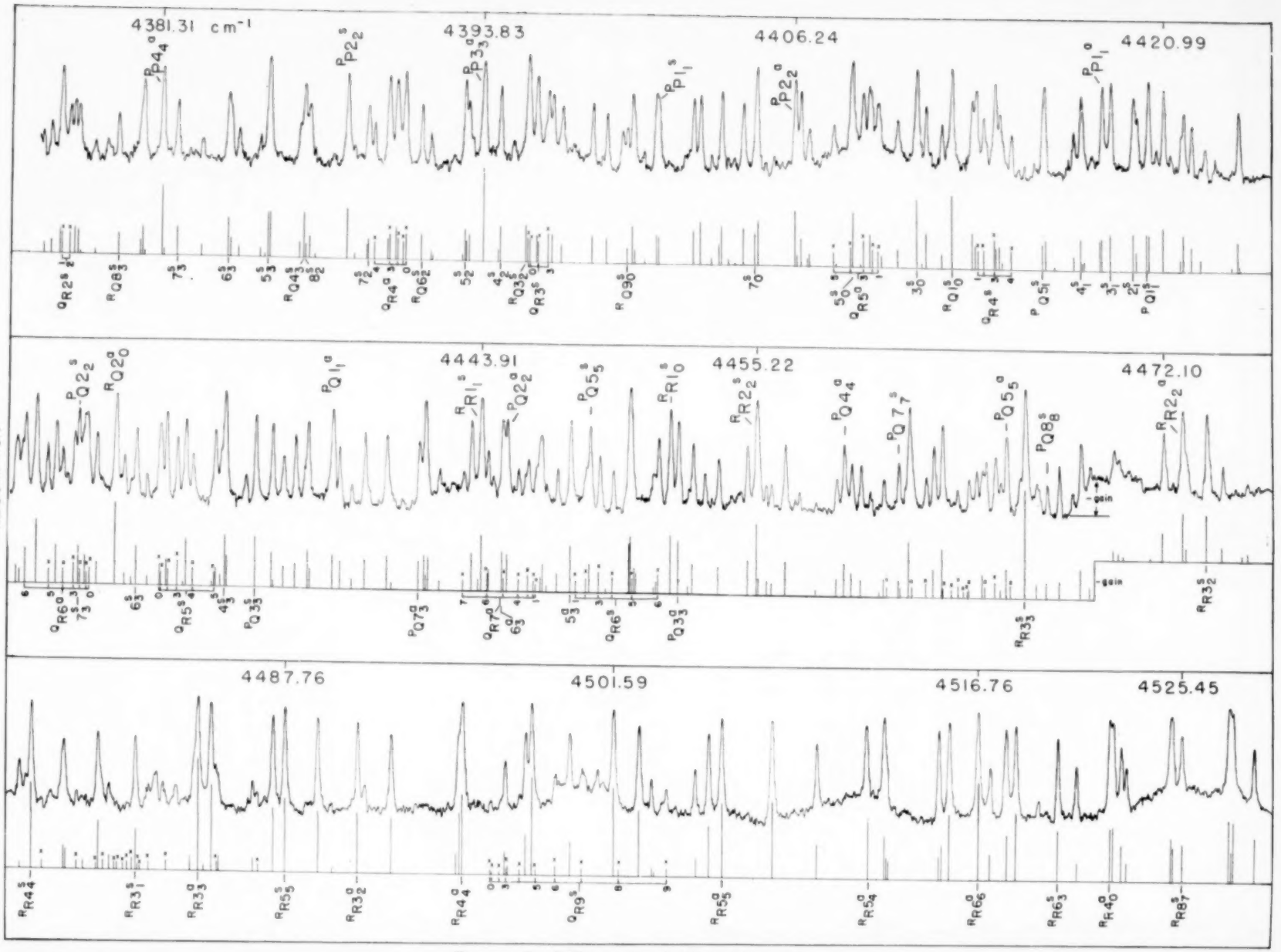

FIGURE 2. NH_3 *spectra, 4,380 to 4,530 cm*$^{-1}$.

Cell length, 10 m; pressure, <1 cm (Hg). Calculated positions and relative intensities are indicated. Lines of the parallel bands $\nu_1+\nu_2$ are distinguished by x. Some prominent features are labeled by branch and $(J,k)''$.

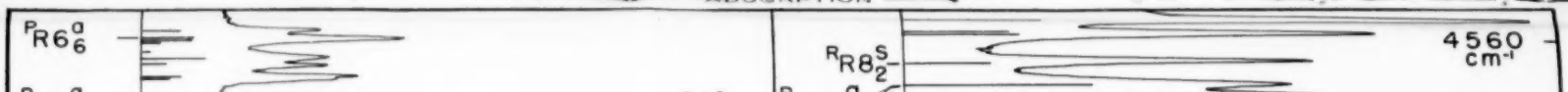

Cell length, 10 m; pressure, <1 cm (Hg). Calculated positions and relative intensities are indicated. Lines of the parallel bands $\nu_1+\nu_2$ are distinguished by x. Some prominent features are labeled by branch and $(J\ell)''$.

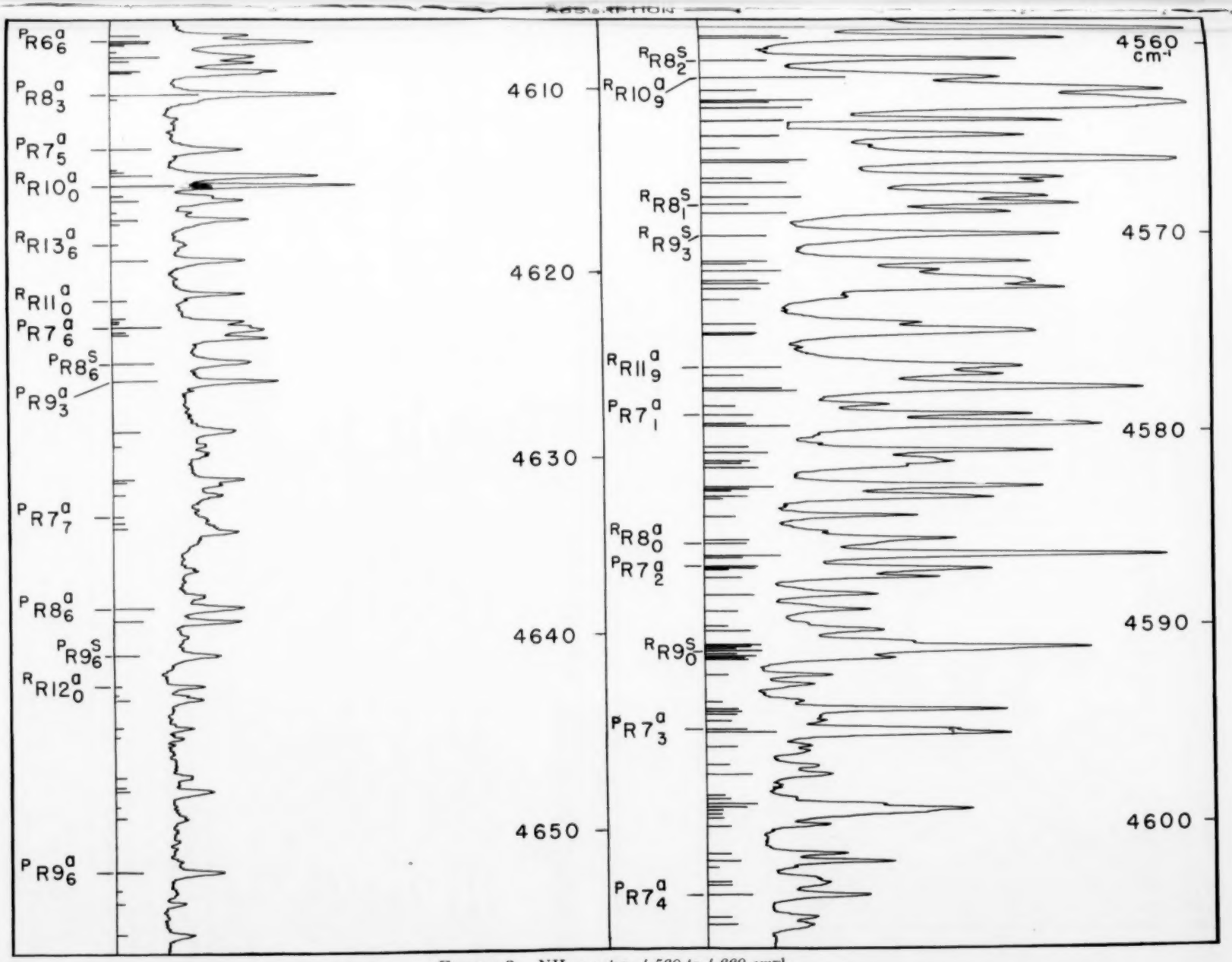

FIGURE 3. NH_3 *spectra, 4,560 to 4,660 cm*$^{-1}$.

Cell length, 10 m; pressure, 9 cm (Hg). Calculated positions and relative intensities are indicated. Some prominent features are labeled by branch and $(J\ell)''$.

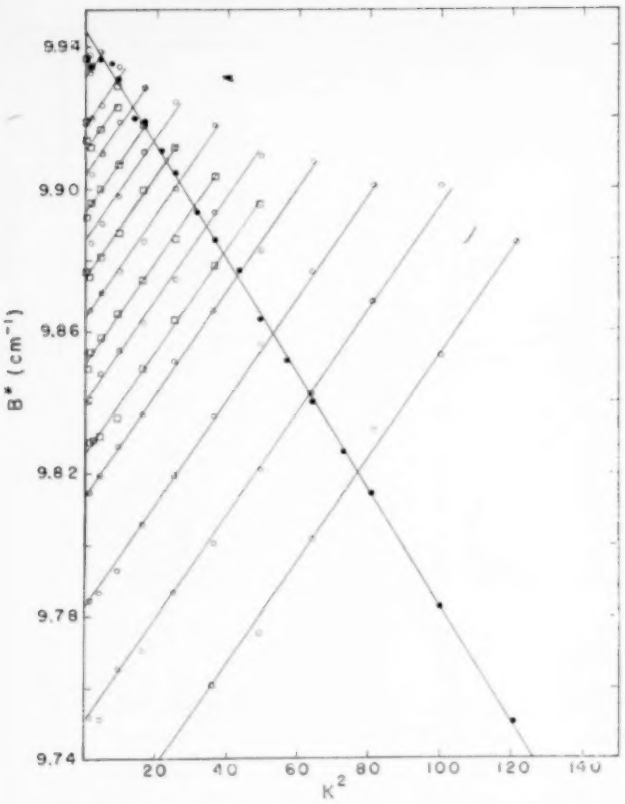

FIGURE 4. *Derivation of rotational constants for* NH_3 *ground state.*

Open circles, $\Delta_2F/(4J+2)$; open squares, $\Delta_1F/2J$. The intercepts of these lines at $K=0$ are plotted as solid circles against $J(J+1)$.

the *a* substate, as required by eq (4). Inasmuch as infrared measurements cannot be as precise as those in the microwave regions, no attempt was made to determine the ground-state inversion constants, those cited above [17] being accepted. The *s* and *a* combination differences were averaged and divided by $2J$ (for Δ_1F) and $(4J+2)$ for Δ_2F. The results are plotted as a function of K^2 as the open points in figure 4; these very nearly form a family of straight lines of equal slope, yielding $D_0^{JK}=-0.001455$ cm^{-1}. The intercepts at $K=0$ are also plotted in figure 4 as solid points as a function of $J(J+1)$; from the slope and intercept of this line is obtained $D_0^J=0.000809$ cm^{-1} and $B_0=9.94428$ cm^{-1}. The combination differences ΔF are given in table 6 as calculated from these constants, and are compared with the observed averages. The agreement is satisfactory. A somewhat better fit might perhaps have been obtained by including sixth-power terms in J and K; that is, by fitting the points in figure 4 to slightly curved parabolas instead of straight lines. It is believed, however, that the precision with which the data are known does not warrant such a procedure at this time; after other bands have been measured with comparable precision, their ground-state combination differences may be included in the averages and improved constants should result.

In order to obtain the constants for the upper states the position of each observed level is first determined relative to the same level in the ground state. For a *Q*-branch line this is the line position; for *P*- or *R*-branch lines, the appropriate ground-state combination differences must be added or subtracted from the observed position. For the parallel bands, there are two observed levels for each (J,K); for the perpendicular bands, four. Straight-line plots of the averages of these, against $J(J+1)$ and K^2, yield ν_0, B_v-B_0, and $[(C_v-C_0)-(B_v-B_0)]$. There appear to be slight but regular deviations from linearity, in the plots against $J(J+1)$, so that it is experimentally justifiable to include the term in $D_v^J-D_0^J$; however, $D_v^{JK}-D_0^{JK}$, and $D_v^K-D_0^K$ appear to be negligible in both bands. The constants are listed in table 7.

The inversion splitting in $\nu_1+\nu_2$ is the difference between the observed *Q*-branch doublings as obtained above and the ground-state splitting. When plotted against $J(J+1)$ and K^2, considerable curvature is noted. This may be largely eliminated by plotting the logarithm of the splitting; that is, by fitting the rotational dependence to eq (4) instead of to a simple power series. The same behavior is noted in $\nu_3+\nu_2$, for which the inversion splitting is the sum of the ground-state splitting and the observed *Q*-doublings. Here it is noted that the inversion splitting is slightly different in the K^+ pairs (^RQ-branches) than in the K^- pairs (^PQ-branches). The differences are nearly proportional to K, and hence may be interpreted in terms of a different ζ for the two inversion levels. The average $(K^++K^-)/2$ splitting is used to derive the constants in eq (4). These constants are also given in table 7, as are the constants for each subband of the inversion doublet obtained by converting to the power-series expansion.

The constants C_0, C_v, ζ, and the associated centrifugal-stretching constants are obtained for $\nu_2+\nu_3$ from the differences $(^PQ-{}^RQ)$ as averaged with the corresponding *P*- and *R*-lines, and averaged for the two inversion states. From eq (3)

$$[^PQ(J',K')-{}^RQ(J'K')]/4K=(B_0-C_0+C_v\zeta_v+2D_0^K)+(D_0^{JK}-\tfrac{1}{2}\zeta_v^J)J(J+1)+(2D_0^K-\tfrac{1}{2}\zeta_v^K)K^2. \quad (9)$$

The data fit rather well the equation $(^PQ-{}^RQ)/4K=3.9485-0.001206\,J\,(J+1)+0.001462K^2$. Using the already derived values of B_0 and D_0^{JK}, the constants listed in table 7 are obtained. Although there is an experimental value for C_0-C_v, the constants C_0 and ζ, and D_0^K and ζ^K cannot be obtained from this band alone. Only from corresponding measurements in a number of perpendicular bands will it be possible to separate accurately the contributions of the upper and lower states. This will be discussed in a later paper. Tentative values are $C_0=6.196$ cm^{-1}, $D_0^K=7.5\times10^{-4}$ cm^{-1}; whence follow the values of ζ given in table 7. A linear fit to the difference in $^PQ-{}^RQ$ for the *a* and *s* components yielded the difference in ζ tabulated.

TABLE 6. *Ground-state combination differences* (cm^{-1})

The first line, for each ΔJ and K in the table, gives the calculated values for the combination difference for the average of the two ground states, s and a, $\pm(s-a)/2$. The second line gives the average values observed in the $(\nu_1,\nu_3+\nu_2)$ bands, the value for the s state being to the left, for the a state to the right, both with the figures preceding the decimal point omitted. When there is no entry on the second line, the corresponding lines have not been observed sufficiently free from blends to yield a reliable value.

ΔJ	$K=0$ →	1	2	3	4	5	6
2−0	59.636−.014 .56						
2−1	----------	39.757±.010 .76 .74					
3−1	99.323+.022 .36	99 338±.024 .33 .33					
3−2	----------	59.581±.014 .59 .60	59.607±.015 .62 .60				
4−2	138.924−.030 .87	138 945±.032 .06 .89	139 005±.034 .96 .95				
4−3	----------	79 364±.018 .38 .33	79 398±.019 .39 .36	79.457±.020 .48 .44			
5−3	178.390+.038 .44	178.417±.040 .46 .34	178.495±.041 .55 .45	178.626±.045 .71 .63			
5−4	----------	99.053±.022 .10 .98	99.097±.022 .11 .08	99.169±.023 .20 .15	99.271±.025 .30 .27		
6−4	217.670−.045 .61	217.703±.046 .72 .69	217.800±.047 .83 .76	217.939±.049 .98 .91	218.183±.052 .25 .14		
6−5	----------	118.650±.024 .62 .61	118.702±.025 .72 .65	118.790±.026 .80 .74	118 912±.028 .97 .87	119.069±.030 .14 .05	
7−5	256.742+.049 .78	256 780±.050 .79 .74	256 895±.052 .00 .79	257.082±.055 .16 .60	257.348±.058 .42 .29	257.688±.062 .80 .61	
7−6	----------	138.130±.026 .13 .10	138.191±.027 .24 .14	138.293±.029 .31 .24	138.436±.030 .42 .36	138.619±.032 .63 .56	138.843±.036 .89 .82
8−6	295.565−.051 .48	295.607±.052 .68 .51	295.739±.054 .85 .68	295.937±.054 .99 .89	296.262±.061 .25 .20	296.656±.065 .64 .51	297.135±.073 .20 .01
8−7	----------	157.478±.026 .53 .36	157.548±.027 .57 .55	157.664±.024 .68 .66	157.827±.031 .81 .78	158 037±.033 .01 .98	158 293±.037 .31 .27
9−7	334.093+.052 .16	334.142±.053 .17 .16	334.292±.055 .26 .21	334.548±.065 .58 .48	334.884±.062 .92 .86	335 330±.068 .40 .30	335.874±.074 .92 .80
9−8	----------	176.664±.026 .69 .64	176.743±.028 .73 .73	176.874±.040 .96 .77	177.057±.031 .09 .00	177.293±.034 .33 .27	177.581±.037 .60 .55
10−9	----------	195.679±.026 .69 .64	195.766±.027 .74 .74	195.912±.008 .94 .79	196.115±.030 .17 .06	196.377±.033 .46 .33	196.697±.037 .77 .65
11−10	----------	214.499±.025 .57	214.595±.026 .50	214.755±.066 .85 .83	214.979±.029 .98	215.267±.031 .39 .24	215.619±.035 .61 .62
12−11	----------	233.106±.024	233.211±.024 .48	233.385±.038 .41	233.630±.027	233.944±.030	234.328±.032 .39 .11
13−12	----------	251.480±.022	251.593±.023	251.782±.128	252.047±.025	252.388±.027	252.804±.030
14−13	----------	269.601±.020	269.723±.021	269.927±.143	270.212±.023	270.579±.025	271.027±.028

ΔJ	$K=7$ →	8	9	10	11	12	13
8−7	158.596±.041 .63 .51						
9−7	336.518±.083 .41						
9−8	177.921±.042 .94 .87	178.314±.048 .38 .28					
10−9	197.074±.041 .13 .11	197.512±.047 .59 .48	198.007±.055 .05 .97				
11−10	216.036±.039 .21 .91	216.516±.045 .56 .47	217.060±.052 .11 .08	217.668±.062 .87 .77			
12−11	234.782±.036 .57	235.306±.042 .17 .29	235.899±.049 .14 .83	236.563±.058 .42	237.296±.070 .16		
13−12	253.296±.034	253.863±.038	254.506±.045	255.225±.054	256.019±.064	256.889±.080 .99	
14−13	271.557±.031	272.168±.035	272.860±.040	273.634±.048	274.490±.058	275.427±.072	276.445±.090

The upper-state levels with $K=1^+$ and 2^- (A_1, A_2 doublets) deviated from the positions calculated with the over-all constants in approximately the way required by eq (4b) and (4c). The resulting constants were $\beta_{1,0110}=1.95\times10^{-2}$ cm^{-1}; $\beta_{2,0110}=1.88\times10^{-4}$ cm^{-1}.

The constants summarized in table 7 give, as tables 4 and 5 show, an excellent representation of the observed spectra up to $J=10$. There are increasing deviations of the observed from calculated lines at higher J. These arise partly from the difficulties of measuring the weak lines of high J', partly from the failure to include additional terms of higher order in the energy expressions, and presumably, to some extent from additional perturbations on the upper-state energy not included in the standard expressions. It will be noted that when the (obs-calc) deviations in the tables are greater than 0.1 cm^{-1}, the deviations for the three lines with a common upper state agree, behavior which is typical of an upper-state perturbation. A partial quantitative explanation can be given for two of these perturbations, which will now be discussed briefly.

TABLE 7. *Molecular constants for* NH_3 *bands* ($\nu_1+\nu_2$ *and* $\nu_2+\nu_3$)

Constants	Units	Band: $\nu_1+\nu_2$			Band: $\nu_2+\nu_3$			Ground-state value
		$s-a$	$a-s$	Average	$a-s$	$s-a$	Average	
ν_0	cm^{-1}	4293.716	4320.060	4306.888	4416.908	4434.610	4425.759	.....
B_s-B_0	$10^{-2}cm^{-1}$	−6.22	−19.38	−12.80	−15.087	−24.421	−19.754	994.43
$(C-B)_s-(C-B)_0$	$10^{-2}cm^{-1}$	−9.83	8.23	−0.80	4.414	17.839	11.126	(−376.9)
C_s-C_0	$10^{-2}cm^{-1}$	−16.05	−11.15	−13.60	−10.673	−6.582	−8.628	(617.5)
$D_s^J-D_0^J$	$10^{-4}cm^{-1}$	1.25	−2.05	−0.4	0.70	−1.90	−0.60	8.09
$D_0^{JK}-D_0'^K$	$10^{-4}cm^{-1}$	−4.5	4.5	0	−3.91	3.14	−.38	−14.55
$D_s^K-D_0^K$	$10^{-4}cm^{-1}$	3.1	−3.1	0	3.52	−1.56	.98	(7.5)
$C_0-2D_0^K-C_0\zeta$	cm^{-1}	.....	.....	.....	6.0065	5.9850	5.9958	.....
ζ	.....	.....	.....	.....	0.0273	0.0310	0.0292	.....
ζ^J	$10^{-4}cm^{-1}$	.....	.....	.....	.....	.....	−4.98	.....
$D_0^K-\frac{1}{4}\zeta^K$	$10^{-4}cm^{-1}$	.....	.....	.....	.....	.....	7.31	.....
E_s^i	cm^{-1}	.....	.....	25.551	.....	.....	18.495	0.7934
b_s^i	10^{-3}	.....	.....	−4.95	.....	.....	−5.32	−6.3700
$C_s^i-b_s^i$	10^{-3}	.....	.....	6.79	.....	.....	7.64	8.8899
C_s^i	10^{-3}	.....	.....	1.84	.....	.....	2.32	2.5199
d_s^{ij}	10^{-6}	.....	.....	0?	.....	.....	0.83	0.8692

The three levels v_1, J, K; v_3, J, $(K+1)^+$; and v_3, J, $(K-1)^-$ are of identical over-all symmetry, and interact due to Coriolis forces. The matrix of the interaction is

	$K-1$	K	$K+1$
$K-1$	$\nu_3+E_r(J,K-1)-E$	$\frac{\alpha}{\sqrt{2}}[(J+K)(J-K+1)]^{1/2}$	0
K	$\frac{\alpha}{\sqrt{2}}[(J+K)(J-K+1)]^{1/2}$	$\nu_1+E_r(J,K)-E$	$\frac{\alpha}{\sqrt{2}}[(J-K)(J+K+1)]^{1/2}$
$K+1$	0	$\frac{\alpha}{\sqrt{2}}[(J-K)(J+K+1)]^{1/2}$	$\nu_3+E_r(J,K+1)-E$,

(10)

where $\alpha=\frac{1}{2}\zeta_{13}B_e(\omega_1+\omega_3)/(\omega_1\omega_3)^{1/2}$, and ζ_{13} is the interaction constant. When, as is the case for most values of K, the energy difference between the interacting levels is large compared with the off-diagonal matrix elements, the latter terms make the normal second-order contributions to the energy that appears as part of the constants α_1^B and α_3^B. When, however, the energy difference becomes of the same order of magnitude as $\alpha[(J-K)(J+K+1)]^{1/2}$ a perturbation occurs, attaining its maximum effect when the two states coincide. The energy differences, neglecting the perturbations and centrifugal-stretching terms, are

$$E_{JK\pm1}-E_{JK}=\nu_3-\nu_1\pm(2K+1)[C_3(1\pm\zeta)] -C_1-B_3+B_1, \quad (11)$$

i. e., it approaches zero for the state $K+1$, corresponding to approach of the lines in the ^QQ- and ^RQ-branches at high K. In the a-s half-band of $\nu_2+\nu_3$, the constants are such that $\Delta E\sim0$ at $K\sim13$; in the s-a half-band, $\Delta\nu_0$ is greater, so that the crossover is at slightly higher K. As is apparent from table 5, the series of strong ^RR lines with $K=J$ can be followed in s-a to $K'=15$, whereas in a-s the sequence becomes irregular. No line of the expected intensity can be found near the calculated positions for $^RR(13,13)$, but two lines of nearly equal strength otherwise unaccounted for occur at frequencies 2.70 cm^{-1} below and 1.70 cm^{-1} above the calculated value of 4554.70 cm^{-1}. It is tempting to assign these to the perturbed level. If the resonance is exact, the derived value of $\alpha=4.40/26=0.17$, corresponding to

$\zeta_{12}=0.017$. This is of the theoretically expected order of magnitude. α is so small that the levels with $K^+<12$, for which $\Delta E>16$ cm^{-1}, would not be shifted greatly from their unperturbed positions, so that the normal method of deriving molecular constants is justifiable, the bulk of the effect of the perturbation being taken up in $D_v^J-D_0^J$. The perturbation would, however, account for the deviations (obs-calc) of from 0.1 to 1 cm^{-1} found in the (a-s) band for $J\geq 11$, which can be fitted only by powers of $(J+K)$ higher than the fourth.

The second perturbation would arise from the resonances caused by the near equality of $2\times\nu_4$ and ν_1. In the present instance the levels $2\nu_4^0+\nu_2$ lie about 100 cm^{-1} below $\nu_1+\nu_2$ for each J_K, and are of like symmetry. Each level of $\nu_1+\nu_2$ will thus be pushed upward; the shifts would be equal if the rotational constants and inversion doubling were the same in $2\nu_4^0+\nu_2$ and $\nu_1+\nu_2$. However, because the observation of other bands involving ν_4 indicates that the inversion doubling will be considerably greater in $2\nu_4+\nu_2$ than in $\nu_1+\nu_2$, and that $B_4>B_2$, the resulting perturbations on the $\nu_1+\nu_2$ levels, particularly those of high J in the upper (a) inversion state, may become too large to fit by the normal power series. Table 4 shows that the deviations are indeed greatest for those levels. The $2\nu_4^2+\nu_2$ levels, as well as those of $2\nu_4^0+\nu_2$ will also interact Coriolis-wise with those of $\nu_3+\nu_2$, however, these effects are presumably of less importance than those discussed in the previous paragraph because the energy differences are greater.

Although, as just mentioned, the states of $2\nu_4+\nu_2$ lie close enough to $\nu_1+\nu_2$ to affect the latter, and their position can be estimated with some probability, it has not as yet been possible to identify any of the lines in those bands. There are a number of quite strong lines below 4,200 cm^{-1} that must belong to the bands, and these are particularly numerous near 4,180 and 4,130 cm^{-1}, where the ^QQ-branches should lie, but no convincing assignment of the strong lines to the expected series has been achieved. Presumably the many possible interactions disturb the intensities, as well as the positions of the expected transitions. In the corresponding bands of ND_3, however, a satisfactory analysis has been achieved, with normal intensities, so that the difficulties encountered in NH_3 remain puzzling.

3.2. Line and Band Strength and Line Width

The problems of relating the observed fractional transmission of a resolved spectrum to the true strength and shape of its component lines have been discussed in detail elsewhere [7]. There are two principal types of difficulties, aside from the experimental problems of accurate measurement of absorbing conditions and transmission. The first arise when the spectrometer slit width is appreciably greater than the line width; these can be overcome if it is possible to obtain measurements at a variety of pressures and path lengths on single lines, free from overlapping by neighboring lines in the spectrum. The second type of difficulties arise from overlapping, and are imposed by the nature of the spectrum. In NH_3 vibration-rotation bands in general, the self-broadened line widths are quite high, from 0.15 to 0.6 cm^{-1}/atm. This is a consequence of the high dipole moment (1.46 Debyes) and the low inversion frequency of the ground state. As a result, with the effective resolution of $\sim$0.10 cm^{-1} available in the region 1,600 to 7,500 cm^{-1}, slit corrections should become of minor significance at pressures of $\frac{1}{3}$ atm and above. Unfortunately, however, in nearly all NH_3 bands the lines are closely spaced, so that overlapping becomes a major problem.

In the bands reported in the present paper, there are only a few regions where overlapping at $P>\frac{1}{3}$ atm is not serious, so that the absolute widths of only those few lines may be determined with fair accuracy. However, from low-pressure measurements the relative strength-width products of most of the lines can be determined, and from high-pressure measurements the strengths may be found. These results are given in this section. Much more satisfactory measurements of the strength, width, and shape of NH_3 vibration-rotation lines have been achieved in the parallel bands $3\nu_2$, where $(B_0-B_v-C_0+C_v)$ is sufficiently large so that overlap is at a minimum. These will be presented in a subsequent paper.

The band strengths, S_v of the perpendicular and parallel bands were determined by two methods. First, by measurement of the integrated absorption in those portions of the bands where such measurements are meaningful, making corrections for overlap of the bands. Second, by measurement of the equivalent width and hence the strengths of individual lines that fell in the near-linear region of the curve of growth, assuming that the band strength is related to the line strength by eq (5).

The first method requires measurements at pressures greater than 30 cm, so that the slit corrections may be neglected, and path lengths such that the absorption is in the range 10 to 90 percent, where the measurements are least subject to experimental error resulting from uncertainties in locating the base lines. These conditions are met in the 5-cm cell for the central region of the bands, from 4,280 to 4,560 cm^{-1}, covering the Q- and R-branches of the weaker bands $\nu_1+\nu_2$, and the main portion of the stronger band $\nu_3+\nu_2$. The 15.5-cm cell provides checks on the regions of weaker absorption in that interval, and in addition provides data on the regions 4,160 to 4,280 cm^{-1}, where lines of the P-branch of $\nu_1+\nu_2$ are relatively free from overlap by other bands, and 4,560 to 4,600 cm^{-1}. The results obtained are for $\nu_1+\nu_2$, $S_v^0=2.9\pm0.5$ cm^{-2} atm^{-1}, and for $\nu_3+\nu_2$, $S_v^0=19.7\pm2$ cm^{-2} atm^{-1}. The above figures refer to an average temperature of 296°K (although the integrated band strength appears, as expected, not to be significantly temperature-dependent), and the pressure refers to the actual temperature, not 273°K.

The best possibilities for measuring strengths of individual lines in $\nu_2+\nu_3$ are in the extreme wings ($J>9$, ^PR- and ^RP-branches), and for those few lines at low J in ^RR and ^PP where the nearest neighbors are more than 1 cm^{-1} distant. The 1,000-cm path provided numerous examples of the first type, the 15.5-cm path several of the second. For these the mean specific

equivalent widths, W/P, are collected and averaged in table 8. The corrections to the observed W/P for the effect of line width were made according to the formula [7]

$$S_{rr}^0 l = (W/P)(1+W/2\pi\gamma^0 P), \tag{11}$$

which is valid when $W/2\pi\gamma^0 P<0.5$. The correction involves the linewidth γ^0, for which the smoothed values to be described later were used, but the average results are not significantly dependent on the choice of γ^0. It will be noted that the observed equivalent widths for the two components of the inversion doublet are in rough agreement, so that their average value was used in the subsequent computations. For each line, using the rigid-rotator value of $S_r r/S_v$ (table 3), a value of S_v^0 (rig) was calculated. If the measurements were precise, and the assumption F=1 valid, these should all be equal to 19.7 cm^{-2} atm^{-1} as obtained from the integrated-band measurements. Considerable variation will be noted, although the agreement is always within a factor of two. The presence of unsuspected blends may occasionally give rise to abnormally high values of S_v^0; these were excluded from the averages. The group averages show regularities, in that the ${}^PR$ lines are significantly weaker, and the ${}^RP$ lines significantly stronger, than the average, while ${}^RR$ and ${}^PP$ show similar but less-marked deviations. It thus appears likely that the observations reveal effects of the vibration-rotation interaction on the intensities. The approximate form of the interaction factor F for a perpendicular band of a symmetric-top is [19]

$$F=(1+am+bk)^2$$

where m is the ordinal line number in a K sub-branch (J' in ${}^RR$ and ${}^PR$, $-J''$ in ${}^RP$ and ${}^PP$), and k the ordinal number of the sub-branch (K' in ${}^RP$, ${}^RQ$, and ${}^RR$; $-K''$ in ${}^PP$, ${}^PQ$, and ${}^PR$). a and b are constants that in principle might be evaluated from the absolute intensities of all of the vibration-rotation bands and the potential function. Because such full information is lacking, it is sufficient to note that a considerable reduction in the scatter of the results for the $\nu_2+\nu_3$ band is achieved by using as tentative empirical values, $a=-0.015$, $b=0.01$. The last two columns of table 8 give the resulting values of $F(0110,JK)$ and S_v^0 (corr)$=S_v^0$ (rig)$/F$. The final value of S_v^0 by this method is 24.0 ± 3 cm^{-2} atm^{-1}. This result is 20 percent higher than obtained by direct integration. The first method is probably slightly the more reliable, its greater uncertainty in locating the zero-absorption level being overcome by the fewer theoretical assumptions involved.

It is interesting to note that the measurements show the $\nu_2+\nu_3$ combination band to be more intense than the ν_3 fundamental, for which McKean and Schatz [20] report a value of 13 cm^{-2} atm^{-1} from measurements of the combined absorption in ν_1 and ν_3. From the high-resolution measurements of those fundamentals, to be reported in a subsequent paper, it appears that the relative contribution of ν_3 to the $\nu_1+\nu_3$ sum has been underestimated, but in any event the combination band is the more intense. This must reflect the highly anharmonic nature of the ν_2 vibration, as well as a considerable breakdown of the separation of modes in the combination band.

Having thus established fairly accurate values of the strength of each individual line, there are now three possible methods for obtaining line widths, assuming the Lorentz shape. The first applies at high pressures, (i. e., above 1/3 atm) when the line width 2γ is greater than the slit width d. It is based on the measurement of the extinction at a line peak, where for a single line,

$$\epsilon_{max}=-\ln(I_{min}/I_0)=(1/\pi l)(S^0/\gamma^0). \tag{13}$$

The measurement is subject to slit corrections which are functions of γ/d and of ϵ_{max}, which may conveniently be evaluated from the graphs of Kostkowski and Bass [21]. ϵ_{max} should be independent of pressure, except insofar as $\gamma=\gamma^0 P$ enters into the slit correction. However, as mentioned previously, at pressures sufficiently high for the slit corrections to be small, the overlap by neighboring lines is appreciable. However, their contribution may be estimated, so that from the observed ϵ and the calculated $S^0\gamma^0$ is obtained. Reasonably concordant results were obtained for a few isolated lines in the 5- and 15-cm cells.

The second method is applicable to the same lines, where slit-correction effects and overlap effects are both small, and consists of the direct measurement of the line breadth b_ϵ at various values of the extinction ϵ. For a Lorentz line,

$$\gamma^0 P=(b_\epsilon/2)[\epsilon_{max}/\epsilon)-1]^{-1/2}. \tag{14}$$

A single measurement of b at $\epsilon=\epsilon_{max}/2$ might suffice to give 2γ directly if observing conditions are very stable. In practice, it is preferable to measure b at several values of ϵ, apply the slit and overlap-corrections, and average the results.

The third method is more generally applicable in these NH_3 bands, being the measurement of equivalent width under the conditions of long path and low pressure, for which overlapping is minimal. The appropriate relation valid for $x>1$, is

$$W/P=2(S^0\gamma^0)^{1/2}\left(1-\frac{1}{8x}\right), \tag{15}$$

where x is $S^0/2\pi\gamma^0$. With $l=1{,}000$ cm, x for the strongest line is of the order of 100, so that most of the observed lines should obey the "square-root law" quite closely. Thus $\gamma^0=4(W/P)^2/S^0$. The principal corrections required here, for the suitable spectra obtained over the pressure range 0.5 to 3 cm, arise from the Doppler effect. The parameter governing those corrections is $a=(\ln 2)^{1/2}\,\gamma_L/\gamma_D$, γ_L, and γ_D being, respectively, the Lorentz and Doppler widths. For NH_3 at 298° K and 4,500 cm^{-1}, $\gamma_D=0.00674$ cm^{-1}, so that if $\gamma^0\cong 0.5$ cm^{-1} atm^{-1}, $a<1$ for $P<0.82$ cm Hg. For $x>5$ the corrections are still very small at the lowest pressures studied, the difficulty of measuring pressures below 1 cm with sufficient accuracy being a greater source of uncertainty.

TABLE 8. *Band strength $\nu_2+\nu_3$ from near-linear lines*

Line	ν_0	W/P	S_ν^0/Sd	$\frac{S_\nu}{10^3 S_\nu}$	S_ν^0 (rig)	F	S_ν^0 (corr)
Weak *R*-branch lines, $l=1{,}000$ cm							
	cm^{-1}	cm^{-1}/cm Hg	cm^{-1}/cm Hg		$cm^{-2}atm^{-1}$		$cm^{-2}atm^{-1}$
$^PR(11, 9)$	4.712	0.0020	0.0025	0.131	13.6	0.53	25.6
	4.699	.0029					
$^PR(10, 9)$	4.698	.0027	.0037	.203	13.1	.56	24.5
	4.684	.0045					
$^PR(11, 7)$	4.690	.0032	.0035	.093	26.6	.56	47?
	4.680	.0035					
$^PR(10, 8)$	4.687	.0025	.0031	.158	14.1	.57	25
	4.674	.0034					
$^PR(9, 9)$	4.684	.0045	.0046	.194	16.9	.58	29
	4.668	.0044					
$^PR(10, 6)$	4.667	.0078	.0079	.460	12.3	.60	20.5
	4.656	.0066					
$^PR(9, 7)$	4.662	.0057	.0063	.329	13.8	.61	23
	4.650	.0061					
$^PR(10, 5)$	4.657	.0035	.0039	.205	10.6	.62	17.3
	4.647	.0038					
$^PR(11, 3)$	4.654	.0035	.0047	.281	12.0	.62	19.2
	4.645	.0053					
$^PR(10, 3)$	4.639	.015	.0167	.693	17.4	.65	27
	4.631	.012					
$^PR(8, 6)$	4.638	.023	.034	1.373	19.3	.65	30
	4.625	.026					
$^RR(11, 3)$	4.600	.014	.0175	0.749	17.0	.74	23
$^RR(11, 4)$	4.603	.0090	0.0107	0.478	15.3	.75	20.3
	4.594	.010					
Average, 23 lines					14.5	---	23.8
Strong *R*-branch Lines, $l=15.5$ cm							
$^RR(8, 2)$	4.573	0.00192	0.00198	4.31	22.0	0.78	28
$^RR(6, 3)$	4.566	.0060	.0065	18.74	16.3	.78	21
$^RR(10, 6)$	4.565	.00157	.00160	4.69	16.2	.75	21.5
$^RR(9, 3)$	4.563	.00252	.0026	4.96	25.0	.78	32.5
$^PR(6, 2)$	4.558	.0139	.0145	24.6	28.0	.85	33
$^RR(5, 2)$	4.557	.0099	.0113	26.1	20.5	.87	23.7
$^RR(9, 8)$	4.553	.0045	.0047	12.4	18.3	.87	21.1
$^RR(8, 6)$	4.548	.025	.029	73.5	18.7	.86	21.7
Average, 8 lines					20.6	---	24.0
Strong *P*-branch lines, $l=15.5$ cm							
$^PP(4, 2)$	4.347	0.0124	0.0147	28.3	25.8	1.08	23.9
$^PP(6, 5)$	4.346	.0128	.0145	32.6	22.1	1.08	20.4
$^RP(3, 1)$	4.345	.0034	.0036	3.25	59	1.13	52?
$^PP(4, 1)$	4.339	.0076	.0086	17.0	25.3	1.10	23.0
$^PP(8, 8)$	4.330	.0096	.0105	26.8	19.6	1.08	18.2
Average, 4 lines					23.2	---	21.4
Weak *P*-branch lines, $l=1{,}000$ cm							
$^PP(11, 7)$	4.249	0.035	0.068	1.04	51.7	1.19	43.5
	4.236	.040					
$^PP(10, 1)$	4.211	.012	.0157	0.507	24.6	1.30	18.9
$^RP(8, 5)$	4.209	.010	.011	.318	27.4	1.12	24.5
$^RP(10, 1)$	4.207	.010	.0115	.333	27.5	1.34	20.5
$^PP(11, 2)$	4.207	.010	.0115	.244	37.5	1.31	28.6
Average, 5 lines					33.7	---	27.2
Over-all average, 40 lines					19.0	---	24.0

Table 9 summarizes some of the numerous measurements made on four of the best lines by the three methods just outlined. They are in fairly good agreement, indicating that the estimates of S^0, and the various assumptions and measurements are reasonably well founded. Since in the three methods γ^0 is proportional respectively to $(S^0)^{+1}$, $(S^0)^0$, and $(S^0)^{-1}$ uncertainties in S^0 should not affect the average values.

It will be noted that there is a considerable variation in the magnitude of γ^0 for the four lines included in table 9. It is largest for the two lines with $K=J$, and decreases with K/J. The same behavior was noted for the many other lines of the

TABLE 9. *Line-width measurements for selected lines*

Conditions	Line	$^{R}R(3,3)^{a}$	$^{R}R(3,0)^{a}$	$^{R}R(5,2)^{a}$	$^{R}R(6,6)^{a}$
	ν_0 (cm^{-1})	4466.3	4489.1	4510.1	4516.8
	S^0 calc (cm^{-2} atm^{-1})	0.301	0.177	0.0479	0.210
Method 1: l=15.5 cm, P=0.32 atm.	ϵ_{max} (obs.)	2.47	2.95	0.79	2.00
	Slit corr.	+0.10	+0.41	+.09	+0.10
	Overlap corr.	−.06	−.16	−.08	−.13
	ϵ_{max} (corr.)	2.51	3.20	.80	1.97
	γ^0 (cm^{-1} atm^{-1})	0.59	0.27	.29	0.53
Method 1: l=5.0 cm, P=0.91 atm.	ϵ_{max} (obs.)	1.10	1.57	0.40	1.04
	Slit corr.	+0.02	+0.05	+.01	+.02
	Overlap corr.	−.18	−.45	−.22	−.38
	ϵ_{max} (corr.)	.94	1.17	.19	.68
	γ^0 (cm^{-1} atm^{-1})	.51	0.24	.40	.49
Method 2: l=15.5 cm, P=0.32 atm.	Range of $b\epsilon$ (cm^{-1})	0.3 to 0.8	0.15 to 0.5	0.4 to 1.2	0.2 to 0.8
	Corrections, %	12 to 5	18 to 5	18 to 8	20 to 5
	Average γ^0 (cm^{-1} atm^{-1})	0.49±.05	0.22±.04	0.43±.03	0.59±.05
Method 3: l=1,000 cm, P=0.0065 atm.	W obs (cm^{-1})	0.171	0.081	0.056	0.137
	Doppler corr. %	−.5	−2.0	−5.8	−.7
	γ^0 (cm^{-1} atm^{-1})	.57	0.21	0.35	.54
Average observed γ^0 (cm^{-1} atm^{-1})		0.54±.04	0.23±.03	0.37±.05	0.55±.04
Microwave γ^0 (cm^{-1} atm^{-1})		.69	.25	.41	.73

TABLE 10. *Smoothed values of line width γ^0 (cm^{-1} atm^{-1}) in $\nu_2+\nu_3$*

$(J'+J'')/2$											$(K'K'')/2$
½	1½	2½	3½	4½	5½	6½	7½	8½	9½	10½	11½	
0.37	0.31	0.27	0.25	0.24	0.23	0.21	0.19	0.18	0.18	0.17	0.16	½
	.47	.38	.32	.29	.28	.27	.26	.24	.22	.21	.20	1½
		.53	.44	.38	.35	.34	.31	.29	.27	.26	.24	2½
			.55	.47	.42	.40	.37	.34	.30	.28	.26	3½
				.56	.50	.46	.41	.38	.35	.32	.30	4½
					.56	.51	.46	.42	.40	.37	.33	5½
						.57	.51	.47	.44	.42	.39	6½
							.57	.52	.48	.45	.43	7½
								.56	.52	.48	.45	8½
									.55	.51	.47	9½
										.55	.50	10½
											.54	11½

band for which measurements, chiefly by the third method, could be made. The absolute results for any single determination appear rather inaccurate, but the relative values as functions of J and K are quite regular. Smoothed average values are given in table 10. The dependence on J and K parallels that found in the microwave region [6]. Anderson [8] has shown that the observed microwave widths are in good agreement with his theory of collision-broadening. Table 9 includes Anderson's values, averaged for the two states involved. It is apparent that the vibration-rotation widths are consistently 20 to 25 percent less than the microwave widths. An application of Anderson's theory to the present situation has not been attempted, because of the complexity of the calculation and the limited accuracy of the data, but it is qualitatively apparent that a decreased width of the observed order is to be expected. For the microwave case, when the vibrational transition is 0^a-0^s, both initial and final states have inversion frequencies <1 cm^{-1}, so that in all encounters with colliding molecules, nearly resonant dipolar transitions can occur. For the infrared bands $01^{a,s}10-0^{s,a}$, the initial state has the same low inversion frequency, <1 cm^{-1}, but for the upper state the inversion frequency is ~ 20 cm^{-1}. Hence a large proportion of the energy interchanges involving simultaneous dipolar transitions of the upper state and a colliding molecule are farther from resonance, resulting, according to Anderson's theory, in a decreased width. Note also that transitions involving $K=0$, which cannot occur in the microwave Q-branch lines, are the narrowest observed, again as a result of the paucity of resonant interactions involving those states.

According to this qualitative interpretation of the observed width data, in other vibration-rotation bands of NH_3 the widths should be greatest when both states have low resonant frequencies (e. g., ν_3), and should be even narrower than observed here when the upper state has very high inversion frequencies (e. g., $3\nu_2$). Work in progress shows that this is indeed the case.

It is of interest to note that the marked variation in half-width among the lines of the band results in easily recognizable alterations in the general appearance of the absorption under varying conditions. At high pressures and short paths the lines of greatest half-width are least prominent, since $\epsilon_{max} \sim S^0/\gamma^0 P$, whereas at low pressures and long paths they are the most prominent, since $I_{max} \sim W \sim (S^0\gamma^0)^{1/2}$. This is illustrated by the three tracings in figure 5, where the same spectral region is reproduced with identical slit widths for the three conditions $1=1000$

cm, P=0.5 cm; 1=15.5 cm, P=24 cm; and 1=5 cm, P=73 cm. In the upper panel, the calculated positions are represented by lines whose height is proportional to $(S^0\gamma^0)^{1/2}$; in the center by lines of height proportional to S^0; (since here γ is of the same order as d) and at the bottom, when overlapping is least extreme, by triangles of width $\sim\gamma^0$ and height $\sim S^0/\gamma^0$. The representations of the spectra are good, and the variations are notable. For example, the line ${}^{R}R(9,8)^{a}$ at 4552.8 cm^{-1} (γ^0=0.52 cm^{-1} atm^{-1}) is barely visible at high pressure, but is prominent at low pressure. Conversely, lines ${}^{R}R(6,0)^{a}$ and ${}^{R}R(7,0)^{s}$, with γ^0=0.20 cm^{-1} atm^{-1}, are very prominent at high pressure, and relatively weak at low pressure.

As a consequence of this variation, it may be pointed out that sets of spectra such as those in figure 5 may be used to distinguish narrow from

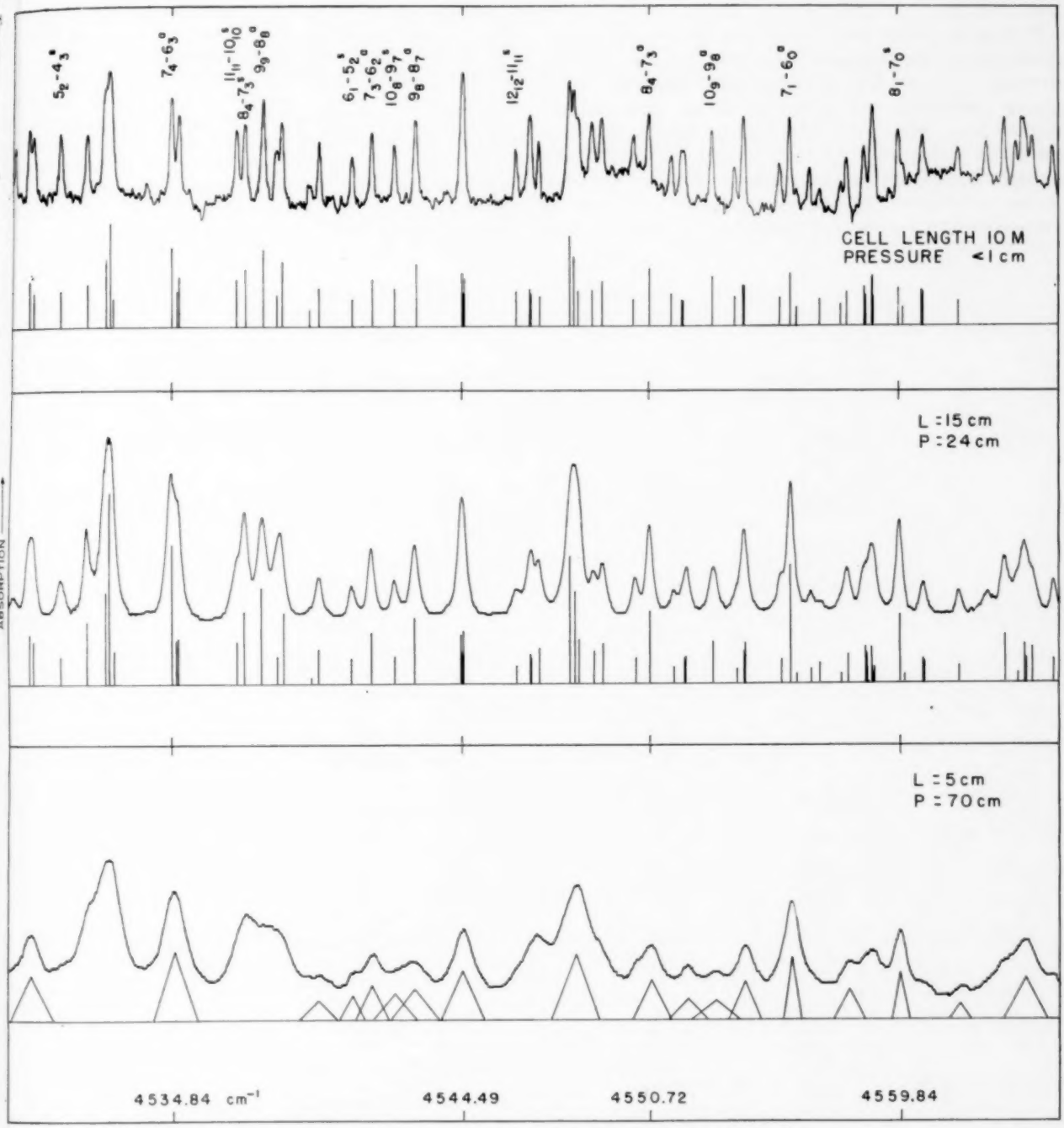

FIGURE 5. NH_3 *spectra, 4,530 to 4,560 cm^{-1}, at three path lengths.*

Upper spectrum, $p\sim$0.5 cm Hg; intensity $\sim(S\gamma)^{1/2}$; center spectrum, p=24 cm Hg, intensity $\sim S$; lower spectrum, p=70 cm Hg, width of intensity triangles $\sim\gamma$, height $\sim S/\gamma$.

broad lines, and thus to sort out lines with $K \sim 0$ from those with $K \sim J$ in otherwise unidentifiable situations. This technique proved of value in extending the analysis of the present bands to their highest J-values, where the series regularities became uncertain, and should also be very useful in beginning the analysis in very complicated bands, such as the higher overtone bands in the visible region [8] where there are many overlapping vibrational transitions with mutual perturbing interactions.

It may be noted that except for the effects of the considerable overlapping of lines in the "high-pressure" (70 cm Hg) tracings, the individual lines appear completely symmetrical about their central frequencies. Moreover, the central frequency does not shift detectably (<0.02 cm^{-1}) in the 70-cm pressure runs from its low-pressure value. This behavior confirms the lower-resolution finding of Nethercot and Peters [12], and has also been verified in all the NH_3 bands studied. It therefore would seem that the apparent shift and asymmetry of the microwave lines at pressures above 20 cm Hg [9] is a result of some property of the line shape when ν_0 and γ are of the same magnitude, rather than of any property of the statistical broadening of the energy levels.

Using the smoothed half-widths (table 10) and line strengths calculated from $S_v^0 = 19.7$ for $\nu_2+\nu_3$ and 2.9 for $\nu_1\nu_2$, a table of all the lines to be expected with the 1,000-cm path have been completed. A portion of the complete list is given as table 11, and, as pointed out earlier, the values of W_{calc} are proportional to the heights of the lines in figures 1 to 3. It is seen that a quite complete and accurate description of the spectrum has been attained. Only in the lower-frequency regions are there any considerable number of unassigned features, presumably due to other vibrational transitions such as $2\nu_4^0+\nu_2$, and $2\nu_4^2+\nu_2$. In the analyzed bands $\nu_1+\nu_2$ and $\nu_2+\nu_3$ both the positions and intensities are well accounted for.

TABLE 11. *Observed and calculated lines, 4,500 to 4,550 cm^{-1}*

ν		Line	100 S^0	γ^0	$(\epsilon_{max})l$ (l=5 cm)	W_L^0 (l=1,000 cm)	
Obs.	Calc.					Calc.	Obs.
cm^{-1}	cm^{-1}		cm^{-2} atm^{-1}	cm^{-1} atm^{-1}		cm^{-1} atm^{-1}	cm^{-1} atm^{-1}
4500.28	0.43	$^{Q}R(9,7)^{s}$	0.17	0.46	0.006	1.3	3.0
00.91							3.0
01.59	1.56	$^{R}R(4,3)^{s}$	20.7	.47	.70	18.3	21.4
	1.88	$^{Q}R(9,8)^{s}$	0.16	.50	.005	1.3	
02.65	2.62	$^{R}R(5,3)^{s}$	12.9	.42	.49	14.7	12.0
03.11	3.11	$^{P}R(2,2)^{s}$	0.76	.38	.032	3.3	4.4
	3.30	$^{P}Q(11,11)^{s}$	.12	.53	.003	1.0	
4503.72	3.67	$^{Q}R(9,9)^{s}$	.22	.53	.007	1.5	1.5
04.06							2.5
04.44							0.8
04.68							.3
04.94	4.96	$^{P}R(3,2)^{s}$	1.31	.32	.065	4.0	5.5
4505.56	5.50	$^{R}R(6,5)^{s}$	7.2	.51	.224	12.1	12.8
06.12	6.11	$^{R}R(5,5)^{s}$	13.2	.56	.374	15.2	15.2
08.16	8.20	$^{R}R(7,7)^{s}$	7.8	.57	.219	12.3	15.6
	8.23	$^{R}R(4,2)^{s}$	7.2	.38	.302	10.4	
09.10							0.3
09.42	9.25	$^{P}Q(12,12)^{s}$	0.09	.52	.003	0.8	.5
4510.05	0.06	$^{R}R(5,2)^{s}$	4.8	.35	.218	8.1	8.1
12.12	2.12	$^{R}R(5,4)^{s}$	9.2	.50	.290	13.5	11.9
12.91	2.83	$^{R}R(6,4)^{s}$	5.1	.46	.178	9.5	18.8
	2.91	$^{P}R(3,1)^{s}$	2.53	.25	.161	5.0	
	3.03	$^{P}R(3,3)^{s}$	0.94	.44	.053	3.9	
13.81							1.2
13.95	4.43?	$^{Q}R(10,6)^{s}$	.17	.40	.007	1.2	1.2
4515.19	5.18	$^{P}R(4,1)^{s}$	2.24	.24	.148	4.6	12.5
	5.22	$^{R}R(4,1)^{s}$	4.9	.29	.271	7.6	
15.55	5.58	$^{R}R(7,6)^{s}$	10.6	.51	.324	14.7	13.8
16.76	6.85	$^{R}R(6,6)^{s}$	21.0	.57	.589	21.9	21.0
17.34	7.57	$^{R}R(5,1)^{s}$	3.27	.28	.186	6.0	8.8
18.08	8.03	$^{R}R(8,8)^{s}$	5.3	.56	.150	10.8	13.8
4518.49	8.45	$^{R}R(5,3)^{s}$	12.7	.42	.48	14.6	14.4
19.37	8.69?	$^{Q}R(10,9)^{s}$	0.18	.49	.006	1.5	1.1
19.57							1.1
20.20	0.16	$^{R}R(6,3)^{s}$	7.2	.40	.280	10.7	8.8
21.01	0.97	$^{P}R(3,2)^{s}$	1.32	.32	.065	4.0	4.9
4522.43	2.42	$^{R}R(4,0)^{s}$	13.5	.24	.89	11.4	14.7
22.57	2.53	$^{R}R(6,5)^{s}$	7.2	.51	.225	12.1	13.5
22.87	2.84	$^{R}R(7,5)^{s}$	3.69	.46	.127	8.2	7.8
23.08	3.11	$^{P}R(4,2)^{s}$	1.40	.29	.077	4.0	5.1
23.97							0.4
4525.00	4.97	$^{R}R(5,0)^{s}$	9.7	.23	.674	9.4	13.5
	5.10	$^{R}R(5,2)^{s}$	4.8	.35	.219	8.1	
25.45	5.42	$^{R}R(8,7)^{s}$	3.53	.52	.108	8.5	7.3
25.87	6.14?	$^{Q}R(11,0)^{s}$	0.05	.17	.005	0.4	0.6
27.44	7.45	$^{R}R(7,7)^{s}$	7.8	.57	.218	13.2	28.9
	7.52	$^{R}R(6,2)^{s}$	2.72	.34	.127	6.0	
27.59	7.56	$^{R}R(9,9)^{s}$	7.1	.55	.205	12.4	

TABLE 11. *Observed and calculated lines, 4,500 to 4,550 cm⁻¹*—Continued

ν		Line	100 S^0	γ^0	$(\epsilon_{max})i$ (1=5 cm)	W_L^0 (1=1,000 cm)	
Obs.	Calc.					Calc.	Obs.
cm^{-1}	cm^{-1}		cm^{-2} atm^{-1}	cm^{-1} atm^{-1}		$cm^{-1}atm^{-1}$	$cm^{-1}atm^{-1}$
4528.55	8.53	$^{R}R(6,4)^{e}$	5.2	.46	.179	9.5	7.6
29.45	9.46	$^{P}R(3,3)^{e}$	0.94	.44	.033	3.9	4.0
30.01	0.05	$^{R}R(7,4)^{e}$	2.63	.41	.066	6.5	6.8
30.21	.24	$^{P}R(4,1)^{e}$	2.24	.24	.148	4.6	6.2
31.17	1.16	$^{P}R(4,3)^{e}$	1.49	.38	.062	4.7	5.6
4532.06	2.07	$^{R}R(5,1)^{e}$	3.28	.28	.186	6.0	6.2
32.66	2.63	$^{R}R(8,6)^{e}$	4.8	.47	.161	9.5	
32.79	2.79	$^{R}R(7,6)^{e}$	10.6	.51	.325	14.7	30.4
	2.93	$^{P}R(5,1)^{e}$	2.15	.23	.153	4.4	
34.03	3.46?	$^{Q}R(11,9)^{e}$	0.08	.46	.003	0.7	1.1
34.84	4.83	$^{R}R(6,3)^{e}$	7.3	.40	.290	10.7	9.6
4535.07	4.96	$^{R}R(6,1)^{e}$	2.06	.27	.121	4.7	8.1
	5.04	$^{R}R(9,8)^{e}$	2.16	.52	.066	6.6	
35.53	5.30?	$^{Q}R(11,10)^{e}$	0.04	.49	.001	0.4	0.9
36.95	6.92	$^{R}R(10,10)^{e}$	1.97	.55	.050	6.4	6.2
37.23	7.24	$^{R}R(7,3)^{e}$	3.76	.37	.161	7.4	7.1
37.86	7.89	$^{R}R(8,5)^{e}$	5.3	.56	.151	10.8	10.1
4538.32	8.28	$^{P}R(4,2)^{e}$	1.40	.29	.077	4.0	6.7
38.48	8.46	$^{R}R(7,5)^{e}$	3.70	.46	.127	8.2	7.8
39.05							0.8
39.39	9.38	$^{P}R(4,4)^{e}$	0.28	.47	.009	1.9	1.7
39.73	9.73	$^{R}R(8,5)^{e}$	1.75	.42	.066	5.3	5.4
4540.18							1.1
40.82	0.84	$^{P}R(5,2)^{e}$	1.16	.28	.066	3.5	4.0
41.46	1.46	$^{R}R(6,2)^{e}$	2.73	.34	.127	6.0	6.8
42.23	2.21	$^{R}R(9,7)^{e}$	1.44	.48	.048	5.1	5.4
42.90	2.90	$^{R}R(8,7)^{e}$	3.54	.52	.108	8.5	7.2
4543.94							0.9
44.49	4.42	$^{R}R(10,9)^{e}$	2.52	.51	.079	7.1	18.5
	4.44	$^{R}R(7,2)^{e}$	1.45	.31	.075	2.1	
	4.54	$^{R}R(7,4)^{e}$	2.64	.41	.066	6.5	
46.31	5.95	$^{R}R(11,11)^{e}$	1.08	.54	.032	4.7	4.1
46.76	6.73	$^{P}R(4,3)^{e}$	1.49	.38	.064	4.7	10.7
	6.80	$^{R}R(8,4)^{e}$	1.25	.38	.053	4.3	
47.06	7.05	$^{P}P(5,1)^{e}$	2.15	.23	.153	4.4	5.0
4548.12	8.05	$^{R}P(9,9)^{e}$	7.1	.55	.206	12.4	7.9
48.29	8.26	$^{R}R(8,6)^{e}$	4.8	.47	.162	9.5	6.2
48.41	8.41	$^{R}R(6,1)^{e}$	2.07	.27	.121	4.7	3.4
48.83	8.90	$^{P}P(5,3)^{e}$	1.50	.35	.068	4.5	5.6
49.18	9.23	$^{R}R(9,6)^{e}$	2.04	.44	.074	5.9	6.0

4. Summary and Conclusions

A quite complete analysis has been obtained of the two strongest combination bands of NH_3 in the region of 2.3 microns. Accurate rotational constants for the ground state have been derived, and for the upper state good values have been obtained for the basic rotational constants, and in addition fine details of the energy levels involving the interaction of the inversion splitting and rotation, and of the Coriolis interaction constants and rotation have been noted. The intensities and collision half-widths of the lines, and the variation of these parameters with rotational state, have also been obtained.

Similar studies have been made of a number of other bands of NH_3 and its isotopic modifications at wavelengths shorter than 6 microns. These results, and derivation therefrom of basic structural paramters of the ammonia molecule, will be reported in subsequent papers.

5. References

[1] D. M. Dennison, Revs. Modern Phys. **12,** 175 (1940).
[2] H. Y. Sheng, E. F. Barker, and D. M. Dennison, Phys. Rev. **60,** 786 (1941).
[3] C. Cumming, Can. J. Phys. **33,** 635 (1955).
[4] E. F. Barker, Phys. Rev. **55,** 657 (1939).
[5] S. C. Chao, Phys. Rev. **50,** 27 (1936).
[6] C. F. Townes and A. W. Schawlow, Microwave spectroscopy (McGraw-Hill Publishing Co., Inc., New York, N. Y., 1956).
[7] W. S. Benedict, R. C. Herman, G. E. Moore, and S. Silverman, Can. J. Phys. **34,** 830 (1956).
[8] P. W. Anderson, Phys. Rev. **76,** 647 (1949).
[9] B. Bleaney and R. P. Penrose, Proc. Phys. Soc. (London) **60,** 548 (1948).
[10] J. H. Van Vleck and V. M. Weisskopf, Rev. Modern Phys. **17,** 227 (1948).
[11] H. Margenau, Phys. Rev. **76,** 1423 (1949).
[12] A. H. Nethercot, Jr., and C. W. Peters, Phys. Rev. **79,** 225 (1950).
[13] W. S. Benedict and E. K. Plyler, J. Chem. Phys. **24,** 904 (1956); Symposium on molecular structure and spectroscopy (The Ohio State University, Columbus, Ohio, 1956, 1957).
[14] H. H. Nielsen, Revs. Modern Phys. **23,** 90 (1951).
[15] R. S. Mulliken, J. Chem. Phys. **23,** 1997 (1955).
[16] H. H. Nielsen and D. M. Dennison, Phys. Rev. **72,** 1101 (1947).
[17] C. C. Costain, Phys. Rev. **82,** 108 (1951).
[18] G. Herzberg, Infrared and raman spectra (D. Van Nostrand Co., New York, N. Y., 1945).
[19] H. Hansen and H. H. Nielsen, Symposium on molecular structure and spectroscopy (The Ohio State University, Columbus, Ohio, 1957).
[20] D. C. McKean and P. N. Schatz, J. Chem. Phys. **24,** 316 (1956).
[21] H. J. Kostkowski and A. M. Bass, J. Opt. Soc. Am. **46,** 1060 (1956).

WASHINGTON, December 3, 1957.

Journal of Research of the National Bureau of Standards Vol. 61, No. 3, September 1958 Research Paper 2895

Evaluation of Tensile, Compressive, Torsional, Transverse, and Impact Tests and Correlation of Results for Brittle Cermets [1]

Matthew J. Kerper, Lewis E. Mong, Maurice B. Stiefel,[2] and Sylvanus F. Holley

Static tests were studied for the determination of mechanical properties of brittle materials. Specimens of brittle materials, represented by cermets having five different compositions, were subjected to tensile, compressive, torsional, transverse, and impact tests. The designs of specimens and apparatus, suitability of the tests to the materials, refinements in test procedures, and the variability of results and their correlation were studied. The elastic properties were obtained from tensile, compressive, and transverse tests, and the modulus of rigidity calculated from the results of these tests agreed with that from the torsional test. Tensile strength was obtained from the tensile, torsional, and transverse tests on specimens of comparable sizes in accordance with a limiting tensile strain. Shear strengths were obtained in the compressive tests. The correlation of impact values with mechanical properties was unsatisfactory.

1. Introduction

The unusual mechanical properties of refractory brittle materials, including cermets, intermetallics, and special ceramic bodies, have renewed the interest in test methods for determining these properties. Because of their heat and erosion resistance, these materials were suggested for many new engineering applications where high temperatures and stresses prevail. Divergent test methods and lack of control in the fabrication of the materials have resulted in confusing data for the mechanical properties. Consequently, the test methods for these brittle materials have been extensively studied in order to give better descriptions of the materials for engineering purposes.

The fabrication of cermet tensile specimens and their design have been studied by Blackburn [1].[3] Duckworth investigated the effects of specimen size [2] and bending [3] on the tensile strength. The causes of second fractures of tensile specimens were discussed by Miklowitz [4]. Stiefel [5] made photoelastic studies of stress distribution for several designs of tensile specimens. The tensile test has been extensively used for ductile materials, but, although tensile data for brittle materials have much theoretical interest, the test has rarely been employed for refractory ceramic materials [6,7].

The stress distribution in the compressive test of brittle materials and the effect of specimen size were studied by Salmassy [8, 9, 10]. The optimum shape for the compressive specimen was investigated by Duckworth [3] and Nadai [11, p. 328].

The torsional test for brittle materials has been studied by Duckworth [3] and Salmassy [9]; and torsion tests of refractory oxides were made by Stavrolakis [12]. Stress corrections for plasticity were presented by Nadai [13, p. 128].

The elastic properties of brittle materials have been obtained from the popular transverse test both by the deflection method [14] and by the surface-strain method [3], which also gave Poisson's ratio. The mathematics for the transverse specimen, with its accompanying anticlastic curvature, were presented by Timoshenko [15], who also reported Seewald's stress correction for the effect of concentrated loads [16, p. 99]. Photoelastic studies for different span-to-depth ratios were given by Frocht [17]. The altered stress distributions for short beams have been investigated by Timoshenko [16, p. 66], Caswell [18], Seewald [16, p. 99], and for short cylinders by Milligan [19]. Nadai [13, p. 164] evaluated the corrections in strength required when plastic flow occurs in the transverse specimens. The statistical theory relating specimen size to strength was discussed by Weibull [20], Griffith [21], and Salmassy [9, 10]. Barriage [22] discussed this theory and gave data indicating causes of heterogeneity of specimens.

The Charpy impact test has been standardized for metals [23] and organic plastics [24]. The types and characteristics of impact tests have been discussed by Sayre [25], and Soxman [26] has studied the drop test for cermets. A highly specialized impact test employing a fly wheel was reported by Maxwell [27]. The reproducibility of the Charpy test results was investigated by Driscoll [28], and the reduction in impact value by notching was studied by Quackenbos [29] who, with others [30], correlated impact values with flexure tests. There has been considerable difference in opinion as to the correct method of test and the interpretation of results for the impact test.

The research work, described in this incomplete list of references, has served to improve the methods of test and the reliability of the results.

These references indicated that brittle materials were characterized by small elongations and small plastic deformations, but that they had widely ranging strengths and moduli of elasticity. The five

[1] This investigation was sponsored by Watertown Arsenal, 00 Project Number TB4-161A.
[2] Present address: 1230 Sixth Avenue, Rockefeller Center, New York 20, N. Y.
[3] Figures in brackets indicate the literature references at the end of this paper.

examples of refractory brittle materials tested in this investigation were selected (1) to emphasize the problems of measuring extremely high strengths on the one hand and of very small strains on the other; and (2) to obtain homogeneous material in order to minimize the complication of material variation in the comparison of the tests. These considerations led to the choice of four cermets and an intermetallic as specimen materials.

In the work reported here, additional refinements in the test methods were made. Each test was evaluated from the viewpoints of compliance with the mathematical assumptions, instrumentation, suitability to the materials, and the variability of the results. A study of the correlation of the results from the tensile, compressive, torsional, transverse, and impact tests was also made to check the over-all performance of each test and to further explain the behavior of the cermets.

2. Materials

The compositions, methods of fabrication, densities, and porosities of the cermet specimens are given in table 1. Manufacturers of cermets supplied the finish-ground specimens.

For each cermet, the same composition was specified for specimens for each of the tests. The manufacturer of cermet IV, however, made improvements in the fabrication of his product during the time interval when specimens were purchased. Transverse specimens were obtained first, followed by tensile, impact, and torsional specimens.

High-strength materials were represented by cermets I and II. Cermet III was an example of a material having considerable plasticity. Materials having small elongations were represented by cermets IV and V. The mechanical properties of cermet V, which was classified also as an intermetallic, were similar to those of some ceramic bodies having large percentages of refractory oxides.

TABLE 1. *Compositions, methods of fabrication, densities, and porosities of cermet specimens*

Cermet designation	Composition: Material	Composition: Percent by weight	Method of fabrication	Density [a]	Porosity [a] range
		%		g/cm³	%
I	Tungsten carbide	94	Cold press, sinter.	14.90	Nil.
	Cobalt	6			
II	Tungsten carbide	87	Cold press, sinter.	14.15	Nil.
	Cobalt	13			
III	Titanium carbide	70	Cold press, sinter.	5.87	Nil.
	Nickel	30			
IV	Alumina	30	Slip cast, sinter.	5.88	0.1 to 9.0 [b]
	Chromium	70			
V	Zirconium boride	>90	Hot press	5.03	0.06 to 11.0 [b]
	Boron	<10			

[a] ASTM Method C20-46 was used except that specimens were pressure saturated with heptane.
[b] Range is for different specimens.

3. Tensile Test

3.1. Evaluation of Specimen Designs

a. Specimens and Linkages

Five specimens each of the five designs shown in figures 1 and 2 (A, B, C, D1, D2) were made of cermet III. This material was selected because it was relatively uniform, had moderate strength, and could be readily fabricated. The dimensions of the pin-end, T-end, and shouldered-end specimens were proportioned in accordance with the information

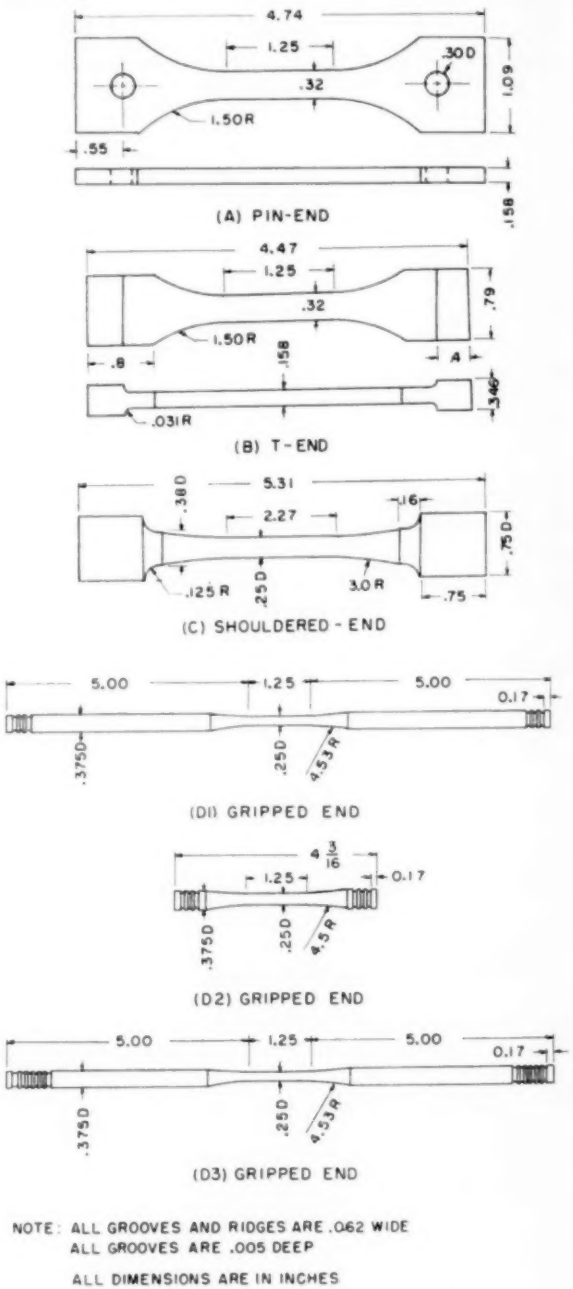

FIGURE 1. *Forms of tensile specimens.*

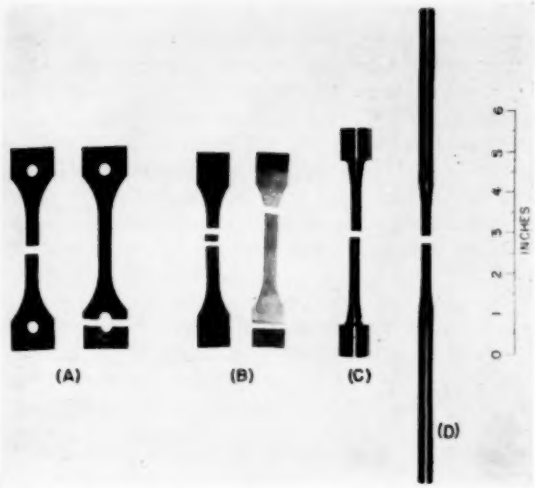

FIGURE 2. *Fractured tensile specimens made of cermet III.*

obtained from the photoelastic studies [5]. The basic design of the gripped-end specimens was developed at the Ohio State University [1]. All specimens had a reduced portion for making strain measurements. This portion was 1.25 in. long with a constant cross-sectional area of 0.05 sq. in.

The adaptors, or grips, for linking the corresponding specimens to the testing machine are shown in figure 3. Precautions were taken in machining to obtain axial loading.

The load was transmitted from the adaptors to the specimen by a pin for specimen A and by bearing surfaces for B and C, figures 1, 2, and 3. These designs gave specimen heads that were massive compared to the gage section.

The load was transmitted for specimens of types D1 and D2, figures 1, 2, and 3, from the grip to the specimen by means of a liner in shear. The grips were tightened sufficiently to force the mild steel liner material, 20 mils thick, into the grooves of the jaws and specimen. The grips were especially designed to obtain axial loading.

The long type of gripped-end specimen, D1 of figure 1, was originally designed to extend out of a furnace for high temperature tests and permit gripping at the colder end. A short type, D2, was machined from the end of each broken D1 form to give data indicating the value of this simpler specimen for room-temperature tests.

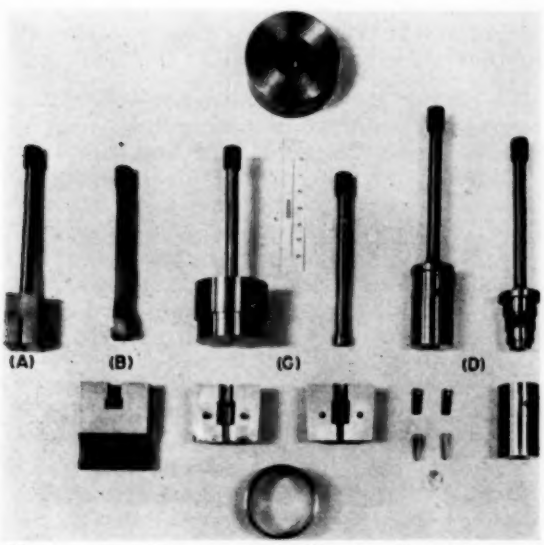

FIGURE 3. *Adaptors for loading tensile specimens.*
Adaptors, or grips, fit specimen forms having corresponding letters, shown in figure 1.

b. Apparatus and Procedure

A hydraulically operated universal testing machine was used for loading the specimens. All grips and adaptors were attached to the testing machine by means of conventional ball-and-socket joints, shown at the top of figure 3.

Figure 4 shows a long gripped-end specimen in position with Tuckerman gaged mounted. The specimen stress was increased in five equal steps, at a rate of 10,000 psi per miute, to a maximum of 10,000 psi, and then decreased in similar steps, to obtain the data for the modulus of elasticity. After determining the modulus of elasticity with the Tuckerman gages, the gages were removed, and SR–4 electric-resistance strain gages were applied to the specimens in positions noted in table 2. The loading procedure with the electric strain gages was the same as that used with the Tuckerman gages. The percent of bending was calculated as 100 times the difference between the maximum surface strain and the average strain divided by the average strain. The method of calculation reported

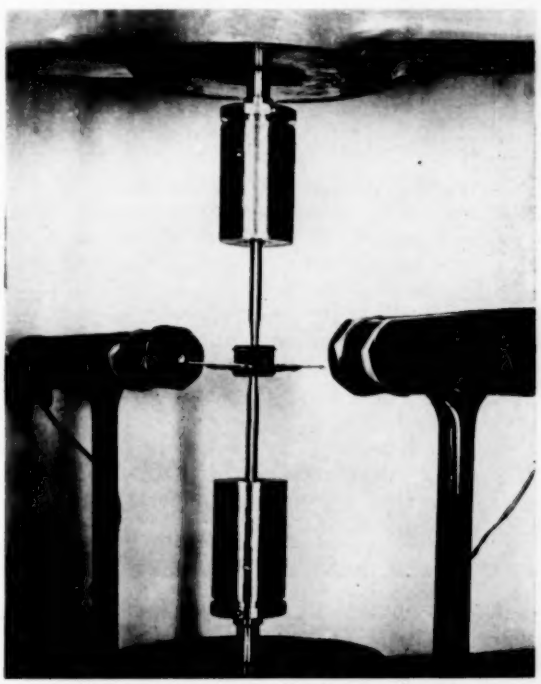

FIGURE 4. *Apparatus for tensile test.*
A long gripped-end specimen with Tuckerman strain gages is shown.

TABLE 2. *Average results for tensile tests on five specimens of each of five designs of specimens made from cermet III*

Specimen form	Modulus of elasticity— from Tuckerman gages—E	Modulus of elasticity— from electric gages, Assembly A, Gages	Modulus of elasticity— from electric gages, Assembly A, E	Modulus of elasticity— from electric gages, Assembly B, Gages	Modulus of elasticity— from electric gages, Assembly B, E	Poisson's ratio [a]	Tensile strength	Bending at rupture [b]	Extensibility, Measured	Extensibility, Calculated [c]	Fracture, Mode	Fracture, Number of specimens
	10^6 *psi*		10^6 *psi*		10^6 *psi*		*psi*	*Percent*	*Percent*	*Percent*		
Pin-end	56.1 (0.8) [d]	Two A-5 [e]	55.0 (1.2)	Four A-12 [f]	54.9 (2.0)	0.23 (6.6)	[g] 72,050 (14.4)	7.0 (37.5)	[g] 0.142 (14.3)	[g] 0.128 (14.0)	Single, in gage Across pin hole	2 3
T-end	55.2 (1.0)	Two A-5 [e]	54.8 (2.3)	Four A-12 [f]	55.4 (1.1)	0.22 (3.7)	[h] 131,000 (5.8)	3.2 (30.2)	[h] 0.278 (2.3)	[h] 0.235 (7.4)	Dougle, in gage Single, in gage At T fillet	2 1 2
Shouldered-end	53.5 (0.6)	Three A-7 [i]	54.0 (0.1)	Three A-12 [i]	55.3 (2.5)	0.22 (nil)	112,940 (11.5)	2.3 (55.2)	0.241 (12.4)	0.204 (9.2)	Single, in gage Single through flaw in gage.	4 1
Long gripped-end	54.8 (0.3)	Three A-7 [i]	57.4 (0.1)	Three A-12 [i]	55.1 (1.1)	0.22 (nil)	141,200 (8.0)	3.3 (65.3)	0.304 (11.6)	0.256 (4.5)	Single, in gage	5
Short gripped-end		Three A-7 [i]	54.5 (2.8)	Three A-12 [k]	54.0 (1.0)	0.22 (4.5)	[l] 127,700 (8.7)	5.2 (68.2)	[l] 0.251 (4.9)	[l] 0.236 (8.4)	Single, in gage Single, in enlarged end. Accidental	3 1 1

[a] Calculated from strains indicated by assembly A gages and an additional lateral A-7 gage.
[b] Average bending at rupture for five specimens calculated by the method given by Duckworth [3]; i. e., bending = 100 (Max surface strain minus average strain)/average strain.
[c] Tensile strength ×100/modulus of elasticity = Percent calculated extensibility.
[d] Numbers in parentheses are coefficients of variation [32].
[e] Placed axially on the wide sides of three specimens.
[f] One gage placed axially on each side of five specimens.
[g] Average for two specimens fracturing in gage; stresses in gage section of remaining three were 82,000, 86,700, and 89,000 psi.
[h] Average for three specimens fracturing in gage; stresses in gage section of remaining two were 102,000 and 117,000 psi.
[i] Placed axially and spaced at 120° on two specimens.
[j] Placed axially and spaced at 120° on five specimens.
[k] Placed axially and spaced at 120° on three specimens.
[l] Average for three specimens fracturing in gage; stresses in gage sections of remaining two were 117,000 and 125,000 psi.

by Duckworth [3] was used to determine the maximum strain. Lateral strains from gages placed at right angles to the longitudinal axis of the specimen were obtained simultaneously with the axial strains for the determination of Poisson's ratio. The electric strain gage measurements were corrected for lateral strains [31].

Following the final determinations of the modulus of elasticity, the specimens were stressed, in steps of 10,000 psi with a rate of 10,000 psi per minute, to failure. Strain readings were taken at each stress increment to obtain the stress-strain curves to rupture.

The extensibility was the maximum tensile strain at fracture. The observed extensibility was the extrapolated strain at rupture from the stress-strain curve to rupture, reported in percent. It was also calculated as the ratio of tensile strength to modulus of elasticity and reported in percent.

Considering the possible errors to be additive, the rms error for the modulus of elasticity was 2.6 percent using the Tuckerman gage and 4.8 percent using the electric strain gages. The rms error in Poisson's ratio was 6.0 percent. These errors were probably less, for some compensation of errors could be expected. Bending introduced uncertainties in the strength determinations [3].

c. Results and Discussion

The results obtained for the five different specimen designs of cermet III are reported in table 2, and a typical stress-strain curve for a specimen having D1 form is shown in figure 5.

The modulus of elasticity values obtained by using the Tuckerman gages had lower coefficients of variation [32] than those obtained by electric strain gages. This difference can occur because: (1) a larger measurement error was possible with the electric strain gages, and (2) a different electric strain gage was used for each gage application while the same pair of Tuckerman gages was used throughout the tests.

The maximum percentage difference between the average moduli of elasticity for the five types of specimens made of cermet III was approximately the same as the experimental error. The average modulus of elasticity of the short gripped-end specimens was slightly less than for the long specimens from which they were cut. A lower value for the short

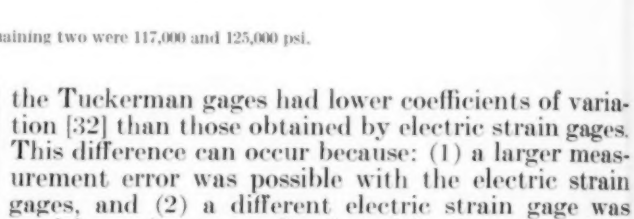

FIGURE 5. *Stress-strain curves for long gripped-end specimens of cermets tested in tension.*
The numbers refer to cermets given in table 1.

specimens was expected because they were prestressed beyond their elastic limit during the tensile tests on the long specimens, and they were subjected to shock when the latter specimens broke. All of the five designs were satisfactory, as expected from the photoelastic studies [5], for the determination of the modulus of elasticity of cermet III.

The Poisson's ratios for the different forms agreed rather well. It appears that electric strain gages are satisfactory for the determination of Poisson's ratio of a cermet in a tensile test.

The amount of bending varied during loading for many specimens, usually decreasing as the load increased. For comparative purposes, the bending at rupture was used. Bending was largest for the pin-end specimens and smallest for the shouldered-end specimens.

Table 2 gives the tensile strengths and the types of fracture for the five designs of specimens of cermet III. The types of fracture are illustrated in figure 2.

Three of the pin-end specimens broke across the pin hole. The two specimens that broke in the gage section had very low strengths when compared to those of other forms.

Two T-end specimens broke at the shoulder. The remaining three specimens broke in the gage section, two with double breaks [4]. The strengths of these three were comparatively high.

All of the shouldered-end specimens failed in the gage section. The average strength for these specimens was approximately 14 percent less than for the T-end form. The double length of the gage portion may have been expected to reduce the strength a small amount [2], but it is doubted that it was the only factor that lowered the strength so much. The modulus of elasticity was also slightly lower for this form, and it was possible that the heavy ends and comparatively slender gage portion contributed to overstressing during machining of this form with the accompanying generation of stress-raisers.

The long gripped-end specimens had the highest average strength of the five forms. All of the specimens fractured with a single break in the gage length.

The short gripped-end specimens had an average tensile strength 10 percent lower than the corresponding long specimens, from which they were cut. This difference may be due in part to the prestressing and shock in the tests on the original specimens. One specimen broke in the enlarged end and the remaining three broke in the gage length.

Both the experimental and the calculated extensibilities are reported in table 2. The ratios of these two values of extensibilities were substantially the same for the different forms because all specimens were made of the same cermet material. As the modulus of elasticity was essentially the same for all five, the extensibility values depended on the strength. The measured extensibility included the plastic strain and represented the behavior of the material more accurately, figure 5.

The pin-end and T-end forms were unsatisfactory for strength tests because breaks occurred outside the gage section. The pin-end specimen may be usable if the heads are made thicker in the direction of the holes. The T-end specimen needs a larger radius between the head and the gage section. This modification would necessitate a thicker head and would increase the fabrication difficulties. For both the shouldered-end and gripped-end designs, the fracture characteristics and the percent bending were reasonably satisfactory. Both designs require careful machining. The shouldered-end specimen requires that a large amount of material be removed to make the gage section. The long gripped-end specimen is slender but can be satisfactorily fabricated, if carefully done.

The long gripped-end design was chosen as the best design of the five for (1) it showed the highest strength, (2) the variation between specimens was relatively small, (3) the bending was reasonably low, and (4) the specimen can be used without further modification for tests at elevated temperatures. The short gripped-end specimen is probably satisfactory for use at room temperature and is relatively easy to fabricate.

3.2. Suitability of the Long Gripped-End Specimen for Different Cermets

a. Specimens, Apparatus, and Procedure

After the long gripped-end specimen design had been chosen as the best, five specimens each of this design of cermets I, II, and IV were obtained. As a precaution against slipping, the design was modified to include more grooves as shown in figure 1, D3. The apparatus and the procedure were the same as those described for testing the long gripped-end specimen, except that the strains were measured with electric strain gages only. All five specimens of cermet IV were improperly fabricated by the manufacturer, the enlarged ends being slightly out of line with the gage portion. The gripped portions of the enlarged ends were reground to aline with the gage portion before testing. The manufacturer of cermet V declined to furnish specimens.

b. Results and Discussion

The moduli of elasticity, strengths, extensibilities, Poisson's ratios, bending percentages, and types of fracture are given in table 3 for cermets I, II, III, and IV. Typical stress-strain diagrams for the cermets are shown in figure 5.

The plot of stress and strain for cermets II, III, and IV showed some curvature. The stress-strain diagram for cermet I was a straight line to rupture.

The cermets I, II, and III had comparatively low coefficients of variation for modulus of elasticity, but the coefficients for strength and extensibility were considerably higher. Nevertheless, these coefficients of variation for strength were considered to reflect material variability and were slightly lower than some reported values for a similar material [3]. The corresponding coefficients were considerably larger for cermet IV.

The specimens all ruptured in the gage length with

TABLE 3. *Average tensile properties of five long gripped-end specimens of each of cermets I, II, III, and IV*

Cermet	Modulus of elasticity [a]	Poisson's ratio [b]	Tensile strength	Bending at rupture [c]	Extensibility		Fracture	
					Measured	Calculated [d]	Mode	Number of specimens
	10^6 *psi*		*psi*	%	%	%		
I	89.9 [e] (0.9)	0.21 (2.3)	176,000 (6.0)	3.4 (70.8)	0.201 (6.0)	0.196 (6.0)	Single, in gage	5
II	78.6 (0.4)	0.23 (nil)	[f] 204,000 (5.0)	0.6 (38.6)	[f] 0.262 (6.1)	[f] 0.259 (4.9)	Single, in gage Single, in fillet Single, thru flaw in fillet	3 1 1
III	[g] 55.1 (1.1)	0.22 (nil)	141,200 (8.0)	3.3 (65.3)	0.304 (11.6)	0.256 (4.5)	Single, in gage	5
IV	43.1 (4.4)	0.22 (nil)	38,100 (13.6)	6.9 (40.1)	0.100 (16.2)	0.089 (15.9)	Single, in gage	5

[a] Average for electric strain gages from Assembly A consisting of three axial A–7 gages at 120° and one lateral A–7 gage on two specimens, and Assembly B consisting of three axial A–12 electric strain gages spaced at 120° on three specimens.
[b] Average for two specimens having gage Assembly A.
[c] Calculated by method given by Duckworth [3] for five specimens.
[d] Tensile strength x100/modulus of elasticity = percent calculated extensibility.
[e] Numbers in parentheses are coefficients of variation [32].
[f] Average for three specimens fracturing in gage; stresses in gage section of remaining two were 169,000 and 225,000 psi.
[g] Average for five specimens having Assembly A gages.

a single break except for two specimens that broke outside the reduced portion. One of these broke through a flaw in the fillet portion. No other flaws were noted.

The average percentage of bending was negligible for cermet II. The results for cermets I and III indicated reasonably low bending, but the bending of cermet IV was larger, due, in part, to the inaccurate shape of the specimens.

3.3. Evaluation of the Tensile Test

The essential requirements for a satisfactory tensile test on cermets are (1) a satisfactory specimen design, such as the long gripped-end of shouldered end specimen, (2) accurately shaped specimens and adaptors, (3) accurate alinement, checked by bending measurements of specimens, adaptors, and testing machine, and (4) sensitive strain gages such as electric-resistance or Tuckerman strain gages.

The tensile test gives reliable values of modulus of elasticity, Poisson's ratio, and tensile strength without complicated corrections.

4. Compressive Test

4.1. Specimens

The compression specimens, 0.424 in. square by 1.27 in. long, were machined from the enlarged ends of fractured flexure specimens (B1 form) to be described later. Five specimens each of cermets I, II, III, and IV, and three specimens of cermet V were prepared.

4.2. Apparatus and Procedure

In the preliminary tests, the bearings for the specimens were blocks of cermet I either in direct contact with the specimen ends or separated by thin metal pads. Parallelism of the blocks was to be obtained either by a hemispheric bearing attachment or by casting a thin plaster of Paris layer between the bearing block and the head of a hydraulic testing machine having a capacity of 300,000 lb.

In the final improved method of test, the bearing blocks, or anvils, consisted of an insert of cermet I in a tool steel holder which was shrink-fitted. The cermet and opposite faces were made parallel by finish grinding. The cermet face of the anvil was reground before each test because the surface was roughened in the preceding test by the end of the specimen at the high stresses required for its fracture. The anvils made direct contact with the crosshead and table, which were accurately parallel, of an "electromatic" testing machine having a capacity of 200,000 lb.

Electric-resistance strain gages were attached at the middle of each of the four sides of the specimen for strain measurements. For axial strains, used to calculate the modulus of elasticity, A–7 gages, (SR–4), were used. AX–7 rosette gages were placed on two opposite sides of each of three specimens of each cermet for both lateral and axial strains, which were used to calculate Poisson's ratio. All strains were corrected for lateral strain [31]. The percent bending was calculated, as in the tensile test, by Duckworth's method [3].

Specimens were stressed in increments of 11,300 psi for modulus-of-elasticity measurements. The specimens were then loaded to rupture in increments of 28,300 psi. Strain and stress were read at each increment.

The root-mean-square errors introduced by the measuring devices were: 15.1 percent for modulus of elasticity, 4.5 percent for Poisson's ratio, and 1.5 percent for compressive strength. The additional error in strength due to bending was indeterminate [3].

4.3. Results and Discussion

In the preliminary tests employing the hemispherical attachment, bending was erratic and sometimes

so large that a side of the specimen was in tension. Satisfactory values of bending were sometimes obtained when a layer of plaster of Paris was used, but the lowest values were obtained with the cermet I tool steel bearings and the well alined testing machine. The use of thin pads between the specimen and the bearings did not reduce bending.

The modulus of elasticity, compressive strength, Poisson's ratio, and the percent bending are presented in table 4. For cermets I, II, and III, the modulus of elasticity and the compressive strengths had low coefficients of variation, and the bending was small. The larger variability and bending noted in cermets IV and V were attributed to the materials and not to the test, for they also had large coefficients of variation in the other tests. The values for Poisson's ratio were in good agreement for specimens of a particular composition. The percent bending for all cermets showed a large coefficient of variation whether the actual bending was large or small. Since all conditions of the test were reproduced as nearly as possible, the large variation in bending seems to be an inherent characteristic of the compression test.

TABLE 4. *Average results from compression tests for each of five cermets*

Cermet [a]	Modulus of elasticity	Bending [b]	Poisson's ratio	Compressive strength	Calculated strain at rupture [c]
	10^6 *psi*	%		*psi*	%
I	91.3	6.8	0.22	588,000	0.646
	(3.4) [d]	(60.3)	(nil)	(2.4)	(5.7)
II	78.8	5.4	0.23	555,800	0.705
	(0.9)	(51.9)	(1.4)	(1.8)	(2.4)
III	50.9	6.1	0.24	374,000	0.735
	(1.4)	(28.9)	(2.0)	(3.1)	(2.2)
IV	41.4	22.1	0.23	118,500	0.289
	(6.5)	(52.5)	(5.2)	(11.2)	(16.6)
V	44.5	14.1	0.17	181,300	0.400
	(11.9)	(57.4)	(3.5)	(27.0)	(18.8)

[a] Five specimens of each of cermets I, II, III, and IV, and three specimens of cermet V were tested. The specimens were 0.424 in. square in cross section by 1.27 in. long.
[b] Calculated according to Duckworth [3].
[c] Calculated strain at rupture = compressive strength x 100/modulus of elasticity.
[d] Numbers in parentheses are coefficients of variation in percent [32].

Figure 6 shows a typical stress-strain curve for a specimen of each of the five cermet materials. The curves for cermets I, II, and III had considerable curvature, and the strains increased rapidly as their compressive strengths were approached making accurate measurements impossible with the portable strain indicator. Cermet IV had an almost straight line to the largest stress shown on the graph. Beyond this point the strain increased so rapidly that it could not be measured accurately. Cermet V was the only material that exhibited a linear stress-strain curve to rupture.

In general the specimens ruptured violently and were reduced to many small fragments, and detection of any flaws on the fracture surfaces was impossible. Specimens of cermet IV did not shatter completely, but broke into small fragments at the ends and left the middle intact. One specimen

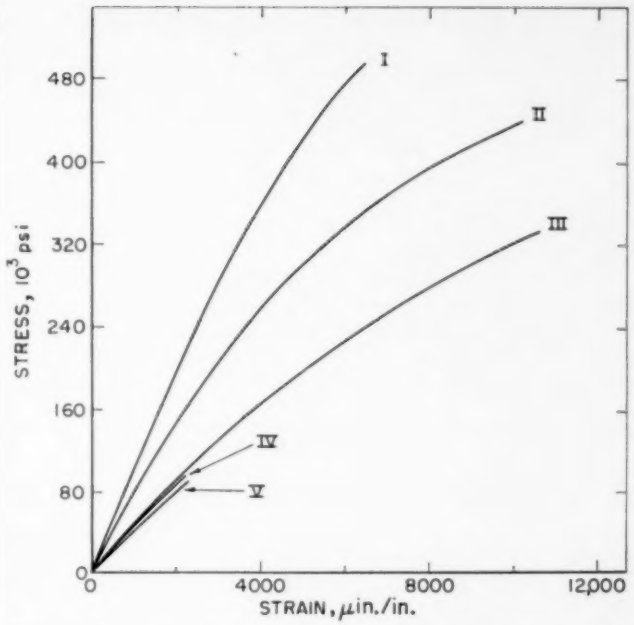

FIGURE 6. *Stress-strain curves of cermets tested in compression.* The numbers refer to cermets given in table 1.

formed a slip plane and did not shatter. This behavior was not surprising because cermet IV contained 70 percent metal.

Friction between the ends of the specimen and the anvils causes a distortion in the stress distribution, resulting in a stress concentration near the end of the specimen with a lowered average stress at fracture. Although this error has not been evaluated, its presence has led to the conclusion that the compression test is not reliable for brittle materials [8]. The results for cermets, table 4, indicate that the coefficients of variation are not appreciably greater than for the other mechanical tests, and that the error is consistent. Suggested means for reducing the error are, (1) lubricate the ends of the specimens, (2) make the ends of the specimen concave to match a cone-shaped anvil having the angle of friction, and (3) enlarge the end of the specimen, and fillet to the gage section [33].

The most common compression test specimens are right prisms or right cylinders, but other shapes are occasionally used [33]. The cylindrical shape is recommended often by the American Society for Testing Materials (ASTM) and also by Duckworth [3]. The shape factor seems to be minor, and the shape of the original stock often dictates the shape of the specimen.

The importance of uniform stress distribution and the effects of nonuniform distribution were discussed by Salmassy [8]. Stress distribution in this work was improved by (1) maintaining accurate alinement of specimen, bearings, and testing machine, and (2) the use of a testing machine having very little lateral movement of the crosshead relative to the table. Subpresses have also been employed to maintain alinement [34].

4.4. Evaluation of the Compressive Test

The major requirements for the compressive test on cermets are (1) accurately shaped specimens, (2) accurate alinement of specimens, bearings, and testing machine, (3) a testing machine with little lateral movement between the head and table, (4) bearings having sufficient hardness and strength, and (5) reducing bending to a minimum as indicated by multiple strain gages.

Prismatic or cylindrical specimens are suitable for the comparison of modulus of elasticity, Poisson's ratio, and compressive strength of cermets. Specimens having special shapes are required to obtain the true compressive strength.

5. Torsion Test

5.1. Specimens and Chucks

The design of the specimen was similar to that used in other laboratories for torsion tests of brittle materials [3, 12]. Figure 7 shows the specimen and gives its dimensions. The chucks consisted of a single piece and had 1.000-in. square sockets to fit the specimen as shown in figure 8.

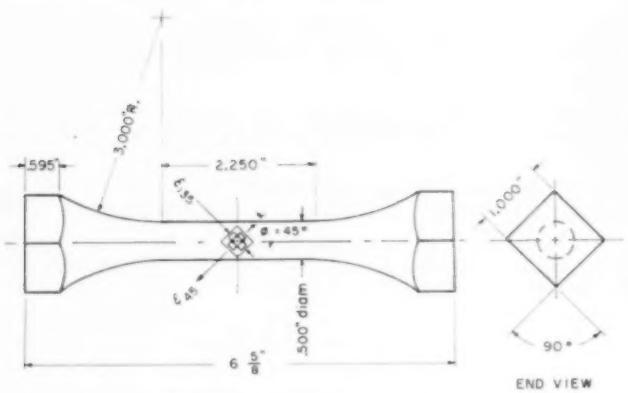

FIGURE 7. *Torsion specimen.*

The square indicates the position of a rosette strain gage, and the arrows indicate the directions of principal tensile and compressive strains.

5.2. Apparatus

A torsion machine having a capacity of 0 to 40,000 in.-lb, in four ranges, was designed especially for torsion testing of brittle materials, which are sensitive to bending. Bending of the specimen was reduced by making the main members of the frame of the testing machine symmetrical about the center line of the specimen, figure 8, as is done for conventional tensile-compressive testing machines. The conventional torsion-testing machine differs in that its frame is not symmetrical, and the applied torque may cause a bending moment to be applied to the specimen.

The angular deformation of the specimen was measured by means of the optical twist gages shown mounted on a specimen in figure 9. The optical systems for measuring twist using Tuckerman auto-

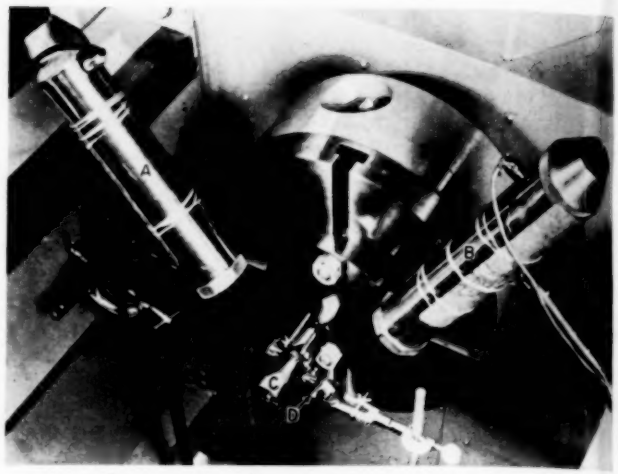

FIGURE 8. *Apparatus for torsional test.*

The torque head of the testing machine is withdrawn from the specimen C. Autocollimators A and B complete the optical system of the Tuckerman twist gage. D is a right angle prism to facilitate readings on B.

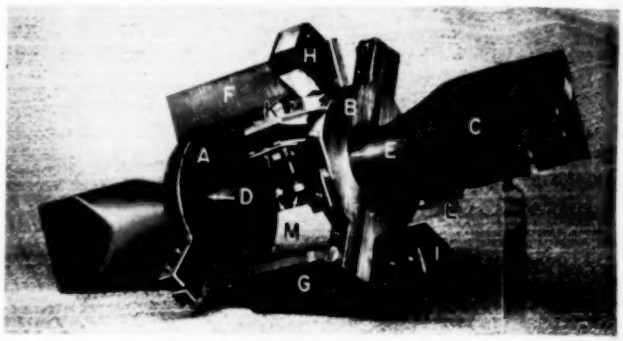

FIGURE 9. *Optical twist gage.*

Clamps A and B contact the gage marks, spaced 2 in., of the specimen C at knife edges, D and E, 1 mm wide. Twist from A is transmitted to Tuckerman prisms H and I by arms F and G. Twist from B is transmitted to first-surface mirrors K and L adjusted by screws M.

collimators [35], (A and B, figure 8) were established on opposite sides of the specimen when mirrors K and L were properly positioned before the roof prisms H and I. The gage was sensitive to 0.00001 radian.

AX–7 electric-resistance strain gages (SR–4) of the rosette type were used to measure surface strains, and were placed at 45° to the long axis at the middle, figure 7, and on opposite sides of the reduced section of the specimen.

All strain readings were corrected for lateral strain effects by the method described by Baumberger and Hines [31].

5.3. Procedure

The optical twist gages were mounted and the specimen placed in the torsion machine, as shown in figures 8 and 9. The torque was applied at a strain rate of 0.005 radian per minute in five increments of 80 in.-lb to a maximum torque of 400 in.-lb and reduced in five decrements to zero. Twist and torque were measured after each increment and decrement. The modulus of rigidity was calculated from these data using the following equation [15, p. 364]:

$$G=\frac{32ML}{\theta\pi d^4} \tag{1}$$

where

G=modulus of rigidity,
M=applied torque,
L=gage length (axial distance between knife edges),
θ=total angular twist in radians for the gage length,
d=diameter of the reduced section.

The optical twist gages were removed after measurements with them were completed, and the electric strain gages placed in position. Data from these gages were used to calculate the modulus of rigidity by the following equations [15, p. 55] for the same loading procedure as that with the optical twist gages:

$$\gamma_{max}=\epsilon_{45}-\epsilon_{135}=2\epsilon_{45}=-2\epsilon_{135} \tag{2}$$

and

$$G=\frac{\tau_{max}}{\gamma_{max}}=\frac{\tau_{max}}{(\epsilon_{45}-\epsilon_{135})} \tag{3}$$

where

ϵ_{45}=principal tensile strain,
$-\epsilon_{135}$=principal compressive strain,
G=modulus of rigidity,
τ_{max}=shear stress,
γ_{max}=shear strain.

After the measurements for the determination of the modulus of rigidity were completed, torque was applied, at the strain rate of 0.005 radian per minute, in increments of 80 in.-lb, to failure. Torque and strain measurements were taken at each succeeding load increment until fracture occurred.

The shear stress at fracture, τ_{max}, was calculated from either [15, p. 264]:

$$\tau_{max}=\frac{16M_{max}}{\pi d^3} \tag{4}$$

or, for materials having nonlinear torque-twist relations to rupture, from Nadai's equation [13, p. 128]

$$\tau_{max}=\frac{1}{2\pi r^3}\left(\theta\frac{dM}{d\theta}+3M_{max}\right), \tag{5}$$

where M_{max}=torque at fracture.

All fracture surfaces were examined for flaws using a binocular microscope.

Some errors were introduced in the measurement of load and strain by the limited sensitivity and accuracy of the measuring devices. The measurement of the applied torque could have introduced an error of 0.5 percent in the modulus of rigidity and of 2 percent in the torsional strength. The optical twist gages could have introduced an error of 0.5 percent in the modulus of rigidity due to the measurement of the span and an error of 0.2 percent due to the gage itself.

Bonded electric-resistance strain gages are subject to a thickness error when they are used for strain measurements in a torsion test. The gage wire used to measure strain at the outer surface of the specimen is actually removed from the outer surface by a distance equal to the thickness of the paper on which the wire is mounted, the cement layer, and half the thickness of the wire. The average distance from midwire to specimen surface was determined by measuring the thickness of several gages before and after mounting on a specimen, and this distance was used in a correction for the strain readings. The variation in this distance was sometimes appreciable and the resulting error in strain may have been as large as one percent of the observed value.

Each electric gage was placed as accurately as possible, and deviation from the proper alinement was undoubtedly small. The gage factor tolerance was 2 percent or less. The strain indicator could possibly introduce an error of 4 percent in the modulus-of-rigidity measurements. The calculated rms error for the torsional strength was 2 percent; for the modulus of rigidity determined by the modified Tuckerman strain gage, it was 0.74 percent; and for the modulus of rigidity determined by the bonded electric-resistance strain gages, it was 4.6 percent.

5.4. Results and Discussion

The modulus of rigidity, determined by both the optical twist gages and the electric strain gages, and the strength in torsion are given in table 5.

The coefficient of variation for the modulus of rigidity determined by the optical twist gages was low for all materials except cermet V. For all materials, the coefficient of variation for the modulus of rigidity was higher when determined from electric-strain-gage data than when determined from optical-twist-gage data.

TABLE 5. *Average results from torsional tests of each of five cermets*

Cermet [a]	Modulus of rigidity—		Torsional strength		Shear strain at rupture	
	From optical twist gages	From electric strain gages	Calculated by equation (4)	Calculated by equation (5)	Calculated [b]	Measured
	10^6 *psi*	10^6 *psi*	*psi*	*psi*	*Percent*	*Percent*
I	38.0	36.0	156,800	156,800	0.436	0.435
	[c] (1.0)	(2.9)	(5.0)	(5.0)	(5.8)	(5.1)
II	32.7	33.0	195,100	180,200	0.547	0.724
	(1.3)	(7.4)	(6.9)	(7.5)	(7.6)	(7.4)
III	22.9	22.8	[d]116,600	[d]109,400	[d] 0.500	[d] 0.668
	(1.8)	(8.6)	(15.0)	(14.7)	(19.1)	(23.2)
IV	17.0	18.5	[e] 43,500	[e] 43,500	[e] 0.243	[e] 0.244
	(1.6)	(7.2)	(3.8)	(3.8)	(5.2)	(6.5)
V	24.5	25.4	23,700	23,700	0.095	0.093
	(10.7)	(11.0)	(9.3)	(9.3)	(15.4)	(16.8)

[a] Five specimens were tested for each cermet except cermet V for which there were four specimens.
[b] Torsional strength $\times 100$/modulus of rigidity=calculated shear strain at rupture.
[c] Numbers in parentheses are coefficients of variation in percent [32].
[d] Defects noted on fracture surface of one specimen which broke at 95,600 psi, not included in the average, by eq (5).
[e] Defects noted on fracture surface of one specimen which broke at 36,600 psi, not included in the average, by eq (5).

For some specimens the modulus of rigidity determined by the electric strain gages did not agree well with the modulus of rigidity determined by the optical twist gages. Although less precise, the electric strain gages had advantages in that it was possible to measure strain to rupture and to detect bending from differences in measured strain. No appreciable differences indicating bending were observed in the strain readings among the four individual electric strain gages, and the specimens were considered to be in a state of simple torsion. The average electric-strain-gage readings were used in the calculations.

The coefficients of variation for strength were rather large, but this variation is common for brittle materials. The torsional strength calculated by the method of Nadai [13, p. 128] eq (5), was less for cermets II and III than that calculated by the elementary eq (4). The necessity of correcting for plastic deformation required the measurement of shear strain to rupture.

Two specimens, one each of cermets III and IV, had pinholes slightly below the surface of the specimen. These specimens had lower-than-average values of torsional strength. All specimens, including those that showed plastic flow, when ruptured exhibited the typical helical fracture of brittle materials caused by tensile stresses [15, p. 55].

Typical stress-strain curves in shear for each of the five cermets are shown in figure 10. The shear strains at rupture, both calculated by dividing the torsional strength by the modulus of rigidity, and measured, are given in table 5. The measured shear strains at rupture were obtained directly from the shear stress-strain curves to rupture and included the additional deformation due to plasticity. For the materials that did not exhibit any plasticity, the experimental shear strains at rupture were the same as the calculated shear strains. For the two "plastic" materials, cermets II and III, the experimental shear strains at rupture were about 24 percent greater than the calculated values.

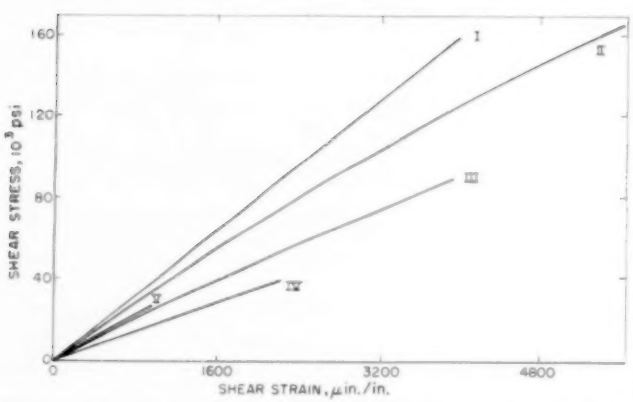

FIGURE 10. *Shear stress-strain curves of cermets tested in torsion.*

The numbers refer to cermets given in table 1.

5.5. Evaluation of the Torsional Test

The essential requirements for the torsional test are (1) specimens designed with adequate fillets and having accurate shaping, (2) accurate alinement of the specimen with a symmetric testing machine to avoid bending, (3) the use of strain gages to measure the principal tensile and compressive surface strains for the calculation of bending, modulus of rigidity, and plasticity, and (4) the correction of strength for errors due to plasticity.

The torsional test gives reliable values of modulus of rigidity and torsional strength of cermets. The torsional strength is related to the tensile strength as discussed in a later section.

6. Transverse Test

6.1. Specimens

Figure 11 shows the shapes, dimensions, and

Form	Dimension									
	D	T	B	R	L	S	O	X	F	E
A-1	0.150	0.212	0.450	0.300	1.100	1.366	3.833	0.450	0.667	0.250
A-2	.150	.212	.450	.300	2.100	1.700	5.500	.450	1.000	.250
A-3	.150	.212	.450	.300	3.100	2.033	7.167	.450	1.333	.250
B-1	.300	.424	.900	.600	1.100	2.117	5.334	.900	0.967	.250
C-1	.424	.600	1.272	.848	1.100	2.737	6.575	1.272	1.215	.250

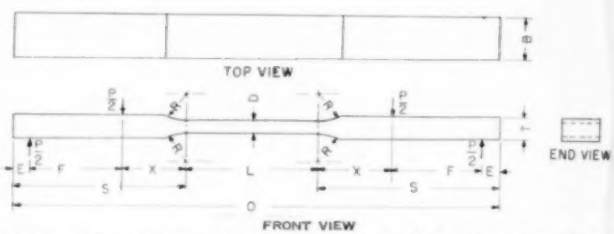

FIGURE 11. *Dimensions and loading points for enlarged end transverse specimens having fifth-point loading.*

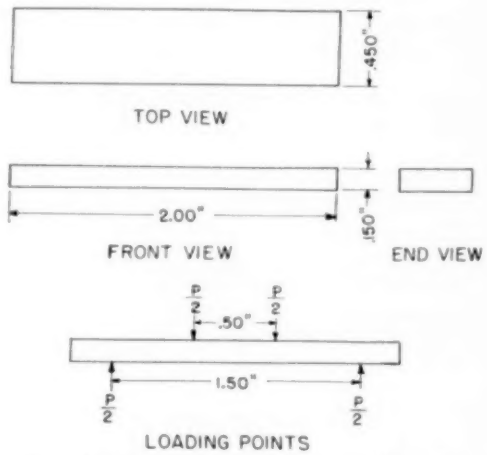

FIGURE 12. *Dimensions and loading points for form-D specimens.*

loading points for five sizes of enlarged-end specimens for the transverse tests. Dimensions of fillets, location of the loading points, and thickness of the enlarged ends were calculated from information given by Duckworth [36] and from data determined in this laboratory.

The shape and dimensions of the prismatic, form-D specimens are given in figure 12. The cross section of these specimens was similar to that used at other laboratories [37], and was the same as the cross section of the A forms.

Five specimens of each cermet in each of the six forms were obtained, with the exception of those for cermet V. The manufacturer of this cermet was unable to furnish the A3 and C1 forms, and only three specimens of each of the remaining forms were obtained.

6.2. Apparatus

Figure 13 shows the loading apparatus used in testing the specimens having enlarged ends. The cylindrical rollers that serve as knife edges are positioned by spring-held side plates. This arrangement allows for movement of the roller in the direction of the longitudinal axis of the specimen, relieving either compressive or tensile stresses due to changes in the length of span during loading.

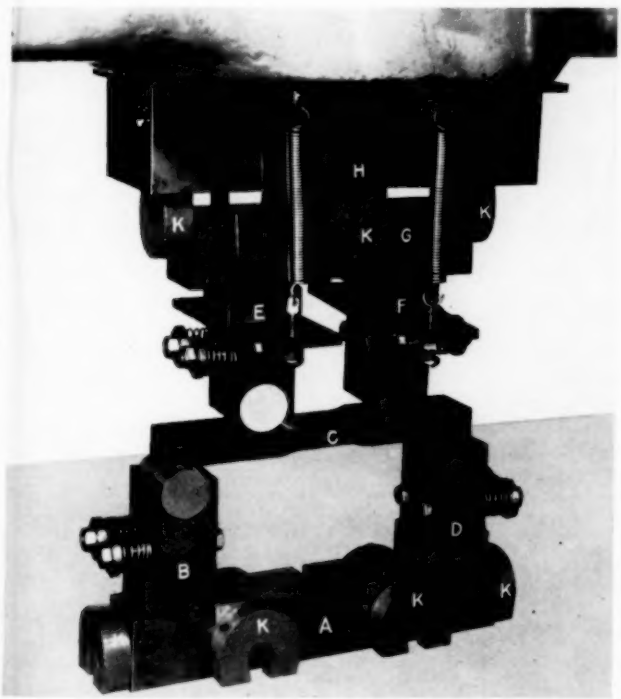

FIGURE 13. *Loading apparatus for enlarged-end specimens.*

Block A spaces the supports B and D, and beam G spaces the loaders E and F. Twist in the specimen C is compensated by rocker bases of D, E, and F, whose center of curvature is at the centerline of the specimen. The load applied by the crosshead is transmitted through H and divided equally by beam G, having a semicylindrical bearing (not visible) at its midpoint. Magnets K position the parts to the testing machine.

Because of the different sizes of specimen forms that were tested on this apparatus, it was necessarily complex. A smaller version of this apparatus was used in testing the form-D specimens.

A deflectometer similar in design to that described by Mong and Pendergast [38, p. 301] was used. When attached to the specimen, it made contact at the midpoint and at one end of the span on the centerline. At the other end of the span, there were two movable contacts located laterally from the centerline to give one of three lateral spans. The sensitivity of the deflectometer was 2 μ in.

Bonded wire-resistance electric strain gages (SR–4) were used to measure surface strains. The gage lengths were selected according to the application and ranged from ¼ to 1 in.

6.3. Procedure

Specimens were loaded and unloaded in five or more increments to obtain a maximum stress of approximately 20 percent of the strength. The rate of stressing between increments was approximately 60,000 psi per minute. At each increment, deflection and load were recorded, and the modulus of elasticity was calculated by the elementary beam formula [38, eq (7)]. The movable pair of contact points of the deflectometer were set to give the smallest lateral span.

The procedure was repeated for each of the other two settings of the lateral span on the deflectometer for eight specimens. The differences in the resulting moduli of elasticity were compared to the calculated differences [38, eq (8)] for each specimen.

After the deflection measurements were completed, wire-resistance strain gages were attached to the specimens on the tensile and compressive surfaces to determine axial and lateral strains, except for form D which had space for only one axial gage on the tensile side. The modulus of elasticity was calculated from longitudinal-strain measurements [38, eq (1) and (2)] obtained with the same loading procedure employed in the tests using the deflectometer. The strain-gage readings were corrected for lateral strain and thickness error as in the torsional test.

When the tests for modulus of elasticity were completed, the specimens were loaded in increments similar to those for modulus of elasticity, to obtain stress-strain curves to rupture and the transverse strength. The strength was calculated by the elementary beam formula, [38, eq. (1)] for cermets having linear stress-strain curves, but for those cermets having plasticity, indicated by nonlinear curves, Nadai's formula [13, p. 164] was used. Seewald's method, [16, p. 99], was used to calculate the strength of the form-D specimens for which concentrated load was a factor.

The rms error for the modulus of elasticity for the deflectometer was 3.3 percent and 5.5 percent for the wire-resistance gages. The error due to the apparatus in the determination of strength was 3.5 percent.

6.4. Results and Discussion

Table 6 gives the differences between moduli of elasticity of specimens of four cermets determined with three different lateral spans on the deflectometer. The calculated values, [38, eq. (8)] of anticlastic curvature were larger than the observed. The disagreement indicated that the anticlastic curvature at the end of the span was less than would be expected. This stiffening by the enlarged ends and loader reaction was also indicated by wire-resistance strain gages placed laterally at the middle and at the ends of the axial span. Anticlastic curvature agreed with the calculated values only at the middle of the A2 and A3 forms as indicated by values of Poisson's ratio, reported subsequently.

Typical stress-strain curves for one specimen of each of the five brands of cermets are shown in figure 14.

The moduli of elasticity of the cermet specimens from both the wire-resistance strain gages and the deflectometer are presented in table 7. The differences between the moduli of elasticity determined by the deflectometer and surface-strain methods were usually insignificant. The coefficients of variation for the moduli of elasticity obtained from surface-strain and deflection measurements were practically the same for all lots of specimens.

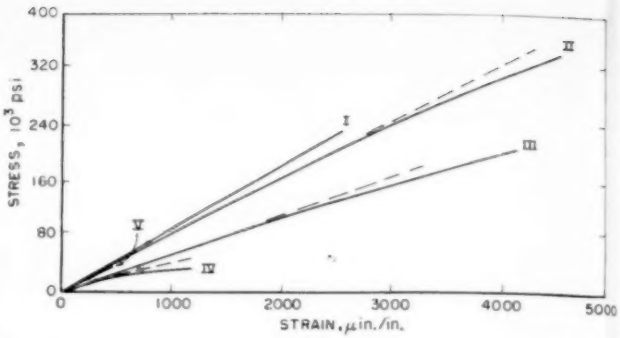

FIGURE 14. *Typical stress-strain curves for one specimen having form A1 of each of five cermets.*

TABLE 6. *Differences in modulus of elasticity resulting from anticlastic curvature and different lateral spans of the deflectometer for specimens having form C1*

Cermet [a]	Differences				
	Small span	Medium span		Large span	
	Increase from zero span, calculated [b]	Increase from small span		Increase from small span	
		Calculated [b]	Observed	Calculated [b]	Observed
	%	%	%	%	%
I	1.1	6.2	5.0	14.4	10.3
II	1.1	6.2	3.9	14.4	12.7
III	1.1	6.2	3.9	14.4	10.9
IV	1.0	5.7	3.3	13.1	12.5

[a] Results are averages for two form C1 specimens of each cermet.
[b] These values were calculated according to [38].

An analysis of the surface-strain data indicated that 48 percent of all specimens had a higher strain on the tensile side of the specimen, 48 percent had a higher strain on the compressive side, and 4 percent had the same strain on both sides. The differences were generally within the error of the gages. The equality of tensile and compressive moduli of elasticity, for transverse specimens in tests where axial restraint of the knife edges was canceled, has been discussed by Duckworth [3]. The strains on the tensile and compressive sides frequently diverged after the elastic limit was exceeded.

Average moduli of rupture for the six forms of the cermets are given in table 8. The value of this tensile stress of the outer fibres, which grades to zero at the neutral axis, was less by 4 to 22 percent when calculated by the method of Nadai for cermets II,

TABLE 7. *Average moduli of elasticity from transverse tests for five cermets calculated from surface-strain and deflection measurements*

Specimen form	Cermet I [a]			Cermet II [a]			Cermet III [a]			Cermet IV [a]			Cermet V [b]		
	Surface strain		Deflection [c]	Surface strain		Deflection [c]	Surface strain		Deflection [c]	Surface strain		Deflection [c]	Surface strain		Deflection [c]
	T [d]	C [e]		T [d]	C [e]		T [d]	C [e]		T [d]	C [e]		T [d]	C [e]	
	10^6 psi	10^6 psi	10^6 psi	10^6 psi	10^6 psi	10^6 psi	10^6 psi	10^6 psi	10^6 psi	10^6 psi	10^6 psi	10^6 psi	10^6 psi	10^6 psi	10^6 psi
A1	92.3 [f]	91.1	95.9	79.9	77.9	83.4	52.1	52.5	51.6	34.1	34.8	37.1	60.4	60.4	64.6
	(0.7)	(1.6)	(3.9)	(1.9)	(1.5)	(1.7)	(1.6)	(2.6)	(2.9)	(19.6)	(20.7)	(17.2)	(2.4)	(2.8)	(3.7)
A2	93.1	93.5	91.2	83.3	83.0	81.0	55.8	55.8	54.4	[g]42.8	[g]42.2	43.6	63.2	63.2	64.1
	(0.8)	(1.0)	(0.9)	(0.8)	(1.0)	(0.9)	(0.8)	(1.1)	(0.6)			(3.1)	(1.6)	(2.8)	(0.7)
A3	91.1	91.1	91.2	81.6	81.1	80.0	55.6	55.0	54.4	41.0	40.7	41.6	-------	-------	-------
	(0.5)	(1.2)	(1.2)	(1.7)	(1.9)	(1.1)	(1.5)	(1.8)	(1.4)	(11.4)	(12.4)	(12.7)			
B1	94.1	93.7	94.7	81.7	81.6	82.1	55.7	55.2	55.4	42.0	42.6	42.7	51.8	52.6	53.7
	(0.8)	(0.6)	(1.4)	(0.4)	(0.4)	(1.1)	(2.1)	(1.8)	(3.3)	(10.9)	(9.5)	(12.3)	(6.1)	(5.4)	(6.8)
C1	92.2	92.7	94.4	80.7	80.4	81.1	53.7	53.8	53.9	42.1	42.3	44.4	-------	-------	-------
	(1.4)	(1.4)	(2.3)	(0.4)	(0.4)	(2.2)	(1.4)	(1.5)	(3.6)	(1.0)	(1.2)	(2.9)			
D	90.1	-------	90.3	78.8	-------	79.5	55.0	-------	54.9	41.7	-------	41.5	49.3	-------	50.8
	(0.9)		(0.9)	(1.0)		(0.8)	(0.6)		(1.0)	(3.5)		(3.3)	(5.3)		(2.6)

[a] Except where noted five specimens were tested.
[b] Average for three specimens except for form A3 and C1 which were not furnished.
[c] Calculated from deflection measurements [38].
[d] Calculated from strain measurements on the tensile side of the specimen [38].
[e] Calculated from strain measurements on the compressive side of the specimen [38].
[f] Numbers in parentheses are coefficients of variation in percent.
[g] Average for two specimens.

TABLE 8. *Average moduli of rupture for five cermets*

Specimen form	Cermet I [a]	Cermet II [a]			Cermet III [a]			Cermet IV [a]				Cermet V [b]
	A [c]	A [c]	B [d]	$\frac{A-B}{A}$	A [c]	B [d]	$\frac{A-B}{A}$	A [c]	B [e]		$\frac{A-B}{A}$ [f]	A [c]
									Tensile	Compression		
	psi	*psi*	*psi*	%	*psi*	*psi*	%	*psi*	*psi*	*psi*	%	*psi*
A1	198,000 [g](11.3)	304,000 (8.9)	293,000 (8.4)	3.8	162,000 (12.3)	154,000 (12.3)	5.1	32,500 (12.6)	26,100 (24.5)	32,200 (17.7)	20.5	27,800 (7.6)
A2	208,000 (9.0)	282,000 (6.5)	271,000 (6.6)	4.1	131,000 (36.0)	122,000 (33.1)	4.8	[h] 43,100	[h] 35,900	[h] 46,100	[h] 16.4	31,800 (11.3)
A3	183,000 (11.5)	286,000 (4.6)	275,000 (4.3)	3.8	179,000 (3.9)	171,000 (5.1)	4.5	39,700 (11.8)	38,100 (11.0)	40,500 (10.1)	8.1	--------
B1	208,000 (5.5)	226,000 (6.2)	217,000 (6.5)	3.9	156,000 (12.7)	149,000 (13.3)	4.7	32,300 (5.3)	30,000 (17.0)	33,100 (2.7)	7.8	24,900 (12.9)
C1	183,000 (10.5)	230,000 (10.8)	218,000 (10.0)	5.0	145,000 (11.8)	137,000 (12.0)	5.2	35,600 (11.0)	27,200 (10.3)	37,300 (22.0)	22.3	--------
D	[i] 223,000 (5.9)	[i] 318,000 (3.5)	[j] 297,000 (2.7)	6.5	[i] 173,000 (5.3)	[j] 162,000 (7.4)	6.5	[i] 40,800 (12.0)	[j] 39,100 (11.8)	--------	4.2	[i] 32,500 (5.5)

[a] Except where noted, five specimens were tested.
[b] Average for three specimens except for forms A3 and C1 which were not furnished.
[c] Calculated by the elementary beam theory [38].
[d] Calculated by the method of Nadai for specimens having equal tensile and compressive strains [13, p. 164].
[e] Calculated by the method of Nadai for specimens having unequal tensile and compressive strains [13, p. 164].
[f] Based on the tensile value.
[g] Numbers in parentheses are coefficients of variation in percent.
[h] Average for two specimens.
[i] Calculated by the method of Seewald for concentrated loads [16, p. 99].
[j] Calculated using the method of Seewald and the method of Nadai based on strains for tensile surface only.

III, and IV which had plastic flow. This correction was not required for cermets I and V which had little plastic flow, as shown by figure 14.

The correction for concentrated loads was approximately 1.0 percent for the form-D specimens. Although this correction is small, it may be considerable for other specimen designs [38, p. 301]. The enlarged-end specimens were designed to diminate this correction.

The deviations from a suggested curve [22] representing the dependence of strength on the size of specimen were quite large. Significant differences of the average values of different forms due to differences in size were found for cermets II and IV only. The smallest specimens of each cermet, however, had a higher strength than that of the largest specimens. The rate of change of strength with size is presumed different for different materials [22], and may not be evident unless there is a many fold change in size.

The coefficients of variation for modulus of rupture were quite variable with values comparable to those obtained in the three preceding tests. The coefficients for strength were considerably larger than for modulus of elasticity and had no correlation with specimen size [22].

The specimens broke with irregular fractures, similar to those for the tensile specimens, in the tensile half. For cermets IV and V, this fracture continued at right angles to the span direction in the compressive half, but for cermets I, II, and III the fractured surface curved in the compressive half to an angle of about 45° to the span direction at the compressive surface. Single fractures were common for specimens of cermets IV and V and for all form-D specimens. Multiple breaks, as many as five, were prevalent for enlarged-end specimens of cermets I, II, and III. The phenomena of multiple breaks has been studied by Miklowitz [4, b].

The average calculated and measured extensibilities of the cermets are given in table 9. The extensibilities paralleled strength in that they were characteristic to each cermet, had similar coefficients of variation, and had a similar dependence on specimen size.

6.5. Evaluation of the Transverse Test

The essential requirements for a satisfactory transverse test for cermets are (1) accurately shaped specimens having large length-to-depth and length-to-width ratios, (2) measurement of strains by deflection or preferably by surface-strain gages, (3) the relief of axial stresses due to change in span length during loading by means of roller knife-edges, (4) the correction of strength for effects of plasticity and concentrated loads when required, (5) the restriction of the test to small deflections where the mathematical assumptions are not exceeded.

The transverse test gives satisfactory values of modulus of elasticity and estimates of Poisson's ratio for cermets. Tensile strength and extensibility may be obtained provided creep is small and necessary corrections for the effects of plasticity and concentrated loads are made. Special shapes of specimens are not appreciably superior to the simple prismatic specimen having sufficient size to accommodate strain gages.

7. Impact Test

7.1. Specimens

The specimens were made in accordance with ASTM Designation (E23–47T) [23]. They were rectangular parallelepipeds 10 mm square by 55 mm long. Five notched and five unnotched specimens

TABLE 9. *Comparison of the average calculated and measured extensibilities from transverse tests on five cermets*

Specimen form	Cermet I [a]			Cermet II [a]			Cermet III [a]			Cermet IV [a]			Cermet V [b]		
	Calculated [c]	Measured [d]	Difference	Calculated [c]	Measured [d]	Difference	Calculated [c]	Measured [d]	Difference	Calculated [c]	Measured [d]	Difference	Calculated [c]	Measured [d]	Difference
	Percent	*Percent*	*Percent*	*Percent*	*Percent*	*Percent*	*Percent*	*Percent*	*Percent*	*Percent*	*Percent*	*Percent*	*Percent*	*Percent*	*Percent*
A1	0.217	0.218 [e](9.6)	0.5	0.386	0.424 (10.5)	8.9	0.310	0.353 (12.4)	12.2	0.095	0.136 (27.9)	30.1	0.046	0.047 (5.6)	2.1
A2	0.223	0.227 (10.0)	1.8	0.339	0.377 (7.1)	10.1	0.235	0.303 (33.6)	22.4	0.102	[f] 0.121	15.7	0.051	0.053 (4.0)	3.8
A3	0.201	0.228 (9.4)	11.8	0.351	0.388 (6.2)	9.5	0.324	0.388 (3.7)	16.5	0.095	0.115 (16.8)	17.4	-----	------	----
B1	0.221	0.226 (5.2)	2.2	0.277	0.305 (6.7)	9.2	0.282	0.327 (20.4)	13.7	0.077	0.087 (18.5)	11.5	0.048	0.048 (12.2)	0.0
C1	0.194	0.202 (11.2)	4.0	0.286	0.310 (11.9)	7.7	0.270	0.310 (11.9)	12.9	0.085	0.104 (24.1)	18.3	-----	------	----
D	0.248	0.260 (6.1)	4.6	0.404	0.481 (4.5)	16.0	0.315	0.390 (6.1)	19.2	0.098	0.109 (32.5)	10.1	0.065	0.068 (28.9)	4.4

[a] Except where noted, five specimens were tested.
[b] Average for three specimens except for A3 and C1 forms which were not furnished.
[c] Extensibility $=100\sigma/E$ in percent, where σ is the average modulus of rupture by the elementary beam formula and E is the average modulus of elasticity from surface strain.
[d] From stress-strain curves similar to those shown on figure 14.
[e] Numbers in parentheses are coefficients of variations in percent.
[f] Average for two specimens.

were obtained for each cermet. The notch had a depth of 2 mm, an angle of 45°, and a fillet radius of 0.25 mm.

7.2. Apparatus and Procedure

A Baldwin-Bell Telephone Laboratory pendulum impact machine was used. It was fitted for Charpy tests and had a capacity of 0 to 2 ft-lb, extended to 16 ft-lb by using heavier hammers. The velocity at impact was 11 fps. The impact tester was designed according to specifications outlined in ASTM Method D256–47T (for plastic materials) [24]. The anvils and striking edge were modified to fit the smaller specimens tested in this work, and these modifications met the conditions set forth in ASTM E23–47T (for metallic materials) [23]. The apparatus was mounted on a firm base.

The standard procedure recommended by ASTM (E23–47T) [23] was used. The friction and windage correction was determined and applied.

By reading the scale to the nearest half division (0.005 ft-lb) a maximum error of 4.2 percent occurred for the notched specimens made from cermet V. Specimen dimensions were within the prescribed tolerances, and errors due to difference in size were considered to be negligible.

7.3. Results and Discussion

The impact values are given in table 10. The results of tests on the unnotched specimens indicated a wide range of impact values for the five cermets.

The notched specimens ranked the cermets in the same order as the unnotched specimens, but the values obtained were much lower. The impact values of the cermets I, II, and III were reduced about 90 percent while the impact values of cermet IV and cermet V were reduced about 72 percent. These results point out the notch sensitivity of cermets. Quackenbos [29] noted a similar reduction of the impact values of some organic plastics.

The coefficient of variation for impact value of the unnotched specimens of each of the cermets was over 10 percent, and was generally larger than that for strength from the tensile, compressive, torsional, and transverse tests.

TABLE 10. *Impact values for cermet specimens*

Cermet	Unnotched [a]		Notched [b]	
	Hammer weight [c]	Impact value	Hammer weight [c]	Impact value
	lb	*ft-lb*	*lb*	*ft-lb*
I	8	6.30 [d](13.9)	2	0.59 (25.4)
II	16	9.23 (20.34)	2	0.95 (9.5)
III	8	4.33 (10.16)	1	0.48 (2.1)
IV	2	0.57 (14.0)	1	0.16 (nil)
V	1	0.44 (11.4)	1	0.12 (nil)

[a] Five specimens 10mm×10mm×55mm (ASTM E23–47T) standard Charpy specimen, except unnotched.
[b] Five standard Charpy specimens (ASTM E23–47T).
[c] The linear velocity of the hammer was 11 fps.
[d] Numbers in parentheses are coefficients of variation in percent.

With the exception of cermet I, all notched specimens had lower coefficients of variation than the unnotched specimens. It should be noted that the limited sensitivity of the impact tester masked the variation in cermets IV and V.

It is well known that the impact value is much less than the stored energy in an identical static simple beam just before fracture. It is also recognized that stress concentrations in the impact specimens are very large, and consequently only a small portion of the specimen has stresses approaching failure. The large coefficients of variation would be expected because, according to the flaw theory, the variability increases as the size decreases [22].

In any impact test, there are many variables, of which some are maintained constant. The various

tests are classified by Sayre and Werring as (1) proof tests, (2) increment drop tests, (3) single blow tests, and (4) pendulum tests. The methods of test have been discussed [25, 26, 29], and there is considerable disagreement as to the measurement and significance of the impact resistance of a material.

The Charpy test was selected for this investigation because (1) it is a standard ASTM test for metallic materials [23], (2) the specimen is broken in a single blow without introducing plasticity, creep, and fatigue as factors, (3) the impact hammer strikes accurately at the desired location, (4) the test is made simply and quickly, (5) when properly made, test results are reproducible [28], (6) the specimen is tested as a simple beam and the error due to gripping is eliminated, and (7) both unnotched and notched specimens can be tested satisfactorily.

7.4. Evaluation of the Impact Test

The requirements of a satisfactory impact test are (1) accurately shaped specimens with a suitable finish, either notched or unnotched, (2) a well constructed Charpy tester, and (3) an adequate number of specimens to give the desired confidence limit.

Cermets are satisfactorily classified by the Charpy impact test according to impact resistance and notch sensitivity. Impact values are not satisfactorily correlated with other properties of the material, and the values for other sizes of specimens cannot be predicted.

8. Correlation of Mechanical Properties

8.1. Elastic Properties

Table 11 gives the average elastic properties for the tests listed.

The average moduli of elasticity of cermets I, II, and III agreed within approximately 10 percen regardless of the method of test. As previously shown, the tensile and compressive moduli for a single cermet were equal within experimental error, and the modulus did not depend on specimen size for th series of transverse specimens. The average moduli of elasticity determined by the different tests varied as much as 17 percent for cermet IV which had the largest coefficients of variation. The variation of the average moduli determined by the different tests for cermet V was even larger, being 37 percent.

The compressive moduli of specimens cut from form B1 transverse specimens were lower than the transverse moduli for this form. These consistently lower values indicated that the material in the ends of the B1 specimens may have been different from that in the thinner midportion, or there may have been systematic errors in the test methods. The differences were within the experimental error except for cermet V.

The correlation of the elastic properties obtained in tension and also in shear, expressed by the eq [15, p. 57],

$$E=2G(1+\mu) \tag{6}$$

is illustrated by the agreement of the modulus of rigidity calculated from the tensile data and that obtained from the torsion test, table 11. This agreement and similarity of the transverse and compressive moduli of elasticity, for specimens having axes at 90°, indicate that these materials, with the possible exception of cermet V, are isotropic.

8.2. Evaluation of the Stresses and Strains in the Cermet Specimen at Fracture

a. Stress and Strain Analyses

(1) *Tensile Specimens.* In the tensile test, the axial strain, ϵ, and lateral strain, ϵ_1 were measured

TABLE 11. *Average values of elastic properties of cermets obtained from tensile, compressive, transverse, and torsional tests*

Cermet	Modulus of elasticity						Poisson's ratio				Modulus of rigidity	
	Tensile test	Compressive test	Transverse test				Tensile test	Compressive test	Transverse test [b]		Torsion test	Calculated [c]
			Form B1	Min [a]	Avg [a]	Max [a]			Min	Max		
	10^6 *psi*	10^6 *psi*	10^6 *psi*	10^6 *psi*	10^6 *psi*	10^6 *psi*					10^6 *psi*	10^6 *psi*
I	89.9 [d](0.9)	91.3 (3.4)	94.7 (1.4)	90.3 (0.9)	93.0 (1.7)	95.9 (3.9)	0.21 (2.3)	0.22 (Nil)	0.14 (14.5)	0.23 (1.3)	36.0 (2.9)	37.1
II	78.6 (0.4)	78.8 (0.9)	82.1 (1.1)	79.5 (0.8)	81.2 (1.3)	83.4 (1.7)	0.23 (Nil)	0.23 (4.4)	0.16 (1.3)	0.24 (2.5)	33.0 (7.4)	32.0
III	55.1 (1.1)	50.9 (1.4)	55.4 (3.0)	53.9 (3.6)	54.1 (2.0)	55.4 (3.3)	0.22 (Nil)	0.24 (2.0)	0.15 (1.9)	0.23 (2.6)	22.8 (8.6)	22.6
IV	43.1 (4.4)	41.4 (6.5)	42.7 (12.3)	37.1 (17.2)	41.8 (8.4)	44.4 (2.9)	0.22 (Nil)	0.23 (5.2)	0.14 (2.1)	0.22	18.5 (7.2)	17.7
V	[e]	44.5 (11.9)	53.7 (6.8)	[f] 50.8 (2.6)	[f] 58.0 (3.7)	[f] 64.6 (3.7)	[e]	0.17 (3.5)	[g] 0.11 (5.7)	[g] 0.14 (2.8)	25.4 (11.0)	[h] 25.

[a] For six forms of transverse specimens.
[b] For five forms of transverse specimens.
[c] Calculated from $E/2G=1+\mu$ using data from the tensile test.
[d] Figures in parentheses are coefficients of variation in percent.
[e] Specimens were not furnished for this material.
[f] For four forms of transverse specimens.
[g] For three forms of transverse specimens.
[h] Data from average of transverse specimens were used because tensile specimens were not furnished.

and the relation expressed as

$$-\epsilon_1 = \mu\epsilon, \tag{7}$$

where μ = Poisson's ratio.
The axial stress corresponding to ϵ is

$$\sigma = E\epsilon = \frac{P}{A} \tag{8}$$

where
E = Young's modulus of elasticity,
P = total load,
A = area of cross section of specimen,
ϵ = extensibility when σ = strength.

The maximum shear stress is for uniaxial loading [39, p. 15],

$$\tau_{max} = \frac{\sigma}{2} \tag{9}$$

and the maximum shear strain

$$\gamma_{max} = \epsilon(1+\mu). \tag{10}$$

(2) *Compressive Specimens.* In the compressive tests, the applied load was axial, and the axial strains, ϵ, and lateral strains, ϵ_1, were measured. Equations (7), (8), (9), and (10), modified for stress direction, apply. In accordance with Nadai [11, p. 208]

$$\text{"equivalent stress"} = E\,\epsilon_1 = -\mu E\epsilon = -\mu\sigma, \tag{11}$$

where "equivalent stress", in the sense of the maximum strain hypothesis of failure, is the value of σ when ϵ_1 is substituted for ϵ in eq (8) and ϵ and σ are the values at fracture in the compressive tests, and are, of course, negative.

(3) *Torsion Specimens.* In the torsional test, compressive and tensile principal strains were recorded to failure in addition to shear strains within the elastic limit. The maximum shear stress was obtained from the applied torque. The maximum induced tensile and compressive strains were equal; therefore, eq (2) and (3) apply.

Also, [39, p. 15]:

$$\sigma_{45} = \tau_{max} = -\sigma_{135}. \tag{12}$$

Since, for the tensile test, the maximum tensile strain from eq (8) is:

$$\epsilon = \frac{\sigma}{E}$$

and for the torsional test, the corresponding maximum tensile strain [11, p. 208] or [39, p. 15], is:

$$\epsilon_{45} = \frac{\sigma_{45} - \mu\sigma_{135}}{E} = \frac{\sigma_{45}(1+\mu)}{E}.$$

Then from [11, p. 208]

$$\text{"equivalent stress"} = \sigma_{45}(1+\mu). \tag{13}$$

(4) *Transverse Specimens.* The stress analysis of the tensile half of the transverse specimen resembles the analysis for the tensile specimen, except that the stress grades from zero at the neutral axis to a maximum at the outer tensile fibres. Similar also to the tensile specimen, the lateral and shear stresses are of minor significance. The compressive half of the transverse specimens resembles the compressive specimen except that the maximum stress can exceed the tensile stress on the tensile side by only small amounts which are due to plasticity and concentrated loads, and the induced lateral tensile strain and shear stress are also limited. The maximum shear due to loads and reactions on transverse specimens is too small, even for spans of 5/16 in., used in some tests, where this stress is approximately 13 percent of the tensile, to be a source of failure.

b. Stress-Strain Relation and Fracture of Cermets

The stress-strain curves to rupture previously reported indicated that the stress-strain relation was linear for specimens of cermets I and V in all tests except for cermet I in compression. The relation for cermet IV also was linear in the torsional and compressive tests. In the remaining tests, curvature of the stress-strain lines was apparent. Porous materials or those with inclusions of a relatively soft or weak substance having stress-strain curves of a similar shape were discussed by Nadai [11, p. 26] under the heading of hysteresis and after effects. Such materials fractured at *strains* low in comparison to those attained by ductile materials [11, p. 3] and, in these respects, resembled the cermets.

The calculation by eq (1) to (13) of stresses and strains present in specimens as the strength is approached depends on the assumption that the material remains elastic until failure.

The fracture surfaces of the tensile, transverse, and torsional specimens indicated that failure of the specimens as a whole occurred in tensile fracture. The compressive specimens broke into fragments from which the mode of failure could not be determined. According to Nadai [11, p. 182] the actual mechanism of failure, however, may be quite different from that apparent from the fracture surface of the specimen.

Several criteria for failure have been proposed, such as a limiting maximum principal stress, a limiting maximum strain, various energy considerations, etc. [11, p. 175]. The criteria for failure given in most theories have been advanced to explain the performance of ductile materials as well as of brittle materials having bi- or triaxial loading. For the cermets reported here, and also for many brittle materials, the criteria usually considered are a limiting tensile stress, a limiting maximum shear stress, and a limiting maximum elastic tensile strain (theory of the so-called equivalent stress, St. Venant) [11, p. 208]. The last criterion would not be expected to apply, however, to these same materials at elevated temperatures for reasons discussed by Nadai [11, p. 175, 208].

Table 12 lists, in a given column, the critical quantities of stress or strain that are equal in the

TABLE 12. *Equal values of maximum stress or maximum strain for different criteria of fracture in the tensile, transverse, compressive, and torsional tests*

Test	Criterion of fracture					
	Max tensile stress		Max tensile strain or equivalent stress		Max shear stress or max shear strain	
	Equal stress	Equal strain	Equal stress	Equal strain	Equal stress	Equal strain
Tensile	σ_t[a]	ϵ_t	σ_t	ϵ_t	$\frac{\sigma_t}{2}$	$\epsilon_t(1+\mu)$
Transverse	σ_{tr}	ϵ_{tr}	σ_{tr}	ϵ_{tr}	$\frac{\sigma_{tr}}{2}$	$\epsilon_{tr}(1+\mu)$
Compressive	---	$-\mu\epsilon_c$	$-\mu\sigma_c$	$-\mu\epsilon_c$	$\frac{-\sigma_c}{2}$	$-\epsilon_c(1+\mu)$
Torsional	σ_{45},	$\epsilon_{45}(1+\mu)$,	$\sigma_{45}(1+\mu)$,	ϵ_{45},	σ_{45},	$2\epsilon_{45}$,
	τ_{max}	$\frac{\gamma_{max}(1+\mu)}{2}$	$\tau_{max}(1+\mu)$	$\frac{\gamma_{max}}{2}$	τ_{max}	γ_{max}

[a] Symbols defined in eq (1) to (13), subscripts t, tr, and c refer to tensile, transverse and compressive tests respectively. For a particular criterion, the values of all of the quantities in a given column should be equal.

four tests when a particular criterion of fracture prevails. An interpretation of the significance of a strength from a given test requires some knowledge of the criterion of fracture. In the torsional test, for example, it might be expected that the shear strength would be obtained, but the torsional strength may be simply the shear stress at fracture as limited by the attainment of a maximum value according to one of the other criteria of fracture given in table 12. If the criteria of fracture can be determined, then the strength from the torsional test can be correlated with the corresponding shear strength, tensile strength, or "equivalent" strength. In a similar manner, the compressive stress present in the compressive test at fracture may be a function of either the shear strength or tensile strength.

Considering the maximum tensile stress and the maximum tensile strain criteria, the prevailing criterion is not evident from the values from the tensile, compressive, and transverse tests because the principal stress relations are similar. These relations are different, however, in the torsional test. A comparison of the experimental values of stress and strain from the torsional test to those from the other tests make possible a distinction between these two criteria of fracture. For example, the tensile strength, from the tensile test, is equal to σ_{45} if the maximum tensile stress is the criterion, but is equal to $\sigma_{45}(1+\mu)$ if the maximum tensile strain criterion is effective. If the maximum shear criteria are applicable, then the strength from the tensile test is equal to $2\ \sigma_{45}$ from the torsional test.

The brittle materials have shear strengths that are larger than their tensile strengths, as suggested by Preston [41]. The shear stress in the tensile specimen, although less than σ, is appreciable and may be the source of failure as it is for some ductile materials, but tensile fracture would be expected for cermets.

In the compressive test, the compressive stress, σ, is comparatively large, and exceeding either the induced lateral strain [11, p. 208] or the shear strength [42] may be the cause of failure. This analysis assumes uniform stressing in the specimen. Even when bending is absent, the friction at the ends of the specimen restrains the lateral strain [8]. Thus the stress distribution at the ends is not simple and can be a determining factor in the compressive test.

The maximum shear stress recorded as the torsional strength should indicate a tensile strength for brittle materials according to Preston [41]. This explanation is also mentioned by Kingery [42], who reported that the tensile strength is obtained from the torsional test on brittle materials.

8.3. Comparison of Data for Cermets

a. Data from Tests

Table 13 gives average values of the measured stresses and strains present in specimens at the moment of failure, and also those calculated by formulas (1) to (13). Table 14 lists the percentage differences between values of pairs of stresses or strains, that are significant in the behavior of the cermets and in the evaluation of the tests.

The manufacturer of cermet IV reported improvements in the product during the time interval that specimens were procured in the order transverse-tensile-torsional. The strengths given in table 13 indicate the improvement, but no correlations of results from these three lots of specimens were made because the materials were admittedly different.

b. Comparison of Measured and Calculated Extensibilities

The differences, in percent, of the average measured extensibilities for the tensile, transverse, and torsional tests from the calculated values, assuming elastic behavior, are given in table 14, line A. The differences indicated that the stress-strain lines were linear for cermets I and V, but the measured extensibilities were appreciably larger for cermets II, III, and IV.

c. Dependence of Strength on the Size of the Specimen

The form-D transverse specimens had only about six percent of the volume of the form-C1 specimens, and the smaller specimens were stronger by from 18.2 to 43.7 percent, as given in line B, table 14. The results indicated that the rate of change in strength with the change in size was different for the five cermets, and that their "material constants" [22], that govern the variation of strength with size, were probably different.

Because the strengths of tensile, compressive, torsional, and transverse specimens may decrease as the size of the specimen is increased [22], the comparison of strengths would preferably be made on specimens having the same, or nearly the same, size. As indicated for transverse specimens, the dependence is approximate only, and a many-fold change in size may be required to produce a significant change in strength. The strengths for cermets I and III, from table 13, are higher than those given by Johnson [43], who used considerably larger specimens. For the tensile and compressive tests,

TABLE 13. *Average stresses and strains for cermet specimens at fracture in tensile, compressive, torsional, and transverse tests*

Cermet E	Tensile test				Compressive test				Torsional test				Transverse test								Ratio [a] $\frac{\tau_{max}}{\sigma}$
	Stress	Strain			Stress		Strain		Stress		Extensibility		Stress for form			Extensibility					
		Extensibility														C1		B1			
	Axial σ [b]	Shear τ_{max}	Measured ϵ	Calculated σ/E	Axial σ	Shear τ_{max}	Lateral ϵ_l	Axial σ/E	Shear tensile σ_t, τ_{max}	Equivalent σ_e $(1+\mu)$	Measured ϵ_s	Calculated $\frac{\tau_{max}}{2G}$	C1 σ	B1 σ	D σ	Measured ϵ	Calculated σ/E	Measured ϵ	Calculated σ/E	Shear strain $\frac{\tau_{max}}{G}$	
	10^3 *psi*	10^3 *psi*	%	%	10^3 *psi*	10^3 *psi*	%	%	10^3 *psi*	10^3 *psi*	%	%	10^3 *psi*	10^3 *psi*	10^3 *psi*	%	%	%	%	%	
I	176 [c] (6.6)	88	0.201 (6.0)	0.196 (6.6)	388 (2.4)	294	0.142	0.646 (5.7)	156.8 (5.0)	189	0.217 (5.1)	0.218	183 (10.5)	208 (5.5)	223 (5.9)	0.202 (11.2)	0.194	0.226 (5.2)	0.221	0.436	1.41
II	204 (5.0)	102	0.202 (6.1)	0.259 (4.9)	555.8 (1.8)	277.9	0.162	0.705 (2.4)	180.2 (7.5)	221	0.362 (7.4)	0.273	218 (10.0)	217 (6.5)	297 (2.7)	0.310 (12.0)	0.286	0.305 (6.7)	0.277	0.547	1.28
III	141.2 (8.6)	70.6	0.304 (11.6)	0.256 (4.5)	371 (3.1)	187	0.176	0.735 (2.2)	109.4 (14.7)	133	0.334 (23.2)	0.250	137 (12.0)	149 (13.3)	162 (7.4)	0.310 (11.9)	0.270	0.327 (20.4)	0.282	0.500	1.26
IV	38.1 (13.6)	19.5	0.101 (16.2)	0.089 (15.9)	118.5 (11.2)	59.2	0.065	0.289 (16.6)	43.5 (3.7)	53.1	0.122 (6.5)	0.121	27.2 (10.3)	30.0 (17.0)	39.1 (11.8)	0.104 (24.1)	0.085	0.087 (18.5)	0.077	0.243	1.97
V	(d)	(d)	(d)	(d)	181.3 (27.0)	90.6	0.069	0.460 (18.8)	23.7 (9.3)	27.0	0.046 (16.8)	0.047	(d)	24.9 (12.9)	32.5 (5.5)	(d)	(d)	0.048 (12.2)	0.048	0.095	3.64

[a] τ_{max} is taken from the compressive tests, while σ is the B1 transverse value.
[b] Symbols are given in eq (1) to (13).
[c] Numbers in parentheses are coefficients of variation in percent.
[d] No tensile or C1 specimens furnished.

TABLE 14. *Differences for pairs of properties of cermets*

Line	Comparison [b]	Differences [a]				
		Cermet				
		I	II	III	IV	V
A	ϵ Avg measured from calculated.	% 2.0	% 17.8	% 22.2	% 10.9	% 0
B	σ_{tr}, Form D from C1	21.8	36.2	18.2	43.7	[c] 30.5
C	ϵ_{tr} from ϵ_t, measured	0.5	6.2	2.0	(d)	(c)
D	ϵ_{tr} from ϵ_t, calculated	−1.0	10.4	5.5	(d)	(c)
E	ϵ_{to} from ϵ_t, measured	7.9	23.4	9.9	(d)	[c] −4.3
F	ϵ_{to} from ϵ_t, calculated	11.2	5.4	−2.3	(d)	[c] −2.0
G	ϵ_{c1} from ϵ_{tr}, calculated	−35.7	−41.5	−37.6	−15.6	43.7
H	σ_{tr} from σ_t	4.0	6.9	−3.0	(d)	(c)
I	σ_{to} from σ_t	−10.9	−11.7	−22.5	(d)	[c] −4.8
J	σ_{to} (equi) from σ_t	7.4	8.3	−5.8	(d)	[c] 8.4
K	σ_e (equi) from σ_{tr}	−38.0	−41.0	−39.7	−9.3	23.7
L	τ_{tr} from τ_c	−64.6	−61.1	−60.4	−74.3	−86.3
M	τ_{to} from τ_c	−46.7	−35.1	−41.5	−26.5	−73.8

[a] Calculated from values given in table 13. Excess of first over second quantity.
[b] Symbols used are: ϵ=average extensibility for tensile, torsional, and transverse tests; ϵ_t, ϵ_{tr}, ϵ_{to}=extensibilities from tensile, transverse, and torsional tests, respectively; ϵ_{c1}=lateral strain from compressive test; σ_t, σ_{tr}, and σ_{to}=tensile stresses in tensile, transverse, and torsional tests, respectively; σ_{te} (equi) and σ_e (equi)="equivalent" stresses from torsional and compressive tests, respectively; τ_{tr}, τ_{to}, and τ_c=shear stresses in tension, torsional, and compressive tests, respectively.
[c] Tensile properties of B1 transverse specimens were used because no tensile or C1 specimens were furnished.
[d] Comparison not made because of changes in material.
[e] Tensile specimens not furnished.

the size comparison is easily made on the basis of the volume within the gage portion of the specimen. The torsional and transverse specimens, however, have only a surface at maximum stress, and, on the basis of volume, an infinitely large specimen would be required to equal a small tensile specimen. Failure may be initiated, however, at stress concentration points below the surface where the calculated average stress is less than at the surface, and, solely for size comparison, it was assumed that the volume having stresses ranging from 90 to 100 percent of the outer fibre stress might contain stress raisers causing fracture. The volumes of specimens used in this investigation for the various tests are given in table 15, and, excepting the volume for form D, were considered sufficiently alike to permit comparisons of strengths.

TABLE 15. *Gage sections of cermet specimens and volume subjected to test stresses*

Test	Section	Volume [a]
	in.	*in.*^{3}
Tensile	0.250 diameter×1.25	0.061
Compressive	.424×0.424×1.27	.228
Torsional	.500 diameter×2.25	.084
Transverse	Form D, third point	.0017
Do	Form B1, constant moment	.0148
Do	Form C1, constant moment	.0296

[a] Transverse and torsional specimens had surfaces only, i. e., zero volume, at maximum stress. For comparison of specimen sizes only, the volume of that portion stressed from 90 to 100% of the maximum stress was considered the volume of these specimens.

d. Criteria of Fracture

The differences of stresses or strains of pairs assumed equal according to the maximum tensile strain criterion [11, p. 208], table 12, are given in table 14, lines E, F, G, J, and K. The comparisons

in lines E, F, and J refer to specimens that had tensile fractures and to the torsional and tensile tests with their distinct principal stress patterns. These comparisons, with the exception of the value for cermet II, line E, indicated that the application of the maximum elastic tensile strain criterion gave values that agreed within 11.2 percent. The lateral strains and "equivalent" stresses calculated from the data from the compressive test according to the maximum tensile strain criterion, lines G, and K, however, were much less than the corresponding extensibilities and transverse strengths for cermets I, II, III, and IV. These differences suggested that some other criterion of fracture, such as a limiting maximum shear stress, was effective in the compressive test before the lateral strain exceeded the extensibility. On the other hand, cermet V was exceptional in that it probably fractured according to the maximum strain criterion in the compressive test, but the lateral strain and "equivalent" stress were higher than expected.

The particularly close agreement of transverse and tensile results, for specimens of comparable size, lines C, D, and H, was expected because the stress patterns were similar. This agreement confirmed, but did not prove, the applicability of either the maximum tensile strain or the maximum tensile stress criteria. The latter criterion seemed less applicable in the comparison of the torsional to the tensile test, in which the stress patterns were different, because the tensile stress in the torsional test was definitely less than in the tensile test, line I. Although the maximum tensile strain criterion overcompensated these stress differences, line J, this criterion gave the better agreement.

The widely different values of shear stress at fracture in the various tests, table 13 and table 14, lines L and M, led to the conclusion that a common maximum shear stress was not a criterion for correlating strength in the four tests. The largest values of shear stress were obtained, for each of the five cermets, in the compressive test. The maximum shear strains were also largest in the compressive test, and ranged from 3.03 to 9.9 times the extensibilities from the transverse test.

No single criterion for failure was evident for the compressive test. In this test, cermet V may have failed as predicted by the maximum strain theory. According to Kingery [42], brittle materials fail in shear in the compressive test. The extensive deformation of compressive specimens at a stress just below the strength is suggestive of failure in shear. That a maximum shear stress or a maximum shear strain is a second criterion of failure cannot be proved or contradicted from the data because sufficiently large shear stresses were not developed in the other tests. Although tests to develop the shear stress to these high levels may yet be devised, especially to evaluate such a shear strength, it seems common practice to accept the maximum shear stress as a criterion and the shear stress in the compressive test as the approximate shear strength [42]. The error in this assumption may not be serious for design purposes, because of the similarity in stress patterns for the compressive specimen and for parts such as cutting tools, punches, and stubby beams.

e. Brittleness

The brittle materials, including cermets, glass, ceramics, etc., are characterized by a texture or structure in which resistance to shearing is well developed, but the tensile strength, or cohesion, is limited by the presence of zones or planes of weakness. The degree of brittleness for these cermets may be expressed as the inverse of extensibility. Preston's requirement that, for a substance to be classified as being brittle, failure occur in tension when the specimen is tested in shear [41] provokes the suggestion that the ratio of τ_{max}/σ could be an index of brittleness. Because τ_{max} is usually derived from compressive tests, it follows that the ratio of compressive to tensile strengths should also be an index. Table 13 gives the values for τ_{max}/σ and there is some correlation since a plot of τ_{max}/σ and extensibility gives a fairly smooth curve. The value of this ratio seems to be a characteristic of the cermet.

8.4. Correlation of Impact Values and Mechanical Properties

Figure 15 gives plots of impact values with three factors derived from mechanical properties.

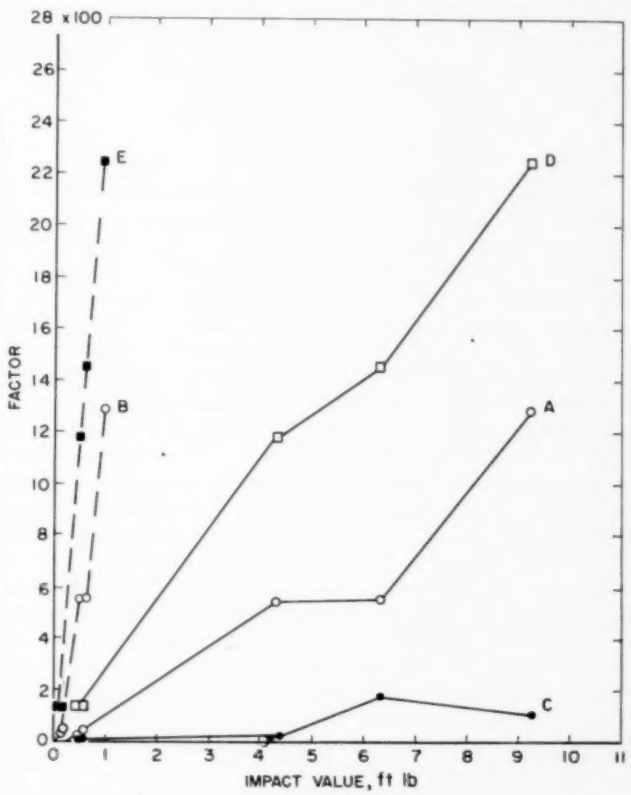

FIGURE 15. *Impact values plotted with factors computed from mechanical properties.*

Energy numbers are plotted with impact values of unnotched specimens on line A and notched specimens on line B; moduli of resiliency and impact values for unnotched on C; and the product of compressive strength and tensile extensibility with impact value, unnotched on D; and with impact value, notched on line E.

The modulus of resiliency [15, p. 282] is given by

$$F_1=\frac{\sigma_y^2}{E} \tag{14}$$

where σ_y is the yield stress. This modulus gives a measure of the energy absorbed elastically by the impact specimen. The correlation of this factor with impact value was unsatisfactory, line C, figure 15.

The energy number [30] is given by

$$F_2=\frac{\sigma^2}{E} \tag{15}$$

where σ is the tensile strength from form-D specimens. This number gives a considerably better correlation with impact values, lines A and B.

Concentrated compressive stresses as well as tensile properties are involved in impact tests. It would seem that a factor derived from results from both tensile and compressive tests would give a better correlation; such a factor is

$$F_3=-\sigma\epsilon \tag{16}$$

where σ is the compressive strength and ϵ is the calculated extensibility from the form-D specimens. This factor gives the best correlation with impact value, lines D and E. None of these correlations is satisfactory for predicting the impact value from the mechanical properties.

9. Summary

Tensile, compressive, torsional, transverse, and impact tests were made on specimens of cermets having five distinct compositions. The tests were evaluated according to the design requirements of the specimens and apparatus, refinements in test procedure, suitability to the cermets, and the variability of the results. The tensile, compressive, and transverse tests gave comparable moduli of elasticity and Poisson's ratios, and the modulus of rigidity calculated from these values agreed with the modulus of rigidity from the torsional test. The stresses and strains present at fracture in the tensile, compressive, torsional, and transverse tests on specimens of comparable sizes indicated that these brittle materials broke either at a limiting tensile strain or at a limiting shear stress. Brittleness was expressed as the ratio of shear to tensile strength and was related to maximum tensile strain. The combination of tensile and compressive tests gave the essential elastic properties and strengths of the materials. The degree of correlation of impact values with mechanical properties was considered too low for the prediction of impact values.

The contribution by Gordon B. Massengale in the planning and design of apparatus during the initial part of this investigation is acknowledged.

10. References

[1] A. R. Blackburn, T. S. Shevlin, and H. R. Lowers, Fundamental study, and equipment for sintering and testing of cermet bodies: III, equipment for cross-bending stress and tensile at high temperature, J. Am. Ceram. Soc. **32,** 93 (1949).

[2] W. H. Duckworth, A. D. Schwope, O. K. Salmassy, R. L. Carlson, and H. Z. Schofield, Mechanical-property tests on ceramic bodies, U. S. Airforce, Air Research and Development Command, WADC Tech. Rept. No. 52–67, 17 (March 1952).

[3] W. H. Duckworth, et al., Mechanical property tests on ceramic bodies, AF Tech. Rept. No. 6512 (April 1951).

[4a] Julius Miklowitz, Elastic waves created during tensile fracture: The phenomenon of a second fracture, Naval Ordnance Test Station Rept. 1961 (1952).

[4b] Julius Miklowitz, Flexural waves in beams according to the more exact theory of bending, Naval Ordnance Test Station Rept. 2049, NOTS 741 (Sept. 1, 1953).

[5] M. B. Stiefel, Application of photoelasticity to the design of tensile specimens for ceramic-metal materials, Am. Ceram. Soc. Bul., **34,** 133 (1955).

[6] R. A. Heindl and L. E. Mong, Young's modulus of elasticity, strength, and extensibility of refractories in tension, J. Research NBS, **17,** 46 (1936) RP923; Ceram. Abstr. **16,** 24 (1937).

[7] R. F. Geller and M. D. Burdick, Strength and creep of special ceramic bodies in tension at elevated temperatures, NACA, ARR 6D–24.

[8] O. K. Salmassy, et. al., Behavior of brittle state materials, Battelle Memorial Institute, WADC Tech. Rept. 53–50, Part II (June 1955).

[9] O. K. Salmassy, W. H. Duckworth, and A. D. Schwope, Mechanical-property tests on ceramic bodies, Battelle Memorial Institute, WADC Tech. Rept. 53–50 (March 1953).

[10] O. K. Salmassy, et. al., material-property tests on ceramic bodies, Battelle Memorial Institute Rept. 19 (Aug. 22, 1953).

[11] Arpad Nadai, Theory of flow and fracture of solids, vol. I, 2d. ed. p. 328 (McGraw-Hill Book Co., New York, N. Y., 1950).

[12] J. A. Stavrolakis and F. H. Norton, Measurement of torsion properties of alumina and zirconia at elevated temperatures, J. Am. Ceram. Soc. **33,** 263 (1950).

[13] A. Nadai, Plasticity (English Translation by A. M. Whal), p. 128 (McGraw-Hill Book Co., Inc., New York, N. Y., 1931).

[14] R. A. Heindl and W. L. Pendergast, Progress report on investigation of fire-clay bricks and clays used in their preparation, J. Research NBS **3,** 691 (1929), RP114; Ceram. Abstr. **9,** 39 (1930).

[15] S. Timoshenko, Strength of materials: Part I, Elementary theory and problems, 2d ed., 13th printing (D. Van Nostrand Co., New York, N. Y., 1951).

[16] S. Timoshenko, Theory of elasticity, 1st ed., p. 99 (McGraw-Hill Book Co., Inc., New York, N. Y., 1934).

[17] M. M. Frocht, Photoelasticity, vol. II, p. 112 (John Wiley & Sons, Inc., New York, N. Y., 1948).

[18] J. S. Caswell, Stress analysis in short beams: II, Theoretical analysis and conclusions, engineering **178,** 656 (Nov. 19, 1954).

[19] L. H. Milligan, Note on modulus of rupture of cylindrical ceramic rods when tested on a short span, J. Am. Ceram. Soc. **36,** 159 (1953).

[20] W. Weibull, Phenomenon of rupture in solids, Ing. Vetenskaps Akad., Handl., **153,** 55 (1939), Ceram. Abstr., **20,** 250 (1941).

[21] A. A. Griffiith, Phenomena of rupture and flow in solids, Trans. Roy. Soc. (London). [A] **221,** 163 (1920); abstracted in J. Am. Ceram. Soc., **4,** 513 (1921).

[22] M. J. Barriage and R. H. Jacobsen, Development and application of brittle material method of stress analysis and study of brittle failure problems (Armour Research Foundation, Chicago, Ill., July 1952).

[23] Impact testing of metallic materials, Am. Soc. Testing Materials Designation: E23–47T, Am. Soc. Testing Materials Standards, Part I, p. 1451 (1952).

[24] Impact resistance of plastic and electrical insulating materials, Am. Soc. Testing Materials Designation: D256–47T, Am. Soc. Testing Materials Standards, Part 6, p. 1025 (1952).

[25] M. F. Sayre and Walter F. Werring, Introduction to symposium on impact testing, Proc. Am. Soc. Testing Materials **38,** Part 2, p. 21 (1938).

[26] E. J. Soxman, J. R. Tinklepaugh, and M. T. Curran, An impact test for use with cermets, J. Am. Ceram. Soc., **39,** 261 (1956).

[27] B. Maxwell and L. F. Rohn, Impact testing of plastics: Elimination of the toss factor, Am. Soc. Testing Materials Bul. No. 161, p. 44 (1949).

[28] D. E. Driscoll, Reproducibility of charpy impact test Symposium on Impact Testing, Am. Soc. Testing Materials Spec. Tech. Publ. No. 176, p. 70 (1955).

[29] H. M. Quackenbos, Jr., J. M. Hill, Jr., and C. E. Staff, The significance of the charpy and flexure tests in evaluating the impact resistance of plastics, Am. Soc. Testing Materials Bul. No. 159, p. 56 (July 1949).

[30] Properties of carboloy cemented carbides, Eng. Bul. HM–100A (Carboloy Co., Detroit, Mich., April 2, 1951).

[31] R. Baumberger and F. Hines, Practical reduction formulas for use in bonded wire strain gages in two dimensional strain fields, Proc. Soc. Exp. Stress Anal. II, No. 1, 113 (1944).

[32] Manual on quality control of materials, p. 14, STP 15–C, part I, Am. Soc. Testing Materials (Philadelphia, Pa., 1951).

[33] L. A. Yerkovich and G. J. Guarnieri, Compression-creep properties of several metallic and cermet materials at high temperatures, Proc. Am. Soc. Testing Materials **55,** 732 (1955).

[34] C. S. Aitchison and J. A. Miller, A subpress for compressive tests, NACA Tech. Note No. 912 (Dec. 1943).

[35] Instructions for the Tuckerman strain gage, Am. Instr. Co. (April 1950).

[36] W. H. Duckworth, Precise tensile properties of ceramic bodies, J. Am. Ceram. Soc., **34,** 1 (1951).

[37] A. M. Burghardt and A. S. Elder, Mechanical tests, development of a standard bend test for cemented carbides Lab. Rept. No. WAL 110/16 (Watertown Arsenal, Watertown, Mass., Feb. 15, 1950).

[38] L. E. Mong and W. L. Pendergast, Dynamic and static tests for mechanical properties of fired plastic refractories and other more resilient materials, J. Am. Ceram. Soc. **39,** 301 (1956).

[39] Stephen Timoshenko and J. N. Goodier, Theory of elasticity, 2d ed., p. 15 (McGraw-Hill Book Co., Inc., New York, N. Y., 1951).

[40] N. M. Parikh, Modes of fracture and slip in cemented carbides, J. Am. Ceram. Soc., **40,** 335 (1957).

[41] F. W. Preston, A note on the concept of brittleness, J. Am. Ceram. Soc., **15,** 176 (1932).

[42] W. D. Kingery, Factors affecting thermal stress resistance of ceramic materials, J. Am. Ceram. Soc., **38,** 3 (1955).

[43] A. E. Johnson, Mechanical properties at room temperatures of four cermets of tungsten carbide with cobalt binder, NACA Tech. Note 3309 (December 1954); Mechanical properties at room temperatures of four cermets of titanium carbide with nickel binder, NACA Tech. Note 3197 (Aug. 1954).

WASHINGTON, April 15, 1958.

Journal of Research of the National Bureau of Standards Vol. 61, No. 3, September 1958 Research Paper 2896

Redetermination of Mass Spectra of Deuteromethanes

Fred L. Mohler, Vernon H. Dibeler, and Edith Quinn

Mass spectra of the four deuteromethanes have been remeasured using samples of improved isotopic purity. The relative abundances of fragment ions involving loss of H or D atoms from the molecules CH_3D, CH_2D_2, and CHD_3 are not proportional to the a priori probabilities of removing H or D atoms but have been expressed in terms of the a priori probability times a weighting factor. The weighting factor for removing one H or D atom from these molecules can be roughly expressed as positive and negative powers of a single constant 1.19 ±0.015 and the same power law holds for the relative abundances of H^+ and D^+. Weighting factors for removing two or more hydrogenic atoms are not consistent with this power law.

1. Introduction

A paper by this title by Dibeler and Mohler [1][1] was published in 1950 and at about the same time a paper by Schissler, Thompson, and Turkevich [2] also included mass spectra of the four deuteromethanes. There are some discrepancies between the mass spectra reported in the two papers, and in both researches the isotopic purity of the molecules CH_2D_2 and CHD_3 left much to be desired. Deuteromethanes of much better isotopic purity have become available and it seemed worthwhile to repeat the measurements. It is important for analytical reasons to have reliable mass spectral patterns for the deuteromethanes. It is also of theoretical interest to know the relative probabilities of removing H and D atoms from the four deuteromethanes.

2. Experimental Details

The deuteromethanes were made by A. T. Morse of Merck and Co., Limited, Montreal, Canada. The isotopic analyses of CH_3D, CH_2D_2, and CHD_3 were made at an ionizing voltage below the appearance potential of CH_3^+. For methane the appearance potential of CH_4^+ is 13.1 v and of CH_3^+, 14.4 v [3, 4]. This small difference makes the measurement rather insensitive and difficult. Tickner, Bryce, and Lossing [5] have pointed out that these measurements are also subject to small systematic errors because of small differences in the ionization potentials of the deuteromethanes. The results are given in table 1. These analyses are consistent with isotopic purities of 98 atom percent and for CD_4 99 percent quoted by the supplier.

Mass spectra were recorded with a Consolidated Model 21–103 mass spectrometer under standard operating conditions. The recorded spectra were corrected for the contribution of the C^{13} isotope, for the isotopic impurities listed in table 1, and for a small amount of air (1.6% or less) probably introduced in handling the sample.

TABLE 1. *Isotopic analysis of deuteromethanes*

Monodeuteromethane	CH_3D, 96.9%; CH_4, 2.2%; CH_2D_2, 0.9%.
Dideuteromethane	CH_2D_2, 98.6%; CH_3D, 1.3%; CHD_3, 0.1%.
Trideuteromethane	CHD_3, 97.1%; CH_2D_2, 2.4%; CD_4, 0.5%.
Tetradeuteromethane	CD_4, 98.5%; CHD_3, 1.5%.

[1] Figures in brackets indicate the literature references at the end of this paper.

3. Results

The corrected mass spectra are listed in table 2 and in the last row is given the sensitivity of the molecule ion peak in divisions per micron. In the spectra of CH_3D and CH_2D_2 two ions contribute to some of the mass peaks. Thus both CH_2^+ and CD^+ contribute to the 14 peak and H_2 and D contribute to the 2 peak. In table 3 the abundance of ions heavier than mass number 12 has been computed on the assumption that the probability of removing one, two, or three hydrogenic atoms from the deuteromethane is proportional to the probability of removing H, 2H, and 3H from methane [1]. The ions CH^+ and CH_2D^+ from CH_3D and CH^+, CHD^+, and CHD_2^+ of CH_2D_2 are observed, and with the above assumption the abundances of the other ions are derived.

TABLE 2. *Mass spectra of deuteromethanes for 70 v electrons*[a]

m/e	CH_4	CH_3D	CH_2D_2	CHD_3	CD_4
1	5.40	4.82	3.04	1.92	------
2	0.42	0.95	1.47	2.64	3.86
3	------	.13	0.18	0.16	------
4	------	------	------	.13	0.28
12	3.54	3.41	3.36	3.37	3.18
13	9.86	5.98	3.35	1.52	------
14	19.4	10.5	7.64	7.89	7.33
15	89.3	23.7	11.3	5.84	------
16	100	79.8	33.3	10.7	13.7
17	------	100	65.7	51.9	------
18	------	------	100	43.5	86.5
19	------	------	------	100	------
20	------	------	------	------	100
Sensitivity	58	57	57	57	57

[a] Relative intensities are corrected for the C^{13} isotope and for isotopic impurities listed in table 1.

The contribution of H_2^+ to the mass 2 peak of CH_3D and CH_2D_2 has been computed differently. It is assumed that the relative abundances of H_2^+ and HD^+ are in the same ratio as the probabilities of removing 2H and H+D from the molecules. There should be a D_2^+ ion from CH_2D_2, which is not observed, but the predicted intensity is 0.014 percent, which is at the threshold for observation. Computed abundances for H_2 and D_2 in table 3 are enclosed in parentheses.

Table 3 includes under P the a priori probabilities for the distribution of H and D in the fragment

ions. The observed abundance ratios are quite different from the a priori probability ratios and the abundance of each fragment ion can be expressed in terms of the a priori probability times a weighting factor. Table 4 gives the weighting factors for each ion with the notation that a_1 is the factor for removing one H atom, a_2 for two atoms, etc., and b is the factor for D atoms. The table includes for comparison the published values for these weighting factors.

TABLE 3. *Ion abundances in methanes and a priori probabilities*

Ion	CH_4	CH_3D	P[a]	CH_2D_2	P[a]	CHD_3	P[a]	CD_4
H	5.40	4.82	3/4	3.04	1/2	1.92	1/4	----
D	----	0.69	1/2	1.35	1/2	2.64	3/4	3.86
H_2	0.42	(.26)	1/2	(0.12)	1/6	----	----	----
HD	----	.13	1/2	.18	2/3	0.16	1/2	----
D_2	----	----	----	(.014)	1/6	.13	1/2	0.28
C	3.54	3.41	--	3.36	--	3.37	--	3.18
CH	9.86	5.98	3/4	3.35	1/2	1.52	1/4	----
CD	----	4.02	1/4	6.73	1/2	7.89	3/4	7.33
CH^2	19.4	6.48	1/2	0.91	1/6	----	----	----
CHD	----	13.2	1/2	11.3	2/3	5.84	1/2	----
CD_2	----	----	----	7.63	1/6	10.7	1/2	13.7
CH_3	89.3	10.6	1/4	----	----	----	----	----
CH_2D	----	79.8	3/4	25.7	1/2	----	----	----
CHD_2	----	----	----	65.7	1/2	51.9	3/4	----
CD_3	----	----	----	----	----	43.5	1/4	86.5

[a] P is a priori probability for distribution of H and D in fragment ions.

TABLE 4. *Isotope weighting factors for deuteromethanes*

Ion	CH_3D	CH_2D_2	CHD_3
H	$a_1=1.17$	$a_1=1.39=1.18^2$	$a_1=1.68=1.19^3$
D	$b_1=0.50=1.19^{-4}$	$b_1=0.616=1.17^{-3}$	$b_1=0.77=1.14^{-2}$
CH	$(a_2b_1=0.798=1.12^{-2})$	$(a_1b_1=0.665=1.12^{-4})$	$(b_1=0.65=1.05^{-6})$
CD	$a_2=1.61=1.17^3$	$(a_2b_1=1.336)$	$(a_1b_2=1.12)$
CH_2	$a_1b_1=0.66=1.16^{-4}$	$(b_2=0.275=1.24^{-6})$	
CHD	$a_2=1.34=1.16^2$	$a_1b_1=0.86=1.16^{-1}$	$(b_2=0.706)$
CD_2		$a_2=2.30=1.23^3$	$(a_1b_1=1.29)$
CH_3	$b_1=0.47=1.21^{-4}$		
CH_2D	$a_1=1.18$	$b_1=0.562=1.21^{-3}$	
CHD_2		$a_1=1.44=1.20^2$	$b_1=0.726=1.18^{-2}$
CD_3			$a_1=1.82=1.22^3$
Ref. 1	$b_1=0.45=1.22^{-4}$	$b_1=0.57=1.21^{-3}$	$(b_1=0.87)$
	$a_1=1.18$	$a_1=1.43=1.20^2$	$(a_1=1.41)$
Ref. 2	$b_1=0.55=1.16^{-4}$	$b_1=0.65=1.14^{-3}$	$b_1=0.76=1.15^{-2}$
	$a_1=1.23$	$a_1=1.48=1.22^2$	$a_1=1.80=1.22^3$

4. Discussion

In a paper by Dibeler, Mohler, and de Hemptinne on the deuteroethylenes [6] it was shown that all the "weighting factors" could be expressed as positive and negative integral powers of one constant. In the present notation, the constant was a_1 of $C_2H_3D=1.10$. In table 4 many of the "weighting factors" have been expressed as powers of numbers, using the power law that applied for ethylene. Results show that this power law does not account for all weighting factors in the methanes. It is a rough approximation for some but not all of the weighting factors. Thus a_1 for CH_3D, CH_2D_2, and CHD_3 is 1.18, 1.20^2, and 1.22^3, whereas b_1 is 1.21^{-4}, 1.21^{-3}, and 1.18^{-2}. For weighting factors of H^+ and D^+, a_1 is 1.17, 1.18^2, and 1.19^3 whereas b_1 is 1.19^{-4}, 1.17^{-3}, and 1.14^{-2}. Weighting factors for removing two or three atoms are in some cases roughly consistent with the power law, but in general the agreement is poor. Values enclosed in parentheses do not fit, and values for C^+ and for all of the CD_4 spectrum do not vary in the manner found for C_2^+ of the ethylenes and for the C_2D_4 spectrum.

It is of interest that in the deuteromethanes the weighting factors for H^+ and D^+ are nearly the same as for removing H and D from the molecule ions. An apparent exception is b_1 for D^+ of CHD_3, but this may be an experimental error. Another set of measurements gave $b_1=0.73=1.17^{-2}$. The sensitivities at mass 1 and mass 2 are not expected to be quite the same and are subject to some variation whenever focusing adjustments are changed. The roots of the weighting factors for removing H or D from the molecule ions and for abundance of H^+ and D^+ have a mean value of 1.19 ± 0.01.

Table 4 includes published values of a_1 and b_1 for CH_3D, CH_2D_2, and CHD_3. The values derived in this research are in satisfactory agreement with published values of Dibeler and Mohler [1] for the first two molecules, but the published data for CHD_3 are evidently in error. Values given by Schissler, Thompson, and Turkevich [2] are roughly consistent with the present values for all three molecules.

The mass spectra reported in table 2 should be more reliable than the previously published values because of the good isotopic purity of the molecules. The fact that weighting factors are not all related by a power law can not be explained as experimental uncertainty. Some of the mass spectra have been remeasured and recomputed several times and results have been consistent.

The mean value of the roots of the weighting factors for deuteromethanes 1.19 can be compared with the constants 1.10 for the ethylenes and 1.1 for acetylenes [5]. Schissler, Thompson, and Turkevich [2] report a value of 1.09 for monodeuteromethane. In monodeuterobenzene and monodeuteronaphthalene it was found that the factor is near unity [7]. There is no obvious explanation for weighting factors that differ much from unity as is the case for the deuteromethanes.

5. References

[1] V. H. Dibeler and F. L. Mohler, J. Research NBS **44**, 441 (1950) RP2155.

[2] D. O. Schissler, S. O. Thompson, and J. Turkevich, Discussions Faraday Soc. **10,** 46 (1951).

[3] D. P. Stevenson and C. D. Wagner, J. Am. Chem. Soc. **70,** 5612 (1952).

[4] F. H. Field and J. L. Franklin, Electron impact phenomena, (Academic Press Inc., New York, N. Y. 1957).

[5] A. W. Tickner, W. A. Bryce, and F. P. Lossing, J. Am. Chem. Soc. **73,** 5001 (1951).

[6] V. H. Dibeler, F. L. Mohler, and M. de Hemptinne, J. Research NBS **53,** 107 (1954) RP2522.

[7] F. L. Mohler, V. H. Dibeler, Laura Williamson, and Helen Dean, J. Research NBS **48,** 188 (1952) RP2304.

WASHINGTON, March 25, 1958.

Effect of Strain-Temperature History on the Tensile Behavior of Titanium and a Titanium Alloy[1]

Glenn W. Geil and Nesbit L. Carwile

This study was made to determine the effect of prestraining specimens in tension under uniaxial and multiaxial stresses at a selected temperature on their tensile behavior at a different temperature. Unnotched and notched cylindrical specimens of initially annealed, commercially pure titanium and initially annealed 4-percent-aluminum, 4-percent-manganese, titanium alloy were extended at selected temperatures to various true strains and then extended to fracture at another temperature. The ductility retained by the prestrained specimens decreased with increase in the prestrain, whereas the strength indices generally were nearly independent of the amount of the prestraining. However, strength indices obtained on some of the deep-notched specimens of the alloy at −196° C were decreased by prestraining at +25° C as a direct result of the very low retained ductility of the prestrained specimens.

1. Introduction

The tensile behavior of metals, in general, is affected by their prior thermal and strain-temperature histories. Ripling and Baldwin [1],[2] in reporting on the phenomenon they called "rheotropic embrittlement" of steel, concluded that a large part of the difference between the ductilities of annealed steels at room temperatures and at low temperatures was rheotropic; that is, the ductility at low temperatures could be improved by prestraining at higher temperatures, at which the ductility of the steel was greater. Similar results were obtained by the present authors [2] for ingot iron, hot-rolled or normalized. However, prestraining annealed ingot iron in tension at room temperature decreased the ductility retained by the specimen at low temperatures.

A recent paper [3] summarized the results obtained in an investigation at the National Bureau of Standards on the effects of low temperatures and multiaxial stresses[3] on the tensile behavior of an annealed commercially pure titanium. However, as no information was available on the effects of strain temperature history on the tensile properties of titanium or its alloys, a study of these effects was made on unnotched and notched specimens of the initially annealed titanium and on an initially annealed 4-percent-Al, 4-percent-Mn, titanium alloy. The results of this investigation are summarized in the present paper.

2. Materials and Test Procedures

2.1. Materials

The test specimens were prepared from bars processed from a single heat of commercially pure titanium (American Society for Testing Materials Designation B265–52T, grade 2) or a single heat of the titanium alloy. The bars were supplied in the form of 1-in. and ¾-in. rounds in the hot-rolled and annealed condition. The chemical compositions, other than titanium, of these materials were as follows:

Element	Titanium (commercially pure)	Alloy (4% Al, 4% Mn)
	%	%
Aluminum	VW	4. 2
Calcium	ND	VW
Carbon	0. 04	<0. 1
Chromium	W	W
Copper	T	VW
Iron	W	M
Magnesium	ND	VW
Manganese	VW	3. 8
Nickel	VW	W
Silicon	0. 02	M
Silver	ND	T
Tin	W	VW
Vanadium	ND	W
Nitrogen	0. 04	0. 02
Oxygen	. 21	
Hydrogen	. 012	0. 006

The numerical values are given in percent by weight. The spectrographic analysis determinations are designated by letters. M denotes moderate (0.1 to 1.0%), W denotes weak (0.01 to 0.1%), VW denotes very weak (0.001 to 0.01%), T denotes a trace (0.0001 to 0.001%) and ND denotes not detected.

Both metals were fine-grained; the titanium had a grain size corresponding to American Society for Testing Materials (ASTM) No. 9 and the alloy had a grain size finer than that corresponding to ASTM No. 10. These materials were tested in the as-received condition (hot-rolled and annealed by the producers).

[1] This investigation was partially supported by the Materials Laboratory, Directorate of Research, Wright Air Development Center, U. S. A. F., and some of the results were incorporated in WADC Technical Report 56-402 (ASTIA Document No. AD-110 436).

[2] Figures in brackets indicate the literature references at the end of this paper.

[3] The stress system was varied by changes in the depth of circumferential 60° V-notches in specimens of circular cross section.

2.2. Specimens

The specimens were of circular cross section. The unnotched specimens had a 2-in. reduced section that was gradually tapered from each end; the diameter at the midsection (0.400 in.) was about 0.003 in. less than that at the ends. The notched specimens were machined with a circumferential V-notch of 60° angle having a root radius of 0.05 in. and a constant minimum diameter of 0.35 in. at the root of the notch. The notch depth was changed by varying the diameter of the cylindrical portion of the specimen adjacent to the notch. A detailed description of the specimens is given in a previous paper [3].

2.3. Test Procedures

A detailed description of the test equipment and the method of maintaining the selected temperature is given in previous publications [2, 4, and 5]. The tension tests were made in a pendulum hydraulic testing machine on notched and unnotched specimens at a temperature of +100°, +25°, or −196°C or at a combination of two of these temperatures. The specimens were extended slowly with the deformation rate maintained at about 0.5 to 1.0 percent contraction in area per minute during the deformation beyond initial yielding. The specimens, except those tested at +25° C, were extended while completely immersed in an appropriate bath maintained at the selected temperature. Simultaneous load and diameter measurements (minimum diameter of unnotched specimens, diameter at the base of the notch in the notched specimens) were made throughout each test.

In the normal (single-stage) tension test the specimens were extended to fracture at a selected temperature. Two-stage tension tests were employed to study the effect of prestraining; the specimens were extended at a constant temperature to selected strains and then extended to fracture at a different temperature. Three series of the two-stage tension tests were made. In two series, the specimens were extended in tension at +25° C to selected strains, then the loads were quickly reduced to 200 lb and maintained at this level until the start of the second stage of the tests about 30 min later. In the second stage, these specimens were extended in tension to fracture at −196° or +100° C, respectively. During the interval between the two stages of the test, each specimen was maintained at the temperature selected for the second stage. In the other series of two-stage tests, the specimens were extended in tension at −196° C to selected strains, removed from the testing machine, and placed in a liquid nitrogen bath. The testing machine and equipment were brought to a temperature equilibrium at +25° C (requiring a period of approximately 30 min). The specimens were then removed from the low temperature bath, warmed in water to +25° C, quickly installed in the testing machine, and extended to fracture in the second stage of the test at +25° C.

3. Results and Discussion

3.1. Effect of Prestraining Specimens at +25° C on Their Tensile Properties at −196° C

The results of single-stage tests at −196° C and two-stage tests at +25° and −196° C, respectively, on unnotched and notched specimens of the initially annealed titanium and titanium alloy are summarized in table 1.

a. True Stress Versus True Strain Curves

The true stress [4] versus true strain [5] curves for the unnotched specimens are shown in figures 1 and 2 and those for notched specimens with notch depths [6]

[4] True stress was determined by dividing the current load by the current minimum cross-sectional area of the specimen.

[5] True strain is expressed as the natural logarithm of the ratio of the original minimum cross-sectional area of the specimen, A_o, to the current minimum cross-sectional area, A.

[6] Notch depth is expressed as the percent of cross-sectional area removed in machining the notch in the specimen.

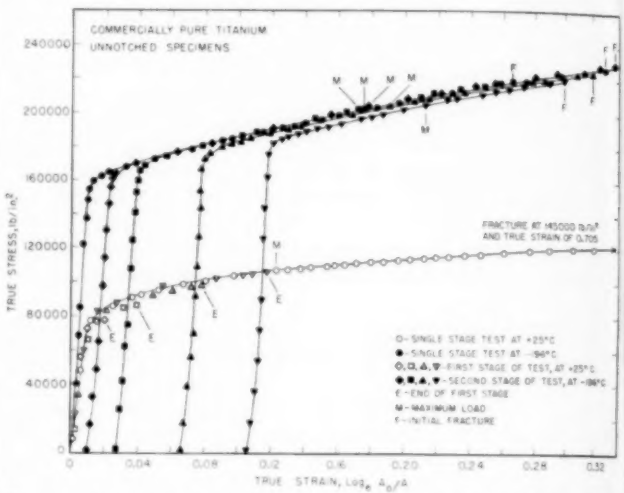

FIGURE 1. *True stress-true strain relations obtained in single- and two-stage tension tests at +25° and −196° C on unnotched specimens of initially annealed commercially pure titanium.*

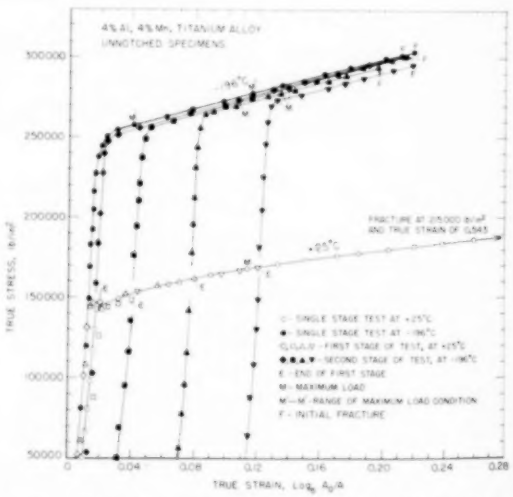

FIGURE 2. *True stress-true strain relations obtained in single- and two-stage tension tests at +25° and −196° C on unnotched specimens of initially annealed 4-percent-Al, 4-percent-Mn titanium alloy.*

TABLE 1. *Tensile properties of unnotched and notched (60° notch angle, 0.05 in. root radius) specimens tested in single stage at −196° C and in two stages at +25° and −196° C, respectively*

Notch depth	D [a]	d [b]	Stress concentration factor, K_t	Triaxiality,[c] S_t/S_l	First stage of test, +25° C		Second stage of test, −196° C							Reduction of area	Elongation [f] in 2 in.
					True strain [d] at end of stage	True stress at end of stage	Tensile [e] strength or notch strength	True stress		Total true strain [d]		Retained true strain			
								at maximum load	at initial fracture	at maximum load	at initial fracture	at maximum load	at initial fracture		
Commercially pure titanium															
						*lb/in.*²	*lb/in.*²	*lb/in.*²	*lb/in.*²					%	%
%	*in.*	*in.*													
0 [g]	-----	0.400	1.00	0.00	0	0	169,000	200,000	228,000	0.167	0.330	0.167	0.330	30	21
0	-----	.400	1.00	.00	.020	77,000	170,000	203,000	229,000	.178	.336	.158	.316	30	18
0	-----	.400	1.00	.00	.039	86,000	170,000	203,000	218,000	.177	.266	.138	.227	22	18
0	-----	.400	1.00	.00	.078	97,000	168,000	203,000	223,000	.191	.321	.113	.243	28	17
0	-----	.400	1.00	.00	.118	106,000	165,000	204,000	219,000	.212	.300	.094	.182	25	17
0	-----	.400	1.00	.00											
10	0.370	.350	1.7	.08	0	0	183,000	(h)	199,000	-----	.081	-----	.081	8	----
10	.370	.350	1.7	.08	.020	85,000	181,000	(h)	198,000	-----	.087	-----	.067	8	----
10	.370	.350	1.7	.08	.040	96,000	181,000	(h)	199,000	-----	.093	-----	.053	9	----
10	.370	.350	1.7	.08	.080	103,000	181,000	(h)	207,000	-----	.132	-----	.052	13	----
10	.370	.350	1.7	.08	.111	113,000	180,000	(h)	209,000	-----	.144	-----	.033	14	----
10	.370	.350	1.7	.08											
30	.418	.350	1.9	.23	0	0	213,000	(h)	221,000	-----	.039	-----	.039	5	----
30	.418	.350	1.9	.23	.020	100,000	213,000	(h)	224,000	-----	.049	-----	.029	5	----
30	.418	.350	1.9	.23	.041	116,000	215,000	(h)	230,000	-----	.064	-----	.023	7	----
30	.418	.350	1.9	.23	.080	123,000	212,000	(h)	237,000	-----	.110	-----	.030	10	----
30	.418	.350	1.9	.23	.121	133,000	209,000	(h)	239,000	-----	.134	-----	.013	13	----
30	.418	.350	1.9	.23											
50 [g]	.495	.350	2.0	.33	0	0	246,000	(h)	259,000	-----	.054	-----	.054	5	----
50	.495	.350	2.0	.33	.021	115,000	244,000	(h)	257,000	-----	.049	-----	.028	5	----
50	.495	.350	2.0	.33	.041	135,000	247,000	(h)	266,000	-----	.071	-----	.030	8	----
50	.495	.350	2.0	.33	.080	149,000	244,000	(h)	272,000	-----	.106	-----	.026	11	----
50	.495	.350	2.0	.33	.121	160,000	240,000	(h)	279,000	-----	.145	-----	.024	14	----
50	.495	.350	2.0	.33											
70	.639	.350	2.1	.39	0	0	258,000	(h)	270,000	-----	.046	-----	.046	5	----
70	.639	.350	2.1	.39	.022	128,000	253,000	(h)	267,000	-----	.047	-----	.025	5	----
70	.639	.350	2.1	.39	.041	137,000	256,000	(h)	273,000	-----	.060	-----	.019	5	----
70	.639	.350	2.1	.39	.080	167,000	258,000	(h)	286,000	-----	.098	-----	.018	10	----
70	.639	.350	2.1	.39	.082	168,000	262,000	(h)	291,000	-----	.102	-----	.020	10	----
70	.639	.350	2.1	.39	.120	177,000	253,000	(h)	293,000	-----	.142	-----	.022	13	----
70	.639	.350	2.1	.39											
87 [g]	.990	.350	2.1	.41	0	0	257,000	(h)	265,000	-----	.034	-----	.034	4	----
4-percent-Al, 4-percent-Mn, titanium alloy															
0 [g]	-----	0.400	1.0	0.00	0	0	246,000	278,000	298,000	0.122	0.213	0.122	0.213	19	7
0	-----	.400	1.0	.00	.021	145,000	246,000	279,000	292,000	.129	.173	.108	.152	16	----
0	-----	.400	1.0	.00	.020	146,000	246,000	274,000	308,000	.112	.251	.092	.231	22	8
0	-----	.400	1.0	.00	.040	148,000	245,000	281,000	300,000	.130	.214	.090	.174	18	8
0	-----	.400	1.0	.00	.080	162,000	243,000	278,000	294,000	.134	.196	.054	.116	17	9
0	-----	.400	1.0	.00	.120	169,000	240,000	274,000	295,000	.132	.219	.012	.099	18	11
0	-----	.400	1.0	.00											
10	.370	.350	1.7	.08	0	0	268,000	(h)	288,000	-----	.070	-----	.070	8	----
10	.370	.350	1.7	.08	.020	158,000	266,000	(h)	288,000	-----	.076	-----	.056	9	----
10	.370	.350	1.7	.08	.039	159,000	264,000	(h)	288,000	-----	.084	-----	.045	7	----
10	.370	.350	1.7	.08	.058	168,000	263,000	(h)	283,000	-----	.077	-----	.019	9	----
10	.370	.350	1.7	.08	.078	173,000	261,000	(h)	286,000	-----	.088	-----	.010	9	----
10	.370	.350	1.7	.08											
30	.418	.350	1.9	.23	0	0	307,000	(h)	317,000	-----	.032	-----	.032	4	----
30	.418	.350	1.9	.23	.020	181,000	307,000	(h)	320,000	-----	.038	-----	.018	4	----
30	.418	.350	1.9	.23	.043	195,000	304,000	(h)	323,000	-----	.057	-----	.014	5	----
30	.418	.350	1.9	.23	.060	211,000	300,000	(h)	322,000	-----	.067	-----	.007	5	----
30	.418	.350	1.9	.23	.079	206,000	277,000	(h)	302,000	-----	.083	-----	.004	9	----
30	.418	.350	1.9	.23											
50 [g]	.495	.350	2.0	.33	0	0	325,000	(h)	334,000	-----	.026	-----	.026	3	----
50	.495	.350	2.0	.33	.021	200,000	331,000	(h)	342,000	-----	.033	-----	.012	4	----
50	.495	.350	2.0	.33	.040	223,000	337,000	(h)	354,000	-----	.049	-----	.009	5	----
50	.495	.350	2.0	.33	.062	238,000	317,000	(h)	339,000	-----	.064	-----	.002	6	----
50	.495	.350	2.0	.33	.081	251,000	207,000	(h)	225,000	-----	.081	-----	.000	7	----
50	.495	.350	2.0	.33											
70	.639	.350	2.1	.39	0	0	337,000	(h)	345,000	-----	.024	-----	.024	3	----
70	.639	.350	2.1	.39	.019	202,000	336,000	(h)	346,000	-----	.026	-----	.007	4	----
70	.639	.350	2.1	.39	.040	239,000	318,000	(h)	331,000	-----	.038	-----	.000	4	----
70	.639	.350	2.1	.39	.059	255,000	311,000	(h)	331,000	-----	.060	-----	.001	5	----
70	.639	.350	2.1	.39	.080	271,000	276,000	(h)	276,000	-----	.079	-----	.000	6	----
70	.639	.350	2.1	.39											
87	.990	.350	2.1	.41	0	0	337,000	(h)	341,000	-----	.012	-----	.012	3	----

[a] Diameter of cylindrical portion of the specimen adjacent to the notch.
[b] Minimum diameter of unnotched specimen or diameter of notched specimen at the base of the notch.
[c] Triaxiality is determined as the ratio of transverse stress to longitudinal stress and is based on the method of Sachs and Lubahn, Trans. ASME **67**, [A] 240 (1945).
[d] Includes elastic and plastic deformation.
[e] Determined by dividing the highest load attained at −196° C by the original minimum cross-sectional area.
[f] Measurements based on punch marks in fillets. Specimens had a reduced section of 2.0 in. length.
[g] Tensile values are the average for 2 or more specimens.
[h] Fractured before the slope of the load-extension curve became zero.

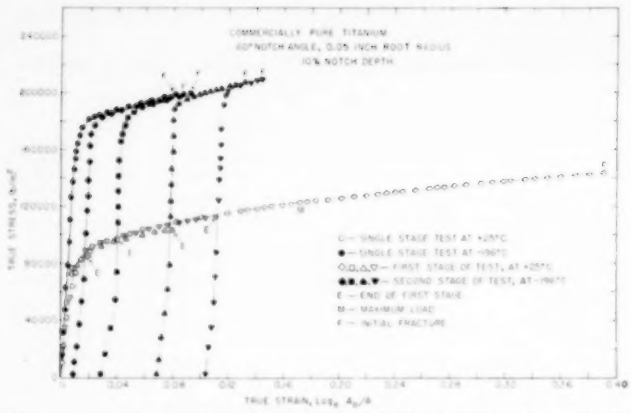
COMMERCIALLY PURE TITANIUM
60° NOTCH ANGLE, 0.05 INCH ROOT RADIUS
10% NOTCH DEPTH
TRUE STRESS, lb/in²
TRUE STRAIN, Log$_e$ A$_o$/A
○ – SINGLE STAGE TEST AT +25°C
● – SINGLE STAGE TEST AT –196°C
○,○,△,▽ – FIRST STAGE OF TEST, AT +25°C
●,●,▲,▼ – SECOND STAGE OF TEST, AT –196°C
E – END OF FIRST STAGE
M – MAXIMUM LOAD
F – INITIAL FRACTURE

FIGURE 3. *True stress-true strain relations obtained in single- and two-stage tension tests at +25° and −196° C on notched specimens (10% notch depth) of the titanium.*

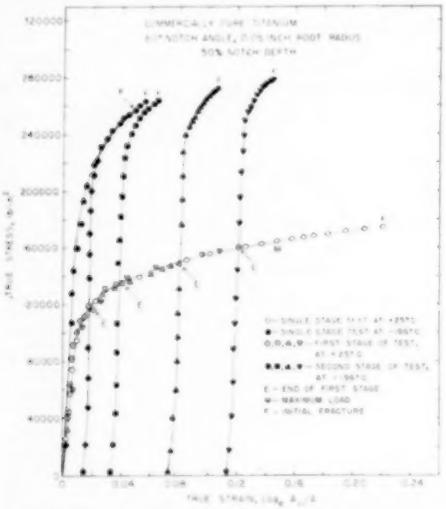
COMMERCIALLY PURE TITANIUM
60° NOTCH ANGLE, 0.05 INCH ROOT RADIUS
50% NOTCH DEPTH
TRUE STRESS, lb/in²
TRUE STRAIN, Log$_e$ A$_o$/A
○ – SINGLE STAGE TEST AT +25°C
● – SINGLE STAGE TEST AT –196°C
○,○,△,▽ – FIRST STAGE OF TEST, AT +25°C
●,●,▲,▼ – SECOND STAGE OF TEST, AT –196°C
E – END OF FIRST STAGE
M – MAXIMUM LOAD
F – INITIAL FRACTURE

FIGURE 4. *True stress-true strain relations obtained in single- and two-stage tension tests at +25° and −196° C on notched specimens (50% notch depth) of the titanium.*

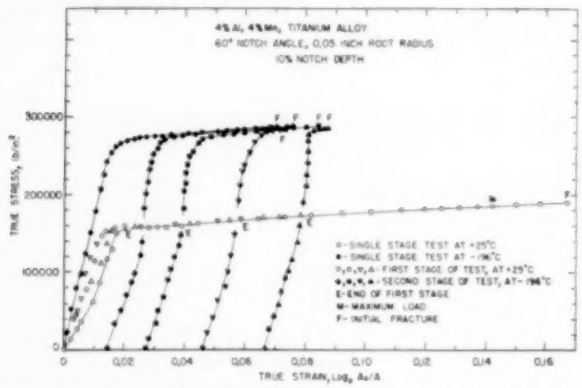
4% Al, 4% Mn, TITANIUM ALLOY
60° NOTCH ANGLE, 0.05 INCH ROOT RADIUS
10% NOTCH DEPTH
TRUE STRESS, lb/in²
TRUE STRAIN, Log$_e$ A$_o$/A
○ – SINGLE STAGE TEST AT +25°C
● – SINGLE STAGE TEST AT –196°C
○,○,○,△ – FIRST STAGE OF TEST, AT +25°C
●,●,●,▲ – SECOND STAGE OF TEST, AT –196°C
E – END OF FIRST STAGE
M – MAXIMUM LOAD
F – INITIAL FRACTURE

FIGURE 5. *True stress-true strain relations obtained in single- and two-stage tension tests at +25° and −196° C on notched specimens (10% notch depth) of the alloy.*

of 10 and 50 percent are shown in figures 3 to 6. For brevity, the true stress-true strain curves for the two-stage tests on specimens with notch depths of 30 and 70 percent are not shown; the forms of these curves were generally similar to those for the specimens with a notch depth of 50 percent.

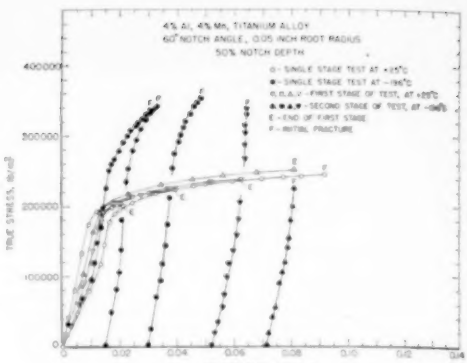
4% Al, 4% Mn, TITANIUM ALLOY
60° NOTCH ANGLE, 0.05 INCH ROOT RADIUS
50% NOTCH DEPTH
TRUE STRESS, lb/in²
TRUE STRAIN, Log$_e$ A$_o$/A
○ – SINGLE STAGE TEST AT +25°C
● – SINGLE STAGE TEST AT –196°C
○,○,△,▽ – FIRST STAGE OF TEST, AT +25°C
●,●,▲,▼ – SECOND STAGE OF TEST, AT –196°C
E – END OF FIRST STAGE
F – INITIAL FRACTURE

FIGURE 6. *True stress-true strain relations obtained in single- and two-stage tension tests at +25° and −196° C on notched specimens (50% notch depth) of the alloy.*

The portion of the true stress-true strain curves (figs. 1 and 2) for the second stage of the tests with the unnotched specimens of each material at −196° C lie near or only slightly below those representing single-stage tests of the same material at −196° C; the lowering of the curves, in general, tends to increase with increase in the prestrain of the specimens at +25° C. A similar trend is indicated in the curves for the notched specimens with a depth of 10 percent (figs. 3 and 5). The ductility of the notched specimens with depths of 30 percent or greater was insufficient at −196° C to make this comparison of the curves. These true stress-true strain data indicate that the total work hardening (strain hardening and strain aging or recovery) during the prestraining of specimens at +25° C is nearly the same as the total work hardening (mainly strain hardening) of corresponding specimens extended to the same strains at −196° C. If any strain aging occurred during the interval of approximately 30 min between the two stages of these tests, it was limited to a very small value as the specimens were maintained at −196° C during this interval.

b. Strength at −196° C

The effects of prestraining unnotched and notched specimens to true strains up to 0.08 or 0.12 at +25° C on their strength indices at −196° C are shown in figures 7 and 8. At −196° C, the tensile strength,[7] true stress at maximum load, and true stress at initial fracture [8] of the unnotched specimens of each material were nearly independent of the prestraining at +25° C.

The data obtained in the two-stage tests on the notched specimens exhibit a general trend of an independence of the strength indices at −196° C on the prestraining at +25° C. This trend was observed for all of the notched specimens of the commercially pure titanium (fig. 7) and for the alloy specimens with a notch depth of 10 percent (fig. 8). However, a relatively large decrease was observed

[7] Tensile- and notch-strength values obtained for a specimen in the second stage of the test are based on the minimum cross-sectional area of the specimen prior to the prestraining.

[8] Initial fracture, as used in this paper, designates the beginning of the very rapid propagation of the main fracture crack across the specimen. The true stress and true strain values at initial fracture are based on diameter measurements made immediately preceding the fracture.

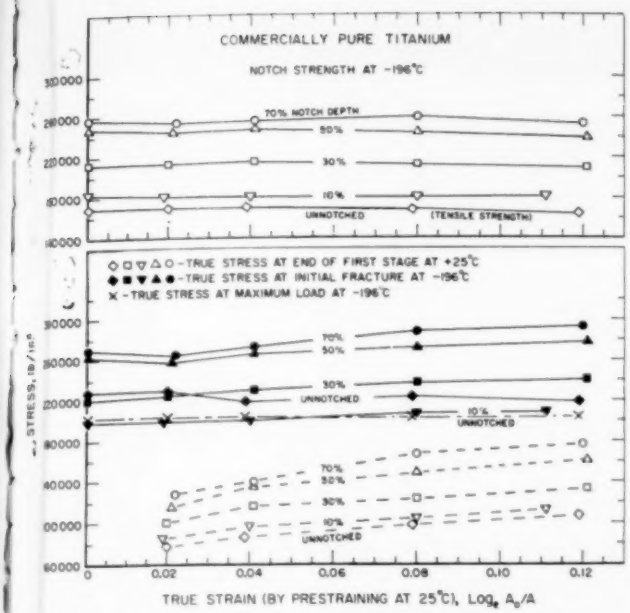

FIGURE 7. *Effect of prestraining in tension at +25° C on the strength at −196° C of unnotched and notched specimens of the titanium.*

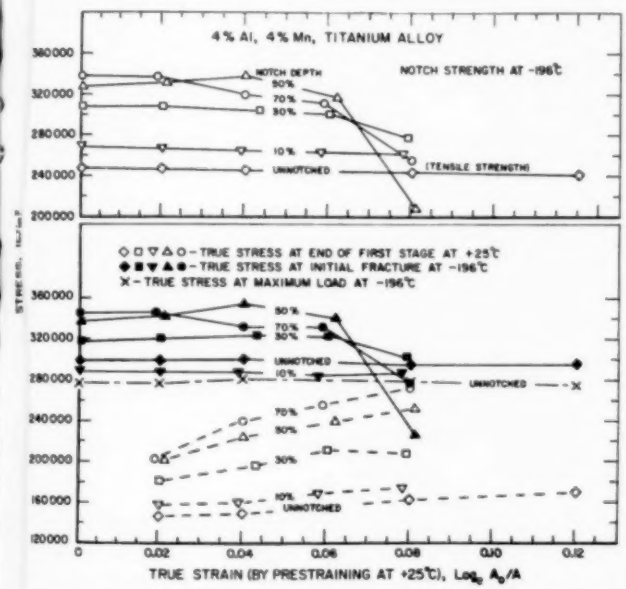

FIGURE 8. *Effect of prestraining in tension at +25° C on the strength at −196° C of unnotched and notched specimens of the alloy.*

in the values of notch strength (see footnote 7) and true stress at initial fracture of the alloy specimens with 30-, 50-, and 70-percent notch depths that were prestrained to a true strain of 0.08. This decrease can be attributed directly to the low ductility of these specimens in the second stage of the test at −196° C; these specimens fractured during the loading in the elastic deformation range.

The ductility of all the notched specimens at −196° C was quite limited as evidenced by the fractures that occurred while the loads were increasing; i. e., before normal maximum load conditions [9] were attained. However, in the limited sense that the loads at fracture were the highest loads on the specimens at −196° C, the values of the true stresses at initial fracture may also be considered as true stresses at maximum load.

c. Ductility

The effects of prestraining unnotched and notched specimens of the titanium and the alloy to selected true strains up to 0.08 or 0.12 at +25° C on their ductility at −196° C are summarized in figures 9 and 10. The "total true strain" values reported for the second stage of the test at −196° C include the true strain at the end of the first stage of the test at +25° C. The "retained true strain" values include only the additional true strain during the second stage of the test.

The total true strain at maximum load of unnotched specimens at −196° C increased slightly with increase in prestrain of the titanium, especially in the range 0.04 to 0.12 (fig. 9), whereas it was nearly constant and independent of the prestrain for the alloy (fig. 10). The retained true strains at maximum load of the unnotched specimens of both metals at −196° C decreased with increase in the prestrain by an amount approximately equal to (alloy specimens) or slighly less than (titanium specimens) the prestrain.

The total true strain at initial fracture of the unnotched specimens of both metals at −196° C was nearly independent of the prestrain at +25° C and thus the retained true strains at initial fracture of these specimens were decreased by an amount approximately equal to the prestrain.

The unnotched specimen of titanium that was prestrained at 25° C to a true strain of 0.039 broke apparently prematurely in the second stage of the test at −196° C; the fracture occurred in the shoulder portion of the necked section and not at the minimum cross-sectional area. Thus, the value obtained for the total true strain at initial fracture (table 1) was not truly representative for this degree of prestrain and it is not included in the plotted points of figure 9. Moreover, the value obtained for the true stress at initial fracture of this specimen (fig. 7) is slightly low due to the premature fracture.

As mentioned previously, the notched specimens did not retain sufficient ductility at −196° C to attain a normal maximum load condition. The true strains at initial fracture of the notched specimens that were extended in single-stage tension tests at −196° C were also very small, especially for specimens with a notch depth of 30 percent or greater.

Prestraining in tension at +25° C generally increased the total true strain at initial fracture of

[9] In this paper a normal maximum load condition is considered as that condition at which the slope of the load-extension curve becomes zero beyond the region of yielding.

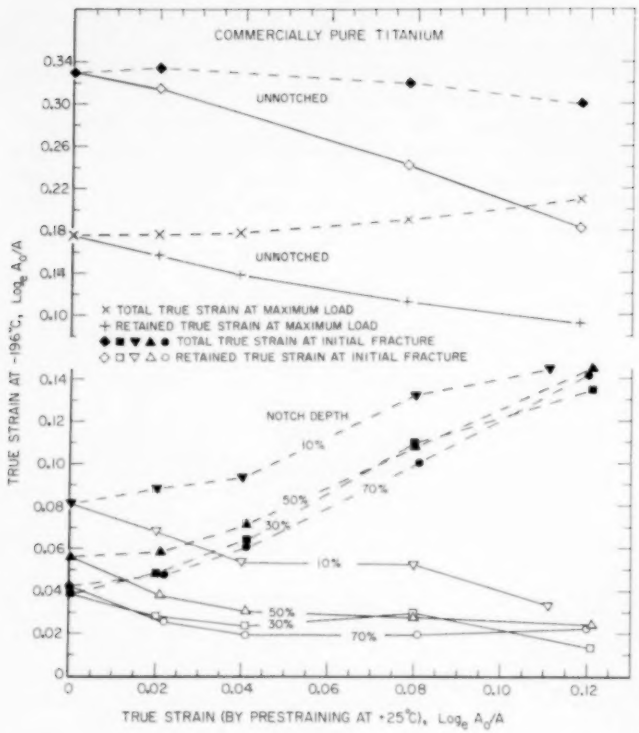

FIGURE 9. *Effect of prestraining in tension at +25° C on the ductility at −196° C of unnotched and notched specimens of titanium.*

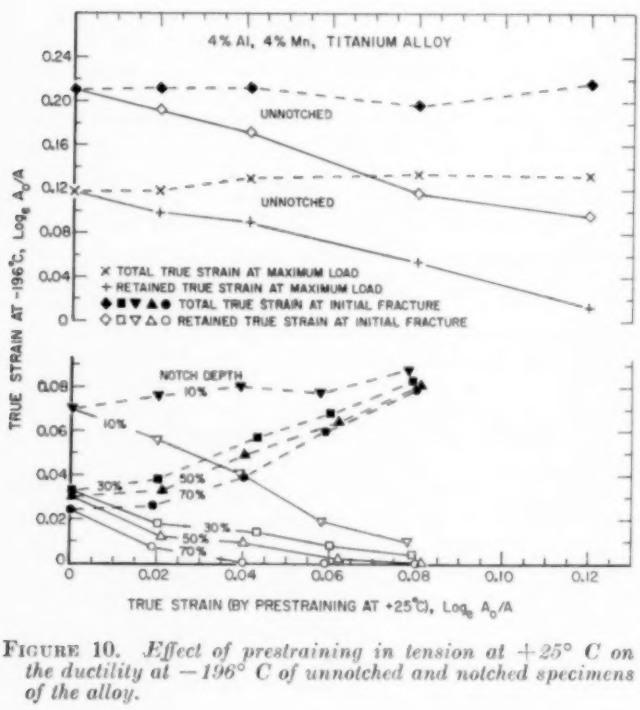

FIGURE 10. *Effect of prestraining in tension at +25° C on the ductility at −196° C of unnotched and notched specimens of the alloy.*

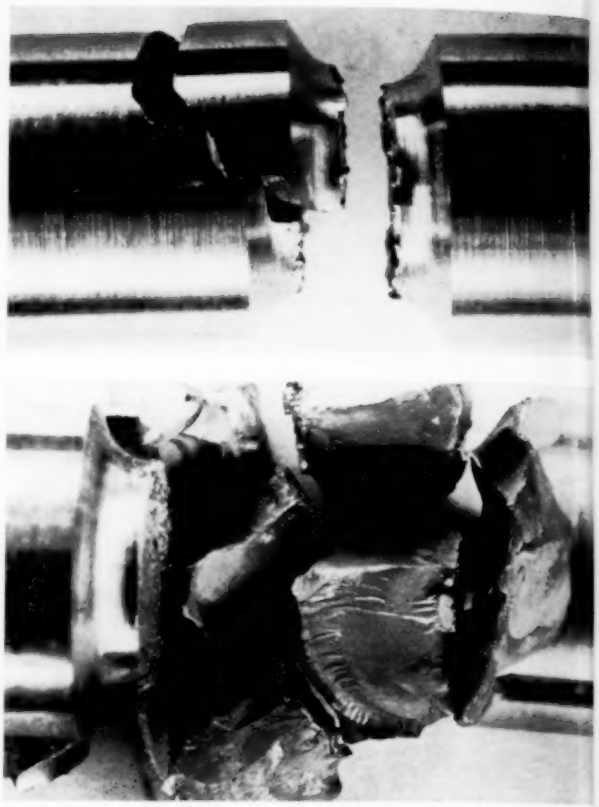

FIGURE 11. *Photographs of notched specimens of 4-percent-Al, 4-percent-Mn, titanium alloy that were fractured at −196° C.*

× 3½ Top: Prestrained to a true strain of 0.04 at +25° C. Bottom: Prestrained to a true strain of 0.06 at +25° C.

the notched specimens at −196° C. A major portion of this increase can be attributed directly to the prestrain. It follows, therefore, that the retained true strains at initial fracture of the notched specimens at −196° C decreased to very small values with increase in the prestrain at +25° C. Some of the prestrained specimens, particularly the deep-notched alloy, broke in a very brittle manner at −196° C. Two examples of these brittle fractures are shown in figure 11.

The results obtained in this series of two-stage tension tests at +25° and −196° C, respectively, on unnotched and notched specimens indicate that multiaxial stresses and prestrain in tension at +25° C both increase the embrittlement of the annealed titanium and the annealed 4-percent-Al, 4-percent-Mn, titanium alloy at −196° C.

3.2. Effect of Prestraining Specimens at +25° C on Their Tensile Properties at +100° C

The results obtained in two-stage tension tests at +25° and +100° C, respectively, on unnotched and notched specimens of the titanium and titanium alloy are summarized in table 2.

TABLE 2. *Tensile properties of unnotched and notched (60° notch angle, 0.05 in. root radius) specimens tested in single stage at +100° C and in two stages at +25° and +100° C, respectively*

Notch depth	D [a]	d [b]	Stress concentration factor K_t	Triaxiality, [c] S_d/S_t	First stage of test, +25° C: True strain [d] at end of stage	First stage of test, +25° C: True stress at end of stage	Second stage of test, +100° C: Tensile [e] strength or notch strength	Second stage of test, +100° C: True stress: at maximum load	Second stage of test, +100° C: True stress: at initial fracture	Second stage of test, +100° C: Total true strain [d]: at maximum load	Second stage of test, +100° C: Total true strain [d]: at initial fracture	Second stage of test, +100° C: Retained true strain: at maximum load	Second stage of test, +100° C: Retained true strain: at initial fracture	Reduction of area	Elongation [f] in 2 in.
						Commercially pure titanium									
%	*in.*	*in.*				*lb/in.²*	*lb/in.²*	*lb/in.²*	*lb/in.²*					%	%
0	-----	0.400	1.0	0	0	0	75,000	85,000	118,000	0.130	0.785	0.130	0.785	57	41
0[g]	-----	.400	1.0	0	.020	80,000	75,000	87,000	123,000	.153	.807	.133	.787	56	36
0	-----	.400	1.0	0	.040	89,000	75,000	86,000	123,000	.135	.799	.095	.759	56	36
0	-----	.400	1.0	0	.080	99,000	75,000	87,000	125,000	.138	.813	.058	.733	56	36
0	-----	.400	1.0	0	.120	107,000	75,000	88,000	123,000	.164	.805	.044	.685	56	36
10[g]	0.370	.350	1.7	0	0	0	82,000	94,000	122,000	.134	.528	.134	.528	40	----
10	.370	.350	1.7	.08	.020	85,000	81,000	92,000	123,000	.131	.533	.111	.513	40	----
10	.370	.350	1.7	.08	.040	95,000	81,000	93,000	123,000	.144	.543	.104	.503	41	----
10	.370	.350	1.7	.08	.081	106,000	81,000	93,000	120,000	.141	.512	.060	.431	39	----
10	.370	.350	1.7	.08	.122	116,000	81,000	95,000	122,000	.159	.508	.037	.386	39	----
30	.418	.350	1.9	.23	0	0	98,000	116,000	130,000	.173	.363	.173	.363	30	----
30	.418	.350	1.9	.23	.020	103,000	96,000	114,000	132,000	.174	.359	.154	.339	32	----
30	.418	.350	1.9	.23	.039	112,000	96,000	115,000	129,000	.181	.346	.142	.307	30	----
30	.418	.350	1.9	.23	.081	123,000	96,000	116,000	128,000	.191	.346	.110	.265	30	----
30	.418	.350	1.9	.23	.121	135,000	95,000	117,000	131,000	.208	.367	.087	.246	30	----
50[g]	.495	.350	2.0	.33	0	0	108,000	128,000	142,000	.158	.343	.158	.343	29	----
50	.495	.350	2.0	.33	.021	120,000	108,000	128,000	143,000	.166	.330	.145	.309	29	----
50	.495	.350	2.0	.33	.041	132,000	108,000	128,000	141,000	.167	.327	.126	.286	28	----
50	.495	.350	2.0	.33	.082	146,000	110,000	133,000	144,000	.185	.329	.103	.227	28	----
50	.495	.350	2.0	.33	.123	155,000	109,000	134,000	143,000	.205	.305	.082	.182	27	----
70[g]	.639	.350	2.1	.39	0	0	119,000	137,000	154,000	.137	.369	.137	.369	31	----
70	.639	.350	2.1	.39	.021	118,000	119,000	137,000	153,000	.141	.364	.120	.343	31	----
70	.639	.350	2.1	.39	.041	144,000	118,000	136,000	152,000	.142	.372	.101	.331	32	----
70	.639	.350	2.1	.39	.082	166,000	120,000	139,000	153,000	.149	.375	.067	.293	31	----
70	.639	.350	2.1	.39	.123	175,000	119,000	143,000	155,000	.182	.360	.059	.237	29	----
87	.990	.350	2.1	.41	0	0	125,000	143,000	157,000	.135	.318	.135	.318	29	----
87	.990	.350	2.1	.41	.020	123,000	122,000	140,000	156,000	.142	.320	.122	.300	28	----
87	.990	.350	2.1	.41	.040	147,000	122,000	142,000	155,000	.146	.314	.106	.274	28	----
87	.990	.350	2.1	.41	.081	163,000	121,000	141,000	155,000	.150	.317	.069	.236	28	----
87	.990	.350	2.1	.41	.123	182,000	123,000	145,000	154,000	.167	.276	.044	.153	25	----
						4-percent-Al, 4-percent-Mn, titanium alloy									
0	-----	0.400	1.0	0	0	0	137,000	155,000	213,000	0.122	0.645	0.122	0.645	47	15
0	-----	.400	1.0	.00	.020	144,000	137,000	155,000	214,000	.125	.665	.105	.645	49	20
0	-----	.400	1.0	.00	.020	145,000	137,000	156,000	216,000	.126	.674	.106	.654	49	20
0	-----	.400	1.0	.00	.041	152,000	137,000	158,000	213,000	.143	.660	.102	.619	49	19
0	-----	.400	1.0	.00	.040	149,000	137,000	157,000	211,000	.140	.646	.100	.606	48	19
0	-----	.400	1.0	.00	.080	160,000	137,000	156,000	211,000	.127	.640	.047	.560	50	20
0	-----	.400	1.0	.00	.112	166,000	138,000	156,000	212,000	.121	.640	.009	.528	48	20
0	-----	.400	1.0	.00	.121	167,000	139,000	159,000	209,000	.135	.610	.014	.489	46	18
10	0.370	.350	1.7	.08	0	0	153,000	176,000	188,000	.138	.224	.138	.224	23	----
10	.370	.350	1.7	.08	.020	160,000	153,000	174,000	186,000	.130	.205	.110	.185	22	----
10	.370	.350	1.7	.08	.040	165,000	151,000	175,000	183,000	.146	.200	.106	.160	22	----
10	.370	.350	1.7	.08	.061	173,000	151,000	174,000	184,000	.141	.204	.080	.143	21	----
10	.370	.350	1.7	.08	.080	177,000	151,000	174,000	184,000	.141	.215	.061	.135	23	----
30	.418	.350	1.9	.23	0	0	175,000	201,000	204,000	.138	.156	.138	.156	17	----
30	.418	.350	1.9	.23	.020	175,000	174,000	199,000	201,000	.134	.147	.114	.127	16	----
30	.418	.350	1.9	.23	.040	195,000	175,000	197,000	201,000	.119	.144	.079	.104	16	----
30	.418	.350	1.9	.23	.061	198,000	173,000	198,000	199,000	.139	.147	.078	.086	16	----
30	.418	.350	1.9	.23	.082	205,000	173,000	195,000	199,000	.123	.136	.041	.054	15	----
50	.495	.350	2.0	.33	0	0	202,000	227,000	232,000	.118	.147	.118	.147	17	----
50	.495	.350	2.0	.33	.020	202,000	199,000	223,000	229,000	.116	.151	.096	.131	17	----
50	.495	.350	2.0	.33	.021	197,000	203,000	227,000	245,000	.113	.157	.092	.136	16	----
50	.495	.350	2.0	.33	.040	216,000	202,000	227,000	234,000	.116	.156	.076	.116	16	----
50	.495	.350	2.0	.33	.060	233,000	201,000	226,000	230,000	.119	.143	.059	.083	16	----
50	.495	.350	2.0	.33	.080	240,000	201,000	220,000	230,000	.089	.142	.009	.062	16	----
70	.639	.350	2.1	.39	0	0	223,000	247,000	249,000	.104	.114	.104	.114	16	----
70	.639	.350	2.1	.39	.020	205,000	222,000	250,000	255,000	.118	.143	.098	.123	17	----
70	.639	.350	2.1	.39	.040	238,000	223,000	250,000	252,000	.115	.128	.075	.088	15	----
70	.639	.350	2.1	.39	.060	257,000	223,000	248,000	251,000	.105	.126	.045	.066	14	----
70	.639	.350	2.1	.39	.081	265,000	223,000	246,000	252,000	.100	.125	.019	.044	18	----
87	.990	.350	2.1	.41	0	0	226,000	252,000	252,000	.100	.110	.100	.110	14	----

See footnotes to table 1.

a. True Stress Versus True Strain Curves

The true stress-true strain curves for the unnotched specimens are shown in figures 12 and 13 and those for the notched specimens with notch depths of 10 or 50 percent are shown in figures 14 to 17. True stress-true strain curves were also obtained for the two-stage tests on specimens with notch depths of 30 and 70 percent for both metals and also on titanium specimens with a notch depth of 87 percent; these curves are not shown. The portion of the true stress-true strain curves for the second-stage tests at +100° C of the unnotched and notched specimens of both metals approximately coincide with the corresponding portion of the curves representing single-stage tests at +100° C. The total work hardening during the prestraining at +25° C of each of the specimens was approximately equal to the total work hardening of corresponding specimens extended to the same strains at +100° C. Thus, the combined effect of the greater rate of strain hardening and the smaller rate of strain aging at +25° C was apparently equal to that of the smaller rate of strain hardening and the greater rate of strain aging at +100° C.

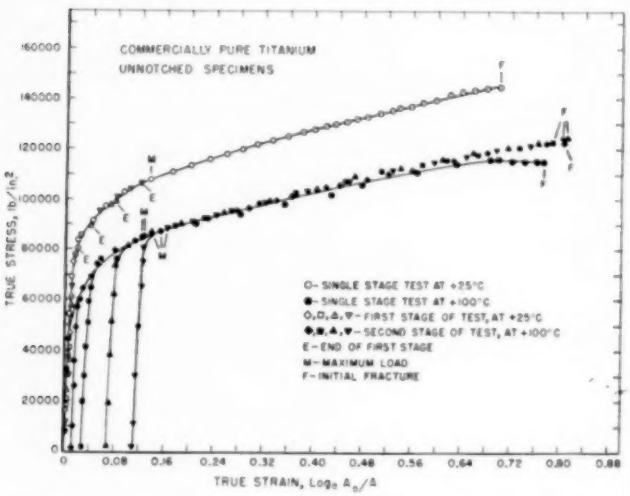
COMMERCIALLY PURE TITANIUM
UNNOTCHED SPECIMENS
TRUE STRESS, lb/in.²
TRUE STRAIN, Log$_e$ A$_o$/A
O- SINGLE STAGE TEST AT +25°C
●- SINGLE STAGE TEST AT +100°C
◇,□,△,▽- FIRST STAGE OF TEST, AT +25°C
◆,■,▲,▼- SECOND STAGE OF TEST, AT +100°C
E- END OF FIRST STAGE
M- MAXIMUM LOAD
F- INITIAL FRACTURE

FIGURE 12. *True stress-true strain relations obtained in single- and two-stage tension tests at +25° and +100° C on unnotched specimens of the titanium.*

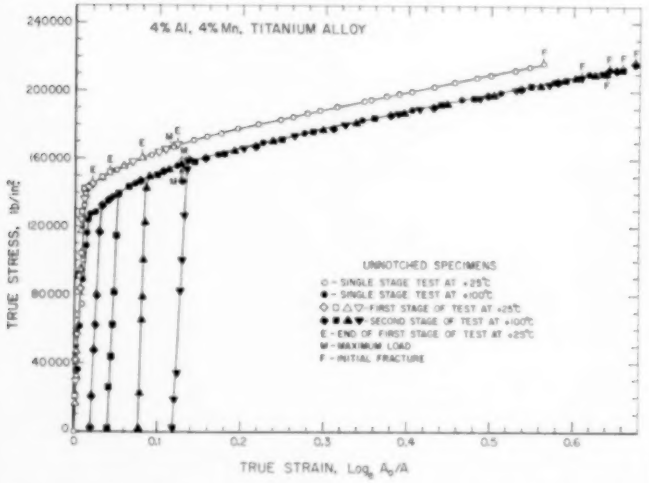
4% Al, 4% Mn, TITANIUM ALLOY
TRUE STRESS, lb/in.²
TRUE STRAIN, Log$_e$ A$_o$/A
UNNOTCHED SPECIMENS
O- SINGLE STAGE TEST AT +25°C
●- SINGLE STAGE TEST AT +100°C
◇,□,△,▽- FIRST STAGE OF TEST AT +25°C
◆,■,▲,▼- SECOND STAGE OF TEST AT +100°C
E- END OF FIRST STAGE OF TEST AT +25°C
M- MAXIMUM LOAD
F- INITIAL FRACTURE

FIGURE 13. *True stress-true strain relations obtained in single- and two-stage tension tests at +25° and +100° C on unnotched specimens of the alloy.*

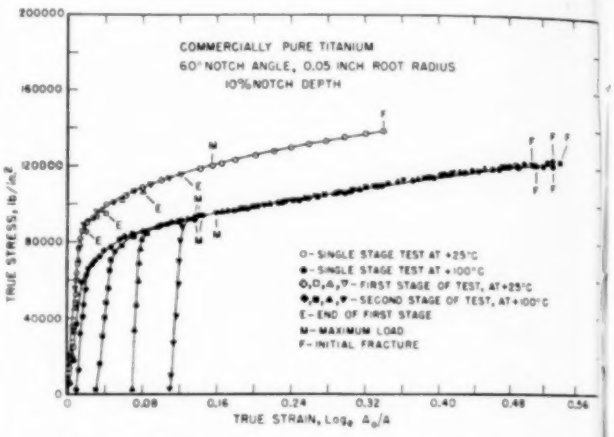
COMMERCIALLY PURE TITANIUM
60° NOTCH ANGLE, 0.05 INCH ROOT RADIUS
10% NOTCH DEPTH
TRUE STRESS, lb/in.²
TRUE STRAIN, Log$_e$ A$_o$/A
O- SINGLE STAGE TEST AT +25°C
●- SINGLE STAGE TEST AT +100°C
◇,□,△,▽- FIRST STAGE OF TEST, AT +25°C
◆,■,▲,▼- SECOND STAGE OF TEST, AT +100°C
E- END OF FIRST STAGE
M- MAXIMUM LOAD
F- INITIAL FRACTURE

FIGURE 14. *True stress-true strain relations obtained in single- and two-stage tension tests at +25° and +100° C on notched specimens (10% notch depth) of the titanium.*

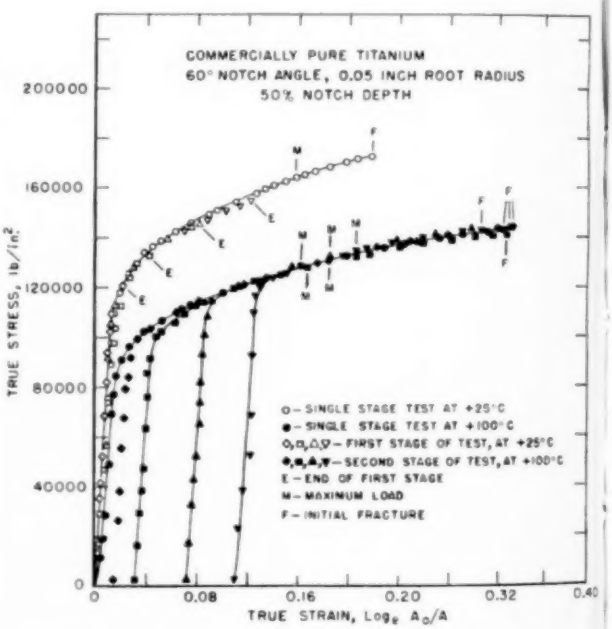
COMMERCIALLY PURE TITANIUM
60° NOTCH ANGLE, 0.05 INCH ROOT RADIUS
50% NOTCH DEPTH
TRUE STRESS, lb/in.²
TRUE STRAIN, Log$_e$ A$_o$/A
O- SINGLE STAGE TEST AT +25°C
●- SINGLE STAGE TEST AT +100°C
◇,□,△,▽- FIRST STAGE OF TEST, AT +25°C
◆,■,▲,▼- SECOND STAGE OF TEST, AT +100°C
E- END OF FIRST STAGE
M- MAXIMUM LOAD
F- INITIAL FRACTURE

FIGURE 15. *True stress-true strain relations obtained in single- and two-stage tension tests at +25° and +100° C on notched specimens (50% notch depth) of the titanium.*

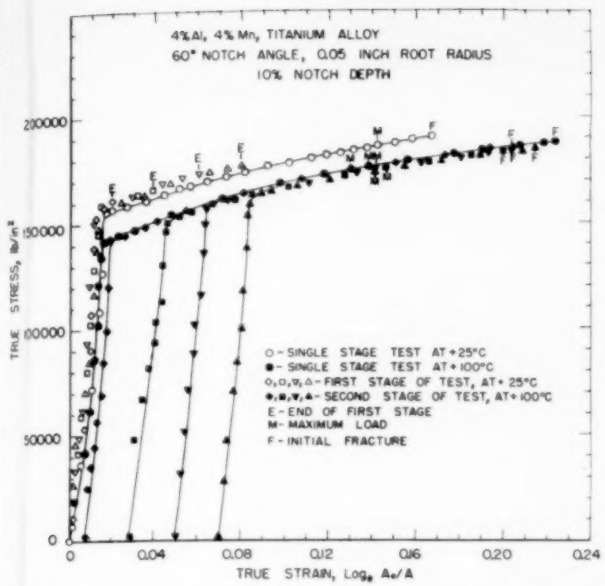
4% Al, 4% Mn, TITANIUM ALLOY
60° NOTCH ANGLE, 0.05 INCH ROOT RADIUS
10% NOTCH DEPTH
TRUE STRESS, lb/in²
TRUE STRAIN, Log$_e$ A$_o$/A
○ - SINGLE STAGE TEST AT +25°C
● - SINGLE STAGE TEST AT +100°C
○,□,▽,△ - FIRST STAGE OF TEST, AT +25°C
◆,■,▼,▲ - SECOND STAGE OF TEST, AT +100°C
E - END OF FIRST STAGE
M - MAXIMUM LOAD
F - INITIAL FRACTURE

FIGURE 16. *True stress-true strain relations obtained in single- and two-stage tension tests at +25° and +100° C on notched specimens (10% notch depth) of the alloy.*

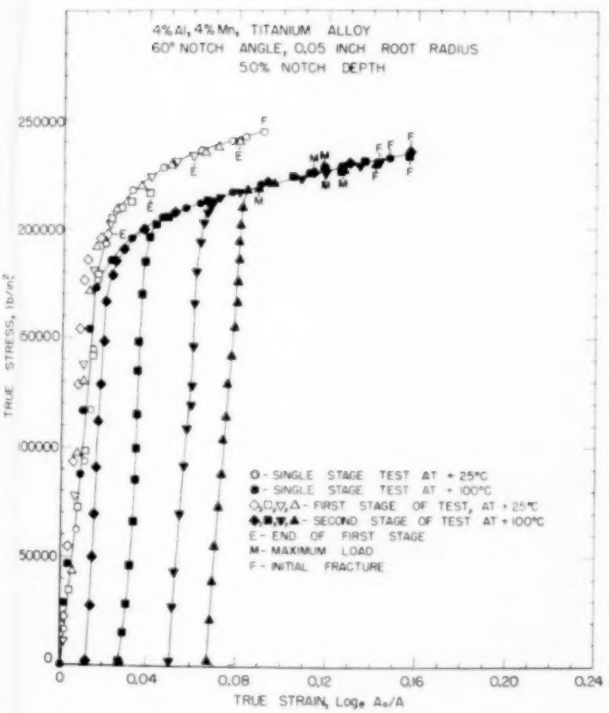
4% Al, 4% Mn, TITANIUM ALLOY
60° NOTCH ANGLE, 0.05 INCH ROOT RADIUS
50% NOTCH DEPTH
TRUE STRESS, lb/in²
TRUE STRAIN, Log$_e$ A$_o$/A
○ - SINGLE STAGE TEST AT +25°C
● - SINGLE STAGE TEST AT +100°C
○,□,▽,△ - FIRST STAGE OF TEST, AT +25°C
◆,■,▼,▲ - SECOND STAGE OF TEST AT +100°C
E - END OF FIRST STAGE
M - MAXIMUM LOAD
F - INITIAL FRACTURE

FIGURE 17. *True stress-true strain relations obtained in single- and two-stage tension tests at +25° and +100° C on notched specimens (50% notch depth) of the alloy.*

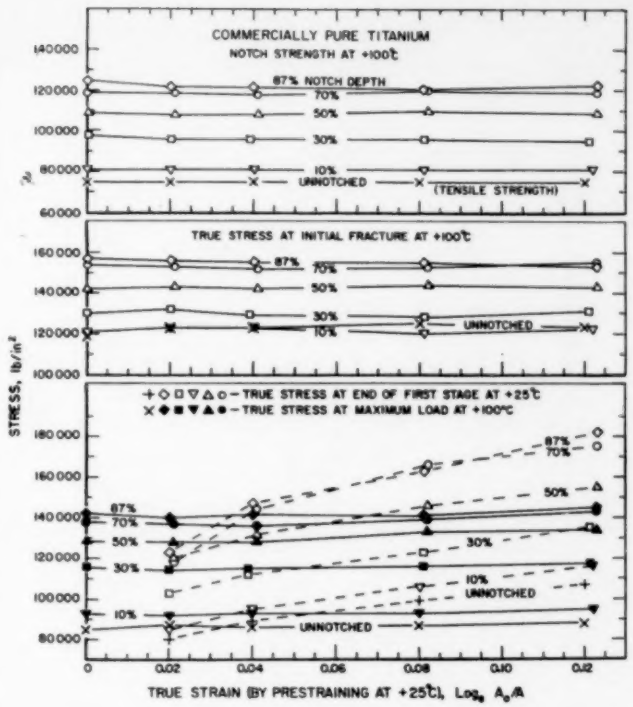

FIGURE 18. *Effect of prestraining in tension at +25° C on the strength at +100° C of unnotched and notched specimens of the titanium.*

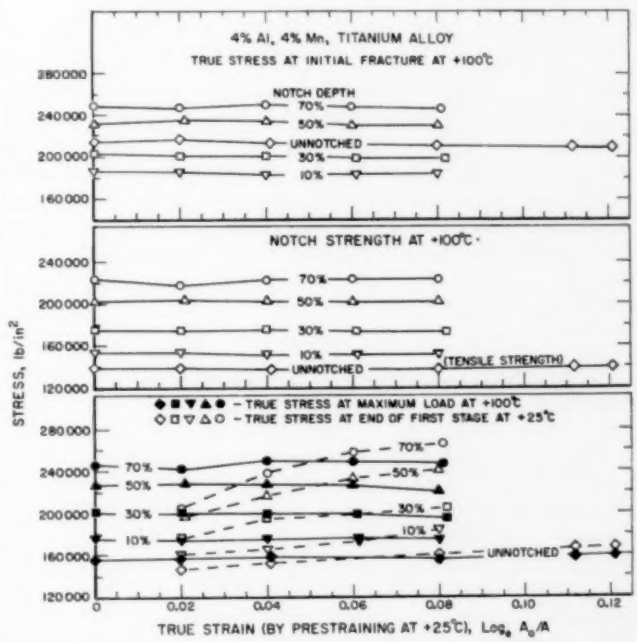
4% Al, 4% Mn, TITANIUM ALLOY
TRUE STRESS AT INITIAL FRACTURE AT +100°C
NOTCH DEPTH
70%
50%
UNNOTCHED
30%
10%
NOTCH STRENGTH AT +100°C
(TENSILE STRENGTH)
◆■▼▲● - TRUE STRESS AT MAXIMUM LOAD AT +100°C
◇□▽△○ - TRUE STRESS AT END OF FIRST STAGE AT +25°C
STRESS, lb/in²
TRUE STRAIN (BY PRESTRAINING AT +25°C), Log$_e$ A$_o$/A

FIGURE 19. *Effect of prestraining in tension at +25° C on the strength at +100° C of unnotched and notched specimens of the alloy.*

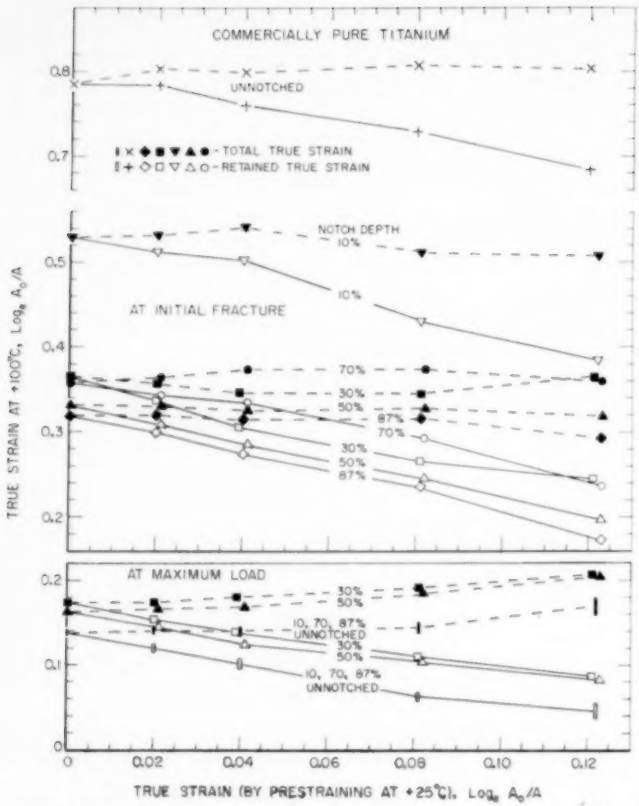

FIGURE 20. *Effect of prestraining in tension at +25° C on the ductility at +100° C of unnotched and notched specimens of the titanium.*

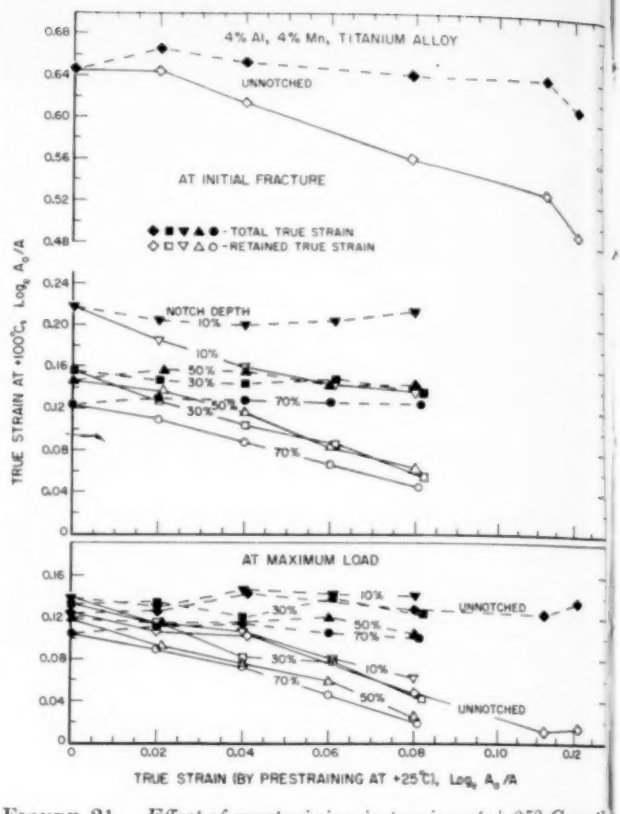

FIGURE 21. *Effect of prestraining in tension at +25° C on th ductility at +100° C of unnotched and notched specimens the alloy.*

b. Strength

The relations observed at +100° C between the tensile or notch strength, true stress at maximum load or true stress at initial fracture, and the prestrain at +25° C of specimens of the titanium and the alloy are shown in figures 18 and 19. These strength indices increased with the increase in triaxial stresses that accompany the increase in notch depth. However, they were independent of the prestraining of the specimens at +25° C.

c. Ductility

The relations between the ductility at +100° C and the prestrain at +25° C of unnotched and notched specimens are shown in figures 20 and 21. A slight increase in the total true strain at maximum load with increase in the prestrain was observed for the titanium specimens (fig. 20). However, the increase was much smaller than the prestrain and hence the retained true strain at maximum load generally decreased with increase in the prestrain. The total true strain at initial fracture at +100° C of the unnotched and notched specimens of both metals (figs. 20 and 21) and the total true strain at maximum load at +100° C of the alloy specimens (fig. 21) were approximately independent of the prestrain. Some scatter was obtained in these data, but no general trend is shown of either an increase or decrease in these total true strains with increase in the prestrain. Thus, the retained true strains a initial fracture at +100° C of both metals and th retained true strains at maximum load at +100° C o the alloy were decreased by the prestraining b amounts approximately equal to the prestrain.

3.3. Effect of Prestraining Specimens at −196° C o Their Tensile Properties at +25° C

The results obtained in two-stage tension tests a −196° and +25° C, respectively, on unnotched an notched specimens of the initially annealed titaniu and on unnotched specimens of the initially anneale alloy are summarized in table 3. The ductility o notched specimens of the titanium at −196° C wa relatively low and the two-stage tests on thes specimens were restricted to small prestrains (tru strains of 0.02 and 0.03) at −196° C. The ductilit of notched specimens of the alloy at −196° C was s limited that it was not feasible to conduct the two stage tests.

a. True Stress Versus True Strain Curves

The true stress-true strain curves obtained on th unnotched specimens of the titanium and the allo are presented in figures 22 and 23, respectively, an those for the notched specimens (50 percent depth) o titanium in figure 24. The curves for the secon stage of these tests at +25° C nearly coincide wit the corresponding portion of the curves for single

TABLE 3. *Tensile properties of unnotched and notched (60° notch angle, 0.05 in. root radius) specimens tested in single stage at +25° C and in two stages at −196° and +25° C, respectively*

Notch depth	D [a]	d [b]	Stress concentration factor, K_t	Triaxiality, [c] S_t/S_l	First stage of test, −196° C		Second stage of test, +25° C							Reduction of area	Elongation [f] in 2 in.
					True strain [d] at end of stage	True stress at end of stage	Tensile [e] strength or notch strength	True stress		Total true strain [d]		Retained true strain			
								at maximum load	at initial fracture	at maximum load	at initial fracture	at maximum load	at initial fracture		
Commercially pure titanium															
%	*in.*	*in.*				*lb/in.²*	*lb/in.²*	*lb/in.²*	*lb/in.²*					%	%
0 s	-----	0.400	1.0	0	0	0	94,000	107,000	145,000	0.130	0.706	0.130	0.706	52	30
0	-----	.400	1.0	0	.020	164,000	95,000	108,000	143,000	.122	.659	.102	.639	50	27
0	-----	.400	1.0	0	.041	169,000	94,000	110,000	142,000	.152	.635	.111	.594	46	23
0	-----	.400	1.0	0	.080	179,000	93,000	105,000	134,000	.127	.577	.047	.497	45	24
0	-----	.400	1.0	0	.122	189,000	94,000	107,000	132,000	.135	.536	.013	.414	42	24
10 s	0.370	.350	1.7	.08	0	0	104,000	122,000	141,000	.160	.360	.160	.360	32	----
30 s	.418	.350	1.9	.23	0	0	123,000	146,000	155,000	.175	.248	.175	.248	23	----
50 s	.495	.350	2.0	.33	0	0	141,000	164,000	174,000	.148	.223	.148	.223	22	----
50	.495	.350	2.0	.33	.020	230,000	142,000	165,000	168,000	.150	.170	.130	.150	14	----
50	.495	.350	2.0	.33	.031	245,000	138,000	[h]	156,000	-----	.122	-----	.091	12	----
70 s	.639	.350	2.1	.39	0	0	159,000	180,000	193,000	.126	.231	.126	.231	23	----
87 s	.990	.350	2.1	.41	0	0	161,000	183,000	194,000	.134	.207	.134	.207	20	----
4-percent-Al, 4-percent-Mn, titanium alloy															
0 s	-----	0.400	1.0	0	0	0	149,000	168,000	216,000	0.116	0.553	0.116	0.553	44	14
0	-----	.400	1.0	0	.020	247,000	150,000	167,000	215,000	.105	.566	.085	.546	45	17
0	-----	.400	1.0	0	.041	253,000	150,000	168,000	219,000	.112	.579	.071	.538	45	17
0	-----	.400	1.0	0	.081	264,000	151,000	168,000	218,000	.109	.576	.028	.495	45	13
0	-----	.400	1.0	0	.122	275,000	151,000	172,000	214,000	.132	.560	.010	.438	44	19
10	0.370	.350	1.7	.08	0	0	161,000	186,000	190,000	.142	.167	.142	.167	17	----
30	.418	.350	1.9	.23	0	0	191,000	[h]	212,000	-----	.101	-----	.101	12	----
50 s	.495	.350	2.0	.33	0	0	223,000	[h]	248,000	-----	.106	-----	.106	13	----
70	.639	.350	2.1	.39	0	0	248,000	[h]	272,000	-----	.101	-----	.101	12	----
87	.990	.350	2.1	.41	0	0	252,000	[h]	270,000	-----	.068	-----	.068	----	----

See footnotes to table 1.

stage tests at +25° C. Thus, the stresses necessary for continued deformation in tension at +25° C were apparently independent of the temperature (−196° C or +25° C) of the prior strain, even though the deformation mechanisms may vary at these two temperatures. The coincidence of the curves also indicates an approximate equivalence of the total work hardening of these specimens during extension in tension to the same selected strains at −196° C or +25° C. This conforms to the evidence presented and discussed previously in the series of two-stage tests at +25° and −196° C.

b. Strength

Strength indices, such as tensile strength, true stresses at maximum load and at initial fracture, of the unnotched specimens at +25° C of the titanium (fig. 25) and the alloy (fig. 26) were approximately independent of the prestrain at −196° C. A similar trend is shown in the limited data on notch strength and true stress at maximum load of the notched specimens of titanium (fig. 25). However, a slight decrease was observed in the true stress at initial fracture at +25° C with increase in the prestrain at −196° C of the notched specimens. This decrease

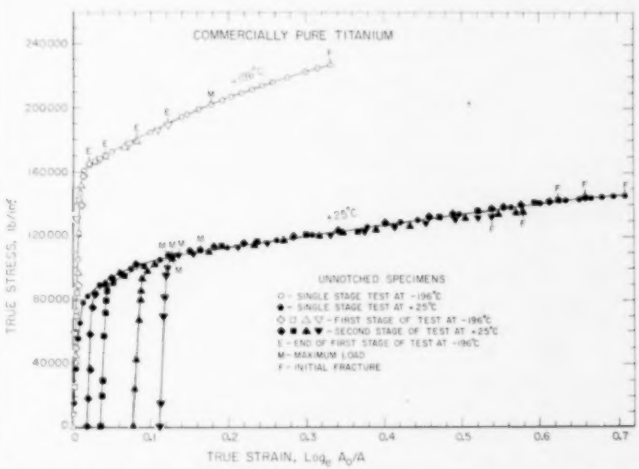

FIGURE 22. *True stress-true strain relations obtained in single- and two-stage tension tests at −196° and +25° C on unnotched specimens of the titanium.*

can be attributed directly to the reduction in the ductility of these specimens at +25° C by the prestraining at −196° C, as no evidence is shown in figure 24 of any decrease in the resistance to deformation of the notched specimens at +25° C.

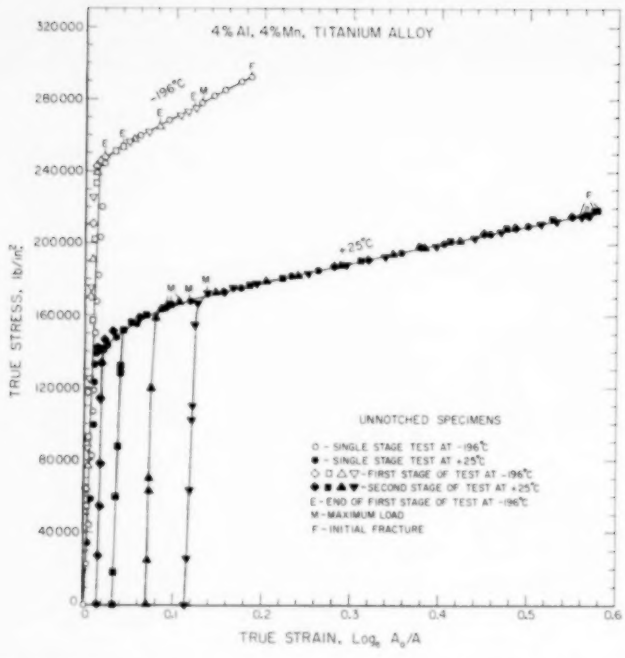
4% Al, 4% Mn, TITANIUM ALLOY
-196°C
+25°C
UNNOTCHED SPECIMENS
○ - SINGLE STAGE TEST AT -196°C
● - SINGLE STAGE TEST AT +25°C
◇ □ △ ▽ - FIRST STAGE OF TEST AT -196°C
◆ ■ ▲ ▼ - SECOND STAGE OF TEST AT +25°C
E - END OF FIRST STAGE OF TEST AT -196°C
M - MAXIMUM LOAD
F - INITIAL FRACTURE
TRUE STRESS, lb/in²
TRUE STRAIN, Log$_e$ A$_o$/A

FIGURE 23. *True stress-true strain relations obtained in single- and two-stage tension tests at −196° and +25° C on unnotched specimens of the alloy.*

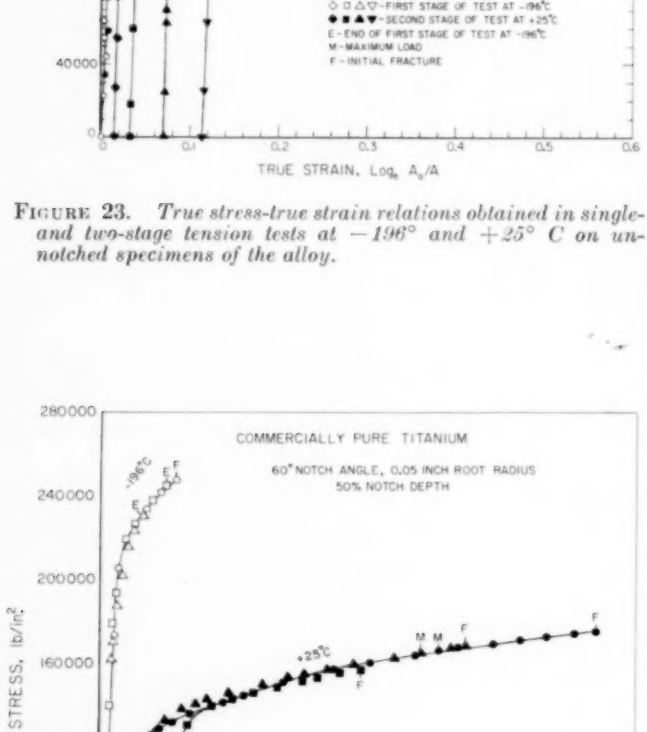
COMMERCIALLY PURE TITANIUM
60° NOTCH ANGLE, 0.05 INCH ROOT RADIUS
50% NOTCH DEPTH
-196°C
+25°C
○ - SINGLE STAGE TEST AT -196°C
● - SINGLE STAGE TEST AT +25°C
△ □ - FIRST STAGE OF TEST AT -196°C
▲ ■ - SECOND STAGE OF TEST AT +25°C
E - END OF FIRST STAGE OF TEST AT -196°C
M - MAXIMUM LOAD
F - INITIAL FRACTURE
TRUE STRESS, lb/in²
TRUE STRAIN, Log$_e$ A$_o$/A

FIGURE 24. *True stress-true strain relations obtained in single- and two-stage tension tests at −196° and +25° C on notched specimens of the titanium.*

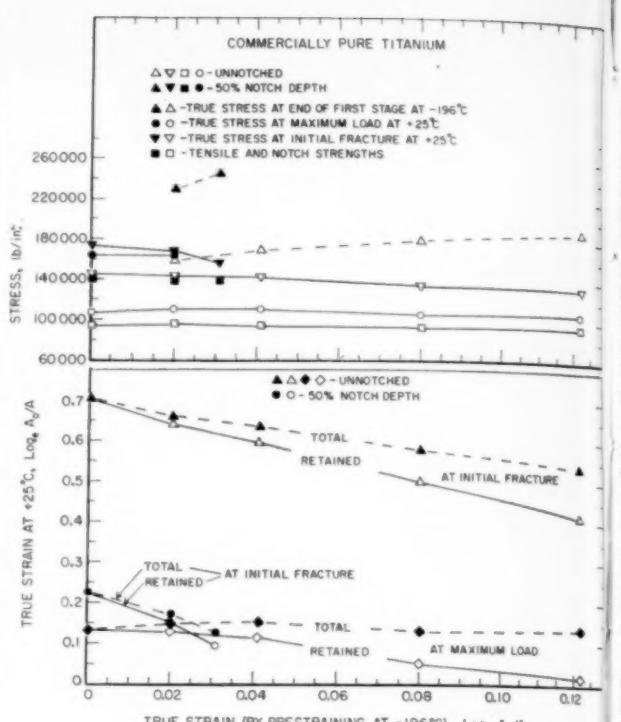
COMMERCIALLY PURE TITANIUM
△ ▽ □ ○ - UNNOTCHED
▲ ▼ ■ ● - 50% NOTCH DEPTH
▲ △ - TRUE STRESS AT END OF FIRST STAGE AT -196°C
● ○ - TRUE STRESS AT MAXIMUM LOAD AT +25°C
▼ ▽ - TRUE STRESS AT INITIAL FRACTURE AT +25°C
■ □ - TENSILE AND NOTCH STRENGTHS
STRESS, lb/in²
▲ △ ◆ ◇ - UNNOTCHED
● ○ - 50% NOTCH DEPTH
TOTAL
RETAINED
AT INITIAL FRACTURE
AT MAXIMUM LOAD
TRUE STRAIN AT +25°C, Log$_e$ A$_o$/A
TRUE STRAIN (BY PRESTRAINING AT -196°C), Log$_e$ A$_o$/A

FIGURE 25. *Effect of prestraining in tension at −196° C on the strength and ductility at +25° C of unnotched and notched specimens of the titanium.*

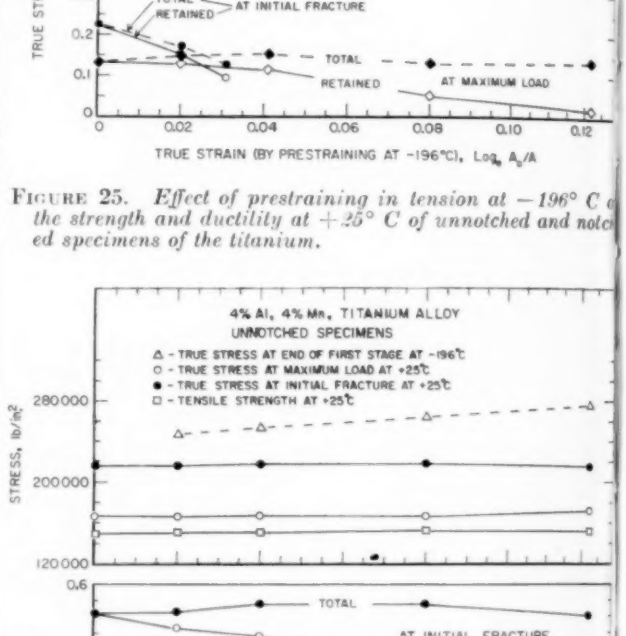
4% Al, 4% Mn, TITANIUM ALLOY
UNNOTCHED SPECIMENS
△ - TRUE STRESS AT END OF FIRST STAGE AT -196°C
○ - TRUE STRESS AT MAXIMUM LOAD AT +25°C
● - TRUE STRESS AT INITIAL FRACTURE AT +25°C
□ - TENSILE STRENGTH AT +25°C
STRESS, lb/in²
TOTAL
RETAINED
AT INITIAL FRACTURE
AT MAXIMUM LOAD
TRUE STRAIN AT +25°C, Log$_e$ A$_o$/A
TRUE STRAIN (BY PRESTRAINING AT -196°C), Log$_e$ A$_o$/A

FIGURE 26. *Effect of prestraining in tension at −196° C on the strength and ductility at +25° C of unnotched specimens of the alloy.*

c. Ductility

The effects of prestraining at −196° C on the ductility of the titanium and the alloy at +25° C are shown by the data as summarized in figures 25 and 26, respectively. The total true strains at maximum load at +25° C of the unnotched specimens of both metals and the total true strain at initial fracture of the alloy were approximately independent of the prestrain. Thus, the retained true strains of these specimens decreased with an increase in the prestraining by amounts approximately equivalent to the prestrain. The total true strain at initial fracture of both unnotched and notched specimens of the titanium (fig. 25) decreased continuously with increase in the prestrain. The decrease in the retained true strain at initial fracture of the unnotched specimens at +25° C was approximately twice the prestrain at −196° C. The effect of the prestrain at −196° C of the notched specimens of titanium on their ductility at +25° C was very pronounced; the retained true strain at initial fracture was decreased by an amount approximately equal to 4 times the prestrain.

The pronounced difference in the effect of prestraining at −196° C on the total ductility (also retained ductility) at +25° C of the unnotched specimens of the titanium and the alloy indicates that the effect of temperature on the mechanisms of deformation is considerably greater for the titanium than for the alloy. No information is readily available on the specific deformation mechanisms of the 4-percent-Al, 4-percent-Mn, titanium alloy either at room temperature or at −196° C. However, results obtained in studies on the mechanisms of deformation for titanium at different temperatures have been reported in several papers [6 to 10]. These studies show that the tensile deformation of titanium at −196° C occurs mainly by twinning, and also by some slip on the prismatic planes. The amount of twinning, in general, decreased with increase in the temperature of deformation. The tensile deformation at +25° C occurs by twinning, and by slip on the prismatic, pyramidal, and basal planes [6, 7, and 9].

The ductility behavior of the titanium specimens in the two-stage tests of −196° C and +25° C, respectively, may be partially explained on the basis of the above mechanisms of deformation and a tentative hypothesis as follows: Prestraining the specimens at −196° C, in which the slip is restricted to the prismatic planes, exhausts a greater proportion of the total available movement of dislocations along the prismatic planes than the same amount of prestrain under the more ductile condition at +25° C, in which the slip is distributed among the prismatic, pyramidal, and basal planes. Thus, the subsequent movement of dislocations along the prismatic planes in the second stage of the test at +25° C is more restricted for the specimens prestrained at −196° C than for those with the same prior strain at +25° C. This embrittlement of the titanium increases with an increase in the prestrain at −196° C and results in a decrease in the total and retained true strains at initial fracture at +25° C. The hypothesis assumes that the initiation of the fracture of the titanium at +25° C is mainly dependent upon the exhaustion of dislocation movements on the prismatic planes.

It may be inferred from the apparent insensitivity of the ductility at +25° C of the titanium alloy specimens to the temperature during the prior straining (prestraining to selected strains at −196° C or testing in a single stage test at +25° C) that the deformation mechanisms of the alloy are not very different at −196° and +25° C. However, this inference must be considered with reservation due to the limited experimental data and lack of information on the specific deformation mechanisms for the alloy.

4. Summary

A study was made of the effect of the prior strain-temperature history on the tensile behavior of unnotched and notched specimens (60° notch angle, 0.05-in. root radius, 0.35-in. diameter at root of notch and selected notch depths) of initially annealed commercially pure titanium and initially annealed 4-percent-Al, 4-percent-Mn, titanium alloy. Three series of two-stage tension tests were made: In two series, the specimens were extended at +25° C to selected strains up to true strains of 0.08 or 0.12 and then to fracture at (1) −196° C or (2) +100° C; in the other series, the specimens were extended at −196° C to selected strains up to true strains of 0.03 or 0.12 and then to fracture at +25° C. It was not feasible to conduct this series of tests on the notched specimens of the alloy due to the very limited ductility of these specimens at −196° C.

The resistance to deformation of both the unnotched and notched tensile specimens of each metal at a selected temperature, in general, was nearly independent of the temperature of the prior deformation. The true stress-true strain data obtained in the single-stage tests and in the two-stage tests on the unnotched specimens indicate that the total work hardening (strain hardening, strain aging or recovery) of each metal during the extension to a selected strain is nearly the same at −196°, +25°, and +100° C.

The tensile or notch strength and the true stress at initial fracture of the unnotched and notched specimens of the titanium and the alloy at −196°, +25° or +100° C, in general, were independent of the amount of prestraining. An exception to this general trend was observed at −196° C with the deep-notched specimens of the alloy that were prestrained at +25° C to true strains above 0.04; the notch strength and true stress at initial fracture of these specimens decreased with increase in the prestraining. However, the decrease in these values can be attributed directly to the very small retained ductility of the specimens at −196° C.

The retained ductility of the unnotched and

notched specimens of the titanium and the alloy at −196°, +25°, and +100° C depended upon the prior strain-temperature history of the specimens. The retained true strain at initial fracture of the unnotched specimens of both metals at −196° or +100° C and the alloy at +25° C, generally decreased by amounts approximately equal to the prestrain. However, prestraining the unnotched specimens of the titanium at −196° C decreased the retained true strain at initial fracture at +25° C by amounts approximately equal to twice the prestrain.

The prestraining of notched specimens of both metals also had a deleterious effect on their ductility. The retained true strain at initial fracture at −196° or +100° C decreased with increase in the prestraining at +25° C. Moreover, the retained true strain at initial fracture at +25° C of the notched specimens of the titanium was reduced greatly by prestraining at −196° C; prestraining to a small true strain of 0.02 or 0.03 decreased the retained true strain at initial fracture by an amount nearly equal to 4 times the prestrain.

The results obtained in this investigation indicate that neither the annealed commercially pure titanium nor the annealed 4-percent-Al, 4-percent-Mn, titanium alloy are subject to "rheotropic embrittlement" as the prestraining of the tensile specimens at +25° C resulted in a decrease instead of an increase in their retained ductility at −196° C.

5. References

[1] E. J. Ripling and W. M. Baldwin, Jr., Rheotropic em brittlement of steel. Trans. Am. Soc. Metals 4 778 (1951).

[2] G. W. Geil and N. L. Carwile, Effect of strain-temper ture history on the flow and fracture of ingot iron a low temperatures, J. Research NBS **48,** 399 (19 RP2329.

[3] G. W. Geil and N. L. Carwile, Some effects of low tem peratures and notch depth on the mechanical behavio of an annealed commercially pure titanium, J. Re search NBS **59,** 215 (1957) RP2790.

[4] G. W. Geil and N. L. Carwile, A reduction-of-area gag for use at low temperatures, J. Research NBS 4 527 (1949) RP2044.

[5] G. W. Geil and N. L. Carwile, Tensile properties of ingo iron at low temperatures, J. Research NBS **45,** 1 (1950) RP2119.

[6] F. D. Rosi, F. C. Perkins, and L. L. Seigle, Mechanism of plastic flow in titanium at low and high temperatures, Trans. Am. Inst. Mining Met. Engrs. **20** 115 (1956).

[7] E. A. Anderson, D. C. Jillson, and S. R. Dunbar, De formation mechanisms in alpha titanium, Trans. Am Inst. Mining Met. Engrs. **197,** 1191 (1953).

[8] C. J. McHargue and J. P. Hammond, Deformation mech anisms in titanium at elevated temperatures, Act Met. **1,** 700 (1953).

[9] A. T. Churchman, The slip modes of titanium and th effects of purity on their occurrence during tensil deformation of single crystals, Proc. Royal So (London) [A] **226,** 216 (1954).

[10] A. T. Churchman, The yield phenomena, kink band and geometric softening in titanium crystals, Act Met. **3,** 22 (1955).

WASHINGTON, APRIL 17, 1958.

Journal of Research of the National Bureau of Standards Vol. 61, No. 3, September 1958 Research Paper 2898

Propagation of Very-Low-Frequency Pulses to Great Distances[1]

James R. Wait

A theoretical study is presented for the propagation of electromagnetic pulses at very low frequencies to large distances. The space between the earth and the ionosphere is represented as a wave guide with sharply bounded and concentric spherical boundaries. The concept of phase and group velocity and its application to the present problem is discussed in some detail. The influence of the propagation medium on the shape of the envelope of a quasi-monochromatic pulse is also considered. Using an alternative approach, the response of an impulsive source is also calculated and is shown to be a damped oscillatory function of time with a quasi-half-period varying in a predictable manner with distance of travel in agreement with the observations of Norinder and Hepburn.

1. Introduction

In recent years there has been a renewed interest in the propagation of VLF (very-low-frequency) radio waves. The wave-guide model has been remarkably successful for the prediction of the field strength as a function of distance and frequency. In most investigations, both experimental and theoretical, the source varies essentially in a sinusoidal manner with time.[2] It is of great interest, however, to have a knowledge of the transient characteristics of a pulse and the way it is influenced by the propagation medium. For example, if the received field strength of a lightning stroke is recorded as a function of time, one may ask how this waveform is related to the source current, distance of travel, electrical constants of the ground, and height and electrical properties of the ionosphere. It is the purpose of this paper to attempt an answer to this question on the basis of a theoretical study.

A general analysis is presented in section 4, applying and extending the classical concepts [3, 4] such as phase and group velocity for propagation in dispersive media. Such an approach is particularly suitable for a quasi-monochromatic source wherein the spectral components are centered in a narrow band about some central or reference frequency. In section 5, an alternative method is described that is applicable to broad-band sources which contain many spectral components. Extensive numerical results are presented for the parameters characterizing the shape of the radiated pulses. Finally, some reference is made to published experimental data concerning the waveforms of radio atmospherics.

2. Quasi-Monochromatic Pulse

In the present study, the earth is represented by a homogeneous sphere of radius a, and the ionosphere is idealized as a sharply bounded concentric reflecting layer at height h. The source of the field is always assumed to be equivalent to a vertical (radially oriented) electric dipole. At large ranges, the field can then be represented as a sum of waveguide modes.

The vertical electric field of any one mode at a range d can be written in the form (see section 7.1)

$$e(\omega)=A_n e^{-\frac{2\pi d}{h}u_n} e^{-j\frac{2\pi d}{\lambda}x_n} e^{j\omega t}, \tag{1}$$

where A_n is a slowly varying function of frequency ω, u_n is a measure of the attenuation of the

[1] The results in this paper were reported at the commission 4 and 6 sessions of the International Scientific Radio Union General Assembly held in Boulder, Colo., August 22 to September 5, 1957.

[2] See VLF issue of Proc. Inst. Radio Engrs. **45,** June 1957, for papers by Budden, Pierce, Wait, and Watt.

[3] J. A. Stratton, Electromagnetic theory, p. 292 (McGraw-Hill Publishing Co., Inc., New York, N. Y., 1941).

[4] IA. L. Al'pert, V. L. Ginzburg, and E. L. Feinberg, Radiowave propagation, pt. II, p. 364 (Moscow, 1953).

473722—58——5

mode per unit distance, and s_n is a dimensionless phase factor. The phase velocity is then given by

$$v_p = c/s_n, \tag{2}$$

where c is the velocity of light. On the other hand, the group velocity of a mode is given by

$$v_g = \frac{c}{\frac{d}{d\omega}(\omega s_n)}, \tag{3}$$

which can be written in terms of $H(=h/\lambda)$ as follows:

$$v_g = \frac{c}{s_n + H\frac{ds_n}{dH}}. \tag{4}$$

The group velocity, so defined, is a measure of the velocity of the envelope of the quasi-monochromatic pulse or group. For example, if the propagation medium were nondispersive, the signal might be represented by the real part of $E_0(t) = A(t)e^{i\omega_0 t}$, where ω_0 is the carrier frequency, and $A(t)$ is the shape of the envelope as a function of time. In the simple case of a broken sinusoid,

$$A(t) = 1 \quad \text{for} \quad -\frac{T}{2} < t < \frac{T}{2},$$

$$A(t) = 0 \quad \text{for} \quad t > T/2 \quad \text{and} \quad t < -\frac{T}{2}.$$

The group velocity concept is valid only when the frequency spectrum,

$$G(\omega) = \int_{-\infty}^{+\infty} E_0(t) e^{-i\omega t} dt, \tag{5}$$

differs substantially from zero only in a small frequency band near the signal carrier-frequency ω_0. In the present case

$$G(\omega) = 2\frac{\sin(\omega - \omega_0)T/2}{(\omega - \omega_0)}. \tag{6}$$

The spectral width is given by $\Delta\omega \sim 1/(2T)$ and this must be small compared to ω_0. In other words, the period of the envelope must be long compared to the period of the carrier frequency.

Now when the pulse propagates through the medium by a distance d, the field $E_0(t)$ of a mode becomes transformed to $E(t)$ whence

$$E(t) = \frac{1}{2\pi}\int_{-\infty}^{+\infty} A(\omega) e^{i[\omega t - \phi(\omega)]} e^{-\alpha(\omega)} G(\omega) d\omega, \tag{7}$$

where

$$\phi(\omega) = \frac{\omega}{c} s_n d = s_n \frac{2\pi d}{\lambda}$$

and

$$\alpha(\omega) = \frac{2\pi d}{h} u_n.$$

The coefficients $\alpha(\omega)$ and $\phi(\omega)$ are phase and attenuation factors of a mode as a function of frequency for the section of path of length d.

Utilizing well-known properties of Fourier integrals,[1 2] the spectral representations of the signals $E_0(t)$ and $E(t)$ can be written

$$E_0(t) = \frac{1}{2\pi}\int_{-\infty}^{+\infty}\int_{-\infty}^{+\infty} A(t') \exp\{i(\omega_0 - \omega)t' + \omega t\} d\omega dt', \tag{8}$$

and

$$E(t)=\frac{1}{2\pi}\int_{-\infty}^{+\infty}\int_{-\infty}^{+\infty}A(t')\exp\{i(\omega_0-\omega)t'+\omega t-\phi(\omega)\}G(\omega)e^{-\alpha(\omega)}d\omega dt'. \tag{9}$$

The phase function $\phi(\omega)$ is now written in a Taylor expansion,

$$\phi(\omega)=\phi(\omega_0)+\Omega\phi'(\omega_0)+\frac{\Omega^2}{2}\phi''(\omega_0)+\ldots, \tag{10}$$

where $\Omega=\omega-\omega_0$. Neglecting terms containing Ω^3, etc., it follows that

$$E(t)=\exp[i(\omega_0 t-\phi(\omega_0))]G(\omega_0)e^{-\alpha(\omega_0)}\times \frac{1}{2\pi}\int_{-\infty}^{+\infty}\int_{-\infty}^{+\infty}A(t')\exp\left\{i\Omega[t-t'-\phi'(\omega_0)]-i\frac{\phi''(\omega_0)}{2}\Omega^2\right\}dt'd\Omega, \tag{11}$$

where the slowly varying factors have been taken outside the integrand. Introducing a new variable z defined by

$$z=\sqrt{\phi''(\omega_0)/\pi}\left[\Omega+\frac{t'-t+\phi'(\omega_0)}{\phi''(\omega_0)}\right], \tag{12}$$

in place of Ω it follows that

$$E(t)=\frac{1-i}{2\pi}\exp\left\{i\left[\omega_0 t-\phi(\omega_0)\right]\right\}G(\omega_0)e^{-\alpha(\omega_0)}\times \int_{-\infty}^{+\infty}\left[\frac{\pi}{\phi''(\omega_0)}\right]^{1/2}A(t')\exp\left[i\frac{(t'-t+\phi'(\omega_0))^2}{2\phi''(\omega_0)}\right]dt', \tag{13}$$

since

$$\int_{-\infty}^{+\infty}\exp\left[-i\frac{\pi}{2}z^2\right]dz=1-i. \tag{14}$$

After a further change of variable, via

$$\frac{t'-t+\phi'(\omega_0)}{\phi''(\omega_0)}=\sqrt{\pi}u, \tag{15}$$

we finally arrive at

$$E(t)=\frac{1-i}{2}\exp\{i[\omega_0 t-\phi(\omega_0)]\}G(\omega_0)e^{-\alpha(\omega_0)}\times\int_{-\infty}^{+\infty}A[t-\phi'(\omega_0)-\sqrt{\pi\phi''(\omega_0)}u]\exp\left(i\frac{\pi}{2}u^2\right)du. \tag{16}$$

In the above, it has been assumed that $\phi''(\omega_0)>0$; if $\phi''(\omega_0)<0$, then by changing the sign in the substitution of variables one would have $\sqrt{\pi|\phi''(\omega_0)|}$ in place of $\sqrt{\pi\phi''(\omega_0)}$.

Now if $\phi''(\omega_0)=0$ and noting that

$$\int_{-\infty}^{+\infty}\exp\left(i\frac{\pi}{2}u^2\right)du=1+i, \tag{17}$$

it follows that

$$E(t)=A[t-\phi'(\omega_0)]e^{-\alpha(\omega_0)}G(\omega_0)e^{i[\omega_0 t-\phi(\omega_0)]}. \tag{18}$$

To this approximation, the pulse has not changed shape, although the pulse amplitude has been modified, the phase has changed by an amount $\phi(\omega_0)$, and the pulse as a whole is delayed by the "group time" $\phi'(\omega_0)$. The effect of a nonzero value of $\sqrt{\pi\phi''(\omega_0)}$ is to modify the pulse shape (see footnote 4). To evaluate this phenomenon, the envelope must be specified and the integration indicated in eq (16) must be carried out. For example, in the case of the broken

sinusoid extending from $-T/2$ to $T/2$, the integral in eq (16) can readily be transformed to a Fresnel integral,

$$E(t)=\frac{1-i}{2}\exp\{i[\omega_0 t-\phi(\omega_0)]\}\int_{u_1}^{u_2}\exp\left[i\frac{\pi}{2}u^2\right]du, \tag{19}$$

where

$$u_1=\frac{-\theta}{\sqrt{\pi\phi''(\omega_0)}}; \qquad u_2=\frac{T-\theta}{\sqrt{\pi\phi''(\omega_0)}},$$

and $\theta=(T/2)+t-\phi'(\omega_0)$. θ is the time measured from the instant $-T/2+\phi'(\omega_0)$. In the case of negligible dispersion of the pulse shape, $\phi''(\omega_0)$ must be sufficiently small to enable u_1 and u_2 to be replaced by $-\infty$ and $+\infty$, and then

$$\begin{aligned} E(t)&\cong\exp\{i[\omega_0 t-\phi(\omega_0)]\} \qquad \text{for} \qquad 0<\theta<T \\ &\cong 0 \qquad \text{for} \qquad \theta<0 \qquad \text{and} \qquad \theta>T. \end{aligned} \tag{20}$$

To illustrate the influence of dispersion, it will be assumed that the signal duration T is large compared to $\sqrt{\pi\phi''(\omega_0)}$. Then the form of the leading edge of the signal is determined by

$$|E(t)|\cong\frac{1}{\sqrt{2}}\left|\int_{u_1}^{\infty}\exp\left[i\frac{\pi}{2}u^2\right]du\right|. \tag{21}$$

The envelope $|E(t)|$ is plotted versus the time parameter $\theta/\sqrt{\pi\phi''(\omega_0)}$ in figure 1, a. It is now convenient to define a build-up parameter t_b, which is the time measured from $\theta=0$ for the envelope $|E(t)|$ to approach within 5 percent of unity. From inspection of figure 1 it is seen that

$$t_b\cong 4\sqrt{\pi\phi''(\omega_0)} \text{ sec.}$$

For numerical presentation it is convenient to introduce a dimensionless build-up parameter T_b defined by

$$t_b\cong\frac{4\sqrt{dh/2}}{c}T_b, \tag{22}$$

where

$$T_b=\left|2\frac{\partial s_n}{\partial H}+H\frac{\partial^2 s_n}{\partial H^2}\right|^{3/2}.$$

The build-up parameter T_b and the build-up time t_b are related by eq (22). The chart in figure 1, b, is to facilitate the conversion for a typical height of 70 km, and for various ranges d in kilometers.

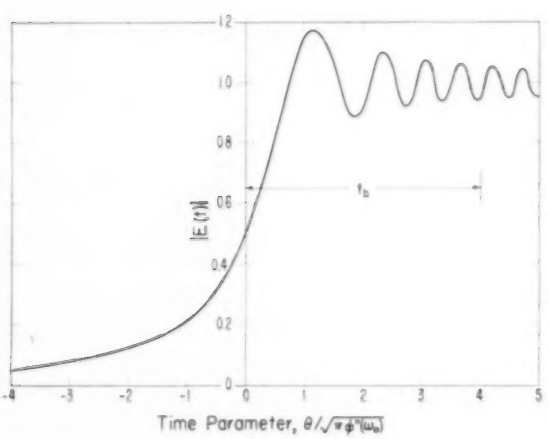

FIGURE 1a. *Leading edge of signal in dispersive media.*

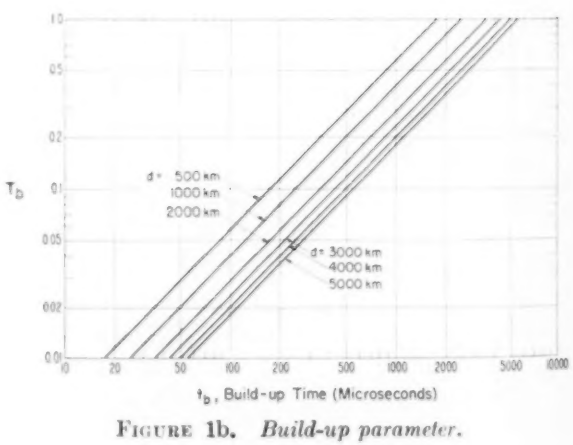

FIGURE 1b. *Build-up parameter.*

h=70 km

3. Numerical Presentation of Waveguide Parameters

The important parameters in specifying the characteristics of pulse propagation in the earth-ionosphere waveguide are attenuation rate, phase velocity, group velocity, and the build-up parameter. In general, these are functions of the dimensions of the guide and the electrical properties of the bounding walls. Those four quantities (u_n, v_p/c, v_g/c, and T_b) are plotted in figures 2 and 3 for mode number 1 (i. e., the dominant mode). The abscissa is

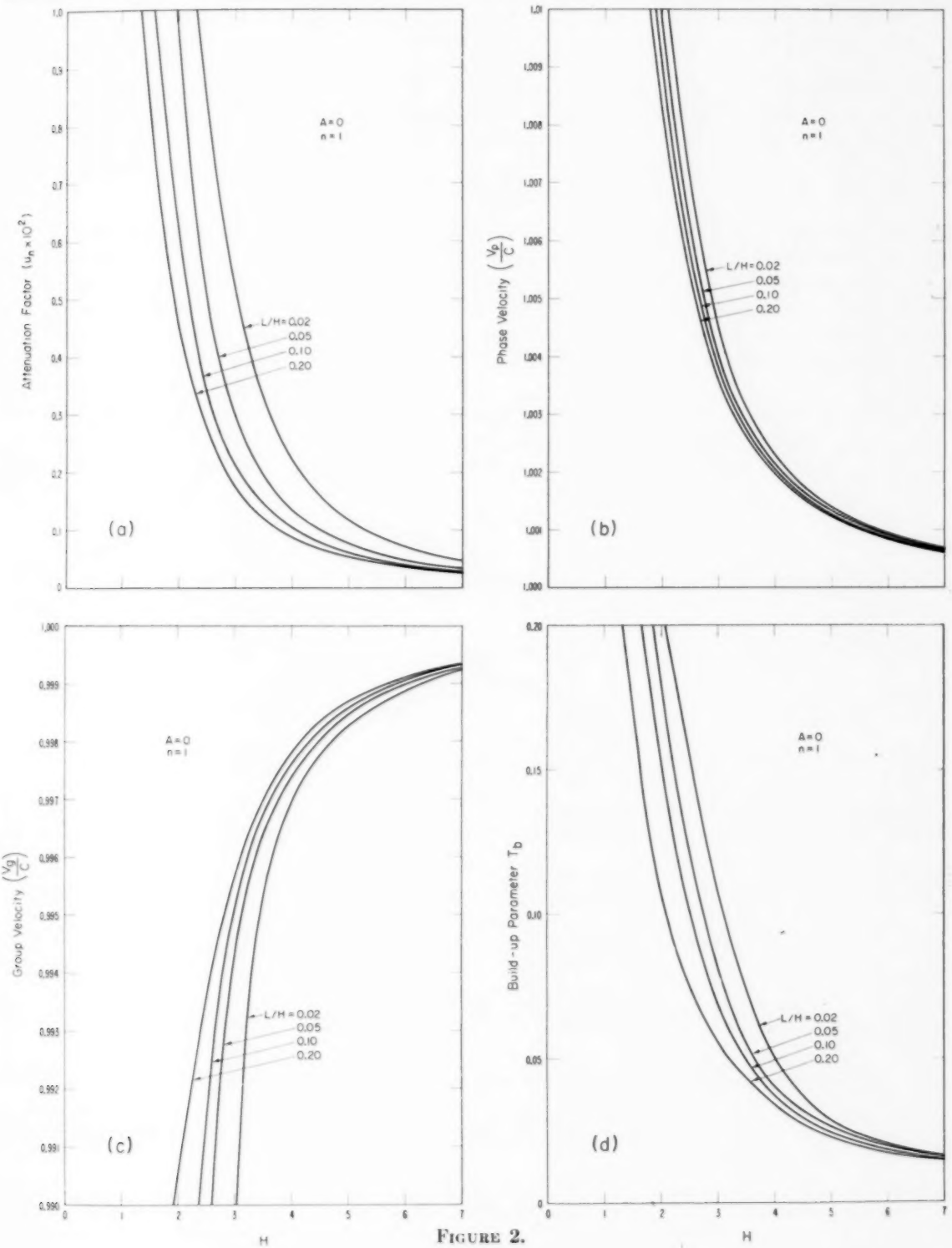

FIGURE 2.

$H(=h/\lambda)$, which is the height of the ionosphere in wavelengths and may be regarded as a frequency parameter.

The dimensionless quantity A is a ground conductivity parameter and is defined by $A=G/H$, where $G=\epsilon_0\omega/\sigma_g$ in terms of the conductivity σ_g of the ground. Alternately, one may write

$$A=\frac{1}{60\sigma_g h}.$$

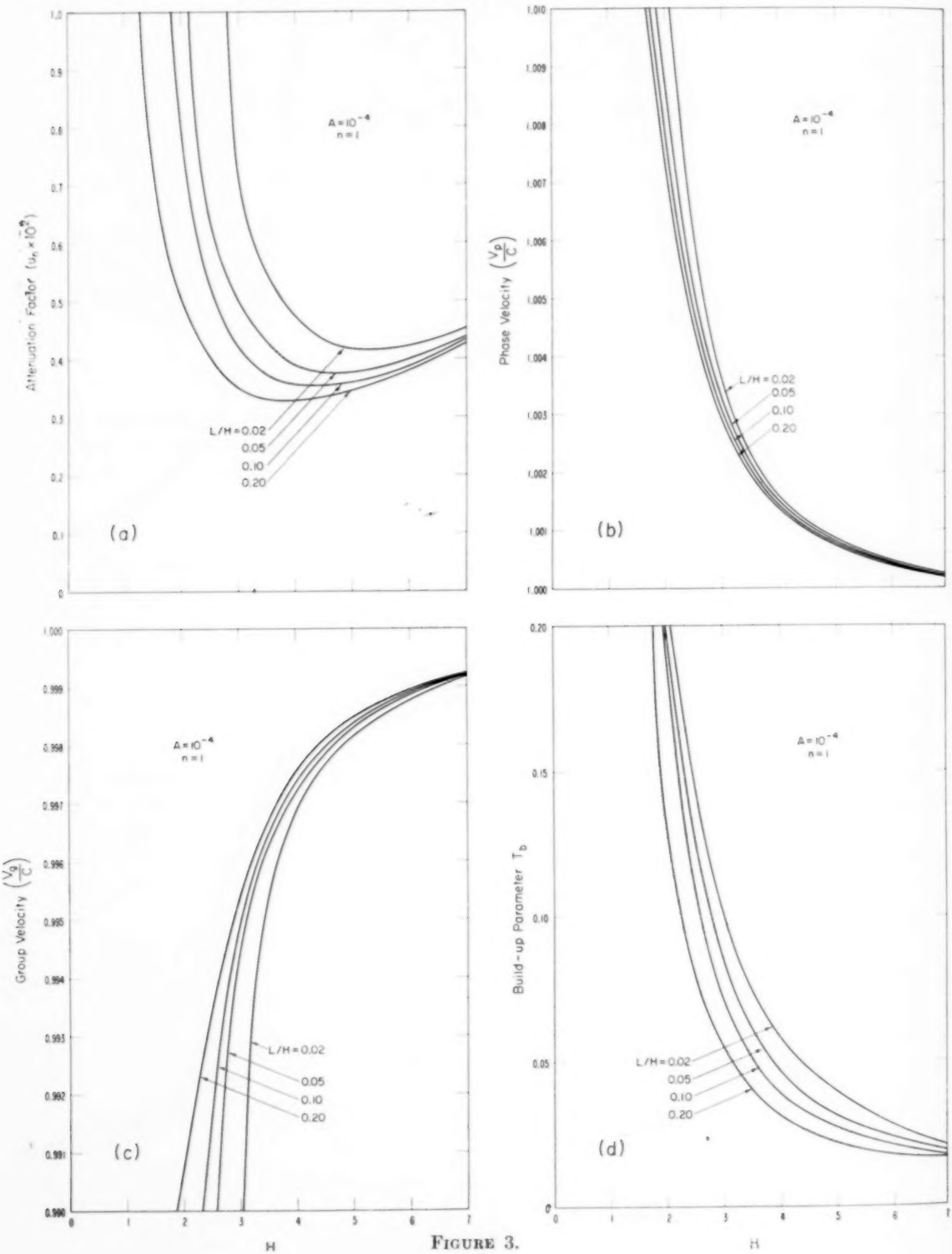

FIGURE 3.

The dimensional quantity B is the corresponding parameter for the (assumed) sharply bounded ionosphere. It is defined by $B=L/H$, where $L=\omega/\omega_r$,

and
$$\omega_r=\omega_0^2/\nu=\frac{(\text{plasma frequency})^2}{\text{collisional frequency}}.$$

In terms of the effective ionospheric conductivity, σ_i,[5] B is given by

$$B=\frac{1}{60\sigma_i h}.$$

The curves in figure 2, a to d, inclusive, are for $A=0$ or $\sigma_g\cong\infty$. This assumption is valid for propagation over sea water for all values of H shown. The curves in figure 3, a to d, inclusive, are for $A=10^{-4}$, which corresponds to moderately conducting ground [2.2 millimhos/m for $h=70$ km].

4. Analysis for Impulse Response

The foregoing analysis is applicable to the description of wave packets wherein the spectral components are essentially contained in a relatively narrow band about the carrier frequency. In the case of a lightning discharge, the pulse contains many spectral components, and as a matter of illustration, if the current was in the form of a Dirac delta function, all frequencies would be contained in a uniform distribution. In this case and for other similar instances, it is desirable to use an alternative approach. In the following, it is assumed that the source is initiated at $t=0$ and $d=0$.

The most convenient description of the source is the (transient) waveform of the radiation component of the vertical field on a perfectly conducting flat ground plane at distance d. This field is denoted $\overline{e}_0(t)$ as a function of t and its Fourier transform is

$$\overline{E}_0(\omega)=\int_0^\infty \overline{e}_0(t)e^{-i\omega t}dt. \tag{23}$$

If the source is a dipole carrying a current $j(t)$ with a height $h(t)$, both functions of t, then the radiation field on the (hypothetical) flat ground plane is

$$\overline{e}_0(t)=\frac{\mu}{2\pi d}\left[\frac{d}{dt}[j(t)h(t)]\right]_{t=t'}\cdot u(t'), \tag{24}$$

where

$$\left.\begin{aligned} u(t')&=1 \quad \text{for} \quad t'>0\\ &=0 \quad \text{for} \quad t'<0\end{aligned}\right\} t'=t-t_0,\ t_0=d/c.$$

The field at range d of the same dipole source when located on a homogeneous spherical earth of radius a with concentric ionospheric reflecting layer at height h is denoted $e(t)$, and its transform is

$$E(\omega)=\int_0^\infty e(t)e^{-i\omega t}dt. \tag{25}$$

The relation between $E(\omega)$ and $\overline{E}_0(\omega)$ has been previously derived (see footnote 2), and the final result is simply quoted here.

$$E(\omega)\cong\left[\frac{d/a}{\sin d/a}\right]^{1/2}\frac{(2\pi cd)^{1/2}}{h}\frac{\overline{E}_0(\omega)}{(i\omega)^{1/2}}\sum_{n=0}^{\infty}s_n^{3/2}\delta_n e^{\frac{-2\pi d}{h}u_n}e^{-iF(\omega)}, \tag{26}$$

where u_n and s_n are the attenuation and phase constants of the waveguide mode of order n, as defined in section 7.1, $\delta_0\cong\frac{1}{2}$, and $\delta_n\cong 1$ for $n\neq 0$, and $F(\omega)=(\omega/c)s_n d-\omega t$. The waveform of the electric field $e(t)$ is now obtained from the inverse Fourier transform

$$e(t)=\frac{1}{2\pi}\int_{-\infty}^{+\infty}E(\omega)e^{i\omega t}d\omega. \tag{27}$$

[5] The concept of an effective isotropic ionospheric conductivity is valid for $\omega<<\nu\cong 10^7$ and highly oblique (low-order) modes.

Unfortunately, the integration, except in certain limiting cases, cannot be carried out in closed form because u_n and s_n are not simple analytical functions of ω. In view of the fact, however, that extensive numerical data is already available for u_n, s_n, and related functions, it seems desirable to evaluate the integral by an approximate saddle-point procedure. The integrals to cope with are of the form

$$J=\int_{-\infty}^{+\infty} G(\omega)e^{-jF(\omega)}d\omega. \tag{28}$$

$G(\omega)$ can be assumed to be slowly varying compared to $F(\omega)$. The saddle point of $F(\omega)$ is at $\omega=\omega_s$, which is a solution of

$$\frac{\partial F(\omega)}{\partial \omega}=0.$$

Expanding $F(\omega)$ in a Taylor series about ω_s leads to $F(\omega)=F(\omega_s)+[(\omega-\omega_s)^2/2]F''(\omega_s)+$terms containing $(\omega-\omega_s)^3$, etc., where

$$F''(\omega_s)=\left[\frac{\partial^2 F(\omega)}{\partial \omega^2}\right]_{\omega=\omega_s}.$$

Retaining only the first two terms in the expansion for $F(\omega)$, the integration can be carried out to yield

$$J\cong\left[\frac{\pi}{2iF''(\omega_s)}\right]^{1/2}G(\omega_s)e^{-jF(\omega_s)}+\left[\frac{\pi}{-2iF''(\omega_s)}\right]^{1/2}G^*(\omega_s)e^{jF(\omega_s)}, \tag{29a}$$

where the asterisk denotes a complex conjugate. When the current is in the form of a unit impulse or Dirac delta function, the radiated field $\bar{e}_0(t)$/is a doublet impulse function. That is,

$$\bar{e}_0(t)=E_1\delta'(t) \tag{29b}$$

where

$$\delta'(t)=\operatorname*{Lim}_{\Delta\to 0}\frac{u(t-\Delta)-2u(t)+u(t+\Delta)}{\Delta^2}.$$

Therefore, the Fourier transform is

$$\overline{E_0}(\omega)=E_1 i\omega. \tag{29c}$$

In this important case

$$G(\omega)=E_1\left[\frac{d/a}{\sin d/a}\right]^{1/2}\frac{(2\pi cd)^{1/2}}{h}\cdot\frac{1}{2\pi}(i\omega)^{1/2}s_n^{3/2}e^{-\frac{2\pi t}{h}u_n}. \tag{30}$$

Therefore, the transient response for the impulse current source is given by

$$e(t)\cong E_1\left[\frac{d/a}{\sin d/a}\right]^{1/2}(2\pi)^{1/2}\left(\frac{c}{h}\right)^2\sum_{n=0}^{\infty}\delta_n e_n(t), \tag{31}$$

where

$$e_n(t)=(H_s)^{1/2}[s_n(\omega_s)]^{3/2}\frac{\cos F(\omega_s)}{T_b(\omega_s)}\exp\left[\frac{-2\pi d}{h}u_n(\omega_s)\right], \tag{32}$$

because

$$F'''(\omega_s)=2\frac{d}{c}\frac{ds_n}{d\omega}+\frac{d}{c}\omega\frac{d^2s_n}{d\omega^2}=\frac{hd}{c^2}[T_b(H_s)]^2. \tag{33}$$

The quantities H_s, $s_n(\omega_s)$, $u_n(\omega_s)$, and $T_b(H_s)$ are the values of H, s_n, u_n, and T_b evaluated at the saddle point $\omega=\omega_s$.

It can be readily seen that the equation for determining the saddle point is equivalent to finding the value of H (or ω) that satisfies

$$\frac{1}{s_n}=\frac{v_g(H)}{c}=\frac{d}{ct}. \tag{34}$$

Because $v_g(H)/c$ is a smooth monotonic function of H, the saddle-point value H_s (or ω_s) is readily determined by using a simple graphical procedure for any specified value of t.

5. Application of the Impulse Responses

The response of the waveguide to an impulsive current source is shown in figure 4 for various ranges. The quantity plotted is $e_1(t)$ given by eq (32) with $n=1$. This is the waveform of the dominant mode for the typical daytime conditions ($h=70$ km and $L/H=0.1$) and propagation over sea water ($A\simeq 0$). It is interesting to note that the pulses have the appearances of damped sinusoids. The oscillating nature of the curves is not due to the source which is impulsive, but rather is a result of the modal characteristics of propagation medium. In general, the initial quasi-period (temporal length of the first half-cycle) is becoming progressively shortened with increasing range, whereas the oscillatory nature of the pulse is becoming enhanced. In each case the frequency of the latter part of the waveform seems to be approaching about 9 kc (i. e., a half-period of about 56 μsec).

It is desirable to repeat this calculation for a source current of finite duration. For example, if the current dipole moment is proportional to $\alpha e^{-\alpha t}$ then the Fourier transform of the primary field $\bar{e}_0(t)$ is

$$\overline{E}_0(\omega)=E_1\cdot\frac{\alpha i\omega}{\alpha+i\omega}, \tag{35}$$

which replaces eq (29c). The transient response, denoted by $e_n(\alpha,t)$, is thus given by

$$e_n(\alpha,t)=(H_s)^{1/2}[s_n(\omega_s)]^{3/2}\frac{\alpha}{(\alpha^2+\omega^2)^{\frac{1}{2}}}\frac{\cos[F(\omega_s)+\psi(\omega_s)]}{T_b(\omega_s)}\exp\left[\frac{-2\pi d}{h}u_n(\omega_s)\right], \tag{36}$$

where $\psi(\omega_s)=\arctan(\omega_s/\alpha)$. As α tends to ∞, $e_n(\alpha,t)$, of course, approaches $e_n(t)$, which is the impulse response.[6]

The response $e_1(\alpha,t)$ for the dominant mode at $d=3{,}000$ km is indicated in figure 5 for the same daytime conditions as the curves in figure 4. Various values of the time constant $1/\alpha$

[6] Note that $\delta(t)=\lim_{\alpha\to\infty}\alpha e^{-\alpha t}$ for $t>0$.

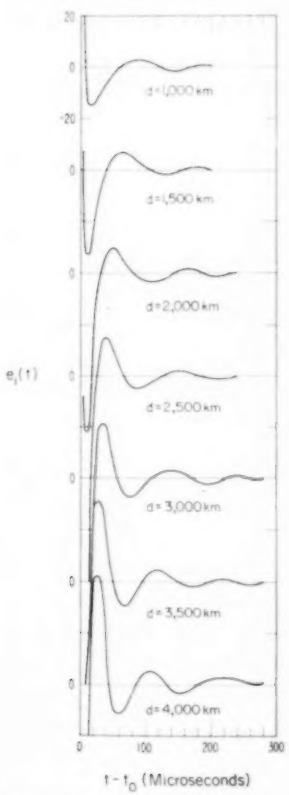

FIGURE 4. *Impulse responses for dominant mode.*
$n=1$, $A\simeq 0$, $h=70$ km, $L/H=0.1$.

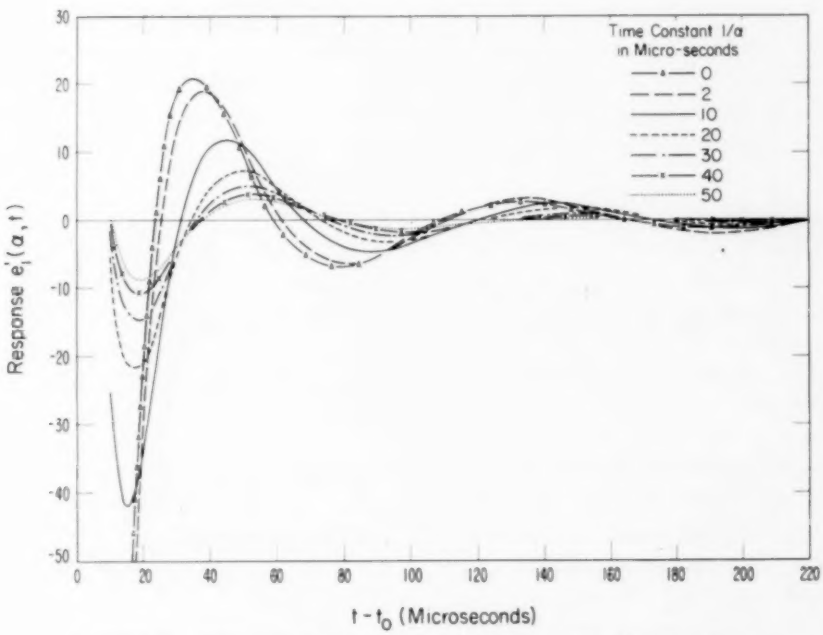

FIGURE 5. *Response of dominant mode for exponential source* $\alpha e^{-\alpha t}$.
$n=1$, $A\simeq 0$, $h=70$ km, $L/H=0.1$, $d=3{,}000$ km.

are indicated on the curves. The impulse response corresponds to the case $1/\alpha=0$. The general nature of the curves is very similar. There appears to be a shift in the phase of the cycles but the quasi-half-periods are essentially unchanged.

A more realistic waveform for the current dipole moment $S(t)$ of a lightning stroke is a pulse which rises up smoothly from zero to a peak value in about 10 or 20 μsec and then decays to zero somewhat more slowly. Examples of such pulses are shown in figure 6, where $S(t)$ is of the form

$$S(t)=\alpha[e^{-\alpha t}-e^{-\alpha_i t}], \tag{37}$$

with $\alpha_i>\alpha$. The response $\bar{e}_1(t)$ to this composite exponential source is then simply obtained by superposition of the exponential responses. For example,

$$\bar{e}_1(t)=e_1(\alpha,t)-\frac{\alpha}{\alpha_i}e_1(\alpha_i,t). \tag{38}$$

Employing the three particular forms of source current $S(t)$, the response $\bar{e}_1(t)$ for the dominant mode is shown plotted in figure 7 for typical daytime conditions over sea water. The curves

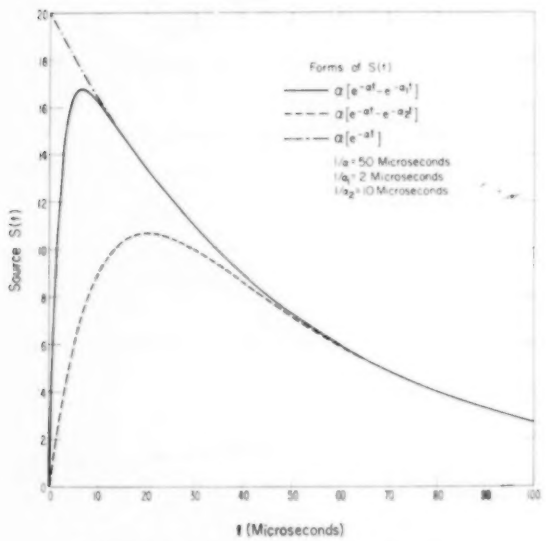

FIGURE 6. *Idealized source functions.*

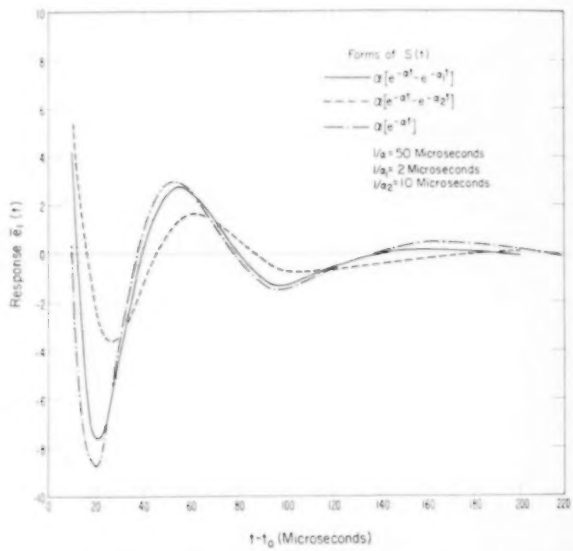

FIGURE 7. *Response of dominant mode for idealized source functions.*

($n=1$, $A\cong 0$, $h=70$ km, $L/H=0.1$) $d=3{,}000$ km; forms of $S(t)$.

again are very similar in appearance to the previous response curves for impulse and single exponential sources. The effect of finite rise time of the source current is to reduce the amplitudes of the peaks in the initial part of the waveform.

It is rather important to note that the quasi-half-periods are not appreciably influenced by the nature of the source pulse. It would therefore seem justified to compare the variation of the quasi-periods with range for the calculated impulse responses and the experimental waveforms of Hepburn.[7] Such a comparison is shown in figure 8. The solid curves are the calculated quasi-half-periods in microseconds for daytime conditions as a function of range. Only the first five half-cycles are shown. The corresponding data from Hepburn's paper is shown by the encircled numbers which indicate the order of the half-cycle. The agreement is quite reasonable.

[7] F. Hepburn, Wave-guide interpretation of atmospheric waveforms, J. Atmospheric and Terres. Phys. **10,** 121 (1957).

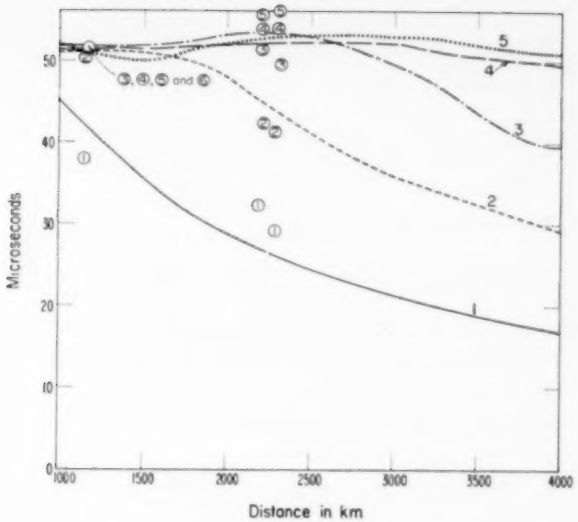

FIGURE 8. *Quasi-half-periods of dominant mode.*
($n=1$, $A\cong 0$, $h=70$ km, $L/H=0.1$),
②From Hepburn's measured waveforms.

The calculated variation of the quasi-half-period with range and time are also in good qualitative agreement with Norinder's [8] observed waveforms who first pointed out the characteristic transformation of the quasi-half-periods.

The transient waveforms presented in figures 4 to 7 are the dominant ($n=1$) mode only. The same procedure can be used to calculate the higher order mode responses. At ranges exceeding about 2,000 km, these do not contribute appreciably to the total field for the range of times shown on the curves.

The transient response of zero-order mode can also be important for longer times. It corresponds to what has been called the "slow tail" in atmospheric waveforms. Again for the range of time shown in figures 4 to 7 it would not be significant. For the sake of completeness, a short analysis of the transient response of the zero-order mode is presented in section 7.3.

6. Conclusion

The analyses and results presented in this paper should be useful in the interpretation of experimental results for the propagation of pulses to large distances over the surface of the earth. It appears to be desirable to separate the transient analyses into two parts depending on whether the source is a quasi-monochromatic pulse containing a narrow band of frequencies or an impulsive type having many spectral components over a wide frequency range. The parameters describing the propagation of these two classifications of pulses have been presented in graphical form.

7. Appendixes

7.1. Waveguide Modes [9]

The earth is taken to be a homogeneous sphere of conductivity σ and dielectric constant ϵ. The lower edge of the assumed homogeneous ionosphere is taken to be at a height h. The collisional frequency is ν and the plasma frequency is ω_0.

Assuming that the source is a vertical dipole radiating P kilowatts, the vertical electric field in millivolts per meter at the great circle distance d in kilometers, for a time factor exp $(i\omega t)$, is given by the mode sum,

$$E=E_0W,$$

[8] H. Norinder, The waveform of the electric field in atmospherics, Arkiv for Geophysik **2**, 161 (June 1954).
[9] J. R. Wait, On the mode theory of VLF ionospheric propagation, Geofis. pura e Appl. **37**, 103 (1957).

where

$$W \cong \left[\frac{(d/a)}{\sin\,(d/a)}\right]^{1/2} \frac{(d/\lambda)^{1/2}}{(h/\lambda)} e^{i\left[\frac{2\pi d}{\lambda}-\frac{\pi}{4}\right]} \sum_{n=0}^{\infty} \delta_n S_n^{3/2} e^{-2\pi S_n (d/\lambda) i}, \tag{1.1}$$

$$E_0 = \frac{300\sqrt{P}}{d},\ \delta_n = \left[1+\frac{\sin\,(4\pi C_n h/\lambda)}{(4\pi C_n h/\lambda)}\right]^{-1} \quad \begin{matrix} \cong \tfrac{1}{2} \text{ for } n=0 \\ \cong 1 \text{ for } n \neq 0, \end{matrix}$$

where $S_n = (1-C_n^2)^{1/2}$, and C_n is a solution of

$$R_g(C) R_i(C) \exp(-4\pi i C h/\lambda) = \exp(-i2\pi n). \tag{1.2}$$

$R_g(C)$ is the Fresnel reflection coefficient at the ground for a plane wave whose (complex) angle of incidence is the arc cosine of C, and $R_i(C)$ is the corresponding Fresnel reflection coefficient at the lower edge of the ionosphere.

It follows from the previous analysis (see footnote 9) that

$$R_g(C) = \frac{(KG-i)C-[(K-1)G^2-iG+C^2G^2]^{1/2}}{(KG-i)C+[(K-1)G^2-iG+C^2G^2]^{1/2}}, \tag{1.3}$$

where $K=\epsilon/\epsilon_0$, and $G=(\epsilon_0\omega)/\sigma$, and

$$R_i(C) = \frac{N^2C-(N^2-S^2)^{1/2}}{N^2C+(N^2-S^2)^{1/2}}, \tag{1.4}$$

where [10]

$$N^2 \cong 1-i/L = 1-i(\omega_r/\omega),\ \omega_r = \omega_0^2/\nu. \tag{1.5}$$

The complex values of $S_n (n=0,1,2,\ \ldots)$ satisfying eq (2) have been obtained from an automatic computor by using a program devised by H. H. Howe. When L is small compared with unity, it was shown previously (see footnote 9) that

$$S_n \cong \left[1-\left(\frac{\lambda n}{2h}\right)^2\right]^{1/2} - \frac{\lambda}{4\pi h} e^{i3\pi/4} (G^{1/2}+L^{1/2}) \frac{\bar{\epsilon}_n}{\left[1-\left(\frac{\lambda n}{2h}\right)^2\right]^{1/2}}, \tag{1.6}$$

where

$$\bar{\epsilon}_0 = 1,\ \bar{\epsilon}_n = 2 (n \neq 0). \tag{1.7}$$

The above formula for S_n is particularly suitable for very low frequencies, in which case only the zero mode is of any consequence.

The exponential term inside the summation of eq (1.1) determines, in the main, the propagation characteristics of the modes. It can be rewritten as follows:

$$\exp[-i2\pi S_n (d/\lambda)] = \exp\left[-\frac{2\pi d}{h} u_n\right] \exp\left[\frac{-i2\pi d}{\lambda} s_n\right], \tag{1.8}$$

where $u_n = -ImS_n(h/\lambda)$, and $s_n = ReS_n$.

7.2. Transient Response of Ideal Waveguides

Most of the complications in the waveguide mode theory of VLF ionospheric propagation are due to the finite conductivity of the bounding walls. The characteristics of the modes are obtained only from a numerical iteration procedure. When the losses in the walls are negligible, it is possible to derive somewhat simpler forms for the transient response and associated parameters.

Assuming that both walls of the waveguide are of perfect conductivity, the phase velocity is given by

$$\frac{v_p}{c} = \frac{1}{s_n} = \left[1-\left(\frac{n}{2H}\right)^2\right]^{-1/2} \tag{2.1}$$

[10] These expressions for the effective refractive index which tacitly neglect the earth's magnetic field are valid for VLF and small values of C.

and the group velocity by

$$\frac{v_g}{c}=s_n=\left[1-\left(\frac{n}{2H}\right)^2\right]^{1/2}. \tag{2.2}$$

Furthermore,

$$F(\omega)=F(H)=\frac{2\pi H}{h}\left(1-\left(\frac{n}{2H}\right)^2\right)^{1/2}d-\frac{2\pi ct}{h}H, \tag{2.3}$$

and, consequently, the saddle point is obtained from

$$\frac{\partial F(H)}{\partial H}=0, \tag{2.4}$$

which is satisfied by

$$H=H_s=\frac{n\,ct}{2X}, \tag{2.5}$$

where

$$X=[(ct)^2-d^2]^{1/2}. \tag{2.6}$$

Consequently,

$$F(H_s)=\frac{-\pi nX}{h}, \tag{2.7}$$

$$[\overline{T}_b]^2=\left[\frac{\partial^2}{\partial H^2}s_nH\right]_{H=H_s}=\left(\frac{2}{n}\right)\frac{X^3}{d^3}, \tag{2.8}$$

and

$$\overline{s}_n=s_n(H_s)=d/ct. \tag{2.9}$$

Inserting these values into the saddle-point formula given by eq (32) leads to

$$e_n(t)=\left(\frac{n}{2}\right)\frac{d^3}{X^2(ct)}\cos\left(\frac{\pi nX}{h}\right), \tag{2.10}$$

for $n=1, 2, 3. \ldots$

The preceding formula is the waveform for the vertical electric field at range d on an ideally perfectly conducting earth with a perfectly conducting ionosphere at height h. It is valid for large distances such that $d>>h$ and X.

If the upper boundary was a perfect magnetic conductor (phase shift of 180° on reflection rather than 0°), the preceding formulas are modified by replacing n by $n-\frac{1}{2}$.

7.3. Transient Response of the Zero-Order Mode

The saddle-point method is valid only if the function $\exp[-iF(\omega)]$ is rapidly varying compared to other factors in the integrand of the inverse Fourier integral. For mode zero this is not so, but in this case it is known (see footnote 9) that

$$\left[\frac{2\pi u_0}{h}+is_0\frac{\omega}{c}\right]d\simeq\left(\frac{1}{\alpha_g}+\frac{1}{\alpha_i}\right)\frac{d}{c}(i\omega)^{1/2}, \tag{3.1}$$

where

$$\alpha_g\simeq\sqrt{\sigma_g\mu}\cdot 2h \qquad \text{and} \qquad \alpha_i\simeq\sqrt{\sigma_i\mu}\cdot 2h.$$

Therefore, for the impulse current source,

$$E(\omega)\simeq\frac{E_1}{2}\left[\frac{d/a}{\sin d/a}\right]^{1/2}\frac{(2\pi cd)^{1/2}}{h}(i\omega)^{1/2}\exp\left[-\frac{d}{c}\left(\frac{1}{\alpha_e}+\frac{1}{\alpha_i}\right)(i\omega)^{1/2}\right] \tag{3.2}$$

The transient response $e_0(t)$ of the zero-order mode is thus given by

$$e(t)=\frac{1}{2\pi}\int_{-\infty}^{+\infty}E(\omega)e^{i\omega t'}d\omega,$$

where $t'=t-t_0$. This can be evaluated to yield

$$e(t)=E_1\left[\frac{d/a}{\sin d/a}\right]^{1/2}(2\pi)^{1/2}\frac{c^2}{h^2}e_0(t)\cdot\tfrac{1}{2}, \tag{3.3}$$

where

$$e_0(t)=\frac{4}{\sqrt{\pi}}\left(\frac{h}{d}\right)^3\left(\frac{h}{c}\right)\left(\frac{d}{c}\right)^{1/2}\left(\frac{\sigma}{\epsilon}\right)^{3/2}P(\beta/t'), \tag{3.4}$$

and

$$P(\beta/t')=\left(\frac{\beta}{2t'}-1\right)\left(\frac{\beta}{t'}\right)^{3/2}e^{-\beta/4t'}, \tag{3.5}$$

with

$$\beta^{1/2}=\left(\frac{d}{2h}\right)\left(\frac{\epsilon_0}{\sigma}\right)^{1/2} \quad \text{and} \quad \frac{1}{\sqrt{\sigma}}=\frac{1}{\sqrt{\sigma_i}}+\frac{1}{\sqrt{\sigma_g}}.$$

The transient response is thus proportional to the characteristic function $P\ (\beta/t')$. In view of the combination in which the ionospheric conductivity σ_i and the ground conductivity σ_g occur, and because $\sigma_g>>\sigma_i$, it follows that $\sigma\cong\sigma_i$. The transient response of the zero-order mode does then not depend to any extent on σ_g. The function $P(\beta/t)$ is plotted in figure 9 as a function of T, where $T=t'/\beta$. The multiple scale shown at the bottom of the figure is to facilitate the conversion of the parameter T to actual time in microseconds.

The transient response of the zero-order mode has been studied extensively by Schumann.[11]

[11] W. O. Schumann, Uber die Oberfelder bei Ausbreitung langer elektrischer Wellen um die Erde und die Signale des Blitzes, Nuovo cimento **9**, 1 (December 1952).

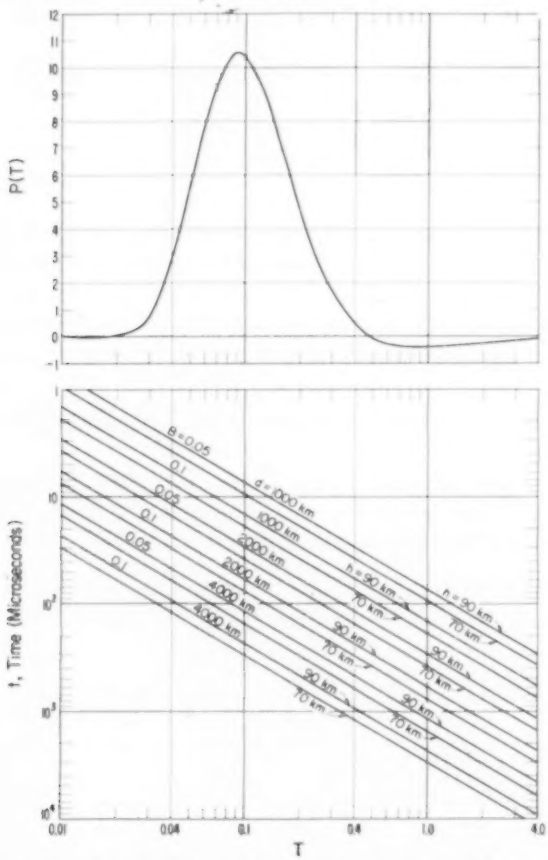

FIGURE 9. *Zero-mode transient response for impulse source.*

7.4. Justification of the Saddle-Point Method

It is worth while to examine the transient calculation from a slightly different viewpoint in order to give further justification to the use of the saddle-point method of integration. When the earth and the ionosphere are represented by perfectly conducting planes with constant separation h, the magnetic field on the earth of a vertical electric dipole on the earth is a sum of modes of the type

$$H_n(\omega)=i\omega\frac{\partial\pi_n}{\partial d}, \tag{4.1}$$

where π_n is a z-directed Hertz vector given by

$$\pi_n=\frac{2i\pi^2}{h}e^{i\omega t}H_0^{(2)}\left[kd\left(1-\frac{\pi^2n^2}{k^2h^2}\right)^{1/2}\right] \tag{4.2}$$

apart from a constant factor. $H_0^{(2)}$ is the Hankel function of the second kind for an impulsive current source (i. e., current moment proportional to $\delta(t)$), the magnetic field of a mode is then given by

$$h_n(t)=\frac{\pi}{h}\frac{\partial}{\partial d}\int_{-\infty}^{+\infty}e^{i\omega t}H_0^{(2)}\left[\left(\omega^2-\frac{\pi^2n^2c^2}{h^2}\right)^{1/2}\frac{d}{c}\right]d\omega. \tag{4.3}$$

This integral can be evaluated [12, 13] to yield

$$h_n(t)=\frac{\pi}{h}\frac{\partial}{\partial d}\frac{c}{X}\left[\cos\frac{\pi nX}{h}-\frac{2}{\pi}\sin\frac{\pi nX}{h}\log_e\frac{ct+X}{d}\right], \tag{4.4}$$

where $X=[(ct)^2-d^2]^{1/2}$. When $X<<ct$ or d and $d>>h$, the term containing the logarithm is negligible, and consequently

$$h_n(t)\simeq\frac{\pi cd}{hX^3}\left\{\cos\left(\frac{\pi nX}{h}\right)+\frac{\pi nX}{h}\sin\left(\frac{\pi nX}{h}\right)\right\}. \tag{4.5}$$

This latter form could have been obtained directly from eq (4.3), using the saddle-point procedure adopted in the main body of the paper.

7.5. Symbols

ω = (angular) frequency,
d = distance from source to observer measured along the surface of the earth,
h = separation between the earth and the lower edge of the ionosphere,
λ = wavelength in free space,
u_n = attenuation factor of the waveguide mode of order n,
s_n = phase factor for a mode of order n,
c = velocity of light in free space,
v_p = phase velocity of a mode,
v_g = group velocity of a mode,
$H=h/\lambda$,
$E_0(t)$ = form of undistorted signal,
$A(t)$ = envelope of undistorted signal,
ω_0 = carrier frequency of undistorted signal,
T = duration or rectangular envelope,
$G(\omega)$ = Fourier or frequency spectrum of $E_0(t)$,
$E(t)$ = form of signal after propagation through dispersive medium,

[12] N. W. McLachlan and P. Humbert, Memorial des sciences mathematiques fascicule **100**, 34. Paris (1941).
[13] K. G. Budden, The propagation of a radio atmospheric, **42**, 1 (January 1951).

$\phi(\omega) = s_n \frac{2\pi d}{\lambda}$ and

$\alpha(\omega) = u_n \frac{2\pi d}{h}$ are phase and attenuation factors of a mode as a function of frequency for a range d,

t' = an integration variable in eq (8) to (15),

$\Omega = \omega - \omega_0$, an expansion parameter,

$\phi'(\omega_0) = [d\phi(\omega)/d\omega]_{\omega=\omega_0}$,

$\phi''(\omega_0) = [d^2\phi(\omega)/d\omega^2]_{\omega=\omega_0}$,

u_1 and u_2 = limits of integration in eq (19),

θ = the time measured from the instant $-\frac{T}{2} + \phi'(\omega_0)$,

t_b = time from $\theta = 0$ to the point where the envelope approaches within 5 percent of unity,

$T_b = \frac{c}{2\sqrt{2dh}} t_b$, a dimensionless build-up parameter,

$\epsilon_0 = 8.854 \times 10^{-12}$, permittivity of free space,

σ_g = conductivity of the ground,

$G = \epsilon_0\omega/\sigma_g$,

$A = G/H = 1/60\sigma_g h$,

ω_0 = (angular) plasma frequency,

ν = (angular) collisional frequency,

$\omega_r = \omega_0^2/\nu$,

σ_i = effective ionospheric conductivity,

$L = \omega/\omega_r$,

$B = L/H = 1/60\sigma_i h$,

$\bar{e}_0(t)$ = the radiated electric field for an ideal flat perfectly conducting ground plane,

$\overline{E_0}(\omega)$ = the frequency spectrum of $\bar{e}_0(t)$,

$j(t)$ = instantaneous average current of the source dipole,

$h(t)$ = instantaneous height of the source dipole,

$\delta(t)$ = unit impulse or Dirac function,

$\mu = 4\pi \times 10^{-7}$, permeability of free-space,

$t_0 = d/c$,

$t' = t - t_0$,

$e(t)$ = resultant field of (transient) dipole sources,

$E(\omega)$ = the frequency spectrum of $e(t)$,

a = radius of the earth,

$\delta_n \cong 1$ for $n \neq 0$,

$\simeq \frac{1}{2}$ for $n = 0$ (see eq (1) for more accurate definition),

$F(\omega) = \frac{\omega}{c} s_n d - \omega t$,

ω_s = the saddle point of $F(\omega)$,

E_1 = constant of proportionality in eq (9b),

$\delta'(t)$ = doublet impulse function,

$T_b(H_s) = T_b$, value of T_b at the saddle point $H = H_s = \omega_s h/2\pi c$,

C_n = cosine of the (complex) angle of incidence of the mode of order n at the bounding walls in the waveguide,

$S_n = (1 - C_n^2)^{1/2}$,

ϵ = dielectric constant of the ground,

$K = \epsilon/\epsilon_0$,

$N^2 = 1 - i/L = 1 - i\omega_r/\omega$,

$\bar{\epsilon}_n = 2$ for $n \neq 0$,

$\bar{\epsilon}_0 = 1$,

$X = [(ct)^2 - d^2]^{1/2}$,

$\beta^{1/2} = \left(\frac{d}{2h}\right)\left[\left(\frac{\epsilon_0}{\sigma_i}\right)^{1/2} + \left(\frac{\epsilon_0}{\sigma_g}\right)^{1/2}\right]$,

$P(x) = \left(\frac{x}{2} - 1\right)(x)^{3/2} e^{-\frac{x}{4}}$,

$H_n(\omega)$ = magnetic field of the nth mode of a dipole source in a parallel plate waveguide,

π_n = the corresponding z-directed Hertz vector.

8. Addendum

Because of certain normalizations, the distance d between transmitter and receiver is measured in terms of the great-circle distance at height $h/2$. The phase and group velocities shown in figures 2 and 3 should then be multiplied by $(1-h/2a)\cong 0.995$, if referred to the great-circle distance on the earth's surface. In other places in the paper, this correction is negligible and can be ignored.

It should be noted that the correction factor $(1-h/2a)$ can vary because of changes in height of the ionosphere and changes in the effective earth radius a. For this reason the velocities were presented in figures 2 and 3 in uncorrected form.

There is a further modification to the attenuation factors when a more recondite mode equation is employed.[14] It appears that the attenuation factors are increased by as much as 50 percent for $H>4$ when $n=1$ and $A=0$ but less for other values of n and A. This will not change the appearance of the waveform shapes for the range of time indicated in figures 5 to 9.

The numerical results in section 3 were obtained by H. H. Howe and A. M. Conda, and those in section 5 were obtained by W. E. Mientka. Many helpful suggestions were received from K. G. Budden, A. G. Jean, E. A. Lewis, K. A. Norton, and W. L. Taylor in the course of this work.

---

[14] This equation is

$$P_e(C)P_i(C)\exp\left[-4\pi iCH\left(1+\frac{S^2h}{C^2a}\right)^{\frac{1}{2}}\right]=\exp(-i2\pi n),$$

which reduces to eq (1.2) for $[ReC]^2>>h/a$.

Boulder, Colo., December 18, 1957.

Journal of Research of the National Bureau of Standards Vol. 61, No. 3, September 1958 Research Paper 2899

Transmission and Reflection of Electromagnetic Waves in the Presence of Stratified Media

James R. Wait

A general analysis is presented for the electromagnetic response of a plane stratified medium consisting of any number of parallel homogeneous layers. The solution is first developed for plane-wave incidence and then generalized to both cylindrical and spherical-wave incidence. Numerical results for interesting special cases are presented and discussed. The application of the results to surface-wave propagation over a stratified ground is considered in some detail.

1. Introduction

In the analysis of antenna radiation and kindred problems, it is usually necessary to consider the inhomogeneous nature of the surrounding media. A good example is when an antenna is located over the surface of the earth. In many cases such as this, it is permissible to regard the ground as a semi-infinite medium with a plane surface. Furthermore, this half-space can often be idealized as a homogeneous medium. As long ago as 1907, Zenneck [1][1] showed that a solution of Maxwell's equation could be obtained for such a region by matching certain wave functions at the interface separating the two half-spaces. His solution was characterized as a wave which propagated along the interface without change of waveform with a velocity greater than that of light and was exponentially attenuated with height above the interface (towards the air).

In 1909 Sommerfeld [2] presented an elegant solution for the fields of dipole sources (electric and magnetic) which were located in the air over a homogeneous flat earth. In the final reduction of the integrals to a form suitable for computation, a small but significant error was made. This error was first pointed out explicitly by Norton [3], but not before many had accepted the earlier solution. To compound the confusion, it turned out that Zenneck's surface wave was very similar to Sommerfeld's solution in his 1909 paper. Since that time a large number of papers have appeared treating this subject. The confusion that remains is largely due to the differences in terminology.

The discussion given here relates to three related aspects of this problem. The first is a general analysis of reflection of plane waves from a parallel stratified medium consisting of M homogeneous slabs, the second is the extension to a line source over the stratified medium, and the third is the generalization to dipoles or current elements over the stratified medium. A special case of the latter is when the number M becomes 1, corresponding to the Sommerfeld problem for a half-space.

2. Plane-Wave Incidence

A plane wave with a time factor exp ($i\omega t$) is incident at an angle θ on a stratified medium composed of M homogeneous layers. The electric vector is in the plane of incidence (xz plane). The situation is illustrated in figure 1 where the y axis is out of the paper. The electrical constants of the layers are σ_m, ϵ_m, and μ_m where the subscript m indicates the mth layer below the surface.

From symmetry it can be seen that the magnetic field has only a y component and for the mth layer, it is a solution of the equation

$$(\nabla^2-\gamma^2_m)H_{my}=0, \tag{1}$$

where

$$\gamma^2_m=i\sigma_m\mu_m\omega-\epsilon_m\mu_m\omega^2.$$

[1] Figures in brackets indicate the literature references at the end of this paper.

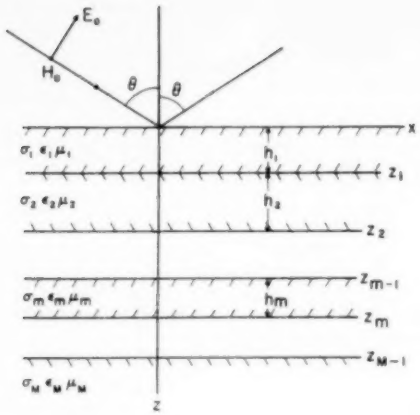

FIGURE 1. *A stratified medium consisting of M homogeneous layers.*

The general solution is of the form

$$H_{my}=[a_m e^{-u_m z}+b_m e^{u_m z}]e^{-i\lambda x}, \tag{2}$$

where

$$u_m^2=\lambda^2+\gamma_m^2,$$

and λ can take any value. The incident field $H^{\text{inc.}}$ can be written

$$H_{0y}^{\text{inc.}}=H_0 e^{-\gamma_0 \cos\theta \cdot z}\times e^{-\gamma_0 \sin\theta x}.$$

Therefore, in eq (2) $a_0 e^{-u_0 z}e^{-i\lambda x}$ can be identified with $H_{oy}^{\text{inc.}}$ if $a_0=H_0$ and $i\lambda=\gamma_0 \sin\theta$. Consequently, $b_0 e^{u_0 z}e^{-i\lambda x}$ is a reflected wave, and the angle of reflection is θ.

The boundary conditions at the interface $z=0$, $z=z_1$, . . ., $z=z_{m-1}$ are that the tangential fields should be continuous. Now since

$$E_{mx}=-(\sigma_m+i\omega\epsilon_m)^{-1}\frac{\partial H_{my}}{\partial z}, \tag{3}$$

this means that the boundary conditions can be written

$$\left[\begin{array}{c} H_{m-1,y}=H_{m,y} \\ (\sigma_{m-1}+i\omega\epsilon_{m-1})^{-1}\dfrac{\partial H_{m-1,y}}{\partial z}=(\sigma_m+i\omega\epsilon_m)^{-1}\dfrac{\partial H_{m,y}}{\partial z} \end{array}\right]_{z=z_{m-1}}, \tag{4}$$

where $m=0, 1, 2, \ldots M-2, M-1$.

Imposing the condition that only outgoing waves are permissible in the lowest layer (which is semi-infinite) it follows that $b_M=0$. The boundary conditions then lead to $2(M-1)$ equations that are linear in a_m and b_m to solve for $2(M-1)$ unknowns in terms of the known coefficient a_0. The solution [2] is

$$\frac{b_0}{a_0}=\frac{K_0-Z_1}{K_0+Z_1}, \tag{5}$$

where

$$Z_1=K_1\frac{Z_2+K_1\tanh u_1h_1}{K_1+Z_2\tanh u_1h_1}$$

$$Z_2=K_2\frac{Z_3+K_2\tanh u_2h_2}{K_2+Z_3\tanh u_2h_2} \tag{6}$$

[2] The quantity λ should not be confused with the wavelength.

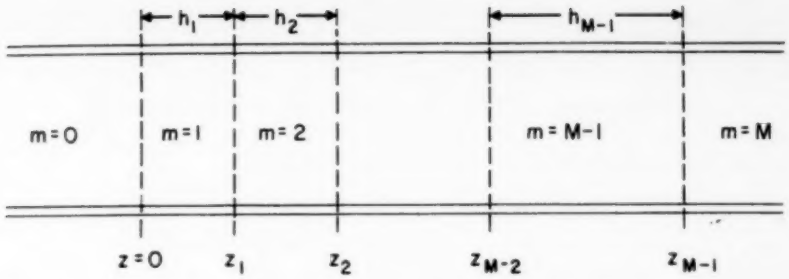

FIGURE 2. *Transmission line analogy for the stratified medium of M layers.*

$$Z_m = K_m \frac{Z_{m+1} + K_m \tanh u_m h_m}{K_m + Z_{m+1} \tanh u_m h_m}$$

$$Z_{M-1} = K_{M-1} \frac{K_M + K_{M-1} \tanh u_{M-1} h_{M-1}}{K_{M-1} + K_M \tanh u_{M-1} h_{M-1}},$$

where

$$K_m = \frac{u_m}{\sigma + i\omega\epsilon_m}, \quad \text{and } u_m = (\lambda^2 + \lambda_m^2)^{1/2}.$$

(Note that h_M is the thickness of the mth slab).

The quantity b_0/a_0 is the ratio of the amplitude of the reflected wave to the amplitude of the incident wave. It is denoted by $R_\parallel$ to indicate that the electric field of the incident wave (and also that of the reflected wave) is in the plane of incidence.

The present problem has a well-defined analogy in transmission line theory.

In this analogy each section of the multiple tandemed line is to correspond to a slab. The voltage across the line is E_{mx} and the current is H_{my} for the mth section. The propagation constant is u_m and the characteristic or surge impedance is K_m of the mth slab. The incident wave that comes from the left in figure 2 is given by $a_0 e^{-u_0 z}$, and the wave reflected at the junction, $z=0$, is $b_0 e^{u_0 z}$. The input impedance of the line that is the ratio of the voltage to the current at $z=0$, is Z_1. Furthermore, the impedance at the junction $z=z_m$ is Z_{m+1}. With this analogy and a knowledge of the behavior of one-dimensional transmission lines, one could write down the solution of the two-dimensional reflection problem.

Some features of the wave problem will now be discussed. The quantity Z_1 will play an important role in the following. Since

$$Z_1 = E_{0x}/H_{0y}]_{z=0} = E_{1x}/H_{1y}]_{z=0},$$

it is called the surface impedance, being the ratio of the tangential fields at the air-ground interface. In the case of normal incidence, $\theta=0$ and $\lambda=0$, so that $u_m=\gamma_m$ and $K_m=\eta_m$, where

$$\gamma_m = [i\sigma_m\mu_m\omega - \epsilon_m\mu_m\omega^2]^{1/2},$$

and

$$\eta_m = [i\mu_m\omega/\sigma_m + i\epsilon_m\omega]^{1/2}.$$

For example, in the case of a homogeneous ground ($h_1 \to \infty$),

$$Z_1 = \eta_1, \quad K_0 = \eta_0,$$

and the reflection coefficient becomes simply

$$R_\parallel = \frac{b_0}{a_0} = \frac{\eta_0 - \eta_1}{\eta_0 + \eta_1}. \tag{7}$$

Another special case of considerable interest is when θ approaches 90° corresponding to glancing incidence, then

$$u_m \cong (\gamma_m^2 - \gamma_0^2)^{1/2}, \quad K_m \cong (\gamma_m^2 - \gamma_0^2)^{1/2}/(\sigma_m + i\omega\epsilon_m),$$

which yields for the homogeneous ground

$$Z_1 = K_1 = \eta_1(1 - \gamma_0^2/\gamma_1^2)^{1/2}. \tag{8}$$

This special value of Z_1, which relates the tangential fields in the limiting case of glancing incidence, turns out to be an important quantity in further work. For this reason, it is denoted by Z^v, where the superscript v indicated that the electric field in the air is nearly vertical for $|\gamma_1| >> |\gamma_0|$. This fact can be shown by evaluating the wave tilt, which is defined by

$$W = \frac{E_{0x}}{E_{0z}}\Bigg]_{z=0} \tag{9}$$

and is the complex ratio of the horizontal to the vertical electric field in the air just above the ground. It readily follows that for the general case [4]

$$W = \frac{E_{1x}/H_{1y}}{E_{0z}/H_{0y}}\Bigg]_{z=0} = \frac{i\omega\epsilon_0 Z_1}{\gamma_0 \sin\theta}. \tag{10}$$

For a homogeneous ground

$$W = \frac{i\omega\epsilon_0 K_1}{\gamma_0 \sin\theta} = \frac{\eta_1}{\eta_0} \frac{\left(1 - \frac{\gamma_0^2}{\gamma_1^2}\sin^2\theta\right)^{1/2}}{\sin\theta}, \tag{11}$$

which for grazing incidence becomes

$$W = \frac{\eta_1}{\eta_0}\left(1 - \frac{\gamma_0^2}{\gamma_1^2}\right)^{1/2} = \left(\frac{\mu_1}{\mu_0}\right)\frac{\gamma_0}{\gamma_1}\left(1 - \frac{\gamma_0^2}{\gamma_1^2}\right)^{1/2}. \tag{12}$$

For radio frequencies ($\omega \cong 10^6$) and moderately conducting ground ($\sigma \cong 10^{-2}$), $|\gamma_0/\gamma_1|$ is of the order of 10^{-2}, and thence W is small and hence $|E_{0z}|$ is much greater than $|E_{0x}|$.

To indicate in a simple way as is possible, the influence of stratification on the reflection of waves from the ground surface, a two-layer case will be considered. This is effected by letting $h_2 \to \infty$. Furthermore, it will be assumed that $|\gamma_1/\gamma_0|$ and $|\gamma_2/\gamma_0| >> 1$. Then for any angle of incidence

$$u_m = \gamma_m\left(1 - \frac{\gamma_0^2}{\gamma_m^2}\sin^2\theta\right)^{1/2} \cong \gamma_m \qquad (m = 1, 2),$$

and

$$K_m = \frac{u_m}{\sigma_m + i\epsilon_m\omega} \cong \eta_m \qquad (m = 1, 2).$$

This leads to the simple relation

$$Z_1 \cong QK_1, \tag{13}$$

where

$$Q = \frac{(\gamma_1/\gamma_2) + \tanh\gamma_1 h_1}{1 + (\gamma_1/\gamma_2)\tanh\gamma_1 h} \quad \text{for} \quad \mu_1 = \mu_2 = \mu_0,$$

and where Q is the correction to the characteristic impedance K_1 of the upper layer to account for the presence of the lower layer. Note then, if $|\gamma_1 h_1| >> 1$, $Q \cong 1$. It can be said that the lower layer is not detectable when $|Q|$ is within 5 percent of unity. Such a condition is met when $(\sigma_1\mu_0\omega)^{1/2}h > 3$.

It should also be noted that Q relates the wave tilts for a stratified (two-layer) ground and that of a homogeneous ground by $W \cong W_0 Q$, where

$$W_0 \cong W]_{h_1=\infty}.$$

An example is here quoted to illustrate the order of magnitude of the quantities involved:

Frequency, $f=\omega/2\pi=125$ kc
Upper layer conductivity, $\sigma_1=10^{-2}$ mho/m,
Dielectric constant of air, $\epsilon_0=8.854\times10^{-12}$ f/m,
Dielectric constant of ground, $\epsilon_1=10\cdot\epsilon_0$,
Magnetic permeability, $\mu=4\pi\times10^{-7}$ h/m.

For these values, $W_0=0.082/\underline{41.1°}$, for a homogeneous ground. In the case of a two-layer ground where h_1 is finite,

$$W=W_0Q$$

$$=0.082|Q|/\underline{41.1°+q},$$

where q is the argument of Q expressed in degrees. For frequencies of this order, $\epsilon_1\omega/\sigma_1$ and $\epsilon_2\omega/\sigma_2$ are small (in the above example $\epsilon_1\omega/\sigma_1=0.0069$). Therefore, $\gamma_1\cong(i\sigma_1\mu\omega)^{\frac{1}{2}}$ and $\gamma_2\cong(i\sigma_2\mu\omega)^{\frac{1}{2}}$. A formula suitable for computation of Q is then given by

$$Q=\frac{(\sigma_1/\sigma_2)^{\frac{1}{2}}+\tanh\sqrt{i}V}{1+(\sigma_1/\sigma_2)^{\frac{1}{2}}\tanh\sqrt{i}V} \tag{14}$$

$$=\tanh[\sqrt{i}\,V+\tanh^{-1}(\sigma_1/\sigma_2)^{\frac{1}{2}}].$$

If $\sigma_2>>\sigma_1$ corresponding to a highly conducting substratum,

$$Q\cong\tanh\sqrt{i}V \tag{15}$$

or if $\sigma_2<<\sigma_1$ corresponding to an insulating substratum,

$$Q\cong\coth\sqrt{i}V. \tag{16}$$

In the above example, the parameter V can be replaced by $h_1/10$, where h_1 is the thickness of the upper stratum in meters. The function Q and its argument q are plotted in figure 3a and 3b as a function of V for various values of the ratio σ_2/σ_1.

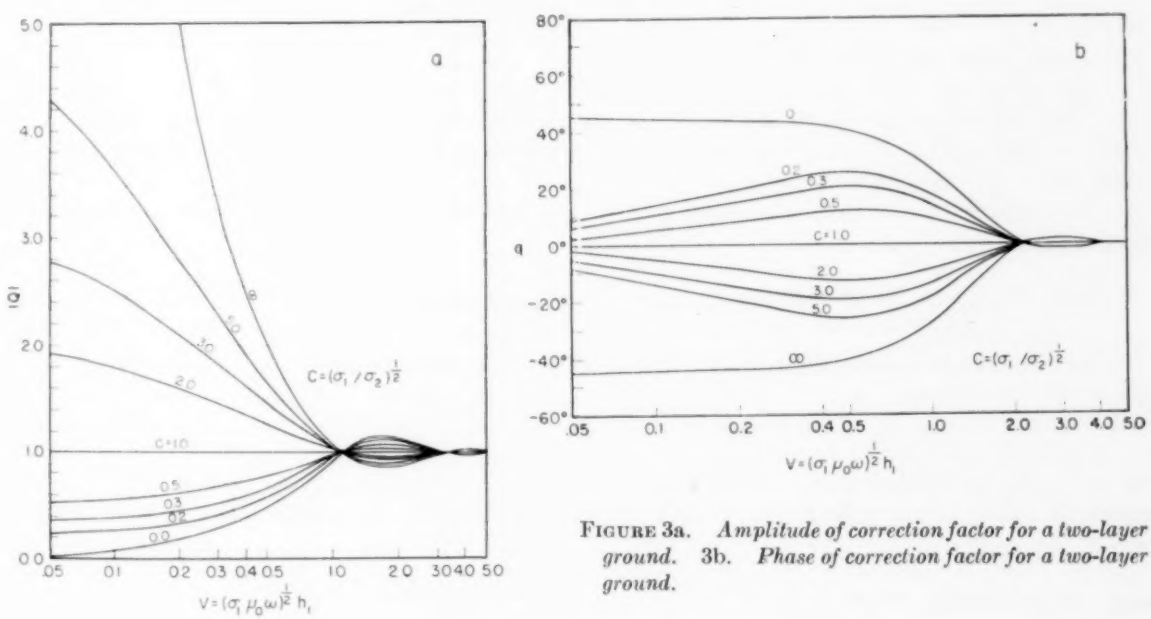

FIGURE 3a. *Amplitude of correction factor for a two-layer ground.* 3b. *Phase of correction factor for a two-layer ground.*

3. Extension to Perpendicular Incidence

In the preceding problem, the incident-plane wave has the electric vector contained in the plane of incidence (and the magnetic vector parallel to the interfaces). For this reason, it is termed "parallel incidence". The other important case is when the electric vector is perpendicular to the plane of incidence. This is termed "perpendicular incidence".

Again choosing the plane of incidence to be the (xz) plane, the incident wave now has only a y component of the electric field. By analogy to eq 2, the general solution is of the form

$$E_{my}=[\bar{a}_m e^{-u_m z}+\bar{b}_m e^{u_m z}]e^{-i\lambda x}, \tag{17}$$

where $u^2_m=\lambda^2+\gamma^2_m$, $\bar{a}_0$ is the amplitude of the incident wave, $\bar{b}_0$ is the amplitude of the reflected wave, and $\bar{b}_M=0$. In this case,

$$i\mu_m\omega H_{mx}=\frac{\partial E_{my}}{\partial z}, \tag{18}$$

so that the boundary conditions now become

$$\left.\begin{aligned} E_{m-1,\,y}&=E_{m,\,y}\\ (i\mu_{m-1}\omega)^{-1}\frac{\partial E_{m-1,\,y}}{\partial z}&=(i\mu_m\omega)^{-1}\frac{\partial E_{m,\,y}}{\partial z}\end{aligned}\right]_{z=z_m}. \tag{19}$$

These are transformable to the boundary conditions for parallel incidence by making the substitutions: E_{my} for H_{my}, $i\mu_m\omega$ for $\sigma_m+i\epsilon_m\omega$. Then using the previous results, the solution for perpendicular incidence can be written down:

$$\frac{\bar{b}_0}{\bar{a}_0}=\frac{N_0-Y_1}{N_0+Y_1}, \tag{20}$$

where

$$Y_m=N_m\frac{Y_{m+1}+N_m\tanh u_m h_m}{N_m+Y_{m+1}\tanh u_m h_m}, \tag{21}$$

for $m=1, 2, 3, \ldots, M-1$ and

$$Y_M=N_M.$$

In the preceding

$$N_m=\frac{u_m}{i\mu_m\omega}, \tag{22}$$

where, as before, $u_m=(\lambda^2+\gamma^2_m)^{1/2}$.

The quantity $\bar{b}_0/\bar{a}_0$, which is the ratio of the amplitude of the reflected wave to the incident wave, is denoted by $R_\perp$. There is a similar transmission line analogy for this problem, which need not be pointed out.

In analogy to the surface-impedance function Z_1, the quantity Y_1 is a surface admittance and is given by

$$Y_1=-H_{0x}/E_{0y}]_{z=0}=-H_{1x}/E_{1y}]_{z=0}. \tag{23}$$

In the case of a homogeneous ground at glancing incidence $(\theta\to\pi/2)$, it follows that

$$Y_1=N_1=(1/\eta_1)(1-\gamma^2_0/\gamma^2_1)^{1/2}, \tag{24}$$

which is denoted Y^h, where the superscript h indicates that the electric field is horizontal in contrast to the near vertical electric field associated with Z^v. It is interesting to note that

$$Y^hZ^v=(1-\gamma^2_0/\gamma^2_1), \tag{25}$$

and for $|\gamma^2_1|>>|\gamma^2_0|$, $Y^hZ^v\cong 1$.

4. Impedance Matching and Natural Oscillations in Stratified Media

In this section, some remarks will be made concerning the nature of extreme conditions where the reflection coefficient on a plane stratified media becomes zero or infinite. The discussion will be confined primarily to parallel incidence, although the results are easily carried over to perpendicular incidence.

As indicated, the reflection coefficient $R_\parallel$ is given by

$$R_\parallel = \frac{K_0 - Z_1}{K_0 + Z_1}, \tag{26}$$

where

$$K_0 = u_0/i\omega\epsilon_0 = (\lambda^2 - k_0^2)^{1/2}/i\omega\epsilon_0$$

and Z_1 is the normal impedance at the interface $z=0$. In the case of a homogeneous half space ($h_1 \to \infty$),

$$Z_1 = K_1 = u_1/(\sigma_1 + i\omega\epsilon_1) = (\lambda^2 + \gamma_1^2)^{1/2}/(\sigma_1 + i\omega\epsilon_1). \tag{27}$$

The condition for matching is that $R_\parallel = 0$ corresponding to the absence of a reflected wave. This requires that

$$K_0 = Z_1. \tag{28}$$

For a homogeneous half-space, the condition is simply

$$K_0 = K_1, \tag{29}$$

which, when solved for λ, yields

$$\lambda = \pm\left[\frac{\mu_1^2/\gamma_1^2 - \mu_0^2/\gamma_0^2}{\mu_0^2/\gamma_0^4 - \mu_1^2/\gamma_1^4}\right]. \tag{30}$$

In the case of no magnetic permeability contrast ($\mu_1 = \mu_0$), the above simplifies [3] to

$$i\lambda = \pm\frac{\gamma_1\gamma_0}{(\gamma_1^2 + \gamma_0^2)^{1/2}}, \tag{31}$$

and if both media are perfect dielectrics $\gamma_1 = ik_1$ and $\gamma_0 = ik_0$,

$$\lambda = \pm\frac{k_1 k_0}{(k_1^2 + k_0^2)^{1/2}}. \tag{32}$$

But, since $\lambda = k_0 \sin\theta$, the preceding equations for a condition of matching can be employed to determine the angle of incidence when there shall be no reflection. In the case of the two dielectric half-spaces, the condition is

$$\sin\theta = \pm\frac{k_1}{(k_1^2 + k_0^2)^{1/2}}, \tag{33}$$

or $\tan\theta = \pm(k_1/k_0)$. This latter equation is well known from optics, and there the angle θ is known as the Brewster angle, and the ratio k_1/k_0 is called the relative refractive index.

It is indeed very interesting to observe that if k_1 is not real, (or γ_1 not imaginary), the quantity λ or θ required for matching is complex. That is, in the language of optics, the Brewster angle for an absorptive homogeneous medium is complex. The existence of plane waves with a complex angle of incidence will not be discussed at this stage, but it is interesting to note that the so-called Zenneck surface wave is very similar to the disturbance propagating along the interface, when there is a condition of wave matching. His solution is briefly described below.

[3] In this case the wave tilt $W = \gamma_0/\gamma_1$, as can be deduced from eq. 11.

Zenneck [1] postulated that a surface wave could propagate along the interface $z=0$ between two homogeneous media. He assumed that in the upper medium ($z<0$)

$$H_{0y}=b_0e^{+u_0z}e^{-\Omega x}, \tag{34}$$

and in the lower medium

$$H_{1y}=a_1e^{-u_1z}e^{-\Omega x}, \tag{35}$$

for propagation in the x-direction. The signs prefixing u_0 and u_1 were chosen to insure that the field decayed to zero for $|z|\to\infty$. The corresponding electric fields are then obtained from Maxwell's equations,

$$E_{0y}=-K_0b_0e^{u_0z}e^{-\Omega x}, \tag{36}$$

and

$$E_{1y}=K_1a_1e^{-u_1z}e^{-\Omega x}. \tag{37}$$

The boundary conditions then require that $b_0=a_1$, and

$$K_0+K_1=0 \quad \text{or} \quad \frac{u_0}{\epsilon_0}+\frac{u_1}{\epsilon_1-i\sigma_1/\omega}=0.$$

The latter condition cannot be met for any value of λ if the imaginary parts of u_0 and u_1 are to be greater than zero. It now appears that Zenneck solved the matching equation $K_0=K_1$ in place of $K_0=-K_1$.

Returning to the general case, it is seen that

$$R_{\parallel}=\frac{K_0-Z_1}{K_0+Z_1} \tag{38}$$

has a pole (i. e., becomes infinite) when

$$K_0+Z_1=0. \tag{39}$$

This is termed the "resonance condition." For the homogeneous half-space, this resonance condition is simply $K_0+K_1=0$, which is identical to Zenneck's equation for a surface wave.

Although it is not possible to set up a surface wave in the sense envisaged by Zenneck, it is possible to retain his solutions if the disturbance in the upper medium is a wave containing a factor e^{-u_0z} in place of e^{+u_0z}, and the boundary condition becomes $K_0=K_1$, which corresponds to the "matching" condition.

In the case of a stratified media, it may well happen that the "resonance" condition $K_0+Z_1=0$ is satisfied. Rewriting this as

$$Z_1=i\,\frac{u_0}{\epsilon_0\omega}, \tag{40}$$

and since for a surface wave u_0 is to be mainly real (i. e., small imaginary component), then Z_1 is to be mainly imaginary (in the positive sense). Such a surface characteristic is described as inductive. The quantity λ, which describes the transverse propagation, is mainly real and somewhat greater than k_0 [i.e., $\lambda^2=u_0^2+k_0^2$].

A simple example of an inductive surface is a highly conducting plane, coated with a thin uniform film of dielectric. From eq 6 with $Z_2=0$ (or $\gamma_2=\infty$)

$$Z_1\cong K_1\tanh u_1h_1, \tag{41}$$

where h_1 is the thickness of the film. For thin films, and $\mu_0=\mu_1$,

$$Z_1\cong K_1u_1h_1=i\mu_0\omega h_1\left[1-\frac{\lambda^2}{k_1^2}\right]. \tag{42}$$

This can be further approximated to

$$Z_1=i\mu_0\omega h_1[1-(k_0/k_1)^2], \tag{43}$$

since λ is near k_0. Such a surface is therefore almost purely inductive. In this case,

$$u_o = \epsilon_0\mu_0\omega^2\bar{h} = k_0^2\bar{h},$$

and

$$\lambda = (u_0^2 + k_0^2)^{1/2} = k_0[1+(k_0\bar{h})^2]^{1/2} \cong k_0[1+(k_0\bar{h})^2/2],$$

where $\bar{h} = h_1(1-k_0^2/k_1^2)$. The wave has a phase velocity in the transverse (x) direction, which is $1-(k_0h)^2/2$ times that of free space, and it decays rapidly in the z-direction. This approximate solution is valid if $k_0\bar{h}$ (or k_0h_1) is small compared to unity.

In general, the determination of the poles in the reflection coefficient $R_{\parallel}$ leads to transcendental equations that must be solved by numerical or graphical means. A discussion of surface waves on dielectric coated conductors without the restriction that h_1 be small has been given by Atwood [5a]. The subject has also been discussed by Goubau [5b].

Further remarks regarding surface waves will be made in a later section following the analysis of the excitation problem.

5. Line-Source Excitation

In problems of reflection from stratified media, it is more meaningful from a physical standpoint to consider the source a localized distribution of current. No physical source in existence produces pure plane waves, although in certain limiting cases the fields have characteristics closely akin to plane waves. An example is a line source of electric current. It was shown that at large distances from the source, the electric and magnetic field were mutually orthogonal to one another and to the direction of propagation [7]. It might then be conjectured that the reflected wave for a line source located high over a plane interface could be computed from the plane-wave reflection coefficient. Such is the case if certain limitations are imposed.

It is the purpose of this section to extend the plane-wave solution to the case of an (infinite) line source of (constant) electric current located at height h above the stratified medium considered in the previous section. The coordinate of the line source is taken as $(0,y,-h)$, as indicated in figure 4.

In view of the symmetry, the electric field only has a y component E_m for any of the layers (the subscript y on E_m is dropped for convenience). The direct, or primary, field E_0^p in the region $z<0$ (above the interface) is expressible as

$$E_0^p = -\frac{-i\mu\omega I}{2\pi} K_0[\gamma_0[x^2+(z+h)^2]^{1/2}], \tag{44}$$

where K_0 is a modified Bessel function. To convert the expression for E_0^p to a more useful

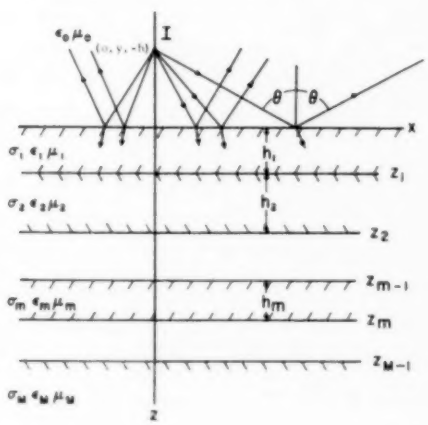

FIGURE 4. *Line source over a layered half-space.*

form, it is written as a Fourier integral as follows:

$$E_0^p = \int_{-\infty}^{\infty} A(\lambda) e^{-i\lambda x} d\lambda. \tag{45}$$

By making use of the inverse property of the Fourier integral, it follows that

$$A(\lambda) = \frac{1}{2\pi} \int_{-\infty}^{\infty} E_0^p e^{i\lambda x} dx \tag{46}$$

$$= \frac{-i\mu_0 \omega I}{4\pi^2} \int_{-\infty}^{+\infty} K_0[\gamma_0[x^2 + (z+h)^2]^{1/2}] e^{i\lambda x} dx. \tag{47}$$

This integral is evaluated to give [4]

$$A(\lambda) = -\frac{i\mu_0 \omega I}{2\pi u_0} e^{\pm u_0(z+h)},$$

where $u_0 = (\lambda^2 + \gamma_0^2)^{1/2}$ and where the + sign is to be employed for $(z+h) < 0$ and the − sign for $(z+h) > 0$.

The resultant field in the space $0 > z > -h$ is then written in the form

$$E_0 = \frac{-i\mu_0 \omega I}{4\pi} \int_{-\infty}^{\infty} u_0^{-1} [e^{-u_0(z+h)} + R_\perp(\lambda) e^{u_0(z-h)}] \exp(-i\lambda x) d\lambda, \tag{48}$$

where the term containing $R_\perp(\lambda)$ accounts for the presence of the stratified medium at $z = 0$ and is as yet unknown. Eq (48) satisfies the equation $(\nabla^2 - \gamma_0^2) E_0 = 0$, and behaves in the proper manner as $z \to -h$ and $x \to 0$. The corresponding expression for E_0 in the region $-h > z > -\infty$ is identical to eq (48), except that the (−) sign on the first exponential should be changed to a + sign. E_0 then decays properly to zero as $z \to -\infty$.

The integral representation for E_0 has a clear physical meaning. When the symbol λ is identified with $k_0 \sin\theta$ or $-i\gamma_0 \sin\theta$, the field E_0^p is a spectrum of plane waves of (complex) angle θ of incidence. The complete field E_0 contains a spectrum of both incident and reflected waves [7]. The structure of the integrand in the integral representation for E_0 is identical to the corresponding factor in the plane-wave solution in the previous section. In fact, the correspondence carries over to each of the sublayers. For example, in the present problem, for $m = 0$ to M,

$$E_m = \int_{-\infty}^{\infty} \left[\bar{a}_m(\lambda) e^{-u_m z} + b_m(\lambda) e^{u_m z} \right] e^{-i\lambda x} d\lambda, \tag{49}$$

and

$$i\mu_m \omega H_{my} = \frac{\partial E_m}{\partial z}, \quad -i\mu_m \omega H_{mz} = \frac{\partial E_m}{\partial x}.$$

The solution of the present problem [5] is thus immediate;

$$R_\perp(\lambda) = \frac{\bar{b}_0(\lambda)}{\bar{a}_0(\lambda)} = \frac{N_0(\lambda) - Y_1(\lambda)}{N_0(\lambda) + Y_1(\lambda)}, \tag{50}$$

where

$$Y_m(\lambda) = \frac{Y_{m+1}(\lambda) + N_m(\lambda) \tanh u_m h_m}{N_m(\lambda) + Y_{m+1}(\lambda) \tanh u_m h_m}, \tag{51}$$

with $m = 1, 2 \ldots, M-1$, and $Y_M(\lambda) = N_M(\lambda)$.

Equation (48), along with (50) and (51), constitutes the formal solution of the problem. The remaining task is the evaluation of the integral in (48). Except in certain limiting cases, certain approximations must be made in order to obtain a useful result.

[4] Campbell and Foster [6], pair No. 917.

[5] It should be noted that eq (50) has the same form as eq (21).

The simplest limiting case is when the interface becomes highly conducting. Then, since $\gamma_1 \cong \infty$, $R_\perp(\lambda) \cong -1$, and

$$E_0 = \frac{-i\mu_0 \omega I}{4\pi} \int_{-\infty}^{+\infty} u_0^{-1} \left[e^{-u_0(z+h)} - e^{u_0(z-h)}\right] e^{-i\lambda x} d\lambda. \tag{52}$$

Both these integrals are of the same type and may be readily evaluated in view of eq (46) and (47). Consequently, for $z<0$,

$$E_0 = \frac{-i\mu_0 \omega I}{2\pi} \left\{ K_0[\gamma_0[x^2+(z+h)^2]^{1/2}] - K_0[\gamma_0[x^2+(z-h)^2]^{1/2}] \right\}. \tag{53}$$

It can be readily verified that $(\nabla^2 - \gamma_0^2)E_0 = 0$ for $-z>0$ and, moreover, $E_0=0$ for $z=0$, which is the required boundary condition for a perfect conductor. It should be mentioned that an equally simple result is obtained for cases where $\mu_1 \cong \infty$, corresponding to a rather hypothetical situation where the interface at $z=0$ is behaving as a perfect magnetic conductor. Then $R_\perp(\lambda) \cong +1$ and the solution for E_0 is identical to eq (53), with the second term inside the braces changing sign.

When $|\gamma_0 h| >> 1$ and $h >> -z$, eq (53) for E_0 can be written in the form [6]

$$E_0 \cong \frac{-i\mu_0 \omega I}{2\pi} \left(\frac{\pi}{2}\right)^{1/2} \frac{e^{-\gamma_0 R_0}}{(\gamma_0 R_0)^{1/2}} \left[e^{-\bar{u}_0(z)} - e^{+\bar{u}_0(z)}\right] e^{-i\bar{\lambda}\bar{x}}, \tag{54}$$

where $\bar{u}_0 = ((\bar{\lambda})^2 + \gamma_0^2)^{1/2}$, $\bar{\lambda} = -i\gamma_0 \sin \bar{\theta}$, and where Q is the geometrical reflection point such that the ray IQ and the ray QP make equal angles $\bar{\theta}$ with the normal at Q. The quantity R_0 is the length of the ray from the line source to the point of reflection Q. In fact, Q is taken as the new origin of the cartesian system $\bar{x}$, y, z, as indicated in figure 5.

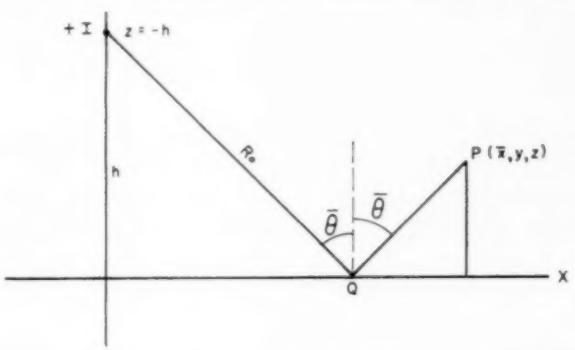

FIGURE 5. *Geometrical interpretation for the secondary field.*

Equation (54) can be simplified even further by noting that the quantity prefixing the square bracket is simply the amplitude of the incident wave. When this is normalized to unity,

$$E_0 = \left[e^{-\bar{u}_0(z)} - e^{+\bar{u}_0(z)}\right] e^{-i\bar{\lambda}\bar{x}}, \tag{55}$$

which is readily identified as an incident and reflected plane wave with an angle of incidence and reflection of $\bar{\theta}$. To generalize, eq (55) for a stratified medium, the reflected wave would be simply modified by a reflection coefficient for an angle of incidence $\bar{\theta}$. The modified form would be

$$E_0 = \left[e^{-\bar{u}_0 z} + R_\perp(\bar{\lambda}) e^{+\bar{u}_0 z}\right] e^{-i\bar{\lambda}\bar{x}}. \tag{56}$$

A suggested modified version of eq (53) to account for the stratified nature of the medium would then be

$$E_0 \cong \frac{-i\mu_0 \omega I}{2\pi} \left\{ K_0[\gamma_0[x^2+(z+h)^2]^{1/2}] + R_\perp(\bar{\theta}) K_0[\gamma_0[x^2+(z-h)^2]^{1/2}] \right\}, \tag{57}$$

when $R_\perp(\bar{\theta})$ is the reflection coefficient for a plane-wave incident at an angle $\bar{\theta}$ on the interface $z=0$. The angle $\bar{\theta}$ is determined by simple geometrical considerations, as indicated above.[7]

[6] The first term of the asymptotic expansion of the modified Bessel function $K_0(\alpha)$ is only retained, i. e., $K_0(\alpha) \cong e^{-\alpha}(\pi/2\alpha)^{1/2}$.

[7] Note then $\tan \bar{\theta} = x/(h-z)$.

This result, which has been derived by an elementary approach, considers only the specular component. For smaller values of $|z|$ and h the situation becomes more complicated because surface waves within the layers may be excited. This question will not be pursued further at the moment.

6. Line Source on a Homogeneous Medium

When the line source is situated at the interface ($h=0$) between two media of semiinfinite extent with electrical properties ϵ_0, μ_0 and σ_1, ϵ_1, μ_0, respectively, the electric field E_0 is given by

$$E_0=\frac{-i\mu_0\omega I}{\pi}\int_0^\infty \frac{\cos\lambda x}{u_1+u_0}e^{+u_0 z}d\lambda, \tag{58}$$

for $z>0$. This is a special case of eq (48) with $h=0$ and $z_1=h_1=\infty$. Noting that

$$\frac{1}{u_1+u_0}=\frac{u_1-u_0}{u_1^2-u_0^2}=\frac{u_1-u_0}{\gamma_1^2-\gamma_0^2},$$

it follows that, for $z=0$

$$E_0=\frac{-i\mu_0\omega I}{\pi(\gamma_1^2-\gamma_0^2)}\left\{\int_0^\infty u_1\cos\lambda x d\lambda-\int_0^\infty u_0\cos\lambda x d\lambda\right\}. \tag{59}$$

Since

$$\lim_{z\to 0}\int_0^\infty \cos\lambda x\frac{e^{-u_0|z|}}{u_0}d\lambda=K_0(\gamma_0 x), \tag{60}$$

which is equivalent to eq (45), it is seen that [8]

$$\int_0^\infty (\cos\lambda x)\,u_0\,d\lambda=\left(\gamma_0^2-\frac{\partial^2}{\partial x^2}\right)K_0(\gamma_0 x)\gamma_0 x=-K_1(\gamma_0 x)\gamma_0 x^{-1}. \tag{61}$$

Making use of this result, the expression for the electric field becomes

$$E_0=\frac{-i\mu_0\omega I}{\pi(\gamma_1^2-\gamma_0^2)x^2}\left[\gamma_0 x K_1(\gamma_0 x)-\gamma_1 x K_1(\gamma_1 x)\right]. \tag{62}$$

This formula is *exact*.

At large values of the argument

$$K_n(\gamma_1 x)\cong\left(\frac{\pi}{2\gamma_1 x}\right)^{1/2}e^{-\gamma_1 x}, \tag{63}$$

and if the real part of $\gamma_1 x$ is $>>1$,

$$E_0\cong\frac{-i\mu_0\omega I\gamma_0}{\pi(\gamma_1^2-\gamma_0^2)x}K_1(\gamma_0 x). \tag{64}$$

Furthermore, if $\gamma_0=ik_0$ where $k_0 x$ is a real number $>>1$, it follows that

$$\begin{aligned}E_0&\cong\frac{-i\mu_0\omega I\gamma_0}{\pi(\gamma_1^2-\gamma_0^2)x}\left(\frac{\pi}{2\gamma_0 x}\right)^{1/2}e^{-\gamma_0 x}\\&\cong\frac{\mu_0\omega k_0 I}{\pi(\gamma_1^2+k_0^2)}\left(\frac{\pi}{2k_0 x^3}\right)^{1/2}e^{-i(k_0 x+\pi/4)}.\end{aligned} \tag{65}$$

It is convenient to express this in terms of the primary field,

$$E_0^p=\frac{-i\mu_0\omega I}{2\pi}K_0(\gamma_0\rho)\cong\frac{-i\mu_0\omega I}{2\pi}\left(\frac{\pi}{2\gamma_0 x}\right)^{1/2}e^{-\gamma_0 x}, \tag{66}$$

[8] In eq (61) use is made of $dK_1/d\alpha=-K_1/\alpha-K_0$, where α is the argument $\gamma_0 x$.

in the following manner:

$$\frac{E_0}{E_0^p} \cong \frac{2\gamma_0}{(\gamma_1^2-\gamma_0^2)x} = \frac{2ik_0}{(\gamma_1^2+k_0^2)x}. \tag{67}$$

The vertical electric field in the interface, for the current line source in the interface, is given by

$$H_{0z}=H_{1z}=-\frac{1}{i\mu_0\omega}\frac{\partial E_0}{\partial x} \tag{68}$$

$$=\frac{1}{\pi(\gamma_1^2-\gamma_0^2)x^3}[2\gamma_0 x K_1(\gamma_0 x)+\gamma_0^2 x^2 K_0(\gamma_0 x)-2\gamma_1 x K_1(\gamma_1 x)-\gamma_1^2 x^2 K_0(\gamma_1 x)] \tag{69}$$

and, if the real part of $\gamma_1 x >> 1$,

$$H_{0z} \cong \frac{\gamma_0 I}{\pi(\gamma_1^2-\gamma_0^2)x^2}[2K_1(\gamma_0 x)+\gamma_0 x K_0(\gamma_0 x)], \tag{70}$$

which simplifies further, for the case $|\gamma_0 x| >> 1$, to

$$H_{0z} \cong \frac{\gamma_0^2 I}{\pi(\gamma_1^2-\gamma_0^2)x}\left(\frac{\pi}{2\gamma_0 x}\right)^{1/2} e^{-\gamma_0 x} \cong E_0/\eta_0, \tag{71}$$

where

$$\eta_0 = i\mu_0\omega/\gamma_0 = \mu_0\omega/k_0 = (\mu_0/\epsilon_0)^{1/2}.$$

The field at very low frequencies near the line source is also of interest. For example if $|\gamma_0 x| << 1$,

$$H_{0z} \cong \frac{I}{\pi\gamma_1^2 x^3}[2-2\gamma_1 x K_1(\gamma_1 x)-(\gamma_1 x)^2 K_0(\gamma_1 x)], \tag{72}$$

which approaches $-I/2\pi x$ as $\gamma_1 x$ approaches zero.

The magnetic field H_{0z} expressed as a ratio to the primary field H_{0z}^p $(=-I/2\pi x)$ is plotted in figure 6 as a function of $|\gamma_1 x|$ under the assumption that $\epsilon_1\omega/\sigma_1 \cong 0$.

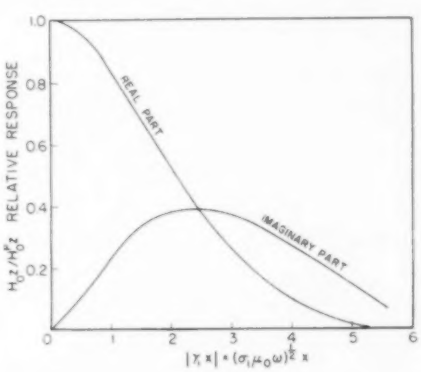

FIGURE 6. *Response of a line source on a homogeneous half-space.*

7. Line Source Over a Thin Layer

The general solution for M layer can also be specialized conveniently to the case of a line source at a height h over a thin sheet of thickness h_1 and conductivity σ_1. The following substitutions in eq (48) are made: $\mu_m=\mu_0$, $M=2$, $\gamma_2=\gamma_0$ where it is supposed that the medium above and below the sheet is homogeneous. The electric field for $z<0$ is given by

$$E_0=-\frac{i\mu_0\omega I}{2\pi}\left\{K_0(\gamma_0 r_1)-K_0(\gamma_0 r_2)+\int_0^\infty \frac{2e^{u_0(z-h)}\cos\lambda x d\lambda}{u_e+u_0}\right\}, \tag{73}$$

where

$$u_e = u_1 \frac{u_0 + u_1 \tanh u_1 h_1}{u_1 + u_0 \tanh u_1 h_1},$$

$$r_1^2 = (z+h)^2 + x^2 \text{ and } r_2^2 = (z-h)^2 + x^2. \tag{74}$$

For small values of the sheet thickness h_1 and large values of the conductivity σ, $\tanh u_1 h_1 \cong u_1 h_1$ and $\epsilon_1 \omega / \sigma_1 << 1$,
and therefore

$$u_1^2 h_1 = (\lambda^2 + \gamma_1^2) h_1 \cong 2iq, \tag{75}$$

where $q = \sigma_1 u_0 \omega h_1 / 2$. With these approximations, $u_e \cong u_0 + 2iq$ and then

$$E_0 \cong \frac{-i\mu_0 \omega I}{2\pi} \left[K_0(\gamma_0 r_1) - K_0(\gamma_0 r_2) + \int_0^\infty \frac{e^{u_0(z-h)} \cos \lambda x d\lambda}{u_0 + iq} \right]. \tag{76}$$

Using the result appropriate for large q,

$$\frac{1}{u_0 + iq} = \frac{1}{iq} \sum_{n=1}^{\infty} \left(\frac{u_0}{iq} \right)^m (-1)^m, \tag{77}$$

and noting

$$u_0^m e^{u_0(z-h)} = \left(\frac{\partial}{\partial z} \right)^{m+1} \frac{e^{u_0(z-h)}}{u_0}, \tag{78}$$

it follows that, asymptotically,[9]

$$E_0 \cong \frac{-i\mu_0 \omega I}{2\pi} \left[K_0(\gamma_0 r_1) - K_0(\gamma_0 r_2) + \sum_{m=0}^{\infty} \frac{(-1)^m}{(iq)^{m+1}} \left(\frac{\partial}{\partial z} \right)^{m+1} K_0(\gamma_0 r_2) \right], \tag{79}$$

where use has been made of the relation

$$\int_0^\infty \frac{e^{u_0(z-h)} \cos \lambda x d\lambda}{u_0} = K_0(\gamma_0 r_2), \tag{80}$$

valid for $(z-h) < 0$.

The field E_0 can thus be developed into an (asymptotic) series of inverse powers of qr_2 where the coefficients involve derivatives with respect of the modified Bessel functions. Using the relations $K_0' = -K_1$ and $K_0'' = -K_1' = K_0 + K_1/x$, the nth derivative of K_0 can be expressed in terms of K_0 and K_1. The first few terms of the resulting series are given below:

$$E_0 = \frac{-i\mu_0 \omega I}{2\pi} [K_0(\gamma_0 r_1) - K_0(\gamma_0 r_2) + T(\gamma_0 r_2, q)], \tag{81}$$

where

$$T(\gamma_0 r_2, q) \cong \sum_{m=0}^{\infty} \left(\frac{i}{q} \right)^{m+1} \left(\frac{\partial}{\partial z} \right)^m \left[\frac{\gamma_0 (z-h) K_1(\gamma_0 r_2)}{r_2} \right]$$

$$\cong \frac{i}{qr_2} \gamma_0 (z-h) K_1(\gamma_0 r_2) + \frac{1}{(qr_2)^2} \left[\gamma_0^2 (z-h)^2 K_0(\gamma_0 r_2) - \gamma_0 r_2 \left(1 - 2 \frac{(z-h)^2}{r_2^2} \right) K_1(\gamma_0 r_2) \right], \tag{82}$$

$$+ \text{terms containing } 1/(qr_2)^3, \quad 1/(qr_2)^4, \quad \text{etc.}, \tag{83}$$

where $qr_2 = \sigma_1 \mu_0 \omega h_1 r_2 / 2$ and $z < 0$.

It can be readily verified that the field below the thin conducting sheet ($z > h$) is given by

$$E_2 = -\frac{i\mu_0 \omega I}{2\pi} \left[T(\gamma_0 r_1, q) \right] \text{ for } z > 0. \tag{84}$$

As a check, it can be seen that $E_0 = E_2$ at $z = 0$. Expressions for the magnetic field components can be found from Maxwell's equations:

$$H_{mx} = \frac{1}{i\mu_0 \omega} \frac{\partial E_m}{\partial z} \quad \text{and} \quad H_{mz} = -\frac{1}{i\mu_0 \omega} \frac{\partial E_m}{\partial x} \quad \text{for } m = 0, 2.$$

[9] A more rigorous derivation of this series expansion is given in reference [7].

The above expansions developed in inverse powers of (qr_2) are particularly suitable for highly conductive sheets when the source *or* the observer are not near the sheet. Alternative expansions can be developed for smaller values of qr_2. These are developed as follows. At low frequencies where $\gamma_0 r_1$ and $\gamma_0 r_2$ are small compared to unity, γ_0 can be set equal to zero, and it readily follows that

$$E_0 = \frac{-i\mu_0\omega I}{2\pi}\left[\log\,(r_2/r_1) + T_0(\beta)\right], \tag{85}$$

where

$$T_0(\beta) = \int_0^\infty \frac{e^{-\lambda\beta}\cos\lambda x}{\lambda + iq}\,d\lambda \quad \text{and} \quad \beta = h - z. \tag{86}$$

Inserting the power-series expansion for $\cos\lambda x$, E_0 becomes

$$T_0(\beta) = \sum_{m=0}^{\infty}\frac{(-1)^m x^{2m}}{(2m!)}\int_0^\infty \frac{\lambda^{2m}e^{-\lambda\beta}d\lambda}{\lambda + iq}. \tag{87}$$

Since

$$\int_0^\infty \frac{e^{-\lambda\beta}}{\lambda + iq}\,d\lambda = -e^{+i\beta q}Ei(-i\beta q), \tag{88}$$

where

$$Ei(-i\beta q) = -\int_{+i\beta q}^{\infty}\frac{e^{-t}}{t}\,dt, \tag{89}$$

it follows that

$$T_0(\beta) = -\sum_{m=0}^{\infty}\frac{(-1)^m x^{2m}}{(2m!)}\,g^{2m}\left(\frac{\partial}{\partial g}\right)^{2m}\left[e^{ig}Ei(-ig)\right], \tag{90}$$

where $g = \beta q = (h-z)h_1\sigma_1\mu_0\omega/2$. This is an ascending-series expansion in g. When $x=0$, it reduces to

$$T_0(\beta) = -e^{i\beta q}Ei(-i\beta q). \tag{91}$$

Using the latter result, it follows that the field E_0 for $z<0$ and E_2 for $z>0$ in the plane $x=0$ is given by

$$E_0 = \frac{-i\mu_0\omega I}{2\pi}\left[\log\frac{|z-h|}{|z+h|} - e^{i|z-h|q}Ei(-i|z-h|q)\right], \tag{92}$$

for $z<0$, and

$$E_2 = \frac{+i\mu_0\omega I}{2\pi}\,e^{i|z+h|q}Ei(-i|z+h|q), \tag{93}$$

for $z>0$.

The exponential integral $Ei(-ig)$ with imaginary argument can be expressed in terms of the cosine and sine integrals as follows:

$$Ei(-ig) = Ci(g) + i\left[\frac{\pi}{2} - Si(g)\right], \tag{94}$$

where

$$Ci(g) = -\int_g^\infty \frac{\cos t}{t}\,dt \quad \text{and} \quad Si(g) = \int_0^g \frac{\sin t}{t}\,dt, \tag{95}$$

are tabulated [8] for real values of g.

It might be mentioned that $T_0(\beta)$ for $x>0$ can also be expressed in terms of exponential integrals, but then the argument is complex. For example,

$$\begin{aligned} T_0(\beta) &= \frac{1}{2}\int_0^\infty \frac{e^{-\lambda(\beta - ix)}}{\lambda + iq}\,d\lambda + \frac{1}{2}\int_0^\infty \frac{e^{-\lambda(\beta+ix)}}{\lambda + iq}\,d\lambda \\ &= -\frac{1}{2}e^{i\beta q}[e^{-iqx}Ei(-i(\beta - ix)q) + e^{iqx}Ei(-i(\beta + ix)q)]. \end{aligned} \tag{96}$$

Unfortunately, the exponential integral of general complex argument is not well tabulated.

8. Radiation Field of the Line Source for Any Number of Layers

The evaluation of the integrals for the general case of any number of layers is not readily carried out unless certain approximating conditions are introduced. The field E_0, for the case of the line source and the observer in the interface ($z=h=0$), is conveniently written

$$E_0=\frac{-i\mu_0\omega I}{2\pi}\int_0^\infty \frac{\cos\lambda x}{u_0+u_e}\,d\lambda, \tag{97}$$

where

$$u_e=u_1\left[\frac{(Y_2/N_1)+\tanh u_1h_1}{1+(Y_2/N_1)\tanh u_1h_1}\right], \tag{98}$$

where Y_2 is the wave admittance associated with the lower layers and is given by eq (48) et al. When h_1 becomes sufficiently large, it is seen that $u_e\cong u_1$ and the fields correspond to a homogeneous half-space.

Now, when the subsurface layers are highly conducting, such that $|\gamma_m|>>|\gamma_0|$, it follows that $u_m=(\lambda^2+\gamma_m^2)^{1/2}\cong\gamma_m$, since the important values of λ are when λ is of the order of $|\gamma_0|$. To this approximation

$$u_e\cong(\lambda^2+\gamma_e^2)^{1/2}\cong\gamma_e,$$

where γ_e can be regarded as an effective propagation constant. It is approximately given by

$$\frac{\gamma_e}{\gamma_1}\cong\left[\frac{(Y_2/N_1)+\tanh u_1h_1}{1+(Y_2/N_1)\tanh u_1h_1}\right]_{\lambda\sim0}. \tag{99}$$

For a two-layer medium ($h_2\to\infty$), $\gamma_e\cong\gamma_1/Q$, where

$$Q\cong\frac{(\gamma_1/\gamma_2)+\tanh\gamma_1h_1}{1+(\gamma_1/\gamma_2)\tanh\gamma_1h_1}, \tag{100}$$

which is identical to eq (13).

In analogy to eq (64) for the homogeneous half-space, the field E_0 for the stratified medium can be written

$$E_0\cong\frac{-i\mu_0\omega I\gamma_0}{\pi(\gamma_1^2-\gamma_2^2)x}K_1(\gamma_0x)Q^2 \quad \text{for } |\gamma_ex|>>1. \tag{101}$$

The factor Q^2 can be interpreted as a correction factor to account for the presence of stratification in the half space. A numerical discussion of Q has already been given.

9. Magnetic Line Source Over a Stratified Medium

In the previous section, a line source of electric current I over a stratified medium was discussed. The corresponding formal solution for a line source of magnetic current K is obtained by making the transformations: $I\to K$, $\sigma_m+i\epsilon_m\omega\to i\mu_m\omega$, $i\mu_m\omega\to\sigma_m+i\epsilon_m\omega$, $E_z\to H_z$, $H_x=-E_x$, and $H_y\to-E_y$. The nature of the resulting integrals in the solution are, however, more complicated than in the electric-current counterpart.

The integral form of the solution can be written, for $z<0$

$$H_0=\frac{-i\omega\epsilon_0K}{4\pi}\int_{-\infty}^{+\infty}[e^{\pm u_0(z+h)}+R_\parallel(\lambda)e^{u_0(z-h)}]e^{-i\lambda x}d\lambda, \tag{102}$$

where the $+$ sign is to be used for $(z+h)<0$ and the $-$ sign for $(z+h)>0$. The reflection coefficient is now given by

$$R_\parallel(\lambda)=\frac{K_0-Z_1}{K_0+Z_1}, \tag{103}$$

where K_0 and Z_1 have their usual meaning. For a homogeneous half-space, for example, $Z_1=K_1$ and if $\mu_1=\mu_0$,

$$R_{\parallel}(\lambda)=\frac{\gamma_1^2 u_0-\gamma_0^2 u_1}{\gamma_1^2 u_0+\gamma_0^2 u_1}.$$

The coefficient $R_{\parallel}(\lambda)$ can have a pole when $\gamma_1^2 u_0+\gamma_0^2 u_1=0$, which is the "resonance" condition discussed previously. This complicates the evaluation of the integral and eliminates the possibility of using the formulas developed for the line-current source in the previous section. (There was no pole in the reflection coefficient $R_{\perp}(\lambda)$ for a homogeneous half-space, because there is no solution of $u_0+u_1=0$.)

If attention is restricted, however, to the field a large distance from the surface, or if the height h is large, it can be expected that contributions from the pole (which are surface waves) are small compared to the specular component. Then with analogy to eq (57), the field is approximately given by

$$H_0\cong\frac{-i\epsilon_0\omega K}{2\pi}\{K_0[\gamma_0[x^2+(z+h)^2]]+R_{\parallel}(\bar{\theta})K_0[\gamma_0[x^2+(z-h)^2]]\}, \tag{104}$$

where $R_{\parallel}(\bar{\theta})$ is the reflection coefficient for a plane wave (parallel polarization) incident at an angle $\bar{\theta}$ on the interface ($z=0$) where $\tan\bar{\theta}=x/(z-h)$. This result is only valid in the asymptotic sense, and hence to the same accuracy the formula reads

$$H_0\cong\frac{-i\epsilon\omega K}{2\pi}\left(\frac{\pi}{2}\right)^{1/2}\left[\frac{e^{-\gamma_0 r_1}}{(\gamma_0 r_1)^{1/2}}+R_{\parallel}(\bar{\theta})\,\frac{e^{-\gamma_0 r_2}}{(\gamma_0 r_2)^{1/2}}\right], \tag{105}$$

where only the first term of the asymptotic expansion of K_0 has been retained. As can be verified by the saddle-point method (see next section), this result for H_0 quoted above is the first term of an asymptotic expansion.

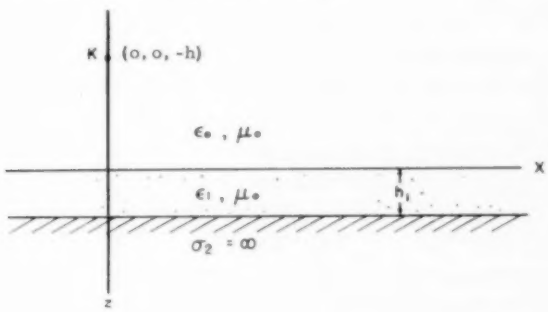

FIGURE 7. *Magnetic line source over a dielectric coated conductor.*

10. Magnetic Line Source Over a Dielectric Coated Conductor

As mentioned above, the integrals appearing in the solution for parallel polarization are complicated by the existence of poles. This occurs even in the case of a homogeneous half-space. Another relatively simple situation is when the upper layer is a pure dielectric and the region below is a metallic conductor [9]. The situation is illustrated in figure 7.

Noting that $Z_2=0$, the field for $z<0$ can be expressed by

$$H_0=\frac{-i\epsilon_0\omega K}{4\pi}\int_{-\infty}^{+\infty}\left[e^{\pm u_0(z+h)}+\frac{u_0-ik_0\Delta}{u_0+ik_0\Delta}\,e^{u_0(z-h)}\right]e^{-i\lambda x}d\lambda, \tag{106}$$

where

$$\Delta=\frac{K_1\tanh u_1 h_1}{\eta_0}\quad\text{and}\quad K_1=\frac{u_1}{\sigma_1+i\omega\epsilon_1}.$$

The integral has a pole where $u_0+ik_0\Delta=0$, and this is denoted by λ_1. Furthermore, there is a branch point where $u_0=0$, which is when $\lambda=k_0$. Now for small values of h_1 (i. e., $k_1 h_1<<1$) Δ is also small (compared to one), and therefore

$$\Delta\cong\frac{K_1u_1h_1}{\eta_0}\cong\frac{i\mu_0\omega h_1}{\eta_0}\left(1-\frac{k_0^2}{k_1^2}\right).$$

Therefore, to a first approximation, Δ does not depend on λ the integration variable, and the surface impedance $Z_1(\cong\eta_0\Delta)$ is almost purely inductive. The pole is then given by

$$\lambda_1\cong k_0[1+(k_0\bar{h})^2]^{1/2}\cong k_0[1+(k_0\bar{h})^2/2] \tag{107}$$

where $\bar{h}=h_1(1-k_0^2/k_1^2)$

The integral for H_0 is now in a form where it can be evaluated directly by the modified saddle-point method. A similar integral appears, in the case of a dipolar excitation. For the present purpose, however, it is possible to develop the first few terms of the asymptotic expansion in a direct manner.

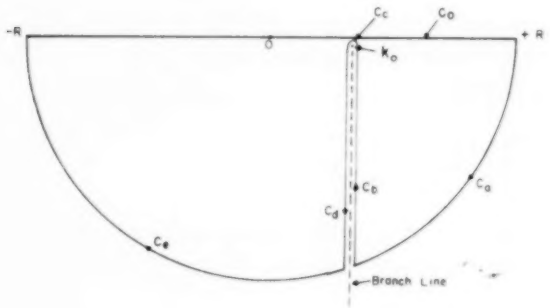

FIGURE 8. *Integration contour in the* λ *plane.*

The integration contour is shown in figure 8. The integration in the original integral is along C_0 from $-\infty$ to $+\infty$. The pole λ_1 and the branch point k_0 can have a small but vanishing negative imaginary part if the conductivity of the air and the dielectric is finite. The contour C_0 then passes above λ_1 and k_0 but passes below $-\lambda_1$ and $-k_0$.

Following standard practice in contour evaluation of integrals, the contour C_0 is closed by an infinite semicircle (C_a+C_e) in the lower plane, with an indentation along C_b, C_c, and C_d to the branch point at k_0. The integral along C_0 is then equal to integral along the complete closed contour C minus the individual contributions of C_a, C_b, C_c, C_d, and C_e. The contributions from C_a and C_b vanish as $R\to\infty$, since the real part of $u_0>0$. Furthermore, the integral along the branch lines can be obtained as an inverse series in x (which is asymptotic in nature) by expanding the integrand in a Taylor series and integrating term by term. The integral around the complete contour C is simply $-2\pi i$ times the residue at the pole λ_1. Finally, it follows that the integral along C_0 is $-2\pi i$ times the residue at λ_1 minus the contribution along the branch lines.

The final result reads, for $x>>(h-z)$

$$H_0=-\epsilon_0\omega K\left[\frac{u_p}{\lambda_1}e^{-u_ph}e^{+u_pz}e^{-i\lambda_1x}+\frac{e^{-i(k_0x+\pi/4)}}{\sqrt{2\pi}}\left(\frac{k_0}{u_p}\right)^2(1+u_pz)(1-u_ph)\cdot\frac{1}{(k_0x)^{3/2}}\right.$$

$$\left.\text{plus terms containing }\frac{1}{(k_0x)^{5/2}},\quad\frac{1}{(k_0x)^{7/2}},\quad\text{etc.}\right],$$

where

$$u_p=\sqrt{\lambda_1^2-k_0^2}=-ik_0\Delta. \tag{108}$$

The first term in the brackets is the residue at the pole λ_1, and the succeeding terms are from the branch-line integration. The latter series is asymptotic and is usable if

$$\left(\frac{k_0}{u_p}\right)^2 << (k_0 r),$$

which requires that the pole λ_1 is not too near k_0. Such a condition is violated when the thickness h_1 of the dielectric coating approaches zero. It is then necessary to apply the modified saddle-point method [10].

11. Fields of a Vertical Electric Dipole Over a Stratified Half-Space

In the previous section, the excitation of the fields over a stratified half-space was by a line source. In this case the problem is a two-dimensional one. It is the purpose of this section to mention the extension to the case where the source is a dipole. This problem was formally solved by Sommerfeld in 1909 for the homogeneous half-space.

A vertical electric dipole is to be located at $z=-h$ over the stratified region of M layers. The dipole is to be regarded as a current element of length ds carrying a current I.

The situation is illustrated in figure 9, where it is noted that cylindrical coordinates

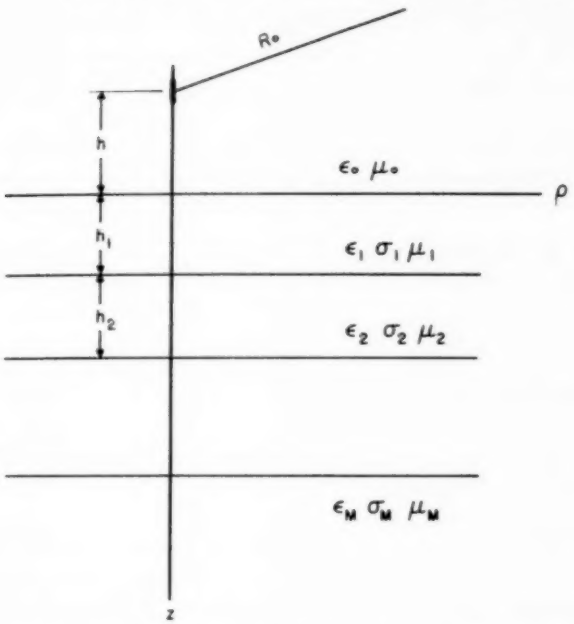

FIGURE 9. *Vertical electric dipole over an M-layered half-space.*

(ρ,ϕ,z) are employed with the z-axis pointing downward as usual. The primary influence in the upper region $(z<0)$ can be expressed in terms of a Hertz vector, which has only a z component π_z^p, which hereafter is denoted ψ^p. Furthermore,

$$\psi^p=\frac{Ids}{4\pi i\omega\epsilon_0}\frac{e^{-ik_0R_0}}{R_0}, \tag{109}$$

where

$$R_0=[\rho^2+(z+h)^2]^{1/2}.$$

It is now assumed that the total fields can be expressed everywhere in terms of a Hertz vector, which also has only a z component, denoted ψ_m. (The justification for doing this is attained by verifying that the final solution satisfies all the boundary conditions and behaves properly at the source and at infinity.) For the mth layer, ψ_m satisfies

$$(\nabla^2-\gamma_m^2)\psi_m=0, \tag{110}$$

except at the source where $\psi_0\to\psi^p$, for $R_0\to 0$. This suggests writing

$$\psi_0=\psi^p+\psi_0', \tag{111}$$

where ψ_0' is the "secondary influence". Since

$$(\nabla^2-\gamma_0^2)\psi^p=0, \tag{112}$$

then

$$(\nabla^2-\gamma_0^2)\psi^s=0. \tag{113}$$

In cylindrical coordinates and for azimuthal symmetry, the equation for ψ_m becomes

$$\left(\frac{1}{\rho}\frac{\partial}{\partial\rho}\rho\frac{\partial}{\partial\rho}+\frac{\partial^2}{\partial z^2}-\gamma_m^2\right)\psi_m=0. \tag{114}$$

It can be readily seen that solutions of this equation are made up of linear combinations of

$$e^{\pm u_m z}\begin{matrix}J_0(\lambda\rho)\\ Y_0(\lambda\rho)\end{matrix}$$

where, as usual, $u_m=(\lambda^2+\gamma_m^2)^{1/2}$, and $\gamma_m^2=(i\sigma_m\mu_m\omega-\epsilon_m\mu_m\omega^2)$, for $m=0, 1, 2 \ldots, M$. Again by convention, the real part of u_m is to be taken positively. Since the resulting solution is to be finite on the axis $\rho=0$ when $z\neq -h$, the $Y_0(\lambda\rho)$ Bessel function can be rejected because it behaves as log ρ for small values of ρ. The $J_0(\lambda\rho)$ Bessel function on the other hand, is finite at $\rho=0$.

As in the previous solution for the line source, the parameter λ can take any value (with a few exceptions). The general solution for ψ_m is then written in the form

$$\psi_m=\int_0^\infty [a_m(\lambda)e^{-u_m z}+b_m(\lambda)e^{u_m z}]J_0(\lambda\rho)d\lambda, \tag{115}$$

for $m=1, 2 \ldots, M-1$. In region (0), for $z>0$

$$\psi_0=\psi_p+\int_0^\infty b_0'(\lambda)e^{u_0 z}J_0(\lambda\rho)d\lambda, \tag{116}$$

and in region (M), for $z>z_{M-1}$

$$\psi_M=\int_0^\infty a_M(\lambda)e^{-u_m z}d\lambda. \tag{117}$$

To express ψ^p as an integral of the appropriate type, use is made of the Fourier-Bessel transforms, which read

$$f(\rho)=\int_0^\infty g(\lambda)J_0(\lambda\rho)\lambda d\lambda, \tag{118}$$

and

$$g(\lambda)=\int_0^\infty f(\rho)J_0(\lambda\rho)\rho d\rho, \tag{119}$$

subject to the conditions that the integrals exist. Letting $f(\rho)=e^{-ik_0\rho}/\rho$,

$$g(\lambda)=\int_0^\infty e^{-ik_0\rho}J_0(\lambda\rho)d\rho. \tag{120}$$

This integral is a standard type [5] and is given by

$$g(\lambda)=\frac{1}{(\lambda^2-k_0^2)^{1/2}}=\frac{1}{u_0}, \tag{121}$$

and therefore

$$\frac{e^{-ik_0\rho}}{\rho}=\int_0^\infty \frac{J_0(\lambda\rho)}{(\lambda^2-k_0^2)^{1/2}}\lambda d\lambda=\frac{e^{-ik_0R_0}}{R_0}\Big|_{z=-h}. \tag{122}$$

To generalize the preceding to any other value of z, the integrand must contain the factor $e^{\pm u_0(z+h)}$ because $e^{-ik_0R_0}/R$ is a solution of the wave equation and necessarily becomes $e^{-ik_0\rho}/\rho$ as $z\to -h$. Consequently,

$$\frac{e^{-ik_0R_0}}{R_0}=\int_0^\infty \frac{J_0(\lambda\rho)e^{\pm u_0(z+h)}}{u_0}\lambda d\lambda, \tag{123}$$

where the sign of the exponent is chosen so that the integral converges.
(i. e., + for $(z+h)<0$ and − for $(z+h)>0$).

The z component of the Hertz vector for the upper region ($z<0$) can then be written

$$\psi_0=\int_0^\infty \left[a_0\frac{e^{\pm(z+h)u_0}}{u_0}+b(\lambda)\frac{e^{u_0(z-h)}}{u_0}\right]J_0(\lambda\rho)\lambda d\lambda, \tag{124}$$

where

$$a_0=\frac{Ids}{4\pi i\omega\epsilon_0} \quad \text{and} \quad b(\lambda)$$

is to be determined from the boundary conditions. Now

$$E_{m\rho}=\frac{\partial^2\psi_m}{\partial\rho\partial z}, \quad E_{m\phi}=0, \quad E_{mz}=\left(-\gamma_m^2+\frac{\partial^2}{\partial z^2}\right)\psi_m, \tag{125}$$

and

$$H_{m\rho}=0, \quad H_{m\phi}=\frac{-\gamma_m^2}{i\mu_m\omega}\frac{\partial\psi_m}{\partial\rho}, \quad H_{mz}=0, \tag{126}$$

and since $E_{m\rho}$ and $H_{m\phi}$ are continuous at the interfaces $z_m(m=0$ to $M-1)$, it follows that $\partial\psi_m/\partial z$ and $(\sigma_m+i\omega\epsilon_m)\psi_m$ are also continuous at the same interfaces. This leads to $2(M-1)$ equations to solve for the $2(M-1)$ unknown coefficients. It readily follows that

$$\frac{b_0(\lambda)}{a_0}=R(\lambda)=\frac{K_0(\lambda)-Z_1(\lambda)}{K_0(\lambda)+Z_1(\lambda)}, \tag{127}$$

where

$$Z_m(\lambda)=K_m(\lambda)\cdot\frac{Z_{m+1}(\lambda)+K_m(\lambda)\tanh u_mh_m}{K_m(\lambda)+Z_{m+1}(\lambda)\tanh u_mh_m}. \tag{128}$$

The algebraic form of $R(\lambda)$ is identical to eq (5) for the plane-wave reflection coefficient for parallel incidence. It is thus clear that the field of a dipole over a stratified half-space can be regarded as a spectrum of plane waves whose angle θ of incidence and reflection is related to the variable λ by $\lambda=k_0\sin\theta$. In this case, the wave normals generate a family of cones coaxial with the z-axis.

Equations (127) and (128) in conjunction with eq (124) constitute the complete formal solution. Approximate evaluations [10] can be carried out by using the same approach as in the previous sections or by a modified saddle-point method [11]. In view of the similarity with the line-source excitation, it does not seem justified to discuss this in detail, and the essential results will simply be quoted.

As has been demonstrated, $Z_1(\lambda)$ for a highly conducting half-space or even for a dielectric coated conductor, is mainly determined by the electrical properties of the layers. In other words, $R(\lambda)$ can be replaced by

$$R(\lambda)=\frac{u_0-ik_0\Delta}{u_0+ik_0\Delta}, \tag{129}$$

where $\Delta=Z_1/\eta_0=Z_1/120\pi$ is assumed to be constant. The form of ψ_0 is then

$$\psi_0=\frac{Ids}{4\pi i\omega\epsilon_0}\int_0^\infty\left[e^{\pm u_0(z+h)}+\frac{u_0-ik_0\Delta}{u_0+ik_0\Delta}e^{u_0(z-h)}\right]J_0(\lambda\rho)d\lambda. \tag{130}$$

This can be rewritten as follows:

$$\psi_0=\frac{Ids}{4\pi i\omega\epsilon_0}\left[\frac{e^{-ik_0R_0}}{R_0}+\frac{e^{-ik_0R_1}}{R^1}-2P\right], \tag{131}$$

where

$$R_0=[\rho^2+(z+h)^2]^{1/2}, \quad R_1=[\rho^2+(z-h)^2]^{1/2},$$

and

$$P=\int_0^\infty \frac{(ik_0\lambda\Delta)\, e^{-u_0(h-z)}}{(u_0+ik_0\Delta)\, u_0} J_0(\lambda\rho)d\lambda. \tag{132}$$

This integral has been previously evaluated [10, 11]. Subject to $|\Delta|<<1$, it is given by

$$P\cong i(\pi p_e)^{1/2}\, e^{-w}\,\mathrm{erfc}(iw^{1/2})\,\frac{e^{-ik_0R_1}}{R_1} \tag{133}$$

where

$$w=p_e\left(1+\frac{h-z}{\Delta R_1}\right)^2,$$

$$p_e=\frac{-ik_0R_1}{2}\Delta^2=|p_e|e^{ib},$$

and

$$\mathrm{erfc}\,(iw^{1/2})=\frac{2}{\sqrt{\pi}}\int_{iw^{1/2}}^\infty e^{-x^2}dx.$$

The expression for P can also be written

$$P=\frac{p_e}{w}\left[1-F(w)\right]\frac{e^{-ik_0R_1}}{R_1}, \tag{134}$$

where

$$F(w)=1-i(\pi w)^{1/2}e^{-w}\mathrm{erfc}\,(iw^{1/2}). \tag{135}$$

It is noted that when $z=h=0$,

$$\psi_0=\frac{Ids}{2\pi i\omega\epsilon_0}\frac{e^{-ik_0\rho}}{\rho}F(p_e),$$

and the vertical electric field is given by

$$E_{oz}\cong\frac{i\mu\omega Ids}{2\pi\rho}e^{-ik\rho0}F(p_e) \quad \text{for } k_0\rho>>1.$$

The function $F(p_e)$ can be regarded as the correction to the field of a dipole on the surface of a perfectly conducting plane. For $|p|<<1$, it approaches unity. $F(p_e)$ has the same functional form as the ground-wave attenuation of Norton [6] who presented numerical values for the case where (in the present notation) b is in the quadrant 0° to −180°. For a homogeneous ground Δ has a phase angle in the range 0° (for a perfect dielectric) to 45° (for a good conductor). The corresponding values of b are −90° and 0°, respectively. For a stratified ground, however, the phase angle of Δ may be outside this range. In the particular case of a two-layer conducting half-space, the parameter p_e can be written

$$p_e=p_1Q^2, \quad \text{where } p_1=\frac{-ik_0\rho}{2}(\eta_1/\eta_0)^2,$$

and where

$$Q=|Q|e^{iq}\cong\frac{(\gamma_1/\gamma_2)+\tanh\gamma_1h_1}{1+(\gamma_1/\gamma_2)\tanh\gamma_1h_1},$$

in terms of the propagation constants γ_1 and γ_2 of the upper and lower layers and the thickness h_1 of the upper layer. This function Q is discussed in section 2. From figure 3b it is seen that

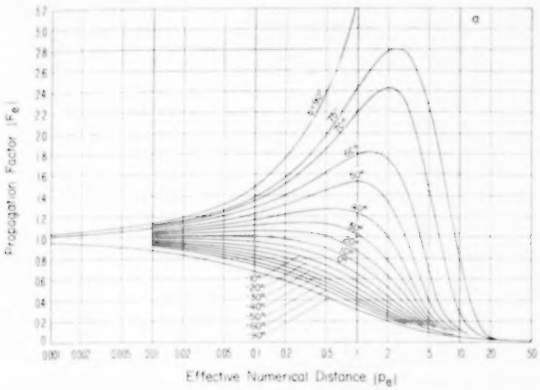

FIGURE 10a. *Amplitude of propagation factor for an impedance boundary.*

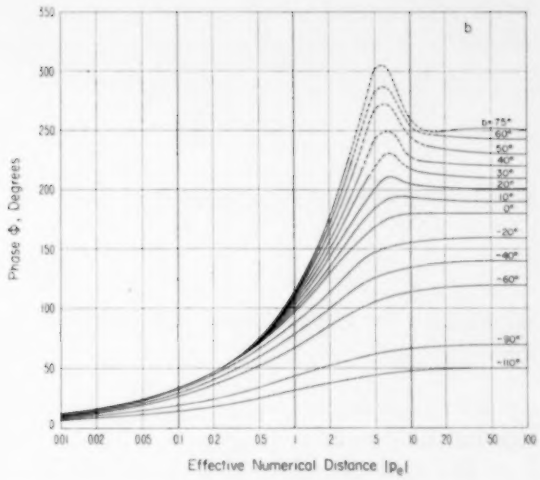

FIGURE 10b. *Phase of the propagation factor for an impedance boundary.*

for a highly conducting substratum q can become positive. Consequently, the phase angle b can exceed 0 and would approach 90° for $|\gamma_2/\gamma_1|\to\infty$, and $\gamma_1 h_1 << 1$.

In analogy to the terminology introduced by Sommerfeld for the homogeneous half-space, p_e is here described as an effective numerical distance. The propagation factor $F_e=|F_e|e^{-i\Phi}$, is shown plotted in figures 10a and 10b, as a function of $|p_e|$ for a range of b values. The curves for $b<0$ correspond to those computed by Norton, and it is interesting to note that for this region, $|F_e|$ never exceeds unity. On the other hand, when $b>0$, $|F_e|$ may exceed unity, and for $b=90°$ this effect is most pronounced. Apparently, in the case where b is positive, the energy is being guided to some extent along the surface. This effect can be seen in the asymptotic development of $F(p_e)$, which, for $|p_e|>>1$, reads

$$F(p_e)\cong -\frac{1}{2p_e}-\frac{1\cdot 3}{(2p_e)^2}-\frac{1\cdot 3\cdot 5}{(2p_e)^3}-\frac{1\cdot 3\cdot 5\cdot 7}{(2p_e)^4}-\cdots \tag{136}$$

when $-2\pi<b<0$, and

$$F(p_e)\cong -2i\sqrt{\pi p_e}e^{-p_e}-\frac{1}{2p_e}-\frac{1\cdot 3}{(2p_e)^2}-\frac{1\cdot 3\cdot 5}{(2p_e)^3}-\cdots \tag{137}$$

when $2\pi>b>0$.

The term $-2i\sqrt{\pi p_e}e^{-p_e}$ has all the characteristics of a surface wave. It is not present in the asymptotic development when b is negative. At $b=0$, 2π, or -2π, p_e is real, and this term vanishes asymptotically. The trapped surface wave is most predominant when $b=90°$, which corresponds to Δ or Z_1 being positive imaginary. For example, if the surface is coated by a thin dielectric film of thickness h_1 with a dielectric constant ϵ_1,

$$Z_1\cong i\mu\omega h_1[1-\epsilon_0/\epsilon_1]\cong iX_1, \tag{138}$$

which is purely imaginary. Then, since

$$p_e=\frac{-ik_0\rho}{2}\,(Z_1/\eta_0)^2, \tag{139}$$

$p_e=|p_e|e^{i\pi/2}$, or $b=\pi/2$ radians$=90°$. The attenuation factor now has the asymptotic development

$$F(p_e)\cong -2e^{i3\pi/4}\sqrt{\pi|p_e|}e^{-i|p_e|}+\frac{i}{2|p_e|}+\frac{3}{4|p_e|^2}-\frac{15i}{8|p_e|^3}\cdots \tag{140}$$

where

$$|p_e| = \frac{k_0\rho}{2}\frac{X^2}{\eta_0^2},$$

and the vertical electric field is

$$E_{0z} \cong \frac{i\mu\omega Ids}{2\pi\rho}\, e^{-ik_0\rho} F(p_e), \tag{141}$$

which shows that the (trapped) surface wave component varies as

$$\frac{1}{\sqrt{k_0\rho}}\, e^{-ik_0\left(1+\frac{X^2}{2\eta_0^2}\right)\rho},$$

which has the characteristics of a cylindrical wave traveling in the positive ρ with a phase velocity

$$\left(1+\frac{X^2}{2\eta_0^2}\right)^{-1}$$

times that of light.

The (trapped) surface wave is not excited when b is negative, and then the distant electric field varies asymptotically as

$$\frac{1}{(k_0\rho)^2}\, e^{-ik_0\rho},$$

which has a phase velocity equal to that of light.

When the source dipole and the observer are both raised above the surface (i.e., $h>0$ and $-z>0$), the field in the upper half-space can be expressed conveniently in the asymptotic sense as the sum of three partial fields in the manner

$$\psi_0 \cong [\psi_a + \psi_b + \epsilon\psi_s]\frac{Ids}{4\pi i\omega\epsilon_0}, \tag{142}$$

where $\epsilon=0$ for $b<0$, and $\epsilon=1$ for $b>0$. An asymptotic development shows that

$$\psi_a \cong \frac{e^{-ikR_0}}{R_0} + \frac{C-\Delta}{C+\Delta}\frac{e^{-ikR_1}}{R_1}, \tag{143}$$

$$\psi_b = -\left\{\frac{1}{p(1+C/\Delta)^3} + \frac{1\cdot 3}{2p^2(1+C/\Delta)^5} + \frac{1\cdot 3\cdot 5}{4p^3(1+C/\Delta)^7} + \cdots\right\}\frac{e^{-ikR_1}}{R_1}, \tag{144}$$

and

$$\psi_s \cong -\frac{2\Delta}{\Delta+C}\,[2i\sqrt{\pi w}\, e^{-w}]\,\frac{e^{-ikR_1}}{R_1}, \tag{145}$$

where

$$C = \frac{h-z}{R_1} = \frac{h+|z|}{R_1},\ k = 2\pi/\text{wavelength} = k_0,$$

and $\Delta = Z_1/\eta_0$.

In terms of ψ_0, the vertical electric field components for $k_0\rho >> 1$ is given by $E_{0z} \cong k_0^2(1-C^2)\psi_0$.

In the above, ψ_a can be identified as a geometrical optical term being just the primary field e^{-ikR_0}/R_0 and a specularly reflected component e^{-ikR_1}/R_1 modified by a reflection coefficient $(C-\Delta)/(C+\Delta)$. ψ_b is an asymptotic expansion containing terms varying as R_1^{-2}, R_1^{-3}, etc. ψ_s, which is only present for positive b values, represents a (trapped) surface wave and has a phase velocity less than that of light. When b is negative there is no (trapped) surface wave present.

Sometimes ψ_a itself is called a space wave and ψ_b a surface wave. This usage would correspond to that of Norton [3]. This would be an obvious designation when the half-space is homogeneous because ψ_s is zero, and there is no trapped surface wave excited.

Equations (143), (144), and (145) enable one to compute the field in the upper half-space ($z<0$) for an electric dipole located at $z=-h$ in terms of the ratio Δ of the surface im-

pedance Z_1 to that of free space η_0. As a first approximation, Z_1 could be replaced by $Z_1(\lambda)$ for $\lambda=0$, which would be the normal surface impedance. Clearly, a better value would be $Z_1(\lambda_s)$, where λ_s is the saddle point of the integral in eq (130) or (132). This would mean that

$$\Delta=\frac{Z_1(\lambda_s)}{\eta_0}, \tag{146}$$

where $\lambda_s=k_0S$, where $S=\rho/R_1=\sqrt{1-C^2}$. For a homogeneous half-space, with $\mu_1=\mu_0$,

$$\Delta=\frac{K_1(\lambda_s)}{\eta_0}=\frac{u_1(\lambda_s)}{(\sigma_1+i\omega\epsilon_1)\eta_0} \tag{147}$$

$$=\frac{\eta_1}{\eta_0}\left(1-\frac{\eta_1^2}{\eta_0^2}S^2\right)^{-\frac{1}{2}}. \tag{148}$$

The coefficient $(C-\Delta)/(C+\Delta)$ in eq (143) now can be identified as the Fresnel reflection coefficient for a plane wave with parallel polarization incident at angle θ. The equations are now in complete agreement with the results of Norton [6] for a vertical electric dipole over a homogeneous conducting ground.

The corresponding treatment for a vertical magnetic dipole located at $z=-h$ over the M layered half-space is almost identical to the above. The quantity ψ_0 is then to be identified with the z component of the magnetic Hertz vector, and then Δ is to be defined by $\Delta=\eta_0 Y_1$, where Y_1 is the surface admittance at the interface $z=0$.

12. Appendix

12.1. Effect of a Transition Region on Reflection

The reflection problems considered above were entirely concerned with layered media. Each layer was assumed to be homogeneous and bounded by a sharp interface.

In certain instances the dielectric constant or magnetic permeability can be regarded to vary in a simple analytical fashion. In such cases, it is sometimes possible to obtain a solution of Maxwell's equations in terms of known functions. The reflection coefficient for a medium in which the dielectric constant may be expressed as a power of one coordinate has been considered in great detail by Försterling [12]. The hyperbolic transition has been considered by Rydbeck [14].

In this appendix, a treatment of the linear transition between two lossless dielectrics will be given. Actually, this is a special case of Försterling's model, but the mathematics is somewhat simpler.

The situation is illustrated in figure 11. A plane wave is incident at angle θ from the air

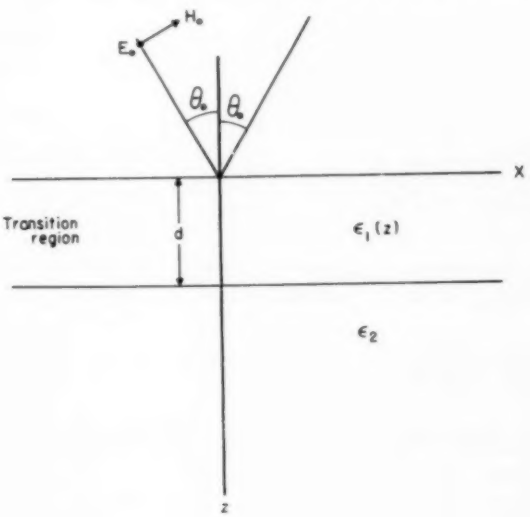

FIGURE 11. *Illustrating a plane-wave incident on a linear transition region.*

to an interface at $z=0$. The electric vector is perpendicular to the plane of incidence. The dielectric constant between $z=0$ and $z=d$ is a function of the coordinate z and denoted $\epsilon_1(z)$. The region below, $z>d$, has a dielectric constant ϵ_2, which does not vary with z. The magnetic permeability of the whole space is taken as μ_0 and assumed to be constant.

The electric field, which has only a y component, can then be written

$$E_0=[e^{-ik_{0z}\cos\theta}+Re^{ik_{0z}\cos\theta_0}]\,e^{-ik_{0x}\sin\theta_0} \quad \text{for } z<0, \tag{149}$$

and

$$E_2=Te^{-ik_{2z}\cos\theta_2}e^{-ik_{0x}\sin\theta_0} \quad \text{for } z>d, \tag{150}$$

where θ_2 is related to θ_1 by $k_2\sin\theta_2=k_0\sin\theta_0$. The constants R and T are to be determined by the boundary conditions at $z=0$ and $z=d$.

Within the transition layer, the field components satisfy Maxwell's equations

$$\frac{\partial E_1}{\partial z}=i\mu_0\omega H_{1x}, \tag{151a}$$

$$i\mu_0\omega H_{1z}=ik_0\sin\theta_0 E_1, \tag{151b}$$

and

$$\frac{\partial H_{1x}}{\partial z}=i[\epsilon_1(z)-\epsilon_0\sin^2\theta_0]\omega E_1, \tag{151c}$$

where E_1 is the y component of the electric field in the transition region. For a linear transition,

$$\epsilon_1(z)=\epsilon_0(1+\beta z), \tag{152}$$

where $\beta=(\epsilon_2-\epsilon_0)/\epsilon_0 d$. A new variable W is now introduced, defined by

$$W=W_0\left(1+\frac{\beta z}{\cos^2\theta}\right)^{3/2} \quad \text{and} \quad W_0=\frac{2(\epsilon_1^{1/2}\cos^3\theta)}{3\beta}. \tag{153}$$

Equation (151a) and (151b) can then be written

$$\epsilon^{1/2}\frac{dE_1}{dW}=i\mu_0\omega H_{1x} \quad \text{and} \quad \frac{dH_{1x}}{dW}=i\omega\epsilon^{1/2}E_1, \tag{154}$$

where $\epsilon=\epsilon_1(z)-\epsilon_0\sin^2\theta$. (155)

These equations are combined to give

$$\left(\frac{d^2}{dW^2}+\frac{1}{2\epsilon}\frac{d\epsilon}{dW}\frac{d}{dW}+\omega^2\mu_0\right)E_1=0. \tag{156}$$

But, since $\epsilon=\text{const.}\times W^{2/3}$,

$$\frac{1}{2\epsilon}\frac{d\epsilon}{dW}=\frac{1}{3W}. \tag{157}$$

Furthermore, if the substitution

$$E_1=W^{1/2}\psi \tag{158}$$

is made, ψ satisfies the equation

$$W^2\frac{d^2\psi}{dW^2}+W\frac{d\psi}{dW}+\left(\mu\omega^2W^2-\frac{1}{3^2}\right)\psi=0, \tag{159}$$

which is Bessel's equation of order 1/3. Independent solutions are $J_{1/3}(\omega\mu^{1/2}W)$ and $J_{-1/3}(\omega\mu^{1/2}W)$.

The general solution for E_1 is then written

$$E_1=(W/W_0)^{1/3}[AJ_{1/3}(\omega\mu^{1/2}W)+BJ_{-1/3}(\omega\mu^{1/2}W)]\times\exp(-ik_0x\sin\theta_0), \tag{160}$$

where A and B are constants. The magnetic-field components are obtained from

$$H_{1z}=\frac{1}{i\mu_0\omega}\frac{\partial E_1}{\partial z}\quad\text{and}\quad H_{1z}=\frac{k_0\sin\theta}{\mu_0\omega}E_1, \tag{161}$$

and need not be written out.

The four unknown constants R, T, A, and B are obtained by matching the tangential fields at $z=0$ and $z=d$. That is,

$$\left.\begin{aligned}E_0&=E_1\\\frac{\partial E_0}{\partial z}&=\frac{\partial E_1}{\partial z}\end{aligned}\right]_{z=0}\quad\text{and}\quad\left.\begin{aligned}E_1&=E_2\\\frac{\partial E_1}{\partial z}&=\frac{\partial E_2}{\partial z}\end{aligned}\right]_{z=d} \tag{162}$$

Omitting algebraic details, the expression for the reflection coefficient can be finally written

$$R=\frac{1-G}{1+G}, \tag{163}$$

where

$$G=\frac{(a_1p_0+q_0b_1)-i(p_0q_1-q_0p_1)}{(b_0q_1+a_0p_1)-i(a_0b_1-a_1b_0)}, \tag{164}$$

where

$$a_0=J_{1/3}(x_0),\quad p_0=J_{2/3}(x_0),$$

$$b_0=J_{-1/3}(x_0),\quad q_0=J_{-2/3}(x_0),$$

$$a_1=J_{1/3}(x_1),\quad p_1=J_{2/3}(x_1),$$

$$b_1=J_{-1/3}(x_1),\quad q_1=J_{-2/3}(x_1),$$

with

$$x_0=\frac{\alpha}{N^2-1}\cdot\frac{4\pi}{3},\quad x_1=\frac{\alpha N^3}{N^2-1}\cdot\frac{4\pi}{3},$$

and

$$\alpha=\frac{k_0l}{2\pi}\cos\theta_0=\frac{d}{\lambda_0}\cos\theta_0,$$

$$N=\frac{(\epsilon_2/\epsilon_0-\sin^2\theta_0)^{1/2}}{\cos\theta}.$$

Employing tables of fractional order Bessel functions [15], the magnitude of the reflection coefficient $|R|$, is plotted in figure 12 as a function of α or $(d/\lambda_0)\cos\theta_0$. The abscissa is proportional to the thickness of the transition region. Two values of N are chosen, 3 and 5.

It is immediately apparent that the effect of the transition region is to reduce the reflection coefficient. For small values of $(d\cos\theta_0/\lambda_0)$, the reflection is governed almost entirely by the (normalized) relative refractive index N. In fact, as $d\to 0$, it is readily seen that

$$R=\frac{1-N}{1+N}=\frac{\cos\theta_0-(\epsilon_2/\epsilon_1-\sin^2\theta_0)^{1/2}}{\cos\theta+(\epsilon_2/\epsilon_1-\sin^2\theta_0)^{1/2}}, \tag{165}$$

which is the classical Fresnel formula for perpendicular incidence. As seen in figure 12 $|R|=0.5$ for $N=3$, and $d=0$; $|R|=0.666$ for $N=5$; and $d=0$.

In the language of transmission line theory, the transition layer is acting as a matching

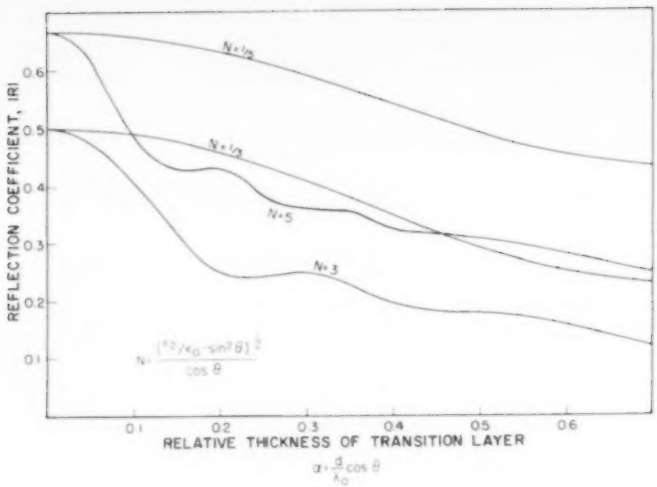

FIGURE 12. *Reflection coefficient for a linear transition layer.*

section. Its function is to match the impedance in the air region ($z<0$) to that of the lower region ($z>d$).

The simplicity of the above analysis is due primarily to the choice of the polarization of the incident wave. In the corresponding problem for parallel incidence, the resulting equations for the magnetic field component in the transition layer are not expressible in terms of Bessel functions.

I thank K. A. Norton for advice and H. E. Bussey and A. G. McNish for constructive criticism of the manuscript.

13. References

[1] J. C. Zenneck, Ann. Phys. **23,** 846 (1907).
[2] A. N. Sommerfeld, The propagation of waves in wireless telegraphy, Ann. Phys. **4,** 665 (1909).
[3] K. A. Norton, Propagation of radio waves over a plane earth, Nature **135,** 954 (June 1935); K. A. Norton, The propagation of radio waves over the earth and in the upper atmosphere, pt. I, Proc, IRE **24,** 1367 (Oct. 1936); pt. II, Proc, IRE **25,** 1203 (Sept. 1937). K. A. Norton, The calculation of ground-wave field intensity over a finitely conducting sperical earth, Proc. IRE **29,** 623 (Dec. 1941).
[4] J. R. Wait, Propagation of radio waves over a stratified ground, Geophysics **18,** 416 (April 1953).
[5a] S. S. Atwood, Surface wave propagation over a coated plane conductor, J. Appl. Phys. **22,** 504 (1951).
[5b] G. Goubau, On the excitation of surface waves, Proc. Inst. Radio Engrs. **40,** 865 (1952).
[6] G. Campbell and R. Foster, Fourier integrals for practical application (Van Nostrand Co. Ltd., New York, N. Y., 1948).
[7] J. R. Wait, Fields of a line current source over a stratified conductor, Appl. Sci. Research, sec. B **3** (1953).
[8] E. Jahnke and F. Emde, Tables of functions, 4th ed. (Dover Publications, New York, N. Y., 1945).
[9] A. L. Cullen, The excitation of plane surface waves, Inst. Elect. Engrs. Monograph No. 93 (Feb. 1954).
[10] J. R. Wait, Excitation of surface waves on conducting, stratified, dielectric-clad, and corrugated surfaces, J. Research NBS **59,** 365 (1957) RP2807.
[11] J. R. Wait, Radiation from a vertical dipole over a stratified ground, pt. I, Trans. IRE, **AP–1,** 9 (July 1953) and pt. II, Trans. IRE **AP–2,** 144 (Oct. 1954).
[12] Karl Forsterling, On reflection in a non-homogeneous medium, Ann. Phys. **11,** 1 (1931) and **8,** (new series) 129 (1950).
[13] P. S. Epstein, Reflection of waves in an inhomogeneous absorbing medium, Proc. Nat. Acad. Sci. Am. **16,** 627 (1930).
[14] O. Rydbeck, The reflection of electromagnetic waves from a parabolic ionized layer, Phil. Mag. **34,** 342 (1943).
[15] Tables of bessel functions of fractional order (Columbia University Press, 1949).

BOULDER, COLO., February 1958.

THE NATIONAL BUREAU OF STANDARDS

The scope of activities of the National Bureau of Standards at its headquarters in [illegible] and its major laboratories in Boulder, Colorado, is suggested in the following listing of the [illegible] engaged in technical work. In general, each section carries out specialized research, [illegible] in the field indicated by its title. A brief description of the activities, and of the [illegible] appears on the inside front cover.

WASHINGTON, D. C.

Electricity and Electronics. Resistance and Reactance. Electron Devices. [illegible] Magnetic Measurements. Dielectrics. Engineering Electronics. Electronic Instrumentation. [illegible]

Optics and Metrology. Photometry and Colorimetry. Optical Instruments. [illegible] Length. Engineering Metrology.

Heat. Temperature Physics. Thermodynamics. Cryogenic Physics. Rheology. Engine Fuels. Free Radicals Research.

Atomic and Radiation Physics. Spectroscopy. Radiometry. Mass Spectrometry. Solid State Physics. Electron Physics. Atomic Physics. Neutron Physics. Radiation Theory. Radioactivity. X-rays. High Energy Radiation. Nucleonic Instrumentation. Radiological Equipment.

Chemistry. Organic Coatings. Surface Chemistry. Organic Chemistry. Analytical Chemistry. Inorganic Chemistry. Electrodeposition. Molecular Structure and Properties of Gases. Physical Chemistry. Thermochemistry. Spectrochemistry. Pure Substances.

Mechanics. Sound. Mechanical Instruments. Fluid Mechanics. Engineering Mechanics. Mass and Scale. Capacity, Density, and Fluid Meters. Combustion Controls.

Organic and Fibrous Materials. Rubber. Textiles. Paper. Leather. Testing and Specifications. Polymer Structure. Plastics. Dental Research.

Metallurgy. Thermal Metallurgy. Chemical Metallurgy. Mechanical Metallurgy. Corrosion. Metal Physics.

Mineral Products. Engineering Ceramics. Glass. Refractories. Enameled Metals. Concreting Materials. Constitution and Microstructure.

Building Technology. Structural Engineering. Fire Protection. Air Conditioning, Heating, and Refrigeration. Floor, Roof, and Wall Coverings. Codes and Safety Standards. Heat Transfer.

Applied Mathematics. Numerical Analysis. Computation. Statistical Engineering. Mathematical Physics.

Data Processing Systems. SEAC Engineering Group. Components and Techniques. Digital Circuitry. Digital Systems. Analog Systems. Application Engineering.

Office of Basic Instrumentation. **Office of Weights and Measures.**

BOULDER, COLORADO

Cryogenic Engineering. Cryogenic Equipment. Cryogenic Processes. Properties of Materials. Gas Liquefaction.

Radio Propagation Physics. Upper Atmosphere Research. Ionospheric Research. Regular Propagation Services. Sun-Earth Relationships. VHF Research.

Radio Propagation Engineering. Data Reduction Instrumentation. Modulation Systems. Navigation Systems. Radio Noise. Tropospheric Measurements. Tropospheric Analysis. Radio Systems Application Engineering. Radio Meteorology.

Radio Standards. High Frequency Electrical Standards. Radio Broadcast Service. High Frequency Impedance Standards. Electronic Calibration Center. Microwave Physics. Microwave Circuit Standards.

Recent Publications of the National Bureau of Standards

Periodicals

Journal of Research of the National Bureau of Standards, Volume 61, No. 1, July 1958 (RP2877 to RP2885 incl.). 60 cents. Annual subscription $4.00, $1.25 additional for foreign mailing.

Technical News Bulletin, Volume 42, No. 7, July 1958. 10 cents. Annual subscription $1.00, 35 cents additional for foreign mailing.

Basic Radio Propagation Predictions for October 1958. Three months in advance. CRPL-D 167. Issued July 1958. 10 cents. Annual subscription $1.00, 25 cents additional for foreign mailing.

Applied Mathematics Series

AMS51. Tables of the exponential integral for complex arguments. $4.50.*

AMS53. Table of natural logarithms for arguments between five and ten to sixteen decimal places. $3.00.*

Circulars

C594. Preparation, maintenance, and application of standards of radioactivity. 35 cents.*

Available from the Superintendent of Documents, U. S. Government Printing Office, Washington 25, D. C. The three NBS periodicals are available on a $1, $2, or $3 per subscription basis, although no reduction in rates can be made.

**Foreign postage, one-fourth additional.*

UNITED STATES
GOVERNMENT PRINTING OFFICE
DIVISION OF PUBLIC DOCUMENTS
WASHINGTON 25, D. C.

OFFICIAL BUSINESS

PENALTY FOR PRIVATE USE TO AVOID PAYMENT OF POSTAGE, $300 (GPO)

Journal of Research of the National Bureau of Standards Vol. 61, No. 3 September 19

Contents

		Page
Vibration-rotation bands of ammonia: 1. The combination bands $\nu_2+(\nu_1,\nu_3)$. William S. Benedict, Earle K. Plyler, and Eugene D. Tidwell.	RP2894	123
Evaluation of tensile, compression, torsional, transverse, and impact tests and correlation of results for brittle-cermets. Matthew J. Kerper, Lewis E. Mong, Maurice B. Stiefel, and Sylvanus F. Holley.	RP2895	149
Redetermination of mass spectra of deuteromethanes. Fred L. Mohler, Vernon H. Dibeler, and Edith Quinn.	RP2896	171
Effect of strain-temperature history on the tensile behavior of titanium and a titanium alloy. Glenn W. Geil and Nesbit L. Carwile.	RP2897	173
Propagation of very-low-frequency pulses to great distances. James R. Wait.	RP2898	187
Transmission and reflection of electromagnetic waves in the presence of stratified media. James R. Wait.	RP2899	205

[A list of recent NBS publications is given on page 3 of the cover.]

For sale by the Superintendent of Documents, U. S. Government Printing Office, Washington 25, D. C. Price 60 cents (single co
Subscription price: $4.00 a year; $1.25 additional for foreign mailing.

UNITED STATES GOVERNMENT PRINTING OFFICE, WASHINGTON : 1958